

Dominic Dirkx
Erwin Mooij

Conceptual Shape Optimization of Entry Vehicles

Applied to Capsules and Winged
Fuselage Vehicles

Springer Aerospace Technology

More information about this series at <http://www.springer.com/series/8613>

Dominic Dirkx · Erwin Mooij

Conceptual Shape Optimization of Entry Vehicles

Applied to Capsules and Winged Fuselage
Vehicles



Springer

Dominic Dirkx
Delft University of Technology
Delft
The Netherlands

Erwin Mooij
Delft University of Technology
Delft
The Netherlands

and

Joint Institute for VLBI ERIC
Dwingeloo
The Netherlands

ISSN 1869-1730
Springer Aerospace Technology
ISBN 978-3-319-46054-3
DOI 10.1007/978-3-319-46055-0

ISSN 1869-1749 (electronic)
ISBN 978-3-319-46055-0 (eBook)

Library of Congress Control Number: 2016954621

© Springer International Publishing Switzerland 2017

This work is subject to copyright. All rights are reserved by the Publisher, whether the whole or part of the material is concerned, specifically the rights of translation, reprinting, reuse of illustrations, recitation, broadcasting, reproduction on microfilms or in any other physical way, and transmission or information storage and retrieval, electronic adaptation, computer software, or by similar or dissimilar methodology now known or hereafter developed.

The use of general descriptive names, registered names, trademarks, service marks, etc. in this publication does not imply, even in the absence of a specific statement, that such names are exempt from the relevant protective laws and regulations and therefore free for general use.

The publisher, the authors and the editors are safe to assume that the advice and information in this book are believed to be true and accurate at the date of publication. Neither the publisher nor the authors or the editors give a warranty, express or implied, with respect to the material contained herein or for any errors or omissions that may have been made.

Printed on acid-free paper

This Springer imprint is published by Springer Nature
The registered company is Springer International Publishing AG
The registered company address is: Gewerbestrasse 11, 6330 Cham, Switzerland

Contents

1	Introduction	1
1.1	Re-entry Missions	2
1.1.1	Re-entry in the 20th Century	2
1.1.2	Re-entry in the 21st Century	8
1.2	Shape Optimization	13
1.3	Overview	16
2	Flight Mechanics	19
2.1	Flight Environment	19
2.1.1	Central Body Shape	20
2.1.2	Gravity	21
2.1.3	Atmosphere	22
2.2	Equations of Motion	24
2.2.1	Reference Frames	24
2.2.2	Forces	28
2.2.3	Entry Equations	30
2.3	Guidance Approach	33
2.3.1	Capsule	33
2.3.2	Winged Vehicle	35
2.3.3	Vehicle Stability	37
3	Aerothermodynamics	41
3.1	Basic Concepts	41
3.1.1	Thermodynamic Properties	42
3.1.2	Characteristics of Super/Hypersonic Flow	45
3.1.3	Viscosity	49
3.2	Aerodynamic Loads	50
3.3	Local-Inclination Methods	53
3.3.1	Description of Methods	54
3.3.2	Method Selection	60

3.4	Heat Transfer	64
3.4.1	Convective Heat Transfer	65
3.4.2	Capsule Considerations	68
4	Numerical Interpolation	73
4.1	Basic Concepts	73
4.1.1	Continuity and Convexity	74
4.1.2	Linear Interpolation	75
4.1.3	Bilinear Interpolation	76
4.2	Cubic Spline Curves	77
4.2.1	Fundamental Concepts	77
4.2.2	Bézier and Hermite Splines	79
4.2.3	Avoiding Self-intersection and Concavity	82
4.3	Hermite-Spline Surfaces	84
5	Vehicle Geometry	87
5.1	Analytical Parameterization	88
5.2	Winged Vehicle Parameterization	92
5.2.1	Fuselage	92
5.2.2	Wings	100
5.2.3	Fuselage-Wing Interface	105
5.2.4	Mass Model	107
5.3	Meshed Surfaces	109
6	Optimization	113
6.1	General Concepts	113
6.1.1	Problem Statement	113
6.1.2	Multi-objective Optimality	114
6.2	Particle-Swarm Optimization	116
6.2.1	Method Overview	117
6.2.2	Handling of Constraints	118
6.2.3	Multi-objective PSO	118
6.3	Shape Optimization	121
6.3.1	Performance Criteria	121
6.3.2	Constraints	123
7	Simulator Design	129
7.1	Simulation Code	129
7.2	Model Validation	134
7.2.1	Aerodynamics	135
7.2.2	Vehicle Trajectories	142
7.3	Simulation Settings	147
7.3.1	General	147
7.3.2	Capsule	148
7.3.3	Winged Vehicle	149

Contents	vii
8 Shape Analysis - Capsule	151
8.1 Monte Carlo Analysis.	151
8.2 Optimization.	159
8.2.1 Two-Dimensional Analysis	160
8.2.2 Three-Dimensional Optimization.	174
8.3 Concluding Remarks	177
9 Shape Analysis - Winged Vehicle	181
9.1 Monte Carlo Analysis.	181
9.2 Optimization Results.	189
9.2.1 Baseline Optimization	189
9.2.2 Pitch-Stable Optimization	209
9.2.3 Heat-Rate Tracking Optimization	214
9.3 Concluding Remarks	221
Appendix A: Relative Viscous-Force Approximation	225
Appendix B: Winged-Vehicle Shape Generation Example	229
Appendix C: Optimal Capsule Shapes	251
Appendix D: Optimal Winged-Vehicle Shapes	257
References	267
Index	273

Symbols

The physical shape parameters are omitted from this list for the sake of brevity and can be found in Tables 5.1 and 5.2 for the capsule and winged shape, respectively.

A	Area (m^2)
AR	Aspect ratio (-)
a	Speed of sound (m/s)
B	Ballistic coefficient (kg/m^2)
B_i^n	Bernstein polynomial (-)
\mathbf{b}_i	Bézier point (Usage dependent)
b	Wing span (Sect. 5.2.4) (m)
C_A	Axial force coefficient (-)
C_D	Drag coefficient (-)
C_L	Lift coefficient (-)
C_l	Roll moment coefficient (-)
C_m	Pitch moment coefficient (-)
C_N	Normal force coefficient (-)
C_n	Yaw moment coefficient (-)
C_p	Pressure coefficient (-)
C_S	Side force coefficient (-)
c_{ref}	Aerodynamic reference length (m)
c_p	Specific heat at constant pressure (J/K)
c_v	Specific heat at constant volume (J/K)
c_1	Self confidence parameter (-)
c_2	Swarm confidence parameter (-)
D	Drag (N)
E	Energy (J)
e	Internal energy per unit mass (J/kg)
\mathbf{F}	Force (N)
F	Weighted total objective function (Chap. 6) (Usage dependant)
f	Objective function (Chap. 6) (Usage dependant)
f	Ellipticity (Chap. 2) (-)

f_c	Bridging function (-)
G	Universal gravitational constant ($=6.67259 \cdot 10^{-11}$) ($\text{m}^3/(\text{kg} \cdot \text{s}^2)$)
g	Gravitational acceleration (m/s^2)
g	Inequality constraint function (Chap. 6) (Usage dependant)
H	Scaling altitude (m)
H_i^j	Hermite polynomial (-)
h	Altitude (m)
h	Enthalpy per unit mass (Sect. 3.1.1) (J/kg)
h	Equality constraint function (Chap. 6) Usage dependent
k_B	Boltzmann constant ($=1.380650 \cdot 10^{-23}$) (J/K)
$k_{1\dots 9}$	Method selection parameters (Sect. 3.3.2) (Parameter dependent)
Kn	Knudsen number (-)
J_n	Zonal gravity field coefficient (-)
L	Lift (N)
M	Mach number (-)
M	Molar mass (mol/kg)
\mathbf{M}	Moment vector ($\text{N} \cdot \text{m}$)
\mathbf{m}_i	Derivative at control point (Usage dependent)
m	Mass (kg)
$\hat{\mathbf{n}}$	Normal vector (-)
n	Load factor (-)
N_c	Number of contours of winged vehicle shape (-)
N_p	Number of points per contour of winged vehicle shape (-)
\mathbf{p}_i	Control point (Usage dependent)
Pr	Prandtl number (-)
p	Pressure (N/m^2)
p_{mut}	Mutation probability (-)
Q	Heat load (J/m^2)
q	Heating rate (W/m^2)
q_{dyn}	Dynamic pressure (N/m^2)
R	Specific gas constant ($\text{J}/(\text{kg} \cdot \text{K})$)
R	Radius (m)
\mathcal{R}	Universal gas constant ($=8.314473$) ($\text{J}/(\text{K} \cdot \text{mol})$)
Re	Reynolds number (-)
\mathbf{r}	Position vector (m)
r_x	Associated parameter of shape parameter x (-)
S	Surface area (m^2)
S	Side force (N)
St	Stanton number (-)
s	Entropy (J/K)
s_g	Ground track range (m)
T	Temperature (K)
t	Time (s)
t	Parametrizing variable, on [0,1] (Chap. 4) (-)

U	Gravitational potential (m^2/s^2)
u	Velocity in x-direction (m/s)
u	Parametrizing variable (Chap. 4) (-)
\mathbf{V}	Velocity vector (m/s)
V	Volume (m^3)
V_c	Circular orbit velocity (m/s)
v	Velocity in y-direction (m/s)
v	Second parametrizing variable for surfaces (Chap. 4) (-)
W	Weight (N)
\mathbf{x}	State variable vector (Usage dependent)
Z	Geometric Altitude (m)
α	Angle of attack (rad)
β	Sideslip angle (rad)
β	Shock angle (Sect. 3.1) (rad)
γ	Flight-path angle (rad)
γ	Ratio of specific heats (-)
δ	Latitude (rad)
ε	Lateral inclination angle (Sect. 3.3.2) (rad)
η	Spline tightening parameter (Sect. 4.2.3) (-)
η	Mutation distribution parameter (-)
η_V	Packing efficiency (-)
θ	Flow deflection angle (rad)
θ	Rotation angle about axis (Sect. 2.2.1) (rad)
Λ	Wing sweep angle (rad)
λ	Mean free path (Sect. 3.1.2) (m)
λ	Wing taper ratio (-)
κ	Curvature (1/m)
μ	Gravitational parameter (Sect. 2) (m^3/s^2)
μ	Viscosity ($\text{kg}/(\text{m} \cdot \text{s})$)
μ	Mach angle (Sect. 3.1.2) (rad)
ν	Prandtl–Meyer function (rad)
ρ	Density (kg/m^3)
σ	Bank angle (rad)
τ	Longitude (rad)
ϕ	Geocentric latitude (rad)
ϕ'	Geodetic latitude (rad)
χ	Heading angle (rad)
ω	Angular rate (rad)
ω	Inertia weight (Chap. 6) (-)

Subscripts

\perp	Perpendicular to
∞	Associated with freestream
0	At sea level or reference condition
1	Before shock wave
2	After shock wave
A	Evaluated in aerodynamic reference frame
a	Due to aerodynamics
aw	Of an adiabatic wall
abs	Absolute
B	Evaluated in body reference frame
b	Of body
bf	Of body flap
c	Convective
c	Of conical middle section (Sect. 5.1)
cm	At or around the center of mass
cog	At center of gravity
cor	On capsule corner radius
cp	About center of pressure
E	At initiation of entry
e	At edge of boundary layer (Sect. 3.4)
e	Of elevon
eq	At the equator
fus	Of fuselage
g	Due to gravity
high	In high hypersonic regime
I	Evaluated in inertial reference frame
irrev	Irreversible
L	Over the entire length L
LE	Of leading edge
low	In low hypersonic regime
n	Normal to shock wave
n	Associated with vehicle nose
q	At matching point (Sect. 3.3)
R	Evaluated in rotating planetocentric reference frame
r	In radial direction
rel	Relative
ref	Reference
s	At stagnation point
sp1	Of nose sphere
sp2	Of rear sphere cap
T	Total
T	Evaluated in trajectory reference frame

t	Of toroidal section
tr	At trim conditions
V	Evaluated in vertical reference frame
w	At vehicle wall
w	Of wing
α	Derivative w.r.t. angle of attack
β	Derivative w.r.t. sideslip angle
δ	In latitudinal direction

Abbreviations and Acronyms

ACM	Aerodynamic Configured Missile
ALTV	Approach and Landing Test Vehicle
APAS	Aerodynamic Preliminary Analysis System
ARD	Atmospheric Reentry Demonstrator
CEV	Crew Exploration Vehicle
CFD	Computational Fluid Dynamics
CNES	Centre National d'Etudes Spatiales
DG-MOPSO	Double Grid Multi-Objective Particle Swarm Optimization
DLR	Deutsches zentrum fur Luft- und Raumfahrt
DUT	Delft University of Technology
EGM	Earth Gravity Model
ESA	European Space Agency
EXPERT	European eXPErimental Re-entry Test-bed
FESTIP	Future European Space Transportation Initiative Programme
FLPP	Future Launchers Preparatory Program
GA	Genetic Algorithm
GEO	Geostationary Earth Orbit
HASA	Hypersonic Aerospace Sizing Analysis
ICBM	Intercontinental Ballistic Missile
LaWGS	Langley Wireframe Geometry Standard
LEO	Low Earth Orbit
MDO	Multidisciplinary Design Optimization
MER	Mass Estimation Relationship
MOPSO	Multi-Objective Particle Swarm Optimization
NASA	National Aeronautics and Space Administration
NSGA	Non-dominated Sorting Genetic Algorithm
NURBS	Non-Uniform Rational B-Splines
OTV	Orbital Test Vehicle
PSO	Particle Swarm Optimization
RCS	Reaction Control System

S/HABP	Supersonic/Hypersonic Arbitrary Body Program
SOSE	Second-Order Shock Expansion
SSTO	Single Stage to Orbit
STS	Space Transportation System
TAEM	Terminal Area Energy Management
TPS	Thermal Protection System
TSTO	Two Stage to Orbit
USAF	United States Air Force

Chapter 1

Introduction

Atmospheric entry is a critical phase for any space mission in which a payload enters a planetary atmosphere. During entry the vehicle transitions from a (super)orbital velocity to a safe touchdown. In the case of vehicles such as the Space Shuttle, this final approach is done by landing like an aircraft. For the Soyuz and Apollo capsule, a parachute is used to decelerate over the final portion of the descent. In either case, the vehicle experiences extreme aerothermodynamic loads that drastically alter its design requirements.

The external shape is one of the main factors in determining a vehicle's aerothermodynamic characteristics. Therefore, by changing its shape the vehicle's behaviour and performance can be greatly modified. During the conceptual design phase of a space vehicle, relatively simple models are used to generate several conceptual designs, which are further analyzed using more sophisticated and often time-consuming methods in subsequent design phases. However, if the design is based on only a small number of vehicle concepts, one runs the risk of overlooking better design choices. By investigating the full range of possible shapes during conceptual design, the external vehicle shape is based on stronger and more rigorous arguments, and the detailed design will consequently start from a more robust preliminary design.

This book will focus on shape optimization of entry vehicles in the conceptual-design phase, where we analyze the full performance during the hypersonic entry. However, since the shape influences many aspects of the vehicle's performance, it must be ensured that none of the constraints placed on either the vehicle systems, its performance or its external loading, are violated. The main question that the methods in this monograph address is therefore the following:

What is the optimal shape for a re-entry vehicle to fulfill its mission, taking into account constraints due to loads and configuration?

To this end, a global, multi-objective optimization methodology is set up and applied to the shape optimization of two different classes of re-entry vehicle. First, we consider a low lift-over-drag capsule-shaped vehicle, such as the Apollo or Atmospheric Reentry Demonstrator (ARD) that is used once to enter an atmosphere on a near-ballistic entry. Second, we apply the methodology to a more complex

winged vehicle, such as the Space Shuttle. Winged vehicles usually perform a controlled landing on a runway and could be reused for future missions. However, the characteristics that allow the vehicles to behave more like an aircraft and be reusable come at the expense of additional mass and complexity. This often makes them economically difficult to justify when compared to simpler vehicles. Therefore, optimization of the vehicle's shape by both reducing mission cost and increasing possible mission revenue is crucial in making such vehicles competitive for the launch and entry market.

After the hypersonic phase, the limit for which is defined as Mach 5, the vehicle enters the supersonic/subsonic regime, where the flight characteristics are quite different from the high-velocity entry. However, the main design drivers are usually derived from the highly demanding hypersonic phase, and we consequently focus our efforts there. Moreover, we limit ourselves to entries from Low Earth Orbit (LEO) for both the capsule and winged vehicle. However, the material that is presented can in many cases be easily modified for other entry scenarios.

Before we dive into the technical details of re-entry flight mechanics and shape optimization, we will give a brief and non-exhaustive overview of some of the past work in atmospheric re-entry and shape-optimization in Sects. 1.1 and 1.2, respectively. This chapter will conclude with a more detailed overview of the contents of this book, in Sect. 1.3.

There are various excellent sources that give a broad overview of the history of atmospheric entry. For instance, the work by Heppenheimer (2007) discusses the historical development of hypersonic vehicles. Jenkins (2001) details the development of the Space Shuttle and its predecessors. More recently, Sziroczak and Smith (2016) give a review of design issues specific to hypersonic flight vehicles. An extensive description of the relation between vehicle shape and aerothermodynamic properties be found in the book by Hirschel and Weiland (2009).

1.1 Re-entry Missions

In this section, we give a short (non-exhaustive) overview of some key historical developments in the field of re-entry, starting from the origins of the field of aerospace engineering, and working our way up to current ongoing projects and the prospects for future advancements in the field.

1.1.1 *Re-entry in the 20th Century*

Although related research into aerodynamic flow phenomena had been conducted by a variety of early researchers, among them Mach and Reynolds, it was not until early 1903 that heavier-than-air flight was achieved and the discipline of aerospace engineering was born as a practical science. Research into rocketry and spaceflight

was also beginning at the start of the 20th century with pioneers such as Goddard, Oberth and Tsiolkovsky. With the emergence of these research and construction efforts, supersonic and hypersonic aerodynamics became topics of interest.

The first concept of hypersonic flight were studied in the 1930s, when Austrian engineer Eugen Sänger and his wife, German mathematician Irene Bredt, proposed a hypersonic bomber, which was to strike the US from Germany (Sänger and Bredt 1944). This *Silverbird* would use a rocket to accelerate and, after dropping off its payload, would follow a skipping entry to extend its range and land on the other side of the world, in Japan. Although it never went into production, the groundbreaking work of Sänger and Bredt on gliding and skipping entry proved to be extremely important for later vehicles and missions.

Research into hypersonic vehicles was pushed ahead during the Second World War with the development of the V-2 rocket in Germany. To support the development of this rocket, a pair of wind tunnels operating at Mach 4.4 was used. Although not quite hypersonic according to the typical definition of Mach 5, research for this vehicle revealed a variety of engineering challenges that are present at high speed, such as controllability and stability issues. After the war, captured V-2 rockets were instrumental in forwarding the American rocket programs.

Following the war, American engineer John Becker proposed building a Mach-7 wind tunnel to study hypersonic flows. This tunnel, which was first operational in 1947, had an 11-inch square test section and was instrumental in the development of vehicles such as the X-15. In fact, for a while it was the only test facility in the US that could simulate hypersonic conditions.

With the invention of the atomic bomb and the V-2 missile, the idea of intercontinental ballistic missiles (ICBMs) soon followed, necessitating further research into high-speed, high-altitude flow phenomena. An ICBM re-enters the atmosphere at Mach 20, so that aerodynamic heating becomes a severe design problem. In a paper by Allen and Eggers Jr (1958), it was shown that the nose radius should be maximized to minimize the heat flux, driving the design of all re-entry vehicles that followed.

Engineers at the time had only a few options of dealing with the extreme heating conditions. For instance, a heat sink could be used, so that most of the heat entering the vehicle would be stored in some material of high heat capacity. Additionally, radiative cooling could be used, where high-temperature surfaces with high emissivity radiate the heat back to the environment. However, these methods become impractical at the high speeds of re-entry, due to excessive aerothermal loads. A heat sink is only capable of taking up a given amount of heat before failure and the size required of such a system for re-entry is prohibitive. For radiative cooling, there is a fundamental limit to the temperature to which a surface can be cooled at a given heat flux (assuming thermal equilibrium), which is not sufficient for the complete vehicle.

A critical method that was devised to cope with the large heat fluxes that occur at re-entry is ablation. When using an ablative heat shield, the heat of entry is absorbed by the Thermal Protection System (TPS), initiating a phase change from solid to gas (or liquid) of the upper layer of this TPS. Although this system is non-reusable, its capability to cope with very high heat rates provides designers with key design

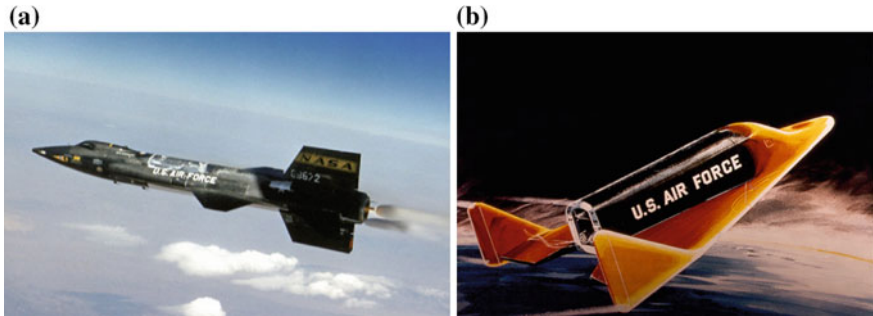
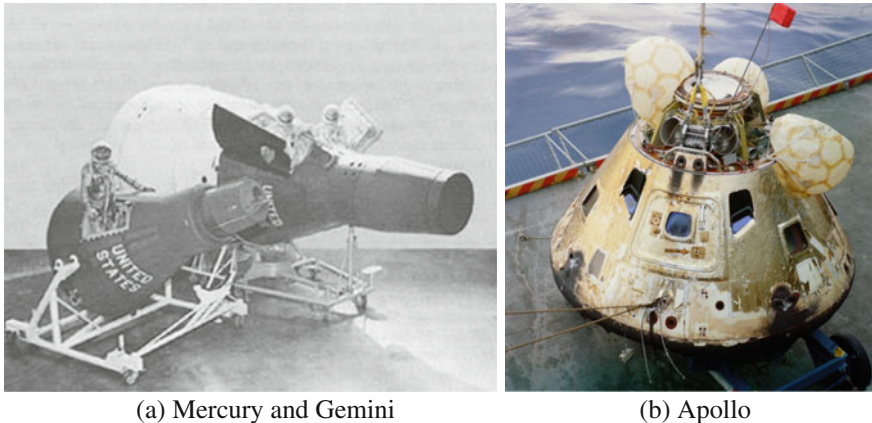


Fig. 1.1 **a** X-15 in flight, **b** Artist's impression of the re-entry of the X-20, Dyna Soar. Images courtesy: NASA

options for high-temperature environments that would otherwise not be available. An extreme example of such a case is the Jupiter entry probe Galileo, of which roughly half of the entry mass consisted of the thermal protection system (TPS).

A milestone in the development of hypersonic vehicles came with the X-15, (Fig. 1.1a), an experimental rocket plane built by North American. The goal of this research plane was to gather flight data and experience at high speeds and high altitude, as well as high-temperature structures. For its thermal control, it used a heat-sink concept made of Inconel X, along with spray-on ablators. The X-15 used both aerodynamic surfaces and reaction-control thrusters for attitude control, as the atmospheric density at its higher operating altitudes was too low to use control surfaces only. It reached velocities of close to Mach 7 and altitudes in excess of 100 km. Although it represented great progress, the X-15 was not truly a re-entry vehicle, as it did not gain nearly enough velocity to reach and stay in orbit.

Concepts for so-called space planes, which could be used repeatedly to transfer cargo and people to orbit and back without major overhauls, were also beginning to emerge during this period. A major series of studies representing the various design challenges involved in the design of such vehicles was performed, under the name ‘Aerospace Plane’. However, the concepts that were developed during this period were often dependent on unproven hypersonic air-breathing propulsion. This would offer a performance superior to that of rockets in terms of fuel consumption, but these concepts proved to be too technologically and financially demanding for their time. A concept that was developed further than others was the X-20 (or Dyna-Soar) vehicle, shown in Fig. 1.1b, a small vehicle developed for the US Air Force. It was to be launched on top of a rocket and glide back to Earth, in a similar fashion as the later Space Shuttle. Unfortunately, this project was canceled just as production had begun, as it was deemed too expensive for the limited types of missions it could fly, and its merits as a research vehicle were insufficient to bring the project to completion. Its development did, however, provide valuable data that would later be used during the design of the Space Shuttle.



(a) Mercury and Gemini

(b) Apollo

Fig. 1.2 Entry capsules of the 1960s. Images courtesy: NASA

Despite the multitude of concept proposals, hypersonic flight and gliding entry technologies did not take off as quickly as was initially forecasted during the initial years of the space age. However, ballistic and low lift-over-drag (L/D) entry using capsule-like vehicles was successfully used to return from space. The first successful human re-entry occurred in 1961 with Vostok 1 safely returning Yuri Gagarin after the first manned spaceflight. Shortly after this, the Americans followed suit with the Mercury-Atlas-6 flight piloted by John Glenn. The Mercury project was followed up by the Gemini project which used a non-zero L/D ratio to decrease the g -loads experienced by the astronauts (see Sect. 2.2.3). The correct determination of this ratio as a function of flight conditions is critical to the correct calculation of the landing point of the vehicle, which proved difficult to do using wind-tunnel models only. Gemini was followed up by the Apollo project, which successfully achieved re-entry upon Lunar return. This caused much greater mechanical and thermal loads on the vehicle than the previously flown Earth-orbit return missions due to the substantially higher entry velocity. Figure 1.2 shows these three entry capsules of the 1960s.

All of the vehicles involved in the first manned space missions utilized a (near-) ballistic entry, as opposed to the lifting-entry vehicle types discussed before. Although a ballistic-entry vehicle is not (or not fully) reusable, such a vehicle is easier to design and usually has a higher payload-mass to dry-mass ratio, as no structure is required for the lifting components.

In addition to the gliding and ballistic entry, a third ‘type’ of entry can be distinguished, namely skipping entry. During skipping entry, the vehicle dips into the atmosphere, but is ‘pushed’ back up by aerodynamic lift, leaving the sensible atmosphere, but this time with a lower kinetic energy. By repeating a number of these ‘skips’, the kinetic energy can be shed in stages. After some skips, the vehicle no longer has enough speed to leave the atmosphere again and is thus captured. The three types of entry are shown schematically in Fig. 1.3.

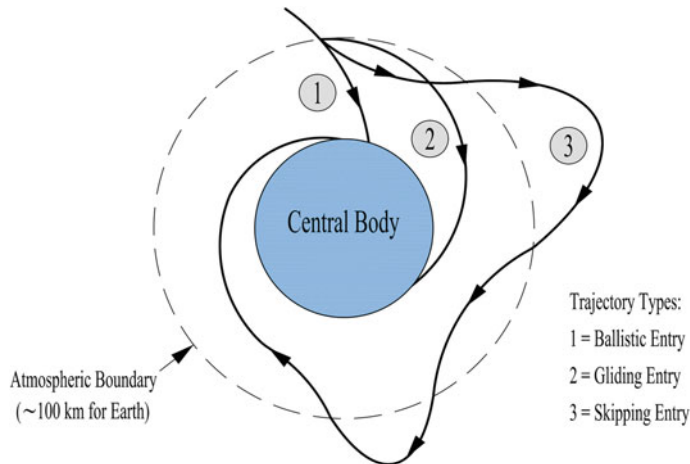


Fig. 1.3 Schematic representation of three types of atmospheric entry

Following the Apollo project, the US decided to pursue the development of a re-usable launch vehicle. This vehicle was to be used repeatedly and cheaply, in a somewhat similar sense to the defunct Dyna-Soar concept, but on a larger scale, allowing it to deploy payloads to orbit. This eventually lead to the development of the Space Transportation System (STS) or Space Shuttle, as it is more commonly known (Fig. 1.4). Although the Shuttle operated for approximately 30 years, the goal of cheap reusable space access has never been achieved, due to the downsides mentioned above for reusable lifting vehicles, in particular due to the high maintenance costs of the TPS.

European concepts for space planes were being developed in parallel with the many American concepts that arose during the 1960s, mostly from French, British and German companies and agencies. Although none of these concepts was to go into production, it did provide the European space industry with crucial design experience working on re-entry vehicles and space planes.

More recently, the Hermes vehicle developed by ESA and CNES, which was to ride on top of an Ariane-5 launcher, was developed during the late 1980s and early 1990s. In roughly the same period, the German company MBB (currently part of the Airbus Group) and the German Ministry of Research developed a concept named Sänger II (Sänger I was one of the concepts developed during the 1960s). This was a Two-Stage-To-Orbit (TSTO) concept, with a hypersonic craft taking the upper stage to a high altitude and velocity where it was to be released, and rockets were to be used to take this upper stage into orbit. Two upper stages were envisioned, CARGUS, which was to be unmanned, and HORUS, which was to be manned. Although the project was, just like the Hermes project, canceled due to lack of funding, the HORUS vehicle has served as a reference vehicle in some G&C design work concerning space



Fig. 1.4 Space Shuttle Atlantis prior to landing at Kennedy Space Center (STS-122). Image courtesy: NASA

planes by Mooij (1998). In Fig. 1.5, a model of the vehicle on the back of Sänger II is shown.

A joint development effort between ESA and NASA to develop a crew return vehicle for the International Space Station (ISS) (with its demonstrator the X-38) was undertaken in the 1990s. The vehicle has a lifting-body shape, and is shown in Fig. 1.6. The vehicle was to use a parafoil during the low velocity landing phase. The external shape of the X-38 was based on the design of a previous lifting body, the X-24A, developed approximately 20 years prior to the development of the X-38. The X-38 program was canceled due to budget cuts, but only after extensive research, including a subsonic drop test, parafoil deployment and landing had been performed.

Although computers were beginning to emerge as practical design tools in the early days of entry-vehicle design, the availability of computing power was still extremely limited compared to the current state-of-the-art. This situation greatly stimulated the development, evaluation and use of conceptual design methods, such as the heat transfer model by Fay and Riddell (1958). Although the accuracy of such methods is obviously lower than current modern Computational Fluid Dynamics (CFD) models, the correct usage of such models, in combination with wind-tunnel and eventually flight-test data, can give adequate results for vehicle design. Another good example of approximate aerodynamic modeling efforts is the Supersonic/Hypersonic Arbitrary Body Program (S/HABP), developed by the McDonnell Douglas Corporation (Gentry et al. 1973). In addition to approximate methods for aerodynamic performance prediction, the analysis of entry vehicle trajectories was also performed using a variety of assumptions. Using these, the differential equations that govern the trajectory are simplified and the vehicle trajectory can be obtained analytically or with substantially less computing power. Two of these efforts are given by Chapman (1958),



Fig. 1.5 Scale model of the HORUS second stage on the back of the Sänger II vehicle, displayed in the Technik Museum Speyer. Image courtesy: Wikimedia commons

and Allen and Eggers Jr (1958), with later textbooks such as those by Loh (1968) and Vinh et al. (1980) giving an overview of these simplified methods.

Even with the advent of modern computing facilities, these conceptual methods continue to have practical applications. In particular, the combination of fast computing and simplified models allows a vast number of vehicle shapes and entry types to be analyzed during the design stage, making the conceptual-design selection much more robust. It is this type of approach on which we focus in this book.

1.1.2 Re-entry in the 21st Century

A number of projects by both government and private institutions related to hypersonic flight and re-entry is currently underway or has been studied in the recent past. Indeed, history has shown that many projects are not often brought to the point of full-scale flight models that can be put into production. However, there has been a number of promising projects that have initiated sound technology programs.

One project, which aimed at gathering more (design) data for hypersonic vehicles, was the EXPERT (European eXPErimental Re-entry Test-bed) program, part of ESA's Future Launchers Preparatory Program (FLPP). It was to fly a sub-orbital



Fig. 1.6 X-38 vehicle during a drop test. Image courtesy: NASA

mission with entry velocities of 5–6 km/s, as discussed by Massobrio et al. (2007). This vehicle was to be launched from a Russian submarine with a VOLNA launcher. Although the vehicle flight model was built, it has unfortunately never been launched.

A second European experimental vehicle, also part of ESA's FLPP, was the Intermediate eXperimental Vehicle (IXV). This concept was developed to validate European reusable-launcher technology. The IXV was successfully launched on 11 February 2015, and completed its 100-minute sub-orbital mission. It became the first-ever lifting body to perform full atmospheric reentry from orbital speed. IXV was derived from previous European studies/vehicles, i.e., Pre-X (developed by the French agency CNES), ESA's AREV (Atmospheric Reentry Experimental Vehicle), and the earlier launched ARD, successfully flown in 1998.

Although the EXPERT and IXV vehicles are interesting in their own right, they are meant to be technology demonstrators and research vehicles, and are not foreseen to be modified to ferry cargo to space. A vehicle concept went into development from the Future European Space Transportation Initiative Programme (FESTIP), is the Hopper concept, described by Spies (2003). The vehicle was to be launched on a horizontal rail-guided system with a frequency of 10–20 flights per year, with most missions bringing cargo into Geostationary Transfer Orbit (GTO). The advantage of such a horizontal launch is that the required thrust can be reduced significantly when compared to a conventional rocket or Space-Shuttle launch. This is due to the fact that for a winged, horizontal launch, the force that lifts the vehicle off the ground is



Fig. 1.7 Test-flight vehicle Phoenix-1, a scaled-down version of the sub-orbital Hopper. Image source: authors

mostly aerodynamic, so that the Thrust/Weight ratio of the engines can be reduced, in turn reducing the total mass. A 1/7th scale model of the Hopper, named Phoenix-1 (shown in Fig. 1.7), was produced and dropped from a helicopter in 2004 to test the low-speed aerodynamics of the vehicle. This program was initiated under the German ASTRA project and was meant as a preparatory research effort for development of a full-scale version of the Hopper. In recent years, no further development of this project has been made, however.

A space-plane concept that is currently under development in Britain is Skylon, an SSTO vehicle described by Varvill and Bond (2004). This vehicle is to use dual-mode engines as propulsion. Up to Mach 5, the so-called SABRE engines will function as air-breathers, using pre-coolers to cool the air to just above the vapor boundary prior to ignition. Above Mach 5, the engines will function as conventional rockets, giving the remaining ΔV required to achieve orbit. Skylon is to be unmanned and will use hydrogen and oxygen as fuel and oxidizer. The concept will be capable of bringing a payload of 15 tonnes into LEO. The design of the vehicle, and in particular the propulsion system, stems from the design effort on the HOTOL space plane concept, which was canceled in 1989. The propulsion concept for this vehicle was itself based on one of the air-breathing concepts of the aerospace-plane era. The project is supported by funding from the British government, and full-scale engine tests are expected by 2019, with unmanned test flights as early as 2025.

Fig. 1.8 The X-37B Orbital Test Vehicle inside the payload fairing before launch. Image courtesy: USAF



A more mature lifting entry vehicle that has been tested for the first time in 2010 is the unmanned X-37B Orbital Test Vehicle (OTV), which is a small (29 feet long, 15 feet wingspan) winged entry vehicle. It has been developed by Boeing Phantom Works, while the program falls under the USAF. Due to the military nature of the program, the amount of information that has been published on it is limited. It is launched on top of an Atlas-5 rocket and lands using an autonomous guidance system. A flight-test vehicle scale-model of the X-37, the X-40, has been built and tested to validate the guidance system and the low speed aerodynamic characteristics. Tests on a full-scale model, the X-37A, dubbed the Approach and Landing Test Vehicle (ALTV), have also been performed, using the White Knight vehicle as a drop vehicle. So far, three successful orbital flights have taken place, i.e., the first one in 2010 (mission duration around 7 months), the second one in 2011 (mission duration well over a year), and the third X-37 mission was launched mid-December 2012 and landed at Vandenberg AFB on 17 October 2014. A fourth X-37 mission was launched on 20 May 2015 and is still in progress as of May 2016. Figure 1.8 shows the X-37B inside the payload fairing of the Atlas-5 before launch.



Fig. 1.9 Space Ship Two, with carrier aircraft. Images courtesy: Wikimedia

An additional vehicle of considerable interest was tested in May 2010, namely the X-51 research vehicle, shaped as a so-called waverider. This vehicle is a reusable scramjet demonstrator. The previous X-plane to demonstrate supersonic combustion, the X-43, demonstrated sustained supersonic combustion for only ~ 10 s. Its copper engine was used as a heat sink, leading to very high temperatures and the planned failure of the engine. The X-51's scramjet has an active cooling system, using its fuel as a cooling liquid, allowing for sustained supersonic combustion on the order of minutes. The successful test demonstrated supersonic combustion for ~ 200 s.

Additionally, space tourism is emerging as a viable market, with a number of companies developing sub-orbital vehicles, which are to bring people to altitudes of >100 km. Although these vehicles are all well short of achieving orbital velocity, with an exo-atmospheric arc lasting only minutes, it indicates that the private sector is taking an interest in exploiting commercial space opportunities outside of the ‘classical’ types of use, i.e., mostly communication and observation satellites. Despite the fact that the technological requirements of an orbital vehicle meant primarily for tourism purposes are significantly more stringent than current designs, these developments are encouraging. In Fig. 1.9 an example of a sub-orbital vehicle for space tourism is shown: Virgin Galactic’s SpaceShip Two.

1.2 Shape Optimization

Due to the increase in performance that can be obtained by modifying the vehicle's external shape, the optimization of this shape has been a topic of considerable interest. An early seminal text on the optimization of aerodynamic shapes is the one by Miele (1965). There, theoretical considerations regarding the optimal shapes of vehicles in different aerodynamic regimes are presented. For a number of simple parameterizations, optimal vehicle-shape results are derived, such as the shape for minimum wave drag, for a body with given length and volume or base area and length.

In the area of shape optimization, the problem of optimizing a re-entry capsule has been tackled by a number of researchers. Since such a shape is generally less complicated than a more general lifting entry vehicle, the number of design variables will generally be relatively low. One recent optimization effort for a Mars entry capsule is discussed by Theisinger and Braun (2009), where a geometry description using so-called Non-Uniform Rational B-Splines (NURBS) surfaces (see Sect. 4.2) with approximately 20 design variables is used to perform a conceptual shape optimization. The optimization criteria are a maximum drag area, $C_D S_{ref}$, a minimum (most negative) static-stability area, $(C_m S_{ref} C_{ref})_\alpha$, and maximum packing efficiency η_V , defined in the next section. A figure of the general NURBS description, as well as the optimal shapes that were found are given in Fig. 1.10 to show the strong diversity of the geometrical description.

An additional research effort regarding the optimization of aeroshell shapes is discussed by Johnson et al. (2007). They use an analytical formulation for the characteristics that allows for a large number of shapes to be evaluated. In this design effort, the entry from a hyperbolic velocity is considered, so that radiative heating is considered as having an important effect on the design of the vehicle. The constraints imposed on the vehicle in this effort are stability in pitch, roll and yaw, as well as a maximum value of the stagnation-point heating. More details on such constraints can be found in Sects. 2.3.3 and 6.3.2.

More recently, starting from the framework discussed in this book, Ridolfi et al. (2012) discuss the robust shape-optimization of unmanned entry capsules returning from Low Earth Orbit. By keeping track of the design objectives not only in the design-parameter space, but also in the uncertainty space – the so-called dual repository approach – optimal shapes and TPS settings were obtained, with a minimum number of simulations. The outcome gave Pareto fronts with optimal configurations for small, fully reusable capsules as well as capsules with ablative materials, for both nominal missions and missions under uncertainties.

For the more complex problem of optimizing hypersonic lifting bodies, two types of problems are distinguished by Golubkin and Negodam (1995). One is the optimization of waverider vehicles, the other is the optimization of general shapes using local-pressure methods, such as those that will be discussed in Sect. 3.3, and used in this optimization framework. Results of a shape optimization of the HL-20 using only inviscid methods (such as those discussed in Sect. 3.3) are described

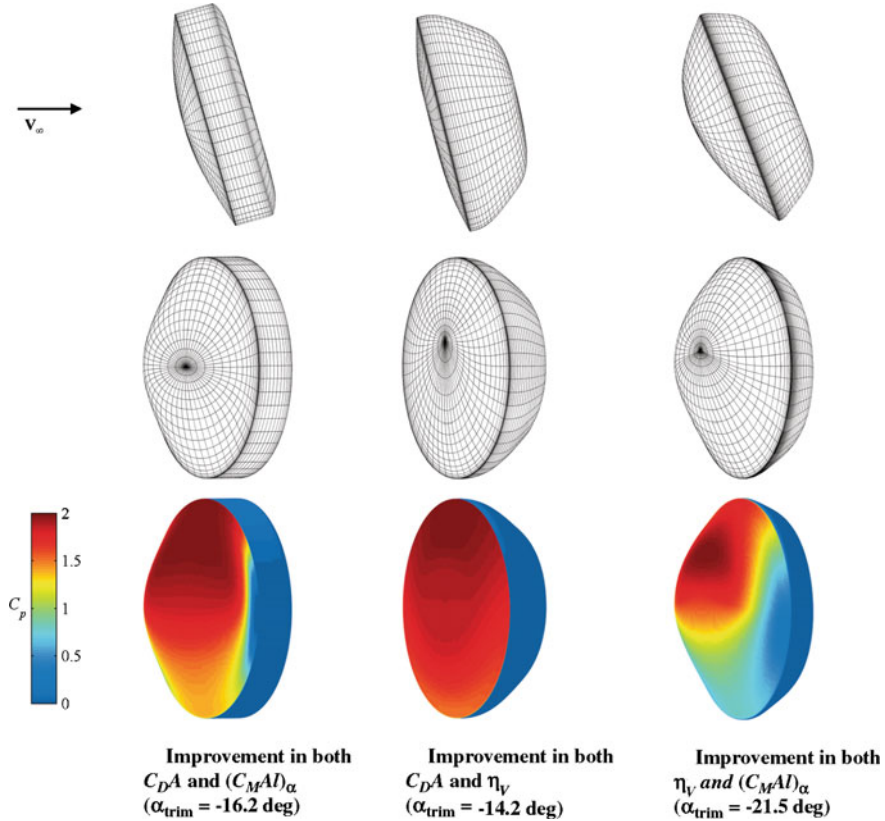


Fig. 1.10 Selected multi-objective optimal shapes from Theisinger and Braun (2009), with calculated pressure distributions

by Kinney (2006) where optimization of L/D at a single design point is considered. In the work described by these authors, the design variables were the locations of all (6,775) nodes in the unstructured grid, leading to 20,325 design variables, optimized using a conjugate-gradient method. The results are shown in Fig. 1.11, where it can be seen that there are sharp transitions that will give adverse aerothermal effects, a problem that is noted by the author. The optimization procedure yielded impressive results, giving a maximum L/D at the preset angle of attack of 20° that is close to double that of the original configuration. Including constraints would most likely decrease this value, however, but it is indicative of the fact that significant modifications of hypersonic L/D can be achieved.

An example of recent work in re-entry vehicle shape optimization can be found in Huertas et al. (2010), where the Multidisciplinary Design Optimization (MDO) of re-entry vehicles using the ASTOS software package is discussed. A model is described for the concurrent optimization of the the shape of a re-entry vehicle, where

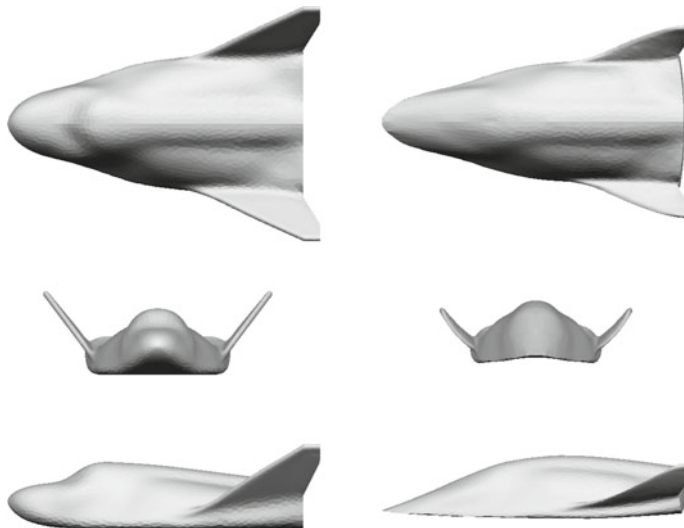


Fig. 1.11 Inviscid hypersonic L/D optimization results of HL-20 (*left* original configuration, *right* Inviscid L/D optimized), from Kinney (2006)

a number of different parameterizations is used, similar to the capsule parameterization described here. Coupling between the following disciplines is considered in the model: (i) aerodynamics, (ii) geometry, (iii) trajectory, (iv) weights, and (v) thermal protection system. The aerodynamics code that is used in this optimization effort is the Second-Order Shock-Expansion (SOSE) code developed by DLR. The computational complexity of using such a method is beyond the scope of the present work, however, as we focus on conceptual design, where the fast analysis of a large number of vehicle shapes is crucial. Consequently, we will use the simpler, but slightly less accurate local-inclination methods.

MDO work by Boeing, applied to the upper stage of a reusable TSTO launch vehicle, is described by Bowcutt et al. (2008). In this article, low- and high-fidelity codes are combined to analyze hypersonic vehicles with an integrated scramjet propulsion unit. A three-dimensional Reynolds-Average Navier Stokes (RANS) aerodynamic model is used to calculate the forebody and scramjet inlet flow, to obtain an accurate result for the complex scramjet flow. Lower-fidelity codes are used for analysis of the aerodynamics of the full vehicle, though. A number of possible vehicle shapes from the parameterization that is used is shown in Fig. 1.12. Although about 50 parameters are used for the full parameterization, only the 12 most important ones were included in the MDO analysis to reduce computational cost.

When using a complex aerothermodynamic analysis code, scanning of the global design space is typically not always possible. In the current study we will balance the level of complexity of the analyses with a global scanning of the design space and an automated way to find the direction of the optimal shape of the vehicle under study.

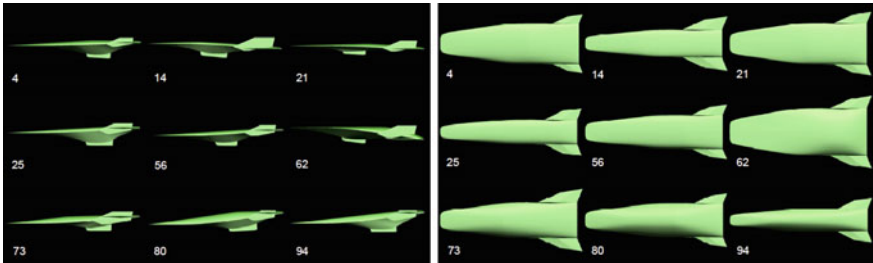


Fig. 1.12 Examples of waverider shapes considered in the optimization described by Bowcutt et al. (2008)

Clearly, modern developments in the market and design options for entry vehicles, combined with comparatively vast computing capabilities, opens up a whole new area of vehicle design. In particular, the performance of many possible entry vehicles can be simulated with reasonable accuracy using very limited computing resources. Consequently, such methods can be used in the inner loop of a vehicle design algorithm, allowing the influence of a set of design variables on the full performance to be analyzed and optimized. In this book, we focus on analyzing the influence of the vehicle shape parameters, combining conceptual-design methodologies with modern optimization techniques, facilitating a powerful exploration of vehicle design in an early design stage.

1.3 Overview

This book is structured as follows. Chapter 2 will discuss the necessary parts of the mechanics of atmospheric entry. The environment models that will be used, the equations of motion and approximations made to obtain them, as well as the guidance and control approach for the capsule-shaped and winged entry vehicle will be covered. Following this, Chap. 3 will discuss the details of the aerodynamic and thermal models which have been used for the analysis of the vehicle's performance. This chapter includes information on a number of basic aerothermodynamic concepts, but is by no means a complete summary of hypersonic flow theory. The focus is on the description of local inclination methods. Methods for determining the heat flux to key areas of the vehicles are also discussed.

Having defined the physical models for flight mechanics and aerothermodynamics, the mathematical tools necessary for the definition of the vehicle shapes are described in Chap. 4, where the focus is on cubic Hermite splines and spline surfaces. With these definitions, the vehicle shape parameterizations are given in Chap. 5. Chapter 6 gives an overview of the optimizer which has been used, the Multi-Objective Particle Swarm Optimization (MOPSO) algorithm. Also, the constraint and objective functions which we use for the vehicles here are discussed. Chapter 7

describes the implementation and validation of the models we use for determining the parameterized vehicle performance. In this chapter, the Space Shuttle and Apollo vehicle shapes are used for reference. Subsequently, Chaps. 8 and 9 give the results of the optimizations of the capsule-shaped and winged vehicle, respectively.¹

¹Key aspects of the methods and result presented in this monograph are summarized by Dirkx and Mooij (2014).

Chapter 2

Flight Mechanics

An object moving through the atmosphere of the Earth is subjected primarily to aerodynamic and gravitational forces. Although gravity acts on this object independent of shape and mass, the object's size and shape *do* determine its aerodynamic characteristics. Therefore, to modify the relative influence of the aerodynamic loads, the influence of the external shape and its internal mass can be modified. For a free-falling vehicle, even a slight variation of size and shape may result in a significantly different trajectory due to the non-linear nature of the problem at hand.

To safeguard a re-entry vehicle, it is typically equipped with a guidance and control (G&C) system, so that changes in the trajectory due to uncertainties in operational aspects and vehicle characteristics can be compensated for. The basis for a G&C system is the availability of a nominal trajectory that – taking the vehicle characteristics and constraints on the thermo-mechanical loads into account – shows whether a particular vehicle design is feasible or not.

Before we dive into the actual vehicle-shape optimization, we will cover the basics of re-entry flight mechanics. We begin in Sect. 2.1 by discussing the flight environment, namely the shape of the Earth, its gravity field and its atmosphere. Following this, the equations of motion for the vehicle will be defined in Sect. 2.2. To do so we will define the relevant reference frames, discuss the external forces and the resulting translational equations of motion. We conclude this chapter by showing the guidance and control approaches that we employ in our simulations in Sect. 2.3. As capsule-shaped and winged vehicles require a different approach they will be discussed separately.

2.1 Flight Environment

The vehicle-shape optimization that is the topic of this book is limited to entering the Earth's atmosphere. Therefore, the flight environment that we need to introduce is that of the Earth, consisting of its shape, gravity field, and atmosphere. This discussion is by no means meant to be exhaustive, as we only seek to discuss the underlying models

for the optimization process. For more information concerning environment models, the reader is referred to the vast and excellent collection of literature that is available on this topic, e.g., the books by Vinh et al. (1980), Regan and Anandakrishnan (1993) and Vallado (2007).

2.1.1 Central Body Shape

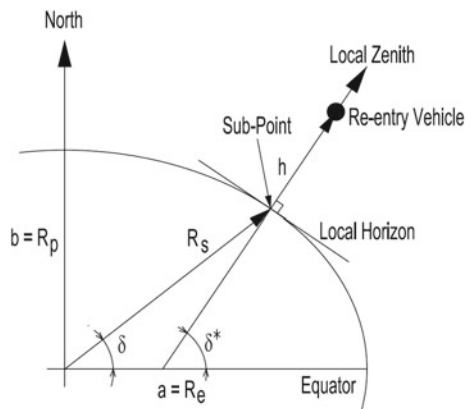
The shape of the Earth has a distinct effect on the atmospheric quantities at a given Earth-centered state, and is therefore a crucial part of the entry environment. Specifically, it is used to determine the vehicle's altitude from its Earth-centered Cartesian state. For aircraft and re-entry studies alike, one typically chooses one of several simplified shape models for the Earth: a flat-Earth approximation, a sphere, a spheroid or an ellipsoid. The particular choice depends on the application, where the vehicle's velocity, mission duration, and flight distance are the key decision drivers. For re-entry studies, one usually chooses between a spheroid. The flattening of the Earth has a noticeable effect on the altitude h of a vehicle for a given Cartesian position. Here, we use an ellipsoidal shape, shown schematically in Fig. 2.1.

The flattening of the central body is typically represented by a parameter f , also called the ellipticity. The flattening follows from:

$$f = \frac{R_e - R_p}{R_e} \quad (2.1)$$

where R_e represents the radius at the equator and R_p at the poles. For defining the location on the Earth's surface, either the geocentric latitude δ or the geodetic latitude δ^* may be used, shown in Fig. 2.1. The two are related as follows:

Fig. 2.1 Schematic representation of difference between the vertical and radial vector



$$\tan \delta^* = \frac{\tan \delta}{(1-f)^2} \quad (2.2)$$

So that δ and δ^* are very similar in magnitude, since f is small. From this value the local surface radius of the body, R_s , can be approximated, starting with the general expression of an ellipse and using polar coordinates:

$$R_s = R_e \left[1 - \frac{f}{2}(1 - \cos 2\delta^*) + \frac{5}{16}f^2(1 - \cos 4\delta^*) - \dots \right] \quad (2.3)$$

Since, to first order, δ can be approximated by δ^* , we may approximate Eq. (2.3) by

$$R_s \approx R_e \left[1 - \frac{f}{2}(1 - \cos 2\delta) \right] = R_e(1 - f \sin^2 \delta) \quad (2.4)$$

The altitude now simply follows from the following approximation:

$$h \approx r - R_s \quad (2.5)$$

Clearly, this relation is the same as what would be used for a perfect sphere, but then by substituting R_e for R_s .

2.1.2 Gravity

The gravitational force is one of the main external forces acting on a re-entry vehicle. Depending on the application one can model this force in different ways, ranging from a constant to a position-dependent quantity that includes the mass distribution inside the Earth.

Two point masses, M and m , separated by a vector \mathbf{r} , attract each other with a force given by Newton's law of gravitation as

$$\mathbf{F}_g = \frac{GMm}{r^2} \hat{\mathbf{r}} \quad (2.6)$$

where G is the universal gravity constant ($= 6.668 \cdot 10^{-11} \text{ m}^3/\text{kg s}^2$) and $\hat{\mathbf{r}}$ is the normalised position vector. Let us now assume that M is the mass of the Earth. It is then convenient to define the Earth's gravitational constant μ as GM , with $\mu = 3.9860047 \cdot 10^{14} \text{ m}^3/\text{s}^2$. Equation (2.6) is thus rewritten as

$$\mathbf{F}_g = m \frac{\mu}{r^2} \hat{\mathbf{r}} = m\mathbf{g} \quad (2.7)$$

with \mathbf{g} being the acceleration due to gravity at a distance, r .

To first approximation, a spherical, radially mass-symmetric body can be assumed, taking the entire mass to be concentrated at its center allowing Eq. (2.6) to be used. When considering the mass distribution inside the body, for (near-) spheroidal bodies the so-called *spherical harmonics* gravity model can be used, which is an expansion of the gravitational potential in terms of Legendre polynomials. In this model, a set of coefficients is used to represent the irregularities in the body's mass distribution (e.g. Vallado 2007).

For precise-orbit determination of satellites orbiting the Earth, expansion to high order and degree are typically required. For entry missions into the Earth atmosphere, though, either central-field models or a model with a first-order corrections for the flattening of the Earth is usually sufficient. This stems from the fact that the aerodynamic forces are orders of magnitude larger than the higher-order gravitational terms. Therefore, for the current study we assume a rotationally symmetric mass distribution and only account for the flattening by including the so-called J_2 zonal harmonic ($J_2 = 1.082626 \cdot 10^{-3}$ for Earth). The gravitational acceleration in the vertical frame (see Sect. 2.2.1) is then given by:

$$\mathbf{g}_V = (g_n \ 0 \ g_d)^T \quad (2.8)$$

with g_n being the gravitational acceleration in north direction, and g_d the (radial) component in down direction. The two components g_n and g_d are given by:

$$\begin{aligned} g_n &= -3J_2 \frac{\mu}{r^2} \left(\frac{R_e}{r} \right)^2 \sin \delta \cos \delta \\ g_d &= \frac{\mu}{r^2} \left[1 - \frac{3}{2} J_2 \left(\frac{R_e}{r} \right)^2 (3 \sin^2 \delta - 1) \right] \end{aligned} \quad (2.9)$$

These components are only dependent on the radial distance to the center of the Earth, r , and the latitude, δ . Because of the rotational symmetry the longitude τ is not present in the potential, hence the component of \mathbf{g}_V in east direction is zero.

2.1.3 Atmosphere

For calculations involving the aero-thermodynamic loads on a vehicle, knowledge regarding the state and composition of the atmosphere is required. Two different categories of atmosphere models can be distinguished. The first category deals with so-called *standard* atmospheres, which represent a distribution of the (average) state of the atmosphere with altitude that is representative for the Earth (or any other body with an atmosphere). The second category includes so-called *reference* atmospheres, which define this state of the atmosphere as a function of the actual position (altitude, longitude, and latitude). Additionally, temporal variations in the state, due to seasonal

and diurnal effects, for instance, can be taken into account. A model of the wind velocity vector can also be included as a function of time and position.

Despite the fact that a reference atmosphere is in general a more precise model of the actual state at any given point in space and time, for (conceptual) entry studies the use of a standard atmosphere is often preferred. First, the conceptual nature of the end-to-end model that is to be developed will most likely include deviations from the actual physics that are greater than those introduced by using a standard atmosphere in favor of a reference atmosphere. Second, the use of a standard atmosphere allows for a better comparison of the results produced by different simulations, as the entry point and time have no influence on the atmosphere that is encountered.

An often sufficiently accurate model of the atmosphere is the so-called US Standard Atmosphere of 1976 (typically abbreviated US76), described by NOAA/NASA (1976). This model is averaged over the diurnal and annual cycles as well as latitudes and longitudes, and represents the mean annual and global atmosphere at 45 degrees latitude, assuming a dry atmosphere (0 % humidity). For the definition of this atmosphere up to 86 km, the atmosphere is divided into seven regions, or strata, with each having its local temperature profile.

For the definition of the thermodynamic variables, two preliminary concepts are required. First of all, the geopotential altitude h_g , as opposed to the ‘actual’ or geometric altitude h is defined as follows:

$$h_g = \left(\frac{R_E}{R_E + h} \right)^2 h \quad (2.10)$$

Secondly, the molecular temperature T_M is defined, in addition to the kinetic temperature T (which corresponds to the conventional notion of temperature) as follows:

$$T_M = \left(\frac{M_0}{M} \right) T \quad (2.11)$$

where M is the molecular weight of the atmosphere at some altitude, with the 0 subscript denoting sea level conditions. Below 86 km, the value of M is almost invariant, having a value $0.999579M_0$ at 86 km, so that the molecular temperature and kinetic temperature can be assumed to be equal there. The definitions of Eqs. (2.10) and (2.11) have the advantage that they both lump the dependency on two variables (h and g ; T and M) into one new, transformed variable, simplifying the calculations.

The basic assumption of the 1976 standard atmosphere is that the variation of T_M in each of the seven layers up to 86 km is constant, with a thermal lapse rate L_{h_i} defined in each layer i as dT_M/dh . The values of these thermal lapse rates are given in Table 2.1. Above 86 km, the thermal lapse rate is not constant in all of the remaining layers. Below 86 km, the hydrostatic equation (which relates the weight of a column of air with the pressure it exerts on a reference surface) is assumed to be valid. Above 86 km however, its validity breaks down, as diffusive mixing and photochemical reactions become more pronounced. If the hydrostatic equation is

Table 2.1 Polytropic exponent and thermal lapse rates in the first seven strata, from NOAA/NASA (1976)

Geopotential altitude h , km	Thermal lapse rate L_h , K/km	Polytropic exponent n
0.0	-6.5	1.2350
11.0	0.0	1.0000
20.0	+1.0	0.9716
32.0	+2.8	0.9242
47.0	0.0	1.0000
51.0	-2.8	1.0893
71.0	-2.0	1.0622
84.8520		

valid, the pressure and density can be determined as follows, by rewriting it by using the definition of h_g and T_m , and assuming a perfect gas (see Sect. 3.1):

$$\frac{dp}{p} = -\frac{g_0 dh}{R_0 T_M} \quad (2.12)$$

Above 86 km, the pressure is obtained by summing the partial pressures of the various species. Due to the very limited interest of the precise atmospheric composition at such altitudes, though, these details are not repeated here.

2.2 Equations of Motion

This section will describe the equations of motion that are used to determine the trajectory of the entry vehicles. First, the reference frames that are used in the computations will be presented in Sect. 2.2.1 as well as the transformation matrices between them. Subsequently, the forces used in the trajectory determination are given in Sect. 2.2.2. Finally, the resultant equations of motion in spherical coordinates for a re-entry problem are presented in Sect. 2.2.3.

2.2.1 Reference Frames

To describe the equations of motion, it is necessary to define a number of reference frames, as the various external forces are obtained in different frames. Besides the definition of the reference frames, conversions between these frames are required to express all relevant components in one and the same frame. The following, right-handed reference frames will be considered here.

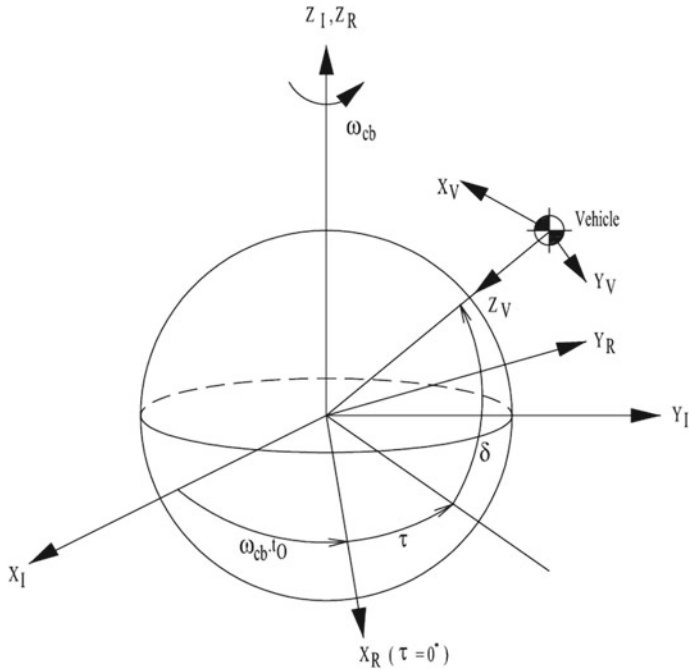


Fig. 2.2 Schematic representation of the inertial (index I) and rotating (index R) planetocentric frames, and the vertical frame (index V)

Inertial planetocentric frame I (Fig. 2.2):

The inertial frame used here has its origin in the Earth's center of mass, with the z -axis pointing in the direction of rotation (north as positive), the x -axis pointing in a reference direction and the y -axis completes the frame. For Earth the reference direction for the x -axis is typically the direction of vernal equinox (First Point of Aries, Υ). The reference frame that is commonly used is the J2000 reference frame.

Rotating planetocentric frame R (Fig. 2.2)

The rotating frame has its origin at the same position as the inertial frame, but is fixed to the Earth. The z -axis is again the rotation axis. The x -axis typically intersects the Greenwich meridian ($\tau = 0^\circ$, with τ being the longitude). The angle between the x - and y -axes of the I and R frames is termed the Greenwich Mean Sidereal Time (GMST) and denoted θ_{GMST} . From its value at $t = 0$ and the angular velocity ω_{cb} , the transformation between the inertial and planet-fixed frame can be determined. However, since this angle is constant for all simulations, it may also be put to zero and have no effect on the results. So, for simplicity, we assume that the I - and R -frame are collinear at $t = 0$. Also the Earth's angular velocity, as well as the rotation axis orientation, are considered to be constant, so any nutation or precession is ignored here.

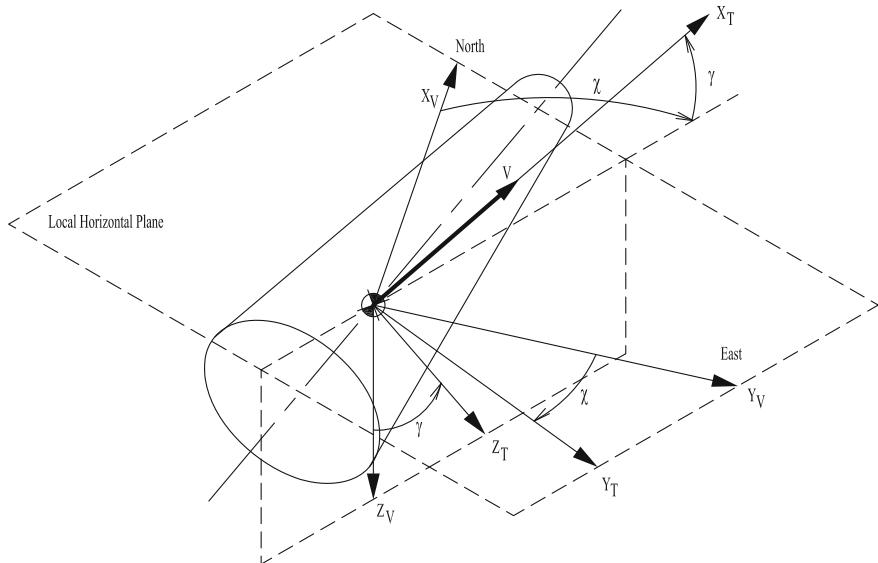


Fig. 2.3 Schematic representation of the vertical (index V) and trajectory (index T) frames

Vertical frame V (Figs. 2.2 and 2.3)

The vertical frame is vehicle-body centered, with its origin chosen at the center of mass of the vehicle. The directions of the axes based on the position relative to the central body. The z -axis points to the center of mass of the central body. The xy -plane is a locally horizontal plane (for a spherical central body), with the x -axis pointing to the north and the y -axis completing the system.

Trajectory reference frame T (Figs. 2.3 and 2.4)

The trajectory frame is body-centered, so again has the origin at the vehicle's center of mass. The trajectory reference frame has the x -axis pointing in the direction of flight, the z -axis lying in the vertical plane, pointing downwards and the y -axis completing the system. It should be noted that since the z -axis must be perpendicular to the x -axis and lie in the vertical plane, its direction is already defined, except for the sign (which is defined positive downwards).

Aerodynamic reference frame A (Fig. 2.4)

The aerodynamic frame has the origin at the center of mass of the vehicle. The x -axis is in the direction of the velocity vector, the z -axis is colinear with the lift force (see Fig. 2.5), but opposite in direction, and the y -axis completes the system. Two aerodynamic frames can be defined, one referenced to the airspeed and one to the groundspeed. However, since wind is not considered in this study, these two frames coincide and no distinction between the two will be made. It is noted that when the bank angle σ is zero, the A and T frames coincide.

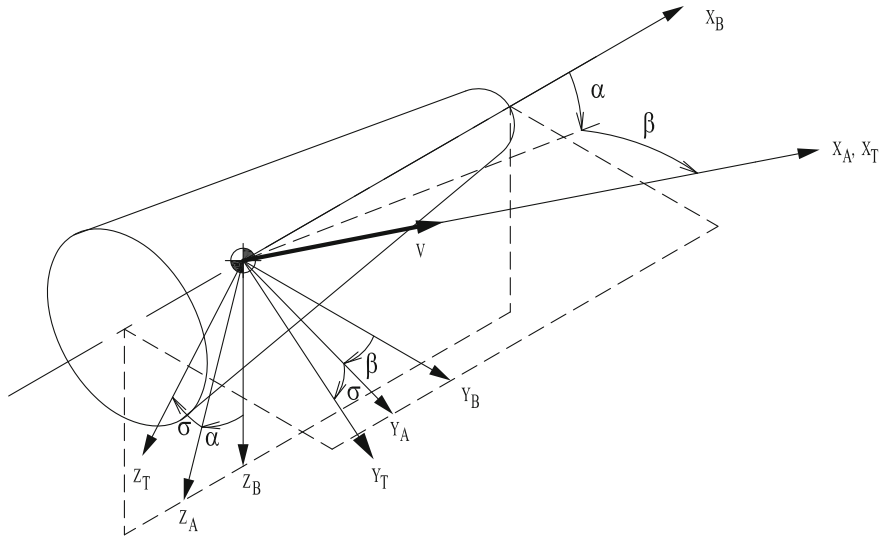


Fig. 2.4 Schematic representation of the B , A and T frames

Body frame B (Fig. 2.4)

The origin of the body frame is located in the center of mass of the vehicle, but, unlike the aerodynamic frame, are also fixed to the vehicle. The x -axis typically points in the direction of the front of the vehicle, the z -axis points down and the y -axis completes the system (corresponding to the direction of the right wing of an aircraft).

The transformations between the frames are handled using Euler angles. By using these, successive rotations about the axes are used to represent the full rotation. It should be stressed that the order of the rotations is not trivial, as changing them will result in a different transformation. The directional cosine matrices of rotation for a positively defined angle θ_i about the i^{th} axes are:

$$\mathbf{C}_x(\theta_x) = \begin{pmatrix} 1 & 0 & 0 \\ 0 & \cos \theta_x & \sin \theta_x \\ 0 & -\sin \theta_x & \cos \theta_x \end{pmatrix} \quad (2.13)$$

$$\mathbf{C}_y(\theta_x) = \begin{pmatrix} \cos \theta_x & 0 & -\sin \theta_x \\ 0 & 1 & 0 \\ \sin \theta_x & 0 & \cos \theta_x \end{pmatrix} \quad (2.14)$$

$$\mathbf{C}_z(\theta_x) = \begin{pmatrix} \cos \theta_x & \sin \theta_x & 0 \\ -\sin \theta_x & \cos \theta_x & 0 \\ 0 & 0 & 1 \end{pmatrix} \quad (2.15)$$

These transformation are called unit-axis transformations, since each of these gives the rotation about the x , y or z axis.

The total transformation matrix from system A to system C is constructed from these individual matrices, e.g., for rotation order j, k, l (first around the axis j , then the axis k and finally the axis l) as follows:

$$\mathbf{C}_{C,A} = \mathbf{C}_l(\theta_l) \mathbf{C}_k(\theta_k) \mathbf{C}_j(\theta_j) \quad (2.16)$$

The order of the matrices follows from the fact that one should successively left-multiply with the relevant rotation matrix. Similarly, when transforming from system A to C , an intermediate step of transformation to system B can be used (in case $\mathbf{C}_{B,A}$ and $\mathbf{C}_{C,B}$ are directly available, for instance) as follows:

$$\mathbf{C}_{C,A} = \mathbf{C}_{C,B} \mathbf{C}_{B,A} \quad (2.17)$$

Although a number of sets of three Euler angles will exist through which the system A can be rotated to find system C , it is possible that these angles will not have a clear physical interpretation. This could make an intermediate step to a system B the preferred method. It should be understood that in a series of three rotations as in Eq. (2.16), two non-successive rotations about the same axis may not be simply taken together as a single rotation over the sum of the angles. This is due to the fact that the orientation of this axis will have changed due to the intermediate rotation.

The rotation order for a number of relevant transformations are the following, from Mooij (1998):

$$\mathbf{C}_{R,I} = \mathbf{C}_z(\omega_{cb}t) \quad (2.18)$$

$$\mathbf{C}_{V,R} = \mathbf{C}_y(-\pi/2 - \delta) \mathbf{C}_z(\tau) \quad (2.19)$$

$$\mathbf{C}_{V,T} = \mathbf{C}_z(-\chi) \mathbf{C}_y(-\gamma) \quad (2.20)$$

$$\mathbf{C}_{T,A} = \mathbf{C}_x(\sigma) \quad (2.21)$$

$$\mathbf{C}_{A,B} = \mathbf{C}_z(\beta) \mathbf{C}_y(-\alpha) \quad (2.22)$$

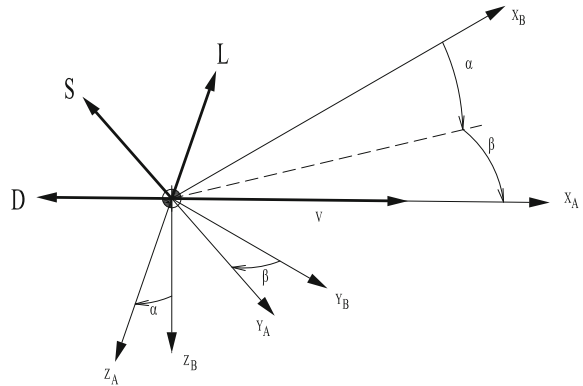
with γ and χ being the flight-path and heading angle, and α and β being the angle of attack and sideslip. Each of the angles has been defined in this section – see Figs. 2.2–2.4. It is noted that inverse transformation matrices are easily obtained. Because the transformation matrices are orthonormal, the inverse of such a matrix is simply its transpose.

2.2.2 Forces

This section will describe forces that describe the translational motion of the vehicle. The assumptions that we use to arrive at them are stated, and the physical implications of the resulting equations are discussed.

It will be assumed here that the aerodynamic and gravitational forces are the only external forces acting on the body, so:

Fig. 2.5 The aerodynamic drag (D), side (S) and lift (L) force



$$\mathbf{F}_{\text{ext},I} = \mathbf{F}_{a,I} + \mathbf{F}_{g,I} \quad (2.23)$$

where the I denotes that the inertial frame is used to evaluate the forces. No inclusion of propulsion is warranted due to the fact that only unpowered entry will be considered.

The gravitational force has been defined previously, Sect. 2.1.2, as follows:

$$\mathbf{F}_{g,V} = m\mathbf{g}_V \quad (2.24)$$

where $\mathbf{g}_V = (g_n \ 0 \ g_d)^T$; these gravity components are expressed in the V -frame, so to obtain the equivalent in the I frame we need to use the static transformation:

$$\mathbf{F}_{g,I} = m\mathbf{C}_{I,V}\mathbf{g}_V \quad (2.25)$$

with $\mathbf{C}_{I,V} = \mathbf{C}_{I,R}\mathbf{C}_{R,V}$, and the individual matrices given by the inverse matrices of $\mathbf{C}_{R,I}$ and $\mathbf{C}_{V,R}$ as shown in Eqs. (2.18)–(2.22).

The aerodynamic forces are defined in the aerodynamic reference frame A and given by:

$$\mathbf{F}_{a,A} = - \begin{pmatrix} C_D \\ C_S \\ C_L \end{pmatrix} \frac{1}{2} \rho V^2 S_{ref} \quad (2.26)$$

where C_D , C_S and C_L represent the drag, side force and lift coefficient, respectively, and V being the vehicle's velocity relative to the atmosphere. For some aerodynamic databases, the side force is defined positive in the positive y_A direction. However, the convention of having the three force coefficients in the aerodynamic frame defined in a right-handed manner, as in the above equation, will be observed here. A schematic representation is given in Fig. 2.5. Alternatively, the aerodynamic force may be represented in the body reference frame B by:

$$\mathbf{F}_{\mathbf{a},\mathbf{B}} = \begin{pmatrix} C_X \\ C_Y \\ C_Z \end{pmatrix} \frac{1}{2} \rho V^2 S_{ref} \quad (2.27)$$

where the relation between the two follows from the transformations described in Sect. 2.2.1.

The aerodynamic force is transformed to the I -frame with

$$\mathbf{F}_{\mathbf{a},\mathbf{I}} = \mathbf{C}_{\mathbf{I},\mathbf{A}} \mathbf{F}_{\mathbf{a},\mathbf{A}} \quad \text{or} \quad \mathbf{F}_{\mathbf{a},\mathbf{I}} = \mathbf{C}_{\mathbf{I},\mathbf{B}} \mathbf{F}_{\mathbf{a},\mathbf{B}} \quad (2.28)$$

with, for instance, $\mathbf{C}_{\mathbf{I},\mathbf{A}} = \mathbf{C}_{\mathbf{I},\mathbf{R}} \mathbf{C}_{\mathbf{R},\mathbf{V}} \mathbf{C}_{\mathbf{V},\mathbf{T}} \mathbf{C}_{\mathbf{T},\mathbf{A}}$, a combination of the (inverse) matrices defined earlier.

2.2.3 Entry Equations

The equations of translational motion follow directly from Newton's Laws of Motion. These laws are only directly valid when considering the motion in an inertial frame. However, by introducing relative rotations and including the resulting apparent forces (e.g., Coriolis; centripetal) between a target frame and the inertial frame, the equations can also be expressed in a rotating frame.

The resulting formulation of the equations is determined by the choice of state variables. For the translational motion through the atmosphere in three dimensions, six state variables are required to fully determine the motion, notably three position coordinates and three velocity components. In our numerical integration, the state is given by the Cartesian position and the velocity in the I -frame.

In its simplest form the state variables describing the inertial motion are $\mathbf{r}_I = (x_I \ y_I \ z_I)$ for the position, and $\mathbf{v}_I = (\dot{x}_I \ \dot{y}_I \ \dot{z}_I)$ for the velocity. With the gravitational and aerodynamic forces transformed to the I reference frame, the general equations of motion are:

$$\frac{d}{dt} \begin{pmatrix} \mathbf{r}_I \\ \mathbf{v}_I \end{pmatrix} = \begin{pmatrix} \mathbf{V}_I \\ \frac{1}{m} (\mathbf{F}_{\mathbf{a},\mathbf{I}} + \mathbf{F}_{\mathbf{g},\mathbf{I}}) \end{pmatrix} \quad (2.29)$$

To determine the trajectory of the vehicle from this set of six first-order, non-linear, coupled ordinary differential equations, no general analytical solution exists, so that numerical integration methods must be resorted to. A wide variety of such integration methods exists, with varying accuracy, computational complexity and numerical stability. Due to the conceptual nature of this study, the required accuracy of the entry trajectories is limited. This is due to the fact that modeling inaccuracies in, for instance, the aerodynamic coefficients and vehicle mass will also result in errors in the trajectories. Since a large number of trajectories has to be propagated, computational time should be kept to a minimum. It is possible to use a variable step-size integrator to allow for larger step sizes in regions of little variation in the solution. However, the fact that a guidance system with a certain update frequency is

used, makes these long time steps less desirable for a comparative analysis of vehicle behaviour.

A common numerical integrator for studies such as the one we discuss here is the Runge Kutta 4th-order method. Alternatively, a more accurate variable-step size methods can be used. Typical examples are the Dormand-Prince 4(5) method – a fourth-order method that is combined with a fifth-order method to determine the stepsize, given a predefined relative and/or absolute tolerance – or the family of Runge–Kutta–Fehlberg methods with different order pairs. Details on these and additional methods, including matters related to method stability, consistency and convergence can be found in a variety of texts, such as Shampine (1994), Lambert (1991), and Press et al. (2007).

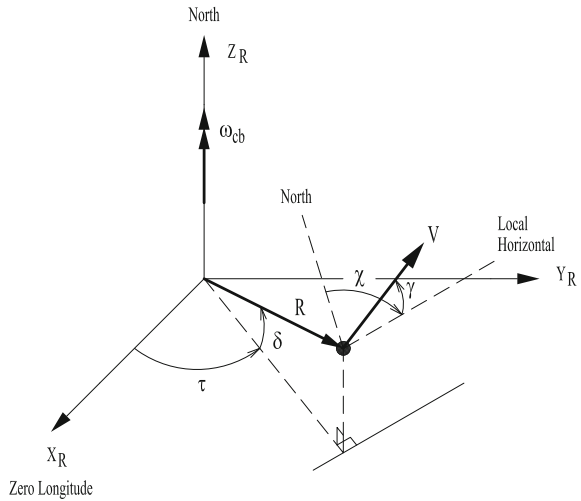
Although Eq. (2.29) may be used to efficiently simulate the trajectory of a vehicle, different representations can be more useful, either from a physical or computational viewpoint. A good example is the use of spherical position and velocity, which leads to a very intuitive formulation and representation of the equations of motion. These equations are commonly used for the development of guidance systems, which is the approach we take here (Sect. 2.3.2).

The spherical position coordinates and velocity components are shown in Fig. 2.6. These six state variables are defined as follows:

- Radial position r , the scalar distance from the center of the Earth to the vehicle’s center of mass.
- Longitude τ , measured from the Greenwich meridian, positive in east direction ($-180^\circ \leq \tau < 180^\circ$).
- Latitude δ , measured along the local meridian starting from the equator, positive in north direction ($-90^\circ \leq \delta \leq 90^\circ$).
- (Relative) velocity V . The scalar velocity is measured w.r.t. the ground, which in this work equals the airspeed, since there is no wind. Note that this velocity differs from the velocity in inertial coordinates due to the rotation of the Earth, so that $V < V_I$ for posigrade entries.
- Flight-path angle γ , which is the angle between the ground velocity vector and the local horizontal plane ($-90^\circ \leq \gamma \leq 90^\circ$).
- Heading angle χ , which is the angle between the north direction in the local horizontal plane and the ground velocity vector projected onto this plane ($-180^\circ \leq \chi < 180^\circ$). It is measured positive clockwise. A heading of 0° is due north, and 90° is due east.

The velocity vector shown here is relative to the rotating central body, so Eq. (2.29) needs to be adapted to take the rotation of the central body with respect to which the velocity is being evaluated into account. The position vector of the vehicle combined with the tangent to the local curvature of the Earth defines the vertical plane; the plane perpendicular to this is called the local horizontal plane and contains the center of mass of the vehicle as well as its horizontal velocity component. Also, this plane is defined by the x - and y -axes of the V -frame. When the vehicle is moving, the local horizontal plane is co-moving with the vehicle, and the rotation of this plane is the second correction to Eq. (2.29) that must be applied.

Fig. 2.6 Definition of spherical position and velocity with respect to a rotating frame



As the derivation of the equations of motion using r , τ , δ , V , γ , and χ is rather long and tedious, we suffice by stating the final result. Note that we assume that $S = 0$, as we set $\beta = 0$ throughout our analysis. For more information, the reader is referred to textbooks, such as those by Vinh et al. (1980), Regan and Anandakrishnan (1993) and Mooij (1998).

$$\begin{aligned}\dot{V} = & -\frac{D}{m} + g_d \sin \gamma - g_n \cos \gamma \cos \chi + \dots \\ & \dots + \omega_{cb}^2 R \cos \delta (\sin \gamma \cos \delta - \cos \gamma \sin \delta \cos \chi)\end{aligned}\quad (2.30)$$

$$\begin{aligned}V \dot{\gamma} = & \frac{L \cos \sigma}{m} - g_d \cos \gamma + g_n \sin \gamma \cos \chi + 2\omega_{cb} V \cos \delta \sin \chi + \dots \\ & \dots + \frac{V^2}{r} \cos \gamma + \omega_{cb}^2 r \cos \delta (\cos \delta \cos \gamma + \sin \gamma \sin \delta \cos \chi)\end{aligned}\quad (2.31)$$

$$\begin{aligned}V \cos \gamma \dot{\chi} = & \frac{S \sin \sigma}{m} + 2\omega_{cb} V (\sin \delta \cos \gamma - \cos \delta \sin \gamma \cos \chi) + \dots \\ & \dots + \frac{V^2}{r} \cos^2 \gamma \tan \delta \sin \chi + \omega_{cb}^2 r \cos \delta \sin \delta \sin \chi\end{aligned}\quad (2.32)$$

$$\dot{r} = \dot{h} = V \sin \gamma \quad (2.33)$$

$$\dot{\tau} = \frac{V \sin \chi \cos \gamma}{r \cos \delta} \quad (2.34)$$

$$\dot{\delta} = \frac{V \cos \chi \cos \gamma}{r} \quad (2.35)$$

It should be noted that the above equations have two singularities: in Eq. (2.31) this singularity is encountered for $\gamma = \pm 90^\circ$, which means a purely vertical flight (up or down). The second singularity is met when $\delta = \pm 90^\circ$, which is at either north or south pole. In this study, neither situation will occur, so these equations will serve the purpose as baseline for guidance-logic design.

Often, the equations are rewritten in terms of the $L/D (= C_L / C_D)$ ratio, along with a ballistic parameter or coefficient, defined as follows:

$$B = \frac{m}{S_{ref} C_D} \quad (2.36)$$

where sometimes the weight (at sea level) instead of the mass is used in this definition. The ballistic parameter denotes the relative influence of gravitational and aerodynamic drag forces. It can be used to give an indication of the altitudes at which maximum heating, deceleration, etc., take place. It will, in general, not be constant, however, due to changes in drag coefficient due to varying flight angles, velocities and altitudes.

2.3 Guidance Approach

To limit the computational time required for the trajectory calculation, targeting of a landing site or TAEM interface is not performed here. Instead, entry conditions are specified, while the end conditions will be kept free. A trajectory optimization is not deemed cost-effective, since this would require an optimization for each of the vehicle shapes that is generated. Since the optimization of a single trajectory can be rather time-consuming, such an approach is unlikely to be cost-effective here. Coupled trajectory and shape optimization has been performed by (Armellin 2007; Grant et al. 2011), but at the expense of a more simplified dynamical/aerodynamics model, which we do not deem to be a good balance of model fidelity for this particular study.

The guidance and control approach differs between the ballistic and winged entry vehicles, which are treated in Sects. 2.3.1 and 2.3.2. Finally, we briefly discuss stability issues in Sect. 2.3.3. Both the longitudinal behaviour, characterized by the angle of attack, α , and the lateral behaviour, characterized by the bank angle, σ , will be discussed. The sideslip angle, β , is always assumed to be zero for both types of vehicles. For definitions of the attitude angles, see Fig. 2.4.

2.3.1 Capsule

Capsule-shaped vehicles are typically controlled by a Reaction Control System (RCS) only, although some concepts using a flap for aerodynamic control have also

been proposed (Andersen and Whitmore 2007). However, attitude propagation will not be included in the simulations and the details of the control system will therefore not be considered. Instead, for the capsule vehicles trimmed conditions will be assumed. The trimmed angle of attack follows from:

$$\alpha_{tr} = \alpha|_{C_m=0} \quad (2.37)$$

That is, the angle of attack is chosen such that the pitch moment coefficient (see Sect. 3.2) equals zero. If such an angle of attack cannot be found within certain bounds, the vehicle will be labeled as untrimmable (see Sect. 6.3.2). In the context here, we define a trim angle to be the angle of attack that fulfills Eq. (2.37).

For symmetric vehicles with the center of mass on the center line, the trim attitude will be $\alpha_{tr} = 0$. For an offset center of mass in z -direction, e.g., as was the case for the Apollo capsule, the trimmed angle of attack will be non-zero. As described in Sect. 5.1, such an offset will also be used here as a design variable. As the moment-coefficient curve is a function of Mach number, the trimmed angle will also be dependent on Mach number. The change in coefficient with Mach number remains limited, though (see Sect. 7.2.1). Since the trajectory propagation has three degrees of freedom (only translational), the time-dependent process by which the capsule changes attitude is not analyzed. Considering the minor changes in angle of attack that are expected to occur, this will not influence the results significantly (assuming the vehicle to be stable). Attitude stability of the vehicle is important, however, as instability will make it unlikely for the vehicle to retain its trimmed conditions throughout the flight. For this reason, the following condition for static stability will be imposed on the capsule:

$$C_{m_\alpha}|_{\alpha=\alpha_{tr}} < 0 \quad (2.38)$$

Whether this relation is fulfilled or not depends on the location of the center of mass with respect to the center of pressure. This constraint is discussed further in Sect. 6.3.2. For the rare cases where a capsule is analyzed with two values of α_{tr} that fulfill Eq. (2.37), only the point that fulfills condition (2.38) is used. Since such cases will always have one controllable and one uncontrollable trim angle of attack, they will thus always be controllable.

In addition to pitch guidance the vehicle also requires lateral guidance, which can be achieved by bank-angle modulation. By modulating this angle, the direction of the lift vector can be controlled, so that influence on the flight-path and heading angles can be exerted, see Eqs. (2.31) and (2.32). To prevent the vehicle from skipping out of the atmosphere, the flight-path angle is controlled in such a manner that the following condition will hold:

$$\dot{\gamma} \leq 0 \quad (2.39)$$

From Eq. (2.31), neglecting the centrifugal term due to the Earth's rotation and the latitudinal gravity term, the following relation is obtained:

$$V\dot{\gamma} = \frac{L}{m} \cos \sigma - \left(g_d - \frac{V^2}{r} \right) \cos \gamma + 2\omega_{cb} V \cos \delta \sin \gamma \quad (2.40)$$

By setting $\dot{\gamma} = 0$, condition (2.39) is satisfied, while keeping the flight-path angle as large as possible, which will increase the vehicle's range. It follows that:

$$\cos \sigma = \frac{m}{L} \left[\left(g_d - \frac{V^2}{r} \right) \cos \gamma - 2\omega_{cb} V \cos \delta \sin \chi \right] \quad (2.41)$$

From the Earth's rotation rate ($\approx 7.27 \cdot 10^{-5}$ rad/s), it can be seen that the Coriolis acceleration can reach values of up to 1.1 m/s^2 for orbital velocity. When considering the fact that the term $g_d - V^2/r$ equals zero for orbital velocity, it can be concluded that the Coriolis term is an important contributor to the flight-path angle derivative. Therefore, it must not be neglected in the bank-angle determination.

The bank angle is modulated according to Eq. (2.41), until $\cos \sigma > 1$, at which point the vehicle no longer has sufficient lift to be able to fly at constant flight-path angle. When this occurs, the bank angle is set to 0° . It has been chosen to use the solution of positive σ of the above equation. This corresponds with banking to the left, as can be seen in Fig. 2.4.

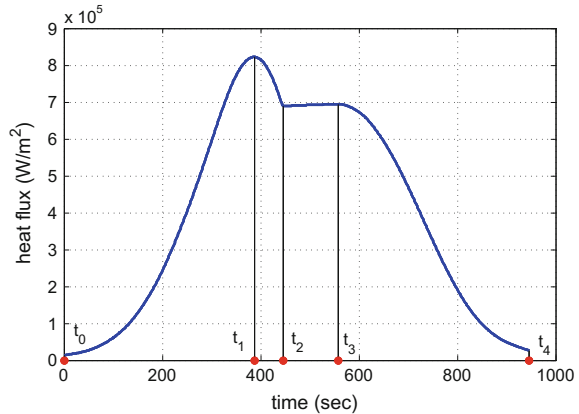
2.3.2 Winged Vehicle

The winged vehicles will be guided to fly a maximum time at a given reference stagnation-point heat rate $q_{c,s,ref}$, which can be seen as a typical mission profile for a class of experimental vehicles. This can yield valuable information of both flow and material behaviour at such a heat flux, aiding in the design effort of future re-entry vehicles (Mooij and Hänninen 2009). It has the virtue of allowing much of the guidance law to be expressed analytically.

For the first portion of the trajectory, the vehicle is commanded to fly at maximum angle of attack, so as to minimize the maximum heat flux. After the maximum value of $q_{c,s}$ is reached, the heat-flux tracking is activated after $q_{c,s,ref}$ is reached, which will guide the vehicle to maintain a constant stagnation-point heat rate. A typical flight profile is shown in Fig. 2.7. In this figure, a number of characteristic times is indicated. These times are: i) t_0 , initiation of entry, ii) t_1 , point of maximum stagnation point heating, iii) t_2 , point of initiation of heat-flux tracking, iv) t_3 , end of heat-flux tracking, and v) t_4 end of hypersonic entry phase ($M < 3$).

If the heat rate at t_1 is smaller than $q_{c,s,ref}$, the heat rate at the heating peak will be tracked instead. In such a case t_1 and t_2 will coincide. A similar approach could be used at the end of the trajectory to maintain constant dynamic pressure, as both rely (approximately) on keeping

Fig. 2.7 Typical heat flux profile for described guidance algorithm



$$K = \rho V^n \quad (2.42)$$

constant, where $n \approx 6$ (exact value depends on the choice of model, see Eq. (3.77)) for constant heat rate and $n = 2$ for constant dynamic pressure. Taking the first derivative with respect to time yields the following:

$$0 = \frac{d\rho}{dt} V^n + \rho n V^{n-1} \frac{dV}{dt} \quad (2.43)$$

$$\frac{dV}{dt} = -\frac{1}{n} \frac{V}{\rho} \frac{d\rho}{dt} \quad (2.44)$$

To enforce this condition, we modulate α to cause the drag to be such that Eq. (2.44) is enforced (see Eq. (2.30)). The bank angle is modulated to enforce Eq. (2.41).

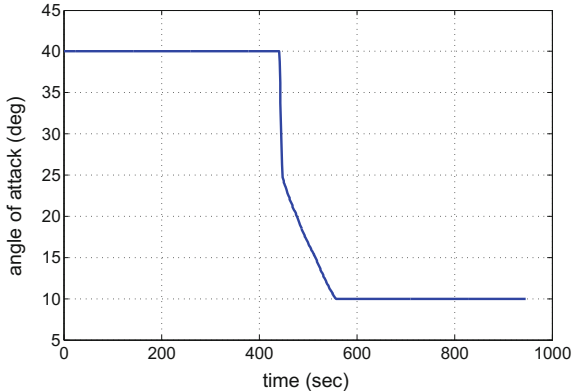
The angle-of-attack profile corresponding to the heat-flux profile shown in Fig. 2.7 is shown in Fig. 2.8, with minimum and maximum values of α set to 10° and 40° , respectively. It can be seen that the initiation of the heat-flux tracking corresponds to the initiation of the reduction of the angle of attack, and the end of the tracking corresponds to the minimum angle of attack.

Neglecting the centrifugal term due to the rotation of the Earth and latitudinal dependency of the gravitational acceleration, substitution of Eq. (2.44) into Eq. (2.35) leads to the following relation for the drag:

$$D_{K=const} = \frac{mV}{n\rho} \frac{d\rho}{dt} - mg \sin \gamma \quad (2.45)$$

From the aerodynamic coefficient database of the vehicle and the flight conditions, this value of the drag can be matched to a required angle of attack. A maximum angle-of-attack rate will be imposed to avoid discontinuities in the angle of attack. The winged-vehicle shapes that are to be analyzed will have active pitch control capability by the use of a body flap and elevons. Since only symmetric ($\beta = 0$)

Fig. 2.8 Typical angle of attack profile for described guidance algorithm



entries are considered, the yaw and roll moments will be zero by virtue of the vehicle symmetry w.r.t. the vertical center plane. The guidance scheme will attempt to trim the pitch moment by body flap and elevon deflections. First, trim by only the body flap is attempted. If this fails, the elevons are also used. The resulting values of δ_{bf} and δ_e lead to the following expressions for the aerodynamic coefficients:

$$C_D = C_{D,0}(\alpha) + \Delta C_{D,bf}(\alpha, \delta_{bf}) + \Delta C_{D,e}(\alpha, \delta_e) \quad (2.46)$$

$$C_L = C_{L,0}(\alpha) + \Delta C_{L,bf}(\alpha, \delta_{bf}) + \Delta C_{L,e}(\alpha, \delta_e) \quad (2.47)$$

$$C_m = C_{m,0}(\alpha) + \Delta C_{m,bf}(\alpha, \delta_{bf}) + \Delta C_{m,e}(\alpha, \delta_e)(= 0) \quad (2.48)$$

If the final non-zero condition on the moment coefficient is not satisfied by the control system, the solution is marked as infeasible in the optimization process. Again, the time-dependent process by which the attitude changes is not included in the simulation. Also, the control surface deflections are assumed to occur instantaneously.

The lateral guidance is performed in a manner similar to the capsule-shaped vehicle, with bank angle modulation based on Eq. (2.39), resulting in Eq. (2.41). Again, this is to prevent the vehicle from skipping out of the atmosphere. This is, due to the high lift of the winged vehicle, a very likely scenario if bank-angle modulation is not included. The bank-angle modulation is only started once the lift becomes the dominant term in Eq. (2.31). For the initial portion of the entry, the density is very low, so the lift will not have a significant influence on the vehicle's behaviour compared to the other forces.

2.3.3 Vehicle Stability

Related to the control capabilities and characteristics of entry vehicles are their attitude-stability characteristics. Although the analysis of attitude stability will be

rather simplified here, as no rotational motion is included in the trajectory propagation, a number of general vehicle characteristics are used that are indicative for stability.

When discussing stability, two different types are distinguished, static and dynamic. For static vehicle stability, only the tendency of the vehicle to move to an equilibrium position is considered, whereas dynamic stability also considers the time-dependent process that is involved. When the vehicle is trimmed, the equilibrium attitude corresponds to its current attitude, as the center of mass coincides with the center of pressure and the resulting moment about this point is zero.

Now, we consider what will happen to the vehicle's attitude when there is a slight difference between the center of pressure and center of mass is introduced, *i.e.*, when the current attitude is slightly perturbed from equilibrium. If the vehicle has the tendency to move back to its equilibrium position, it is considered to be statically stable. This behaviour is characterized by a number of stability derivatives, which denote the resulting moments as a result of a change of attitude. Three stability derivatives will be used here, C_{m_α} , C_{l_β} and C_{n_β} , which denote the changes in pitch, roll and yaw moment due to a change in angle of attack, angle of sideslip and angle of sideslip, respectively, so:

$$C_{m_\alpha} = \frac{\partial C_m}{\partial \alpha} \quad (2.49)$$

$$C_{l_\beta} = \frac{\partial C_l}{\partial \beta} \quad (2.50)$$

$$C_{n_\beta} = \frac{\partial C_n}{\partial \beta} \quad (2.51)$$

The value of C_{m_α} is a measure for the pitch stability of the vehicle. To clarify this, consider the situation when the angle of attack of the vehicle is slightly increased from its equilibrium position. If this causes the value of C_m to increase (corresponding to positive C_{m_α}), this would cause a positive value of $\dot{\alpha}$, which increases the angle of attack further, as well as C_m , etc. As such, the equilibrium point is unstable for pitch motion. Similarly, deviations in sideslip angle must not cause the yaw or roll moment to increase.

The influence of control-surface deflections on the vehicle stability can be quite substantial. Specifically, upward and downward deflections of the control surfaces yield different contributions to the pitch moment derivative. A clear explanation of this is given by Hirschel and Weiland (2009), where a flat plate with a control surface at the end is analyzed. In general, an upward control-surface deflection will aid in pitch stabilizing the vehicle, whereas a downward deflection will decrease the pitch stability. However, since a downward deflection of the control surface will increase the L/D of the vehicle, a trade-off must be made between these conflicting requirements. The results of this trade-off, as performed by the optimizer, will be discussed in Sect. 9.2.

For dynamic stability, the dynamic behaviour of the attitude dynamics must be considered. However, this behaviour is typically characterized by the derivatives of the moment coefficients with respect to attitude rates and quantities involving the moments and products of inertia. To include such matters, the trajectory simulation could be extended to six degrees of freedom, to include attitude propagation. Such an extension of the analysis would introduce the need for the determination of dynamic aerodynamic derivatives. For hypersonic vehicles, the embedded Newtonian method (Ericsson 1975; East and Hutt 1988) is a good candidate in the context of the methods we use. Alternatively, the theory described by McNamara et al. (2010) for non-rigid structures at hypersonic velocities could be adapted. In addition, attitude dynamics would require knowledge of the inertia tensor of the vehicles. This would require that the mass model be extended, as the specific mass distribution is then needed. The additional required computational cost would be extensive, at a limited addition to the model fidelity. Consequently, we limit ourselves to static stability considerations here.

Chapter 3

Aerothermodynamics

To evaluate the performance of re-entry vehicles, it is crucial to have a model for their aerothermodynamic performance. In this study, we only discuss the hypersonic phase of the entry. Consequently the present chapter is limited to this aerodynamic regime.

We focus on discussing the models that are used to obtain a conceptual approximation for the aerodynamic forces and moments coefficients on the vehicle, as well as the heat flux at a number of key areas (stagnation point, wing leading edge etc.). First, the fundamentals of aerothermodynamics relevant to our discussion are presented in Sect. 3.1. Subsequently, in Sect. 3.2 we present the explicit relations between the vehicle's pressure distribution and the resulting aerodynamic forces and moments (we neglect the viscous forces during the entry; Sect. 3.1.3 and Appendix A). The prediction of the pressure distribution itself will be discussed in Sect. 3.3. Finally, models for heat transfer are presented in Sect. 3.4.

3.1 Basic Concepts

In this section we discuss a number of basic concepts of (hypersonic) aerothermodynamics that are relevant to our discussion. In Sect. 3.1.1, we start by outlining some general thermodynamic properties in hypersonic flow, followed by a discussion on the general aspects of the structure of hypersonic flow around an entry vehicle in Sect. 3.1.2. Finally, we give a short overview on viscous effects in Sect. 3.1.3. A more detailed analysis on the approximate magnitude of viscous effects on aerodynamic properties is given in Appendix A.

To provide a contextual framework, matters fundamental to assumptions that are made on the flow characteristics in the computational scheme that we use are included. A broad variety of dedicated texts discussing various aspects of hypersonic aerothermodynamics in excellent detail is available, such as Anderson (2006), Bertin (1994), Rasmussen (1994), Dorrance (1962), Hayes and Probstein (1966) and Hirschel (2005).

3.1.1 Thermodynamic Properties

As will be discussed in Sect. 3.2, the dynamical behaviour of the entry vehicle is determined largely by the pressure distribution on its surface. In freestream flows that are of interest here, the ideal gas law may be used:

$$p = \rho RT = \frac{RT}{v} \quad (3.1)$$

where p , ρ , v and T denote the local pressure, density, specific volume and temperature of the gas, respectively, and R is the value of the specific gas constant of the gas. Equation (3.1) is based on the assumption that all intermolecular forces may be neglected, so that the particles can be modeled as experiencing non-elastic collisions. This leads to the elegant ‘particles-in-a-box’ model (see Anderson 2006).

The value of the specific gas constant R is related to the universal gas constant \mathcal{R} and the molar mass of the gas \mathcal{M} by:

$$R = \frac{\mathcal{R}}{\mathcal{M}} \quad (3.2)$$

It should be stressed that R is dependent on the mixture, whereas \mathcal{R} is universal, having a value of $\approx 8.317743 \text{ J/(K}\cdot\text{mol)}$. For air at sea level conditions, the value of the specific gas constant is $287.05 \text{ J/(kg}\cdot\text{K)}$. The two are understood to be the gas constant per ‘unit mass’ and ‘per mole’, respectively. A related constant is the Boltzmann constant k_B , which is the gas constant ‘per particle’ and has a value of $1.380650 \cdot 10^{-23} \text{ J/K}$.

The key extrinsic variables describing the properties of the gas are the energy and enthalpy. Here we denote the energy and enthalpy per unit mass as e and h , respectively. The two quantities are related as follows (assuming the gas to be calorically perfect):

$$h = e + pv \quad (3.3)$$

From this relation, it can be seen that the enthalpy is a measure of the energy in a system that includes the work that the system can do, due to the inclusion of the term pv .

To relate the internal energy and enthalpy to the gas temperature, the specific heats c_p and c_v are introduced, which are defined as follows:

$$c_p = \left(\frac{\partial e}{\partial T} \right)_p \quad (3.4)$$

$$c_v = \left(\frac{\partial h}{\partial T} \right)_v \quad (3.5)$$

where the subscripts denote that the derivatives are taken at constant p and v , respectively. Consequently, the value of c_p is affected by how much the gas expands, so how much work is done, whereas c_v is not. This is due to the fact that to have the pressure remain constant at an increasing temperature, the (specific) volume should increase, see Eq. (3.1). This leads to the conclusion that $c_p > c_v$. A related quantity that is crucial in the aerothermodynamic analysis of entry vehicles is the ratio of specific heats γ , which is defined as:

$$\gamma = \frac{c_p}{c_v} \quad (3.6)$$

which must always be greater than 1. In certain approximate schemes, however (see Sect. 3.3.1) the assumption $\gamma = 1$ is made, which implies that the gas cannot expand due to heating. By substituting (3.1) into (3.3), it can be seen from the definitions of the specific heats in Eqs. (3.4) and (3.5) that, for constant R , the following relation will hold:

$$R = c_p - c_v \quad (3.7)$$

At low temperatures, up to about 800 K for air at 1 atmosphere, the flow may be considered to be calorically perfect. A calorically perfect gas is one where the specific heats, as well as the ratio between the two, is constant, and the following will hold:

$$h = c_p T \quad (3.8)$$

$$e = c_v T \quad (3.9)$$

Physically, this assumption is valid due to the fact that the only degrees of freedom that the particles have are translational and rotational, so that the molecules may be considered ‘rigid rotors’.

An additional key extrinsic property of the flow is the entropy s , which is a measure of the disorder of the particles in the system. Entropy is a quantity that plays a key role in the behaviour of gases through the second law of thermodynamics, which states that

$$ds = \frac{\delta q}{T} + ds_{irrev} \quad (3.10)$$

$$ds \geq \frac{\delta q}{T} \quad (3.11)$$

where δq is the variation of the internal energy of the system, and s_{irrev} denotes the entropy increase due to irreversibility of the process. Entropy is in essence a statistical quantity, so that the above relation should be viewed in a ‘mean’ sense. However, the number of particles that are dealt with in aerodynamics are such that the inequality will hold in all practical situations.

Processes for which $ds = 0$ are termed isentropic. For an isentropic process, the following equations can be used to relate thermodynamic quantities at two points on the streamline:

$$\frac{p_2}{p_1} = \left(\frac{T_2}{T_1} \right)^{\frac{\gamma}{\gamma-1}} \quad (3.12)$$

$$= \left(\frac{\rho_2}{\rho_1} \right)^\gamma \quad (3.13)$$

which are based on the assumption of a calorically perfect gas. A process is isentropic if it is reversible and adiabatic. An adiabatic process is one where no heat is externally added to the system.

In addition to the properties of the flow such as pressure, density, temperature, etc., their related total (or stagnation) properties are also of interest for calculation of the aerothermodynamic properties of a vehicle. These quantities are those that are obtained when bringing the flow adiabatically to rest, causing p , ρ and T to increase. For the calculation of the total enthalpy h_T , the following is a typical approximation (which follows from constant c_p and c_v):

$$h_T = h + V^2/2 \quad (3.14)$$

with h the freestream enthalpy with velocity V . The total temperature can be obtained from this relation and Eqs. (3.6)–(3.8) for calorically perfect gasses as follows:

$$\frac{T_T}{T} = 1 + \frac{\gamma - 1}{2} M^2 \quad (3.15)$$

By also assuming the stagnation process to be isentropic, Eqs. (3.12) and (3.13) can then be used to determine the total pressure and density. Although only valid for an isentropic, adiabatic deceleration of a calorically perfect gas, this simple model allows for acceptably accurate descriptions of some key aspects of the aerothermodynamic behaviour during re-entry, at least for a conceptual design (Sect. 3.3).

For the description of supersonic flows, an essential characteristic is the speed of sound in the gas, which is the velocity at which infinitesimal pressure changes propagate through the flow. If the velocity of a vehicle moving through the flow is greater than this velocity, the particles upstream of the vehicle will be unaware of it. The consequences of this will be discussed in more detail in the next section. This characteristic velocity is termed the speed of sound, denoted by a . It can be determined as follows:

$$a = \sqrt{\gamma RT} \quad (3.16)$$

Related to this quantity is the Mach number, which denotes the ratio of a velocity V to the speed of sound, so it is defined as:

$$M = \frac{V}{a} \quad (3.17)$$

The Mach number is one of the main characteristics of supersonic and hypersonic flow and is a crucial independent variable as a function of which many properties, such as aerodynamic coefficients, are typically provided.

3.1.2 Characteristics of Super/Hypersonic Flow

In flows with $M > 1$, the vehicle moves at a velocity that is greater than the velocity with which disturbances can propagate upstream in the flow. This means that the air ahead of the vehicle does not ‘know’ that the vehicle is approaching. This leads to the formation of a shock wave, which is a discontinuity in velocity and thermodynamic properties. Depending on the shape of the vehicle that is flying at supersonic speeds, the shock wave may be attached or detached, and straight or curved (Fig. 3.3), for reasons will be discussed shortly.

The relations for the flow quantities after a steady shock, denoted by the 2 subscript, from those before the shock, denoted by 1, are given by the so-called Rankine–Hugoniot relations (3.18)–(3.22). They follow from conservation of mass, momentum and total enthalpy across a shock:

$$\frac{p_2}{p_1} = 1 + \frac{2\gamma}{\gamma + 1} (M_{n,1}^2 - 1) \quad (3.18)$$

$$\frac{\rho_2}{\rho_1} = \frac{(\gamma + 1)M_{n,1}^2}{2 + (\gamma - 1)M_{n,1}^2} \quad (3.19)$$

$$M_{n,2}^2 = \frac{1 + ((\gamma - 1)/2) M_{n,1}^2}{\gamma M_{n,1}^2 - (\gamma - 1)/2} \quad (3.20)$$

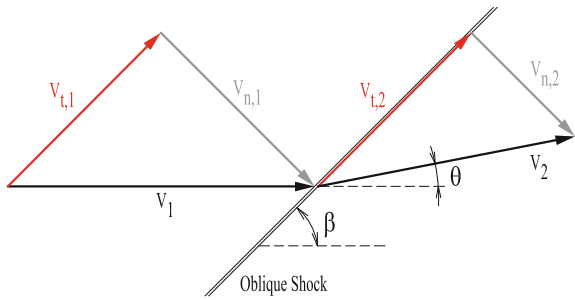
$$M_{t,2}^2 = M_{t,1}^2 \quad (3.21)$$

$$s_2 - s_1 = c_p \ln \left(\left(1 + \frac{2\gamma}{\gamma + 1} (M_{n,1}^2 - 1) \right) \frac{2 + (\gamma - 1)M_{n,1}^2}{(\gamma + 1)M_{n,1}^2} \right) - \dots \\ \dots - R \ln \left(1 + \frac{2\gamma}{\gamma + 1} (M_{n,1}^2 - 1) \right) \quad (3.22)$$

The equation for the entropy rise assumes a calorically perfect gas. It can be seen from these relations that the pressure and density, and through Eq. (3.1) the temperature, are increased over a shock. This is due to the decrease in velocity and the conservation of mass and momentum. Also, the rise in these quantities increases with increasing values of $M_{n,1}$, so with an increase in either free stream Mach number or shock angle.

After crossing a shock wave that is not perpendicular to the incoming flow, the flow will be deflected over an angle θ w.r.t. its initial direction (see Fig. 3.1). The

Fig. 3.1 Schematic representation of flow over an oblique shock



angle θ is related to the freestream Mach number and the shock angle β by the following relation:

$$\tan \theta = 2 \cot \beta \frac{M_1^2 \sin^2 \beta - 1}{M_1^2 (\gamma + \cos 2\beta) + 2} \quad (3.23)$$

The relation between θ , β and M is shown in Fig. 3.2. From this figure two key properties of shock behaviour can immediately be observed. First of all, for deflection angles greater than some $\theta_{max}(M)$, there does not exist any oblique shock solution, leading to a detached shock (Fig. 3.3). Secondly, Fig. 3.2 shows that for each value of θ below θ_{max} , there are two possible solutions for the shock angle, the so-called weak solution (smaller β) and strong solution (larger β). These names stem from the size of the jump of the flow quantities over the shock, which is greater for the strong solution. In reality, however, the weak shock solution is typically the one that occurs, unless there is information to the contrary, such as the inability of a weak shock to form for a given situation.

An infinitely weak oblique shock wave is termed a Mach wave. The shock angle of such a wave is denoted μ , called the Mach angle:

$$\mu = \arcsin \left(\frac{1}{M} \right) \quad (3.24)$$

In cases where an attached shock cannot form on the body, a detached shock forms, as on the right-hand side of Fig. 3.3. For such a detached shock, the flow will be perpendicular to the shock on a single streamline and curve to higher values of β away from this intersection. As a result, different streamlines will pass through shocks of different strengths, complicating the analysis of the flow field behind the shock wave. A blunt nose is, however, typically used on re-entry vehicles, since a pointed nose would suffer from excessive heating (if not actively cooled). As can be deduced from Eq. (3.20), the flow behind a shock with sufficiently high β will be subsonic. This leads to a region near the stagnation point of the vehicle where the flow is subsonic, while the flow further away from it is supersonic. The line between the shock and the body where the flow transitions from subsonic to supersonic is

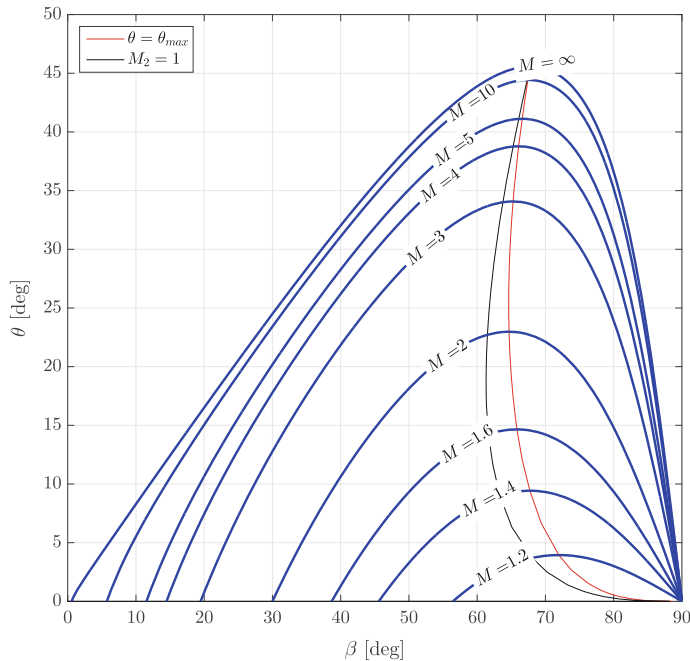


Fig. 3.2 $\theta - \beta - M$ plot for oblique shock waves

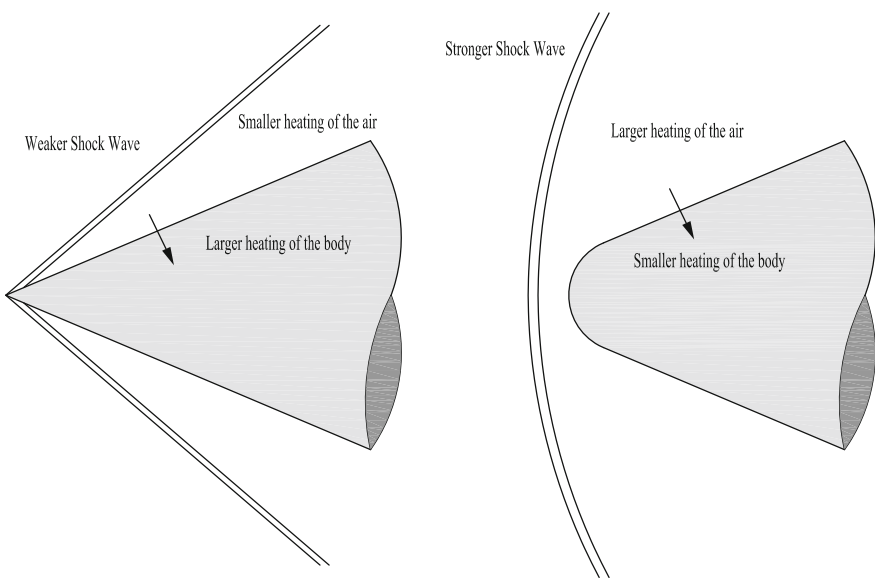


Fig. 3.3 Comparison of flow behaviour of sharp and blunt vehicles in supersonic and hypersonic flow

called the sonic line and the point on the body (or more precisely at the boundary layer edge) where $M = 1$ is called the sonic point.

In addition to the presence of shock waves, which compress the flow, expansion waves can occur in supersonic flows. Shock waves are caused by a decrease in cross-sectional area through which the air can travel (due to, for instance the ‘sudden’ appearance of a re-entry vehicle). Expansion waves, on the other hand, are caused by an increase in this cross-sectional area, which occurs after the flow passes over the vehicle, for instance. For a known deflection angle θ , the Mach number after the deflection (subscript 2) can be obtained from the state before the deflection through the Prandtl–Meyer function $v(M)$ as:

$$|\theta| = v(M_2) - v(M_1) \quad (3.25)$$

$$v(M) = \sqrt{\frac{\gamma + 1}{\gamma - 1}} \tan^{-1} \sqrt{\frac{\gamma - 1}{\gamma + 1} (M^2 - 1)} - \tan^{-1} \sqrt{M^2 - 1} \quad (3.26)$$

An expansion wave is isentropic, so the thermodynamic state after the wave can be related to that before it by Eqs. (3.12) and (3.13). It can be seen as a ‘fan’ of Mach waves, from which the angle with which the expansion fan is inclined to the flow before and after the expansion can be determined from Eq. (3.24). The maximum possible turning angle $|\theta|$ can be determined from the maximum value of $v(M_2)$, which corresponds to expansion to a vacuum. The corresponding value of $v(M_2)$, termed v_∞ is the following:

$$v_\infty = \frac{\pi}{2} \left(\sqrt{\frac{\gamma + 1}{\gamma - 1}} - 1 \right) \quad (3.27)$$

To obtain the Mach number after expansion from Eq. (3.26), an inversion of the function $v(M)$ is required. Unfortunately, no closed-form solution is available, so it is necessary to use either a numerical solution or an approximate relation such as a correlation. An approximate solution for the inversion is given by Hall (1975):

$$y = \left(\frac{v(M_2)}{v_\infty} \right)^{\frac{2}{3}} \quad (3.28)$$

$$M = \frac{1 + Ay + By^2 + Cy^3}{1 + Dy + Ey^2} \quad (3.29)$$

The values of the coefficients for $\gamma = 1.4$ are given in Table 3.1.

A final flow effect that should be discussed here, although not strictly a part of supersonic or hypersonic flow, is that of rarefied flow. At high altitudes, where the density is very low, the assumption that the flow is a continuum is no longer valid and its behaviour and its effect on the vehicle change. For rarefied flow, the Knudsen number Kn is a defining parameter:

Table 3.1 Coefficients in empirical Prandtl–Meyer function inversion, Eq. (3.29), for $\gamma = 1.4$

Coefficient	Value
A	1.3604
B	0.0962
C	-0.5127
D	-0.6722
E	-0.3278

$$Kn = \frac{\lambda}{L_{ref}} \quad (3.30)$$

Here, L_{ref} is a characteristic length of the vehicle and λ is the mean free path, which is the average distance that a particle travels before colliding with another particle. Now, three different flow regimes can be distinguished: free molecular flow, $Kn > 1.0$, transitional flow, $0.03 < Kn < 1.0$ and continuum flow, $Kn < 0.03$.

In continuum flow, a particle will impact another particle very close to the body following an impact with the body, so that the fluid may be considered to be a continuum of particles. For rarefied flow, however, the particles travel relatively long distances after hitting the vehicle before impacting another particle, making the continuum flow assumption invalid. Instead, it is better to model the flow as a discrete number of particles with statistically determined quantities. Since there is no clear line where continuum and rarefied flow begin and end, an intermediate regime, termed transitional flow, is typically also used. Due to the high altitude, and resultantly low density, at which free molecular flow effects occur, the influence on the dynamics and thermal state of the vehicle will remain limited. For this reason, the continuum assumption will be made for all calculations in this study.

3.1.3 Viscosity

In addition to the inviscid transport of mass, momentum and energy, viscous effects due to intermolecular interaction result in additional transport of these quantities. The flow properties that determine the magnitude of these fluxes are the diffusion, viscosity and conductivity coefficients, respectively. The viscous transport is caused by gradients in the concentration of a specie, momentum and temperature. This transport causes the formation of a boundary layer at the wall, due to the no-slip condition, which requires that the velocity at the vehicle surface be zero. In addition, the temperature at the surface must equal the flow temperature at the surface. As a result, gradients in velocity and temperature arise, which in turn cause a friction force and heat transfer.

The viscosity μ determines the viscous transfer of momentum and is an important factor in determining the effect on the aerodynamic forces that viscosity has. To this end, the Reynolds number, with respect to a characteristic length x , is defined as:

$$\text{Re}_x = \frac{\rho Vx}{\mu} \quad (3.31)$$

which is a measure for the ratio of inertial and viscous forces.

Using these basic concepts, as well as a number of additional techniques, a derivation followed by a number of simulations are given in Appendix A. There, a simple model (Eckert 1955; Hansen 1958; White 2006) is used to estimate the relative viscous force magnitude w.r.t. the pressure force, for cases relevant for our further analyses. The results indicate that the viscous force is sufficiently small to be neglected for our purposes (at most <5 % of the pressure force for the majority of cases).

Although viscous flow effects on the aerodynamic loads will be neglected in the analyses that will be executed, some additional matters for the context of aerodynamic heating are given in Sect. 3.4. Extensive details on viscous flow can be found in e.g., White (2006), Schlichting and Gersten (1999) and Dorrance (1962).

3.2 Aerodynamic Loads

During entry, the airflow around the vehicle causes forces and moments that are a major factor in its dynamical behaviour (Sect. 2.2.2). In general, two physical contributions add to these loads on the vehicle: pressure and friction. During the continuum hypersonic phase, pressure is the primary contributor to the aerodynamic loads, as discussed in Sect. 3.1.3. Consequently, viscous forces are often neglected in conceptual studies into the behaviour of entry vehicles, and we take the same approach here. This section will give a brief overview of how the pressure distribution on the vehicle is related to the aerodynamic forces and moments.

Neglecting friction, the aerodynamic forces and moments can be determined from the distribution of the pressure p over the closed vehicle surface as follows:

$$\mathbf{F}_a = \iint_S (p \hat{\mathbf{n}}) \, dS \quad (3.32)$$

$$\mathbf{M}_a = \iint_S ((\mathbf{r} - \mathbf{r}_{ref}) \times p \hat{\mathbf{n}}) \, dS \quad (3.33)$$

where \mathbf{r}_{ref} is a chosen reference point about which the aerodynamic moments are evaluated, \mathbf{r} is the position on the vehicle surface element dS , and $\hat{\mathbf{n}}$ is the outward unit normal.

The relation between the aerodynamic moments following a change of reference point (denoted by ') and the forces and moments prior to this change is the following:

$$\mathbf{M}'_a = \mathbf{M}_a - (\mathbf{r}' - \mathbf{r}) \times \mathbf{F}_a \quad (3.34)$$

Related to the moment coefficients is the point in the vehicle known as the center of pressure. The defining property of this point is that the moments around it are zero, so that;

$$\mathbf{M}_{cp} = \mathbf{0} \quad (3.35)$$

whence the location of this point can be found.

Equations (3.32) and (3.33) can be used to evaluate the forces and moments in two manners. The first option is to derive analytical formulations for the pressure distribution over the vehicle surface and (numerically) integrate the above. Alternatively, the vehicle surface can be discretized into a number of panels on each of which the pressure is determined analytically or numerically. When discretizing the surface, the above integrals become summations over all n_p vehicle panels that approximate the force and moment, as follows:

$$\mathbf{F}_a = \sum_{i=1}^{n_p} -p_i A_i \hat{\mathbf{n}}_i \quad (3.36)$$

$$\mathbf{M}_a = \sum_{i=1}^{n_p} -p_i A_i (\mathbf{r}_i - \mathbf{r}_{ref}) \times \hat{\mathbf{n}}_i \quad (3.37)$$

The vector \mathbf{r}_i now denotes the centroid of the panel, p_i the (mean) pressure on the panel, A_i the panel area and $\hat{\mathbf{n}}_i$ the panel unit normal.

Aerodynamic forces and moments are typically defined by non-dimensional numbers, leading to the following expressions for the aerodynamic force and moment coefficients in the body frame (see Sect. 2.2.2):

$$S_{ref} \begin{pmatrix} C_X \\ C_Y \\ C_Z \end{pmatrix} \approx - \sum_{i=0}^n C_{p_i} A_i \hat{\mathbf{n}}_i \quad (3.38)$$

$$S_{ref} \begin{pmatrix} C_l \\ C_m \\ C_n \end{pmatrix} \approx - \sum_{i=0}^n C_{p_i} A_i (\mathbf{r}_i \times \mathbf{r}_{ref}) \times \hat{\mathbf{n}}_i \quad (3.39)$$

Here, C_p denotes the pressure coefficient, which is defined as:

$$C_p = \frac{p - p_\infty}{q_{dyn}} \quad (3.40)$$

$$= \frac{2}{\gamma M_\infty^2} \left(\frac{p}{p_\infty} - 1 \right) \quad (3.41)$$

The term involving p_∞ in the summations of Eqs. (3.36) and (3.37) drops out, since integrating a constant value over a closed surface evaluates to zero. The dynamic pressure is defined as the following:

$$q_{dyn} = \frac{1}{2} \rho V^2 \quad (3.42)$$

which for a calorically ideal, perfect gas can be written as:

$$q_{dyn} = \frac{1}{2} \gamma p M^2 \quad (3.43)$$

The methods described in Sect. 3.3 will be used to determine the pressure on each vehicle panel. For a number of these methods, such as the Newtonian approximation, the possibility of deriving (semi-)analytical formulations for shapes that have an analytical formulation is feasible (Grant and Braun 2010). However, multiple aerodynamic methods will be applied here, so that such an approach cannot be taken. For this reason, a surface discretization (see Sect. 5.3) will be applied here.

In this study, the viscous forces are ignored and the ratio of specific heats γ is assumed constant. Therefore the functional dependency of a given aerodynamic coefficient C_i can be written as follows:

$$C_i = C_i(M, \alpha, \beta) \quad (3.44)$$

As will be discussed in the next section, in our simplified model the only environmental dependency of the pressure coefficient is the Mach number. The variables α and β denote the angle of attack and sideslip, respectively (see Sect. 2.2.1), which define the orientation of the vehicle w.r.t. the oncoming flow.

In the case where the vehicle has non-zero control-surface deflections, the change in aerodynamic coefficients due to these deflections must be included. In this study, control surfaces are only used for the winged vehicle shape (see Sect. 2.3), in particular a body flap and elevons. With the methods used here, a deflection of the control surface will be assumed to have an effect on the pressure distribution of the deflected panel only. Consequently, the aerodynamic coefficients of a vehicle with deflected coefficients can be split into two parts. The first part, which is independent of control-surface deflection, gives the coefficients of the configuration with flush (undeflected) control surfaces. This contribution is denoted by a 0 subscript. The second part gives the influence of the control surfaces only, quantifying the influence of the deflections w.r.t. the flush configuration. This influence on the aerodynamics is characterized by control-surface increments. These are defined as follows for a coefficient C_i , for the body flap and elevon, respectively:

$$\Delta C_{i,bf}(\alpha, \beta, M, \delta_{bf}) = C_{i,bf}(\alpha, \beta, M, \delta_{bf}) - C_{i,bf}(\alpha, \beta, M, \delta_{bf=0}) \quad (3.45)$$

$$\Delta C_{i,e}(\alpha, \beta, M, \delta_e) = C_{i,e}(\alpha, \beta, M, \delta_e) - C_{i,bf}(\alpha, \beta, M, \delta_{e=0}) \quad (3.46)$$

where the coefficients with bf and e subscript are obtained by integrating the pressure distribution over the body flap and elevon only, respectively. The aerodynamic coefficient C_i of a vehicle with deflected body flap and elevon then becomes:

$$C_i(M, \alpha, \beta, \delta_{bf}, \delta_e) = C_{i,0}(M, \alpha, \beta) + \Delta C_{i,bf}(\alpha, \beta, M, \delta_{bf}) + \Delta C_{i,e}(\alpha, \beta, M, \delta_e) \quad (3.47)$$

where it should be realized that, in the context of the guidance algorithm used by our winged vehicle (see Sect. 2.3.2), $\delta_{bf} = \delta_{bf}(M, \alpha)$ and $\delta_e = \delta_e(M, \alpha)$ (as we fix the sideslip angle to zero).

In general, different methods are applicable for the aerodynamic analysis at low and high hypersonic Mach numbers (Sect. 3.3.2). To have a database of aerodynamic coefficients that is continuous in M , a bridging between the low and high hypersonic aerodynamic coefficients is employed, similar to what is often employed for the transitional region between rarefied and continuum flow, (Regan and Anandakrishnan 1993). A cubic bridging polynomial $f_c(t)$, with t running from 0 to 1, is used.

To use this method, it is required that there is an overlap between the low and high hypersonic regimes. In the overlap region $M_{high,min}$ to $M_{low,max}$, the following is used when an aerodynamic coefficient C_i is retrieved:

$$t = \frac{M - M_{low,max}}{M_{high,min} - M_{low,max}} \quad (3.48)$$

$$C_i = C_{i,high}f_c(t) + (1 - f_c(t))C_{i,low} \quad (3.49)$$

3.3 Local-Inclination Methods

An important class of force estimation methods in hypersonic flow is formed by the so-called local-inclination methods. For these methods, the dependency of the vehicle shape on the local pressure coefficient is significantly reduced. Specifically, only the angle by which the surface is (locally) inclined w.r.t. the freestream flow is needed for the calculation. For an outward surface normal $\hat{\mathbf{n}}$, the following can be used to directly relate the geometry mesh to the pressure coefficient:

$$\sin \theta = -\frac{\mathbf{V}_\infty \cdot \hat{\mathbf{n}}}{V_\infty} \quad (3.50)$$

Although these local-inclination methods are obviously highly simplified, acceptable results for conceptual studies can often be obtained from them (as we discuss here in Sect. 7.2). Due to their combination of simplicity and acceptable fidelity, this class of methods finds wide use in preliminary design and analysis, and are therefore perfectly suited to our goal. The long heritage has also made them well documented. An excellent introduction is given by Anderson (2006), with their formulation and implementation extensively discussed by, e.g., Gentry et al. (1973), Bonner et al. (1981) and Hoeijmakers et al. (1996).

Generally, two classes of methods are used, one for the windward side and one for the leeward side. The leeward side methods are also applied to ‘shielded’ (or

shadowed) sections. Shielding occurs when a vehicle is oriented to the flow in such a manner that a part of it is shielded from the oncoming flow by another part of it. In such cases, the windward surface inclination method should be applied only to the surface the flow encounters first, the second part should use an appropriate leeward method.

Section 3.3.1 will give a description of the various local-inclination methods that will be used, Sect. 3.3.2 will describe how these methods are selected based on the vehicle's geometry.

3.3.1 Description of Methods

The simplest local inclination method for the estimation of the aerodynamic forces and moments on a hypersonic body is the Newtonian method. This method assumes that upon hitting a surface, the flow velocity loses its component normal to the surface while retaining all of its tangential motion. This method was first devised by Isaac Newton to describe the effects of bodies in a fluid flow. Although it does not work well for low velocities, at hypersonic speeds it gives a reasonable estimation for the pressure force on a body, at least for relatively high inclinations. An in-depth discussion of the theory of Newton and its relation to hypersonic flow is given by Hayes and Probstein (1966). The assumptions of Newtonian flow effectively mean that the shock wave coincides with the vehicle body, which is the limiting case for $M \rightarrow \infty$ and $\gamma \rightarrow 1$.

The assumptions of Newtonian flow lead to the following relation for the local pressure coefficient:

$$C_p = 2 \sin^2 \theta \quad (3.51)$$

where θ is the inclination of the surface with respect to the flow. so that the Newtonian pressure coefficient at the stagnation point equals 2.

A modification of the Newtonian method that is typically used to improve the accuracy of the prediction involves an additional physical consideration of supersonic flow, namely the loss of total pressure over a shock wave. This is done by first determining the stagnation pressure coefficient behind a normal shock wave, which can be done from Eqs. (3.18)–(3.20). Subsequently, an isentropic deceleration is assumed and Eqs. (3.12) and (3.13) are used to determine the stagnation conditions, yielding the following result for the stagnation pressure coefficient:

$$C_{p,s} = \frac{2}{\gamma M_\infty^2} \left(\left(\frac{(\gamma + 1)^2 M_\infty^2}{4\gamma M_\infty^2 - 2(\gamma - 1)} \right)^{\frac{\gamma}{\gamma-1}} \left(\frac{1 - \gamma + 2\gamma M_\infty^2}{\gamma + 1} \right) - 1 \right) \quad (3.52)$$

The modified Newton method is then obtained as follows:

$$C_p = C_{p,s} \sin^2 \theta \quad (3.53)$$

which will yield results for the pressure coefficient slightly below the Newtonian value (see Figs. 3.5 and 3.6). Only the stagnation streamline passes through a normal shock (for axisymmetric vehicles at zero angle of attack). The vehicle surface further downstream is modeled in the Newtonian method as being ‘impacted’ by a streamline that passes through a shock with $\beta \neq 90^\circ$. As the loss in total pressure is less over such a shock wave than over a normal shock, the value of $C_{p,s}$ in the above relation is taken too low when using the modified Newtonian method. Although inclusion of such effects would theoretically increase the fidelity of the results, such an approach is typically not used, as it requires a description of the geometry of the shock, greatly increasing its complexity.

As previously mentioned, the Newtonian method provides good results for high inclinations, but decreases in accuracy for small inclination angles. For such regions, a different inclination method, such as the tangent-wedge/cone (discussed below) can be used. Alternatively, Modified Newtonian-Prandtl Meyer theory can be used. This method is based on finding the point along the nose (or other component) where the pressure gradient that is obtained from Modified Newtonian and Prandtl–Meyer expansion (from the stagnation point onwards) are equal (see Sect. 3.1.2). Before this matching point, the Modified Newtonian method is used for pressure determination. After it, Prandtl–Meyer expansion is used. Denoting the matching point by a subscript q , the following equation is obtained for this position:

$$\frac{p_\infty}{p_T} = \frac{p_q}{p_T} \left(1 - \frac{\gamma^2 M_q^2 \frac{p_q}{p_T}}{4(M_q^2 - 1) \left(1 - \frac{p_q}{p_T} \right)} \right) \quad (3.54)$$

This equation needs to be solved iteratively to find the point q . While solving it, it should be realized that there are two positions q for which the above relation holds. The one with the lower value of M_q (furthest forward along the nose) should be chosen, otherwise the Newtonian method is applied over the entire nose, which is exactly the case that was to be prevented.

Two additional popular local inclination methods are the tangent-cone and tangent-wedge. Using these methods, the pressure distribution is modelled as one on the ‘equivalent’ cone and wedge, respectively, for which the shock structure and pressure distribution can be calculated analytically (for a non-reacting inviscid ideal gas). The tangent-cone method is shown schematically in Fig. 3.4, indicating that geometry is locally approximated as an ‘equivalent cone’ with the same semicone angle as the local surface deflection angle.

For the tangent-wedge method, a similar approach is taken, but the equivalent shape is a wedge instead of a cone, which is more applicable for ‘flat’ geometries. The inviscid pressure distribution over a supersonic wedge with an attached shock follows simply from the shock relations in Eqs. (3.18)–(3.22), this directly yields the surface pressure at the cone’s surface. In fact, an analytical solution exists for this situation, which involves finding the roots of a cubic polynomial in $\sin \beta$. For the cone flow (tabulated) solutions to the Taylor-Maccoll equation, which gives a

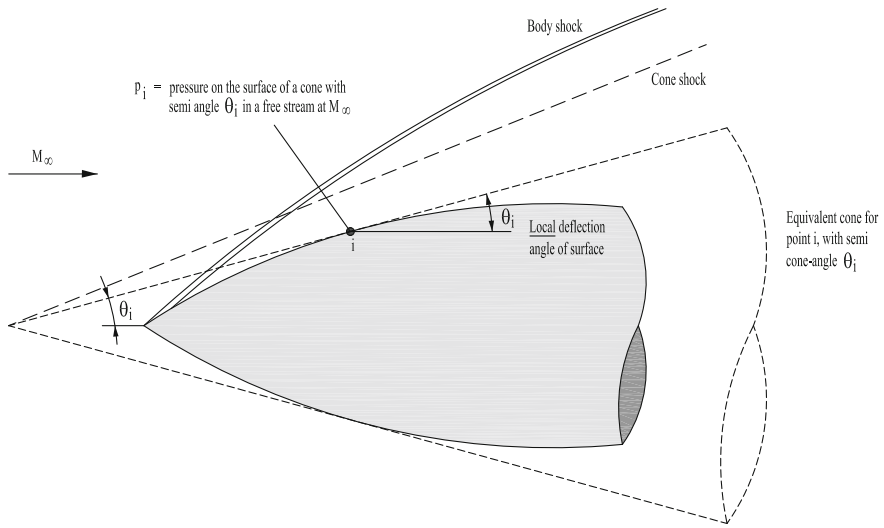


Fig. 3.4 Schematic representation of the tangent cone method

solution to inviscid flow around a cone at zero angle of attack (Anderson 2003), can be used. By applying such a method to axisymmetric shapes, or a two-dimensional tangent-wedge method to symmetrical two-dimensional profiles, inviscid results that coincide quite well with an exact solution of the Euler equations can be obtained. This method is, strictly speaking, only applicable over a configuration or component that has an attached (or in practice, very small stand-off distance) shock, seemingly making its applicability limited in practical re-entry configurations. However, it has been used for a variety of analyses, such as those by Cruz and Ware (1989) and Cruz and White (1989), with good results for a conceptual analysis.

To reduce computational complexity, approximate formulations (correlations) for the tangent-cone and wedge methods can be used. These correlations are based on perfect-gas flow and give good results for inclination angles below the critical value (above which no attached shock solution exists) and high Mach numbers.

To indicate the influence of the choice of local inclination method on the value of the local pressure coefficient C_p , we show the predictions for various methods and various Mach numbers over the full range of inclination angles in Figs. 3.5 and 3.6. We discuss the manner in which the analysis methods are selected in Sect. 3.3.2.

When using an impact method such as the Newtonian method, this method must only be used on those sections of the vehicle directly exposed to the external flow. For the determination of the pressure coefficient at the leeward side of the vehicle, a different method must be used. The Newtonian approximation is the following:

$$C_p = 0 \quad (3.55)$$

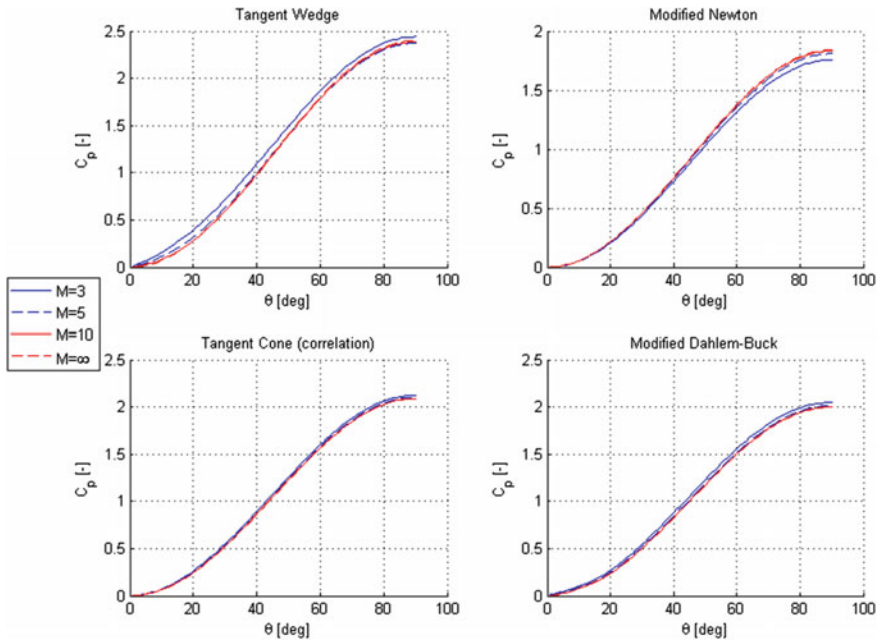


Fig. 3.5 Effect of Mach number on local inclination method pressure prediction

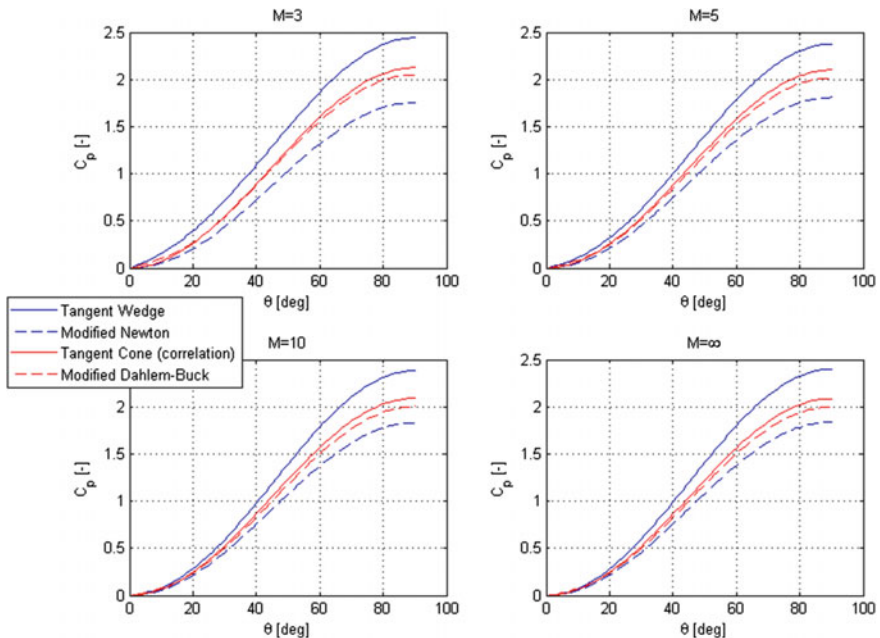


Fig. 3.6 Effect of local inclination method on pressure prediction

at the leeward side of the vehicle. From Eq. (3.41), this can be seen to arise as $p \rightarrow p_\infty$, an often used hypersonic approximation. An alternative expression may be obtained by only assuming that $p/p_\infty \ll 1$, so that the leeward pressure coefficient becomes:

$$C_p = -\frac{2}{\gamma M_\infty^2} \quad (3.56)$$

The physical situation that typically occurs on a hypersonic rearbody is influenced by viscous effects, resulting in flow circulation, which have a significant impact on the pressure characteristics there. A rough modification of the above relation can be used to account for such effects is:

$$C_p = -\frac{1}{M_\infty} \quad (3.57)$$

A further modification of this equation is the so-called ACM empirical method, from Krieger (1989). This method takes into account the fact that the flow expands along the low absolute inclination angle expansion region to a more or less constant low pressure coefficient for sufficiently low inclination angle. The pressure coefficient is determined as follows using this method:

$$C_p = \max \left(\frac{\theta}{16M_\infty^2}, \frac{-1}{M_\infty^2} \right) \quad (3.58)$$

with θ in degrees.

Aside from these purely local methods no knowledge of the flow aside from freestream conditions, are required. Prandtl–Meyer expansion can be used, as described by Eq. (3.26), from the point for which $\theta = 90^\circ$ onwards. It is based on the physical assumption of attached flow that undergoes isentropic expansion.

Clearly, for high hypersonic velocities the contribution from the leeward pressure distribution to the aerodynamic coefficients is quite small, as the pressure coefficient approaches zero for infinite Mach number. This is also the case for the Prandtl–Meyer expansion method, where the minimum pressure coefficient that can be attained is the vacuum pressure. For lower hypersonic/supersonic velocities, however, its influence becomes more noticeable.

A comparison of a number of local inclination methods is shown in Figs. 3.5 and 3.6. As can be seen, the influence of the Mach number on the pressure prediction is quite small, as was to be expected from the Mach number independence principle. Note that no influence of real gas effects is included. The effect of changing the local inclination method can be seen to be much stronger, with a difference of greater than 33 % being observed. For this reason, the selection of the local inclination method is of importance for the accuracy of the results that are generated. A discussion on the automatic selection of methods is given in Sect. 3.3.2.

To illustrate the methods described here, in Fig. 3.7 the pressure distribution on the Space Shuttle is shown for 4 angles of attack at Mach 20. These figures clearly

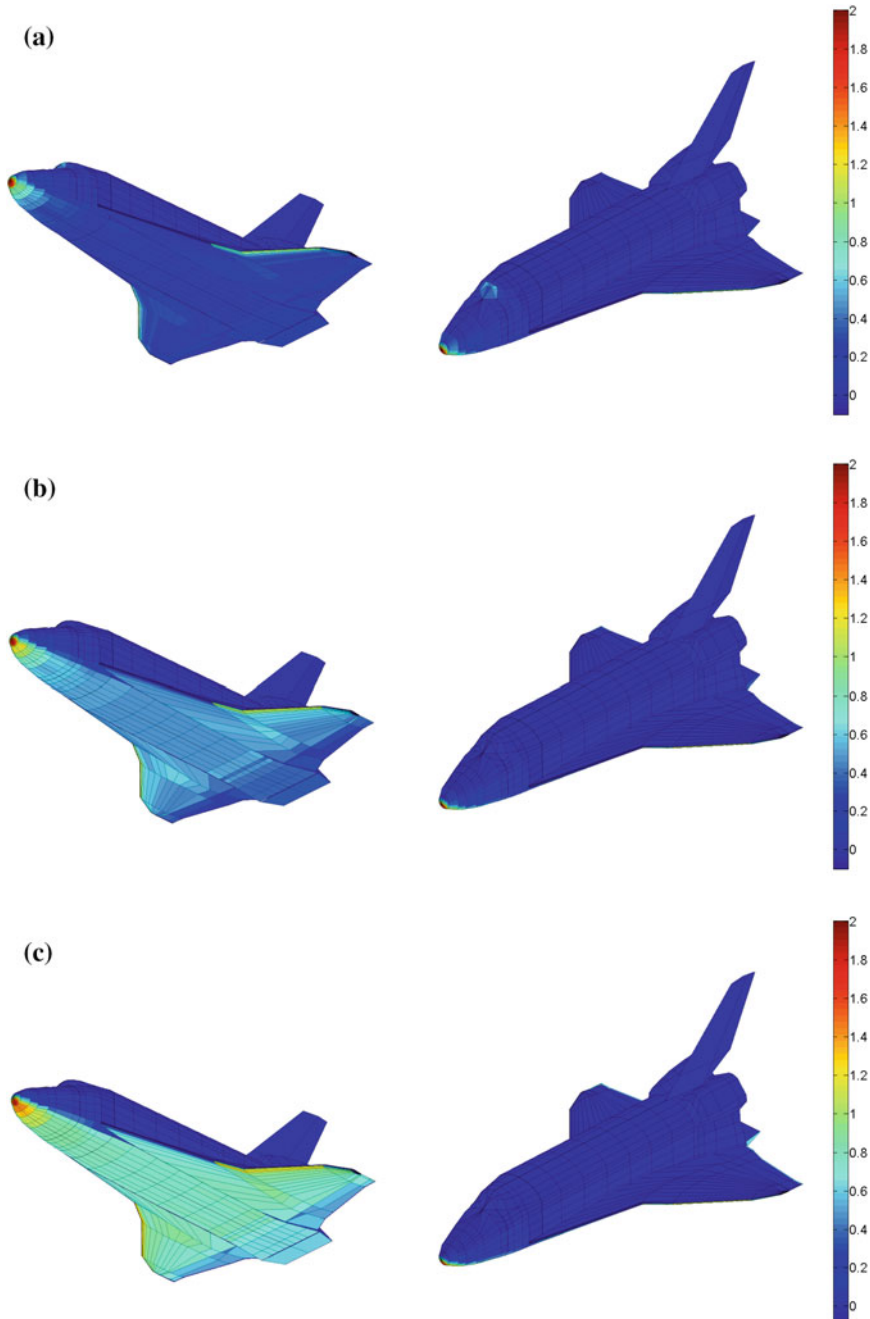


Fig. 3.7 Pressure distribution for $M = 20$ at **a** $\alpha = 20^\circ$, $\beta = 0^\circ$, **b** $\alpha = 30^\circ$, $\beta = 0^\circ$, **c** $\alpha = 40^\circ$, $\beta = 0^\circ$. Analysis method selection was done as described in Sect. 3.3.2

show that the expansion surfaces add little to the total aerodynamic coefficients, as the pressure coefficient becomes ≈ 0 .

The aerodynamic analysis methods described in this section are by design conceptual in nature. The large number of aerodynamic analyses that are required for our purposes preclude the use of an in-the-loop Navier–Stokes solver. Nevertheless, a variety of model extensions could be made to extend the validity of the analysis. These proposed modifications would only *locally* modify the methodology we propose, allowing an easy incorporation into the simulation and analysis chain. To extend the simulation validity to the full flight envelope, the aerodynamic analysis could be extended to other regimes in addition to the hypersonic one. Extensions of the methods presented here may include some form of sub- trans- and supersonic aerodynamic analysis, to be able to include the feasibility and optimality of the vehicles in these flight regimes. Due to the computational limitations of modern computers, such methods will most likely be relatively simple, similar in accuracy to the local inclination methods used in this study. One possible candidate for this is the PANAIR code (Derbyshire and Sidwell 1982; Saaris and Tinoco 1992), which is an inviscid panel code for subsonic and supersonic analysis. In addition, the inclusion of free molecular aerodynamic analysis, such as described by Fuller and Tolson (2009) and Doornbos (2011), coupled with a bridging between the hypersonic and rarefied regime (Regan and Anandakrishnan 1993), would give a more realistic approximation of high-altitude aerodynamics and would extend the methodology applied here to superorbital entry, aero-assist and aero-capture problems, where high-altitude aerodynamics is more influential. Here, however, we limit ourselves to the hypersonic regime, as it is typically the most demanding segment of the entry. In addition, a viscous analysis could be included (Sect. 3.1.3), which becomes especially important when considering the hypersonic heating, and the non-hypersonic force modelling. Again, we stress that due to the modular setup of our analysis methodology, such modifications would only impact the aerodynamic analysis code we use, not the overall code architecture.

3.3.2 Method Selection

The use of local inclination methods has been common in conceptual hypersonic aerodynamics. However, the quality of the results that are obtained depend substantially on the type of method that is used, as shown in the previous section (Figs. 3.5 and 3.6). Therefore, it is important to make a good determination of which method to use on which part of the entry vehicle. An automatic selection algorithm has been developed (Dirkx and Mooij 2011), which analyzes the vehicle shape and assigns regions where each of the various methods is to be applied. After the guidelines from Maughmer et al. (1993), Moore and Williams (1989) and Gomez (1990), as well as a number of tests performed for various vehicles, the methods were chosen as shown in Table 3.2.

Table 3.2 Selection of applicable methods per vehicle part type (Dirkx and Mooij 2011)

	Low hypersonic compression	High hypersonic compression
Blunt	Modified newtonian	Modified newtonian
Low inclination ‘round’	Tangent cone	Modified newtonian
Low inclination ‘flat’	Tangent wedge	Modified newtonian
	Low hypersonic expansion	High hypersonic expansion
Blunt	ACM empirical	High mach base pressure
Low inclination ‘round’	Prandtl–Meyer expansion	Prandtl–Meyer expansion
Low inclination ‘flat’	Prandtl–Meyer expansion	Prandtl–Meyer expansion

In the selection of the method, we distinguish two hypersonic regimes: low hypersonic and high hypersonic (as discussed in the Sect. 3.2). Additionally, we distinguish three types of vehicle shapes. First, we consider blunt segments such as noses and leading edges, separately from low inclination regions such as fuselage afterbodies and wing planforms. For the low inclination regions, we make a further distinction between round (fuselage) and flat (wing) shapes.

In our analysis, we use a structure grid, discussed in further detail in Sect. 5.3. As discussed there, each vehicle part consists of contours in lateral and longitudinal direction, with quadrilateral panels formed from the node points on these contours. In this section, contours in lateral direction are denoted with an index i , and those in longitudinal direction with index j . A panel i, j is defined by node points $(i+1, j+1)$, $(i+1, j)$, $(i, j+1)$, (i, j) . The x -direction is from the vehicle front to the back, the z -axis points upwards and the y -axis completes the right-handed system.

Our method selection is performed per vehicle part (see Sect. 5.3 for a definition) and for each part a single method is selected. If necessary, a part can be split into two, on each of which a separate method is then selected. This is critical for analyzing a fuselage nose separately from the afterbody, for instance. If the front of a part is not blunt, the entire part is treated as ‘low inclination’. If it is blunt, then each subsequent contour is analyzed to decide whether the vehicle part should be treated as not being blunt from some point onwards. Figure 3.8 shows an example for an STS shape, where the front of the fuselage, as well as the leading edges, are treated as blunt, while the rear body and the majority of the wings are not.

We start by describing our algorithm for determining whether the frontmost contour of a part (leading edge, nose, etc.) is ‘blunt’ or ‘low inclination’. As discussed in Sect. 5.3, we distinguish two different types of vehicle shapes: ‘fusiform’ and ‘flat’, for which the determination of the bluntness is done in a slightly different manner. For both types of shapes, however, only the front-most contour on the part is analyzed for the bluntness determination. For a fusiform shape, the bluntness determination must correctly identify whether the nose of the vehicle part is ‘sufficiently blunt’ to warrant the use of the appropriate method defined in Table 3.2. To this end, the average inclination $\bar{\theta}$ over the contour (with n panels) is used, weighted by the panel areas A_i :

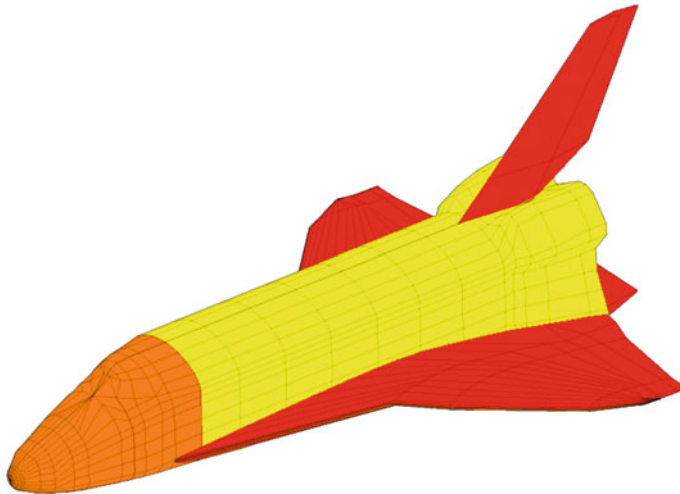


Fig. 3.8 Geometry type identification on Space Shuttle configuration. *Orange = blunt, yellow = low inclination curved, red = low inclination flat*

$$\bar{\theta} = \frac{\bar{A}}{n} \sum_{j=0}^n \left(\frac{\theta_j}{A_j} \right) = \frac{1}{n^2} \left(\sum_{i=0}^n A_j \right) \left(\sum_{j=0}^n \left(\frac{\theta_j}{A_j} \right) \right) \quad (3.59)$$

The most forward contour of a fusiform part (denoted by a 0 subscript) must satisfy the following criterion to be considered blunt:

$$\bar{\theta}_0 > k_1 \quad (3.60)$$

Values for k_1 , as well as the other parameters on which the algorithm is based, are given in Table 3.3.

For a planar part, the determination of the bluntness is done in a different manner, since (for instance) a wing leading edge should be analyzed as a blunt segment if a sufficient part of the leading edge has a sufficiently high inclination. For instance, if only a very small part of a (blunted) wing has a small sweep angle, using the aerodynamic method for a flat shape is likely warranted. For a flat part (such as a wing), the panels of the most forward contour are analyzed separately and a single panel is determined to be blunt if:

$$\theta_{i,j} > k_2 \quad (3.61)$$

The contribution of a single panel to the bluntness of the entire contour is determined by its lateral, and not its longitudinal, extent, as we want to determine which fraction of, for instance, the leading edge is blunt. The relevant (lateral) panel width $L_{p,ij}$ is:

Table 3.3 Choice of coefficients for method selection algorithm

Parameter	Value
k_1	45°
k_2	30
k_3	35°
k_4	30°
k_5	1.2
k_6	0.4

$$L_{p,ij} = \sqrt{\left(\frac{y_{i+1,j+1} + y_{i+1,j}}{2} - \frac{y_{i,j+1} + y_{i,j}}{2}\right)^2 + \left(\frac{z_{i+1,j+1} + z_{i+1,j}}{2} - \frac{z_{i,j+1} + z_{i,j}}{2}\right)^2} \quad (3.62)$$

Using Eq. (3.61), the following is then used to determine the fraction of the leading edge that can be considered ‘blunt’:

$$n_{blunt} = \frac{\sum_{j:\theta_{ij}>k_2} L_{p,ij}}{\sum_{j=0}^n L_{p,ij}} \quad (3.63)$$

The part is now considered blunt from the current contour onwards if:

$$n_{blunt} > k_3 \quad (3.64)$$

For our algorithm, we now have one aspect remaining: determining whether a part for which the frontmost contour is blunt should be treated as being blunt in its entirety, or if it should be treated as ‘low inclination’ from some point onwards (as is the case for the Space Shuttle example shown in Fig. 3.8). A part that is blunt at the front is split if the downstream segment of the part has a sufficiently low inclination for a sufficiently large fraction to warrant the use of a non-blunt method.

For fusiform parts, the criterion for splitting a part is quantified by finding the front-most lateral contour on which the following is satisfied:

$$i_{low} = \min_i (\bar{\theta}_i < k_4) \quad (3.65)$$

That is, the first contour (when moving in rearwards direction) on which the average inclination goes below a certain value. For a planar part, a similar criterion is used. However, only panels on those longitudinal contours that were determined to have a blunt panel on lateral contour 0, i.e. for which Eq. (3.61) holds, are considered. In addition, for planar parts the average is computed weighted by $L_{p,ij}$, not A_{ij} (as discussed above).

If Eq. (3.65) is met, the part is not split immediately. Instead, it is checked whether the part of the vehicle to the rear of the split point is sufficiently large to warrant the split. This aids the fidelity of the results, as non-blunt parts are analyzed by methods for which it is implicitly assumed that the shock wave is attached at the nose. As discussed in the previous section, being ‘sufficiently far’ downstream of a detached shock makes this approximation reasonable. For these reasons, the average x -value of the contour where the part is to be split is determined as:

$$\bar{x}_{\text{split}} = \bar{x}_{\text{low}} + k_5 (\bar{x}_{\text{low}} - \bar{x}_0) \quad (3.66)$$

All of the above assumes a convex vehicle part, i.e., $\bar{\theta}_i$ is continuously decreasing with i . For a Space Shuttle geometry, for instance, this assumption is invalidated by the presence of the front windows and engine nacelles. For this reason, a convexity check is included for the split point determination. If a convexity is found at a contour for which:

$$\bar{x} < k_6 L \quad (3.67)$$

where L denotes the part length, a relevant convexity is identified. If this condition is met, the split is delayed until after this convexity. This criterion delays the part splitting until after the front windows, but ignores the nacelles (in the case of the Shuttle).

A final aspect, which we do not consider explicitly here, concerns the analysis of whether a low-inclination part is flat (wing) or round (fuselage). For the shape parameterization defined in Chap. 5, this determination is made *a priori*, and is not determined by an algorithm. For geometries where this distinction cannot be made manually in a robust manner, the algorithm described by Dirkx and Mooij (2011) can be used.

It must be noted that the algorithm defined here has six free parameters. Table 3.3 gives a list of parameters that have been shown to perform well for a variety of geometries that we have analyzed. An example of selected methods is shown in Fig. 3.8.

3.4 Heat Transfer

The aerodynamic heating of entry vehicles poses a serious design challenge due to the high heat fluxes that are reached during re-entry. For a detailed analysis of hypersonic heating over a full configuration, CFD and/or experimental data are required, which is not feasible for the methodology described here. Luckily, a range of conceptual design tools is available that can be used to estimate the heat transfer to key areas of the vehicle. We discuss such models for convective heat transfer in Sect. 3.4.1, followed by several specific considerations for the heating of capsules in Sect. 3.4.2. We omit the influence of radiative heating, as such effects are typically negligible for the LEO entries that we consider.

3.4.1 Convective Heat Transfer

In viscous continuum flow, two conditions that must hold at the vehicle body surface (wall) are the velocity and temperature no-slip conditions, which are expressed as follows:

$$\mathbf{V}_{\perp,w} = 0 \quad (3.68)$$

$$T_w = T|_{y=0} \quad (3.69)$$

where the y -coordinate is perpendicular to the wall and the former of these indicates that the flow velocity tangent to the wall equals zero and the second one indicates that the flow temperature at the wall must equal the temperature of the wall. The basic equation for convective heat rate, assuming a non-reacting flow, follows from this viscous transfer of energy and is expressed as:

$$q_w = \left(k \frac{\partial T}{\partial y} \right)_w \quad (3.70)$$

with k the conductivity. Due to the formation of a thermal boundary layer, the temperature profile will vary over this layer, with its gradient at the wall determining the heat transfer. The similarity parameter that is typically used for the analysis of heat transfer is the Stanton number St :

$$St = \frac{q_w}{\rho_e V_e (h_{aw} - h_w)} \sim \frac{\text{Heat transferred to body}}{\text{Heat contained in gas}} \quad (3.71)$$

It is a measure how much of the energy content in the flow is convected into the body. The Stanton number based on freestream density and velocity, denoted here by St_∞ , is also used for certain applications. In this equation, the adiabatic wall enthalpy is the enthalpy at the wall at which $\frac{\partial T}{\partial y} = 0$ and the heat transfer rate equals zero. It can be determined as follows:

$$h_{aw} = h_e + r \frac{u_e^2}{2} \quad (3.72)$$

where the e subscript denotes the conditions at the edge of the boundary layer, and u denotes the relevant velocity component. It can be seen that this expression bears a close resemblance to the definition of total enthalpy in Eq. (3.14), the recovery factor r being the only difference. This factor is a measure for how much of the total enthalpy that is present in the flow can be ‘recovered’ at the wall. The following is often used as an approximation:

$$r = \begin{cases} Pr^{1/2} & \text{Laminar flow} \\ Pr^{1/3} & \text{Turbulent flow} \end{cases} \quad (3.73)$$

in which Pr is the Prandtl number, defined as follows:

$$Pr = \frac{\mu c_p}{k} \sim \frac{\text{Viscous dissipated energy}}{\text{Conducted energy}} \quad (3.74)$$

For standard air $Pr \approx 0.71$, so the recovery enthalpy is slightly lower than the total enthalpy from Eq. (3.14), somewhat lessening the thermal load on the vehicle. The Prandtl number in equilibrium air will always be ≤ 1 , so that using the total enthalpy as recovery enthalpy may be used as a ‘limiting value’ in a certain sense. Additionally, setting $Pr = 1$ significantly simplifies the analysis of heat transfer and is often used in first approximations of the heat transfer.

A relation for the heat transfer to the stagnation point of a cylinder or hemisphere is given by van Driest (1958):

$$St_\infty = K \left(\frac{\left(\frac{du_e}{dx} \right)_e R}{V_\infty} \right)^{0.5} \left(\frac{\rho_\infty V_\infty R}{\mu_\infty} \right)^{-0.5} Pr^{-0.6} \left(\frac{\rho_e \mu_e}{\rho_\infty \mu_\infty} \right)^{0.5} \quad (3.75)$$

where the ∞ subscript on the Stanton number denotes that the freestream conditions (pre-shock wave) have been used for non-dimensionalizing the heat transfer. As can be seen, the velocity gradient at the wall is required for this relation. The assumption of Newtonian flow can be used to obtain this velocity gradient. The result is, for the stagnation velocity gradient:

$$\left(\frac{du_e}{dx} \right)_e = \frac{1}{R} \sqrt{\frac{2(p_e - p_\infty)}{\rho_e}} \approx \frac{V_\infty}{R} \sqrt{\frac{2\rho_\infty}{\rho_e}} \quad (3.76)$$

In addition to stagnation-point heat transfer relations involving the Stanton number, a semi-empirical relation that directly yields the stagnation-point heat transfer can be used (Chapman 1958):

$$q_{c,x} = k \rho^{N_1} V^{N_2} \quad (3.77)$$

where the values of k , N_1 and N_2 that are used in literature vary somewhat. The values used here, assuming laminar flow conditions, are $N_1 = 0.5$ and $N_2 = 3$ (Tauber et al. 1987). For k the following relation is used (Anderson 2006):

$$k = \frac{1.83 \cdot 10^{-4}}{\sqrt{R_n}} \left(1 - \frac{T_w}{T_{aw}} \right) \quad (3.78)$$

where R_n is the nose radius, T_w the wall temperature and T_{aw} the adiabatic wall temperature. As a first approximation, the cold wall approximation can be used, so that $T_w/T_{aw} \approx 0$ is assumed. Since Eq. (3.77) is much simpler to implement, as no calculations of conditions at the edge of the boundary layer are required, it is preferable to use this relation over (3.75). However, Eq. (3.77) is as a conservative estimate of the heat rate, since flow dissociation will decrease the heat transfer, as

discussed in detail by (Anderson 2006), when neglecting wall catalicity (see Smith 1997).

For the winged vehicle, a relation for the convective heat transfer to the leading edge of a wing with sweep angle Λ is used here, after Tauber et al. (1987):

$$q_{c,LE} = \left(\frac{1}{2} q_{c,s} \cos^2(\Lambda) + q_{c,FP} \sin^2 \Lambda \right) \quad (3.79)$$

where LE stands for leading edge and FP for flat plate. This can be seen as a kind of average from a stagnation point and a flat plate. Here, approximations for the flat-plate heating are given as follows. The relations are of the form of Eq. (3.77), but with values as in Table 3.4. In this table, x is the running variable along the flat plate and x_t is the running variable, starting at the virtual origin of the turbulent boundary layer.

The methods we describe are well suited for conceptual design, as they consider the key issues in a typical vehicle design, while omitting the many complicated mathematical-physical modelling issues. However, for increased fidelity at a later design stage (or design validation during conceptual design), various extensions to the heating models would be needed. For instance, by performing a viscous analysis of the full vehicle, the heat rate and load over the entire vehicle's surface could be determined, as opposed to the simple approach taken in this work. By doing so, the total effect of thermal loads on, for instance, the required TPS mass and vehicle feasibility could be determined. In addition, matters such as viscous interaction, which were neglected in this book, could be included. Also, the control surface deflection limits could be selected in a vehicle specific manner by investigating the influence of strong shock interactions for high flow deflections angles. The streamline pattern over the vehicle could be determined using the pressure distribution and the method described by Kenwright et al. (1999). This method is also used by Kinney (2004). A heating analysis used in the entry vehicle shape optimization of Theisinger et al. (2010), described by Brykina and Scott (1998) could also be used in a follow-up of this study. However, such extensions are not cost-effective for our approach, where the strength lies in the rapid analysis of many different vehicle shapes.

Table 3.4 Parameters in Eq. (3.77) for flat-plate heating (Tauber et al. 1987)

	k [W ^{1-N₁} .m ^{5N₁-N₂-2} .s ^{-3N₁+N₂}]	N_2 [-]	N_1 [-]
Laminar flow	$2.53 \cdot 10^{-5} \cos^{1/2} \theta \sin \theta x^{-1/2} \left(1 - \frac{T_w}{T_{aw}} \right)$	3.2	0.5
Turbulent $V \leq 2962$ m/s	$3.35 \cdot 10^{-4} \cos^{1.78} \theta \sin^{1.6} \theta x_T^{-1/5} \left(\frac{T_w}{556} \right)^{-1/4} \left(1 - 1.11 \frac{T_w}{T_{aw}} \right)$	3.37	0.8
Turbulent $V > 2962$ m/s	$2.20 \cdot 10^{-5} \cos^{2.08} \theta \sin^{1.6} \theta x_T^{-1/5} \left(1 - 1.11 \frac{T_w}{T_{aw}} \right)$	3.7	0.8

3.4.2 Capsule Considerations

For capsule-shaped vehicles, the fact that the stagnation region is typically spherical for only a small angular range will influence the stagnation region flow field, due to the different shock shape, curvature and downstream flow characteristics compared to the stagnation region. Zoby and Sullivan (1965) provide a semi-empirical relation for an effective nose radius R_{eff} as a function of the capsule parameters R_N , R_m and R_s (see Sect. 5.1). The relation is based on measurements of the heat rate on a number of capsule shaped vehicles with hemispheres under the same conditions. A plot is shown in Fig. 3.9. As can be seen, the difference between the capsule and hemisphere become more pronounced as the ratio R_m/R_N becomes smaller. This can be explained by the fact that the shock shape will be more strongly influenced in these cases. The effect of the value of R_s can be seen to be almost negligible for values of R_m/R_N above 0.6.

The effective nose radius is, for instance, used in a study by Robinson and Wurster (2009), where the superorbital entry from both Mars and the Moon is analyzed. This paper, as well as the study reported by Crowder and Moote (1969), points to an additional heat-transfer consideration that must be taken into account for capsule-shaped vehicles. Specifically, the location of the maximum heat-rate will not be

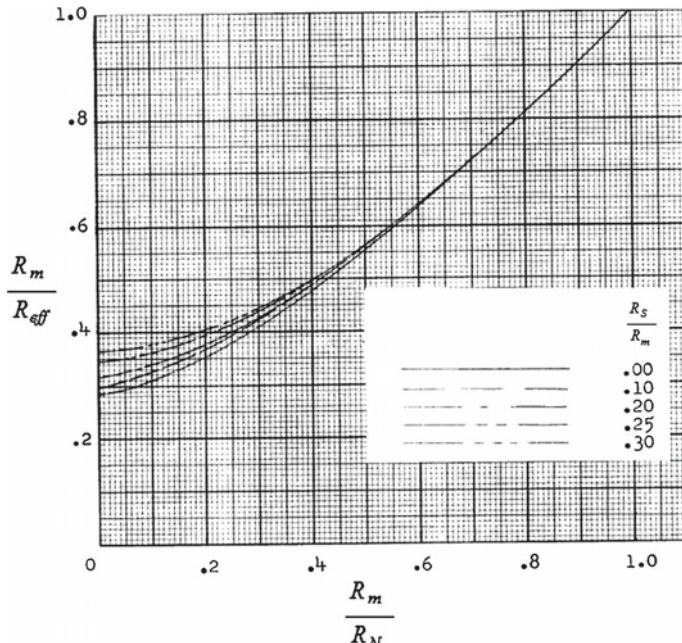


Fig. 3.9 Relation for effective nose radius of a capsule shaped vehicle, from Zoby and Sullivan (1965)

located at the stagnation point. This is due to the fact that the radius of curvature at the vehicle shoulder may be much smaller than that of the heat shield. Such a small radius of curvature would cause a large velocity gradient and, consequently, significantly increase the heat transfer in this region. In addition, capsule-shaped vehicles typically enter at an angle of attack, so that the flow field on the vehicle is no longer axisymmetric and the stagnation point will lie closer to the vehicle shoulder. A comparison between the windward centerline pressure distribution of the wind tunnel and flight results is given by Lee and Goodrich (1972), who show that the stagnation point lies very near to the vehicle shoulder ($s/R = 0.732$). As noted by Robinson and Wurster (2009), this causes two issues for the heat-rate predictions discussed here:

- The flow field and shock shape are different for the non-axisymmetric case, so that the effective-nose-radius correction is insufficient and still yields an underprediction of about 15 % for an angle of attack of 20°.
- The point of maximum heat transfer lies on the shoulder instead of the nose region. The cold-wall heat transfer is about 60 % greater here than at the stagnation point. However, due to transient effects and the higher temperature that will occur at the shoulder, the difference is only about 20 % for the point of maximum heat rate during a super-orbital entry.

Partly mitigating the effect of both of these discrepancies, the maximum angle of attack will be constrained, as discussed in Sect. 6.3.2.

The problem of the heat-rate difference at the shoulder, though, is mitigated by the fact that the influence it has on the total heat load is limited, since the surface area of the shoulder region is typically significantly smaller than that of the nose region. For cases where this area is similar to that of the nose region, the value of R_S will be much higher than on Apollo, so that the hot-corner effect will be mitigated by a certain degree.

In this work, the problem of the shoulder heating will be dealt with by using wind tunnel results from Marvin and Sinclair (1967), Wadhams et al. (2009) and Jones (1963), as well as flight data from Lee and Goodrich (1972). Although these data are not fully adequate to make a proper estimate of the influence of all independent variables (M, α, R_S, R_N, R_m), general trends can be identified and an estimate of the shoulder heating can be made. The influence of the corner radius itself is derived from data presented in Marvin and Sinclair (1967). There, a rounded flat-faced cylinder with a number of values for R_S/R_m is analyzed at zero angle of attack and a Mach number of 10.5, with values given in Table 3.5. We note that more elaborate approaches, for instance based on the work of Marvin and Sinclair (1967) or Brykina and Scott (1998) could be used for a more detailed study. However, this would be at the expense of a significantly increased computational complexity.

Additional data are taken from Jones (1963), where a sharp-cornered ($R_S \rightarrow 0$) capsule is analyzed at Mach 8. In that study, two different values of the rear cone half-angle θ_c are used: 11.5° and 23°. A consistent difference is observed between the two, where the second cone angle produces higher corner heating in each case. This is possibly caused by the difference in attached/separated flow, or a difference

Table 3.5 Influence of corner radius on maximum corner heating (Marvin and Sinclair 1967), $M = 10.5$, $\alpha = 0^\circ$

$\frac{R_S}{R_m}$ [-]	0.05	0.15	0.25	0.5
$q_{c,max}/q_{c,s}$ [-]	1.35	1.28	1.2	1.1

Table 3.6 Influence of angle of attack on maximum corner heating (Jones 1963), $M = 8$, $R_S \approx 0$

α [deg]	0	15	30
$q_{c,max}/q_{c,s}$ [-]	1.35	1.55	2.0

Table 3.7 Influence of angle of attack on maximum corner heating of Orion CEV (Wadhams et al. 2009), $M = 10$, $\frac{R_S}{R_m} \approx 0.05$

α [deg]	0	20	28
$q_{c,max}/q_{c,s}$ [-]	1.25	1.5	1.7

in velocity gradient at the point of maximum heat flux at the corner. However, the conservative values, measured at 23° will be used for the estimate here. The data are shown in Table 3.6.

Although the conditions of the measurements presented in Tables 3.5 and 3.6 are similar, it would appear from these measurements that there is no increase in corner heating between $R_S/R_m = 0.05$ and $R_S/R_m = 0$.

The influence of varying angle-of-attack is further evaluated by using the wind tunnel results of the Orion Crew Exploration Vehicle (CEV) by Wadhams et al. (2009). Here the CEV, with $R_S/R_m \approx 0.05$ is analyzed for various angles of attack. Although the position of the stagnation point is not stated explicitly for each case, an analysis of the similarly shaped Apollo capsule by Lee and Goodrich (1972) and Robinson and Wurster (2009) allows for a reasonable estimate of its position. The relevant data that are obtained are given in Table 3.7.

The combination of the literature data shown here has been used to generate an approximate function for the value of $q_{c,max}/q_{c,s}$. The following functional dependency is postulated for $q_{c,max}/q_{c,s}$:

$$\frac{q_{c,max}}{q_{c,s}} = f(M_\infty, \alpha, R_S/R_m, \theta_{sph1}) \quad (3.80)$$

Due to the limited number of data points, the precise functional form is kept simple. Since the results seem to be only weakly dependent on M and approximately linear in α and R_S/R_m , the following form is used:

$$\frac{q_{c,max}}{q_{c,s}} = c_1 M_\infty + c_2 \alpha + c_3 R_S/R_m + c_4 \theta_{sph1} + c_5 \quad (3.81)$$

The assumption of dependency on R_N/R_m is difficult to determine, due to the limited number of data points that are available. For this reason, this dependency is omitted.

The coefficients $c_1 \dots c_5$ are determined using a least squares curve fit, yielding the following results, with α in degrees in the above correlation:

$$c_1 = -0.0006, c_2 = 0.0185, c_3 = -0.5321, c_4 = -0.2939, c_5 = 1.3630$$

The coefficient of determination R^2 of the fit is 0.9532. The coefficient of determination is the fraction of the variation in the data which can be accounted for by the fit that is made. A value of exactly 1 indicates that the fit passes through all the data points. The value obtained here indicates that the fit is capable of reproducing the original values of $q_{c,max}/q_{c,s}$ relatively well. The deviations between the results from the curve fit and the data that were used to generate it are <5 % in most cases. The largest discrepancies were observed in the data points in Table 3.7, as well as the high- α data point from Table 3.6. Due to the limited number of data points used, the accuracy of the relation for general cases is difficult to ascertain. Especially for data points that need to be extrapolated from the input data, most notably large values of θ_{sph1} (see Sect. 5.1), larger errors may occur. However, in view of the available computational tools for the problem and the lack of a sufficiently computationally efficient estimation tool, the relation will be used in the optimization to calculate a constraint function, see Sect. 6.3.2.

Chapter 4

Numerical Interpolation

Numerical interpolation is a mathematical tool that is used to extend a discrete data set to a continuous domain. Typical applications of this tool in re-entry vehicle dynamical simulations include the retrieval of atmospheric properties and aerodynamic coefficients, both of which are often given in tabulated form. During trajectory propagation, however, these values need to be used at any of a continuous set of values (see Chap. 2). In addition to these typical applications of numerical interpolation, it takes a central role here for the definition of a generic winged vehicle shape. For the winged-vehicle parametrization (see Sect. 5.2.1), the vehicle surface is to be defined from a limited number of points on the vehicle surface, the positions of which are to be optimized. To achieve this, the complete vehicle shape is interpolated from these points by using splines and spline surfaces.

To start with, this chapter will give some of the basic mathematical concepts of interpolation in Sect. 4.1. Subsequently, splines of a single independent variable will be discussed in Sect. 4.2. Finally, spline surfaces, which will be used for the vehicle parametrization, will be discussed in Sect. 4.3.

4.1 Basic Concepts

Before discussing the basics of interpolation, a number of basic mathematical properties of curves and simple interpolation examples will be reviewed. We start by reviewing the concepts of continuity and convexity, which will play a central role in the definition of the vehicle shapes, in Sect. 4.1.1. Subsequently, linear interpolation in one and two dimensions is reviewed in Sects. 4.1.2 and 4.1.3, respectively, as a precursor to the spline interpolation discussion in the subsequent sections.

4.1.1 Continuity and Convexity

The ‘degree of smoothness’ of the mathematical description of a curve is an important property in defining a shape. This property can be quantified by so-called C^n continuity. Informally, a curve is C^n continuous, if its n^{th} derivative is continuous (but not necessarily smooth) over its entire domain. Three types of continuity will be considered here:

1. C^0 continuity: Implies that the curve is continuous and no ‘jumps’ in its value are present.
2. C^1 continuity: Implies that the curve has no ‘kinks’ in it, since the 1^{st} derivative is continuous.
3. C^2 continuity: Implies that there are no jumps in the curvature κ of the curve. The curvature of a function y of a single variable x is defined as:

$$\kappa = \frac{\left| \frac{d^2y}{dx^2} \right|}{\left(1 + \left(\frac{dy}{dx} \right)^2 \right)^{3/2}} \quad (4.1)$$

Figure 4.1 shows the function $f(x) = x^2|x|$ and its first three derivatives to illustrate the above. The function itself is C^2 , the first derivative is C^1 , the second derivative is C^0 and the third derivative is not C^0 , since it is not continuous (at $x = 0$). For a function of multiple independent variables, multiple curvatures in independent directions can be defined. For instance, for a function of two independent variables, a direction of minimum and a direction of maximum curvature can be defined.

For a function of multiple independent variables, multiple curvatures in independent directions can be defined. For instance, for a function of two independent variables, a direction of minimum and a direction of maximum curvature can be defined. A quantity related to the curvature, the radius of curvature R , is especially important for aerothermodynamic analysis (Sect. 3.4). It is related to κ by the following simple relation:

$$R = \frac{1}{\kappa} \quad (4.2)$$

An additional geometrical concept that will be used in this section, as well as in Sect. 5.2, is convexity. For a closed curve in two dimensions, the following is a necessary and sufficient condition for convexity:

Definition 4.1 The continuous function $f(t) : \mathbb{R} \rightarrow \mathbb{R}^2$ defining a closed curve, with $t \in D \subset \mathbb{R}$, is convex if and only if for any $t_1, t_2 \in D$, the connecting line between the points $f(t_1)$ and $f(t_2)$ is wholly contained inside the region bounded by f .

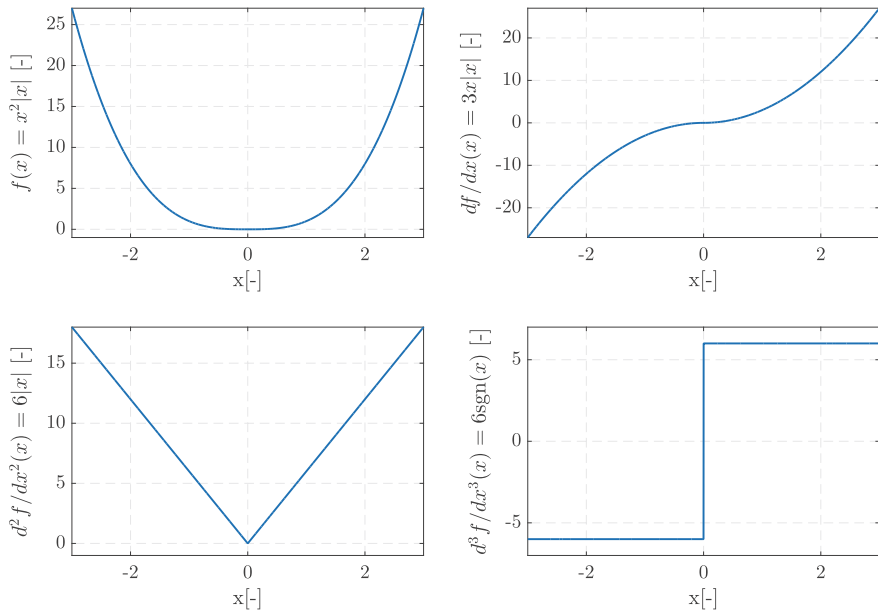


Fig. 4.1 Illustration of degrees of continuity. The function $f(x)$ is C^2 continuous, while each consecutive derivative is one order of continuity lower

4.1.2 Linear Interpolation

The most basic C^0 interpolation method is linear interpolation. Given two points, this method assumes a linear variation of the curve between these two points. This results in the following interpolation in two dimensions between point (x_0, y_0) and point (x_1, y_1) :

$$y = y_0 + \frac{y_1 - y_0}{x_1 - x_0}(x - x_0) \quad (4.3)$$

Although this method is both conceptually simple and computationally fast, it has a number of important limitations. If it is used to approximate a curve, the truncation error that is made decreases only linearly with the step size, meaning that a large number of data points is required for attaining a certain level of error. Additionally, when more than two points are used, this method will, in general (except if the points are collinear) not yield an interpolated curve that is C^1 continuous. This may lead to numerical difficulties when using the interpolation. However, it is a computationally cheap manner in which to perform interpolation. Therefore, when selecting an interpolation method, linear interpolation should not be discarded *a priori* for its possible lack of precision and continuity.

4.1.3 Bilinear Interpolation

Linear interpolation can be extended to interpolation in multiple dimensions. Such a type of interpolation is of interest here, since the shapes that are to be defined for the optimization of entry vehicles are mappings f from two independent variables to three Cartesian coordinates, i.e., $f : \mathbb{R}^2 \rightarrow \mathbb{R}^3$. Although multi-dimensional linear interpolation will not be used explicitly in the simulations described in this text, it is presented here to give a simple example of interpolation of a function of multiple independent variables.

Given four points in three-dimensional space, the two-dimensional generalization of linear interpolation, termed bilinear interpolation, can be used to generate an interpolated surface. Since it has two independent variables, it can be constructed from a two-dimensional rectangle in \mathbb{R}^3 . We parametrize this rectangle with two parameters u and v , here both running from 0 to 1. The surface ‘patch’ $\mathbf{x}(u, v)$, spanned by four points $\mathbf{p}_{i,j}$, with $i = 0, 1$ and $j = 0, 1$ gives the following:

$$\mathbf{x}(u, v) = \sum_{i=0}^1 \sum_{j=0}^1 \mathbf{p}_{i,j} B_i^1(u) B_j^1(v) \quad (4.4)$$

$$B_0^1(u) = (1 - u) \quad (4.5)$$

$$B_1^1(u) = u \quad (4.6)$$

The surface this yields is shown in Fig. 4.2. As can be seen, the lines over this surface in u or v direction are straight line segments, showing that it is a two-dimensional generalization of linear interpolation.

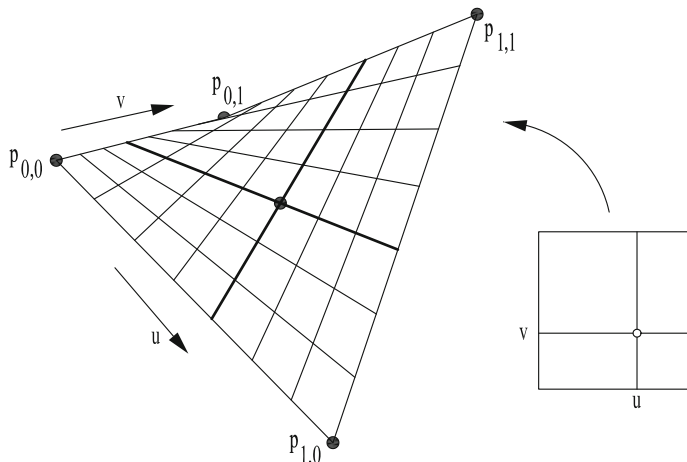


Fig. 4.2 Creation of a bilinear interpolation patch in \mathbb{R}^3 from four corner points and a parametrization u, v in \mathbb{R}^2

4.2 Cubic Spline Curves

A flexible and widely applicable method of interpolation is spline interpolation, a method that is often used in computer modeling and visualization of curves and surfaces. A good introduction into the theory of splines is given by Shirley et al. (2005), with a more extensive discussion found in Farin (2003). Splines are curves that are fitted between each two subsequent data points, typically using some additional criteria or data for smoothing the curve to obtain a higher-order interpolation. Certain constraints can be imposed at the interfaces between the different spline segments, such as C^1 or C^2 continuity. The combination of all spline segments is termed the spline.

The use of splines and spline surfaces for the definition of aerospace vehicle shapes can be found in various literature sources. The versatility of using splines has clear advantages in an optimization process, as it allows more freedom in the range of possible shapes than more classical methods Thomas et al. (2004). The use of splines to generate the surface of a body of revolution is described by Grant and Braun (2010). By using such a method, the vehicle shape is defined by only a single curve, which has clear computational advantages. The downside is, of course, that this method is limited to axisymmetric configurations. Theisinger and Braun (2009) use rational B-splines to define a very generic vehicle shape, explicitly use the convex hull and variation-diminishing properties (which we discuss in the next section) to control whether a section of the vehicle is convex or concave. These are just two examples, indicating that spline surfaces can be used to generate vehicle shapes with broad range of freedom.

The material presented in this section will be used primarily as a precursor to the definition of spline surfaces, which are discussed in Sect. 4.3. These will in turn be used for the generation of the winged vehicle shapes, described in Sect. 5.2. The material discussed here is limited to that which is relevant for the discussion of the vehicle shape generation and should by no means be considered as an exhaustive presentation on splines. Some fundamental concepts of splines are discussed in Sect. 4.2.1, with the formulation of the specific cubic Bézier and Hermite splines presented in Sect. 4.2.2. Finally, we present a method for eliminating self-intersection and concavity of such curves in Sect. 4.2.3.

4.2.1 Fundamental Concepts

A spline can be defined from a set of m -dimensional data points, so that it becomes a mapping of $\mathbb{R} \rightarrow \mathbb{R}^m$, but here only applications with 2 or 3 dimensions will be considered. From these data points, a curve as a function of an independent variable u

is generated when making the spline. As a result, the spline will produce the following sort of result in three dimensions:

$$\begin{aligned} x &= f(u) \\ y &= g(u) \\ z &= h(u) \end{aligned} \tag{4.7}$$

with f , g and h functions being of u . The value of u is continuously increasing over the spline. For our discussion and application, we define the subsequent interpolating points (i.e., where the discrete data is available) at $u = 0, 1, 2, 3, \dots$. Note that splines for which the interpolating points are not equally spaced, termed a non-uniform spline can provide additional freedom in curve shape, but we do not require such a generalization for our purposes.

In this context, a derivative of the spline here is the derivative with respect to the parameterizing variable u , so that:

$$\begin{aligned} x' &= \frac{df(u)}{du} \\ y' &= \frac{dg(u)}{du} \\ z' &= \frac{dh(u)}{du} \end{aligned} \tag{4.8}$$

For spline interpolation from n data points, the task is to find $n - 1$ curves that interpolate between the data points. In some cases, however, additional points besides the points to be interpolated, called intermediate points, will be used for the formation of the spline. In this situation, the spline does not (necessarily) pass through these intermediate points. Here, the original data points (through which the spline passes) are termed control points.

A variety of types and order of splines exists, and we will restrict ourselves to a specific case of B-splines, namely Bézier curves of third order. A third-order spline is chosen for the following reasons, e.g., Shirley et al. (2005):

- It is the lowest-order polynomial that can have an inflection point.
- The curve is typically quite smooth, thereby avoiding Runge's phenomenon. Runge's phenomenon can occur when using high order polynomial interpolation, where the control points themselves are properly interpolated, but the regions between the control points show strong, undesirable, variations in the function value.
- A cubic is fully defined by defining the value and slope at the end points.

The cubic spline definitions that will be discussed here are the Bézier spline and Hermite spline. These two types of splines have a one-to-one relationship, in that for each Bézier spline, a single Hermite spline exists that yields the exact same curve, and *vice versa*. The difference arises only in the construction of the curve. For the

Bézier curve of n^{th} order, two interpolating points and $n - 1$ intermediate points need to be defined. For a Hermite spline, with n an odd number, two interpolating points and the 1st derivative w.r.t. u up until the $((n - 1)/2)^{th}$ derivative w.r.t. u are required at both control points. We discuss both types of curves here, since the construction of Hermite splines can be more readily related to spline shape, but use the Bézier spline formulation in Sect. 4.2.3 to impose certain constraints on the curve shape.

The basis for creating either of these splines is a set of n control points:

$$\mathbf{p}_1, \mathbf{p}_2, \dots, \mathbf{p}_n \quad (4.9)$$

and the values of the independent variable u at which these points lie:

$$u_1, u_2, \dots, u_n = 0, 1, \dots, n - 1 \quad (4.10)$$

Although the spacing of the points in the independent variable u does not need to be uniform (nor unity), it will be assumed for the work here that this is the case.

4.2.2 Bézier and Hermite Splines

For generating the j^{th} segment of a cubic Bézier spline from data points in Eq. (4.9), the four points, $\mathbf{b}_{3j} = \mathbf{p}_j$, \mathbf{b}_{3j+1} , \mathbf{b}_{3j+2} and $\mathbf{b}_{4j} = \mathbf{p}_{j+1}$ are needed. From these points, the interpolating spline between control points \mathbf{p}_j and \mathbf{p}_{j+1} , using the additional points \mathbf{b}_{3j+1} and \mathbf{b}_{3j+2} as intermediate points (the construction of which is discussed later on in this section), is created algebraically as follows:

$$\mathbf{b}^{n,j}(u) = \sum_{i=0}^n \mathbf{b}_{3j+i} B_i^n(u) \quad (4.11)$$

$$B_i^m(t) = \binom{m}{i} t^i (1-t)^{m-i} \quad (4.12)$$

where m represents the order of the curve, 3 for our cubic spline, and $B_i^m(t)$ is a Bernstein polynomial. A number of practical properties of Bézier curves that can be exploited are the following (see, e.g., Shirley et al. (2005) for proofs):

- The convex hull property (illustrated in Fig. 4.4):

Definition 4.2 The convex hull of a spline is the polygon defined from the area enclosed by the set of all connecting lines between all combinations of control points.

Theorem 4.1 *A spline is fully bounded by its convex hull.*

- The curve is ‘affinely invariant’:

Theorem 4.2 *Translating, scaling, rotating or skewing the control points results in the same spline as applying these operations on the spline itself.*

- The variation-diminishing property:

Theorem 4.3 *If the set of all connecting lines between all combinations of control points intersects a given line m times, the spline defined by these control points intersects this line $\leq m$ times.*

This can very roughly be seen as a measure of how oscillatory the spline is and will not be explicitly exploited in this work. The convex hull and variation-diminishing properties give bounds on the region, where the curve can lie and how ‘oscillatory’ it is, while the affinely-invariant property allows for transparent manipulation of the curve by manipulating its control points.

An alternative definition, termed the Hermite spline, is defined from the locations \mathbf{p}_i and derivatives \mathbf{m}_i at the i^{th} control point, instead of the extra intermediate control points. Note that the derivative is with respect to the parameterizing variable t , not one of the physical coordinates x , y or z (see Eq. 4.8). The first two of the three properties of the Bézier curve shown above pass over to the Hermite curve. The affine invariance, though, is not inherited in the general case. For our assumption of Eq. (4.10), though, this property also holds for the Hermite-spline representation. The spline is then constructed as follows:

$$\mathbf{p}(u) = \mathbf{p}_i H_0^3(u) + \mathbf{m}_i H_1^3(t) + \mathbf{m}_{i+1} H_2^3(t) + \mathbf{p}_{i+1} H_3^3(t) \quad (4.13)$$

$$H_0^3(u) = (1 + 2u)(1 - u)^2 \quad (4.14)$$

$$H_1^3(u) = u(1 - u)^2 \quad (4.15)$$

$$H_2^3(u) = u^2(t - 1) \quad (4.16)$$

$$H_3^3(u) = u^2(3 - 2u) \quad (4.17)$$

The basis functions H_i^3 are visualized in Fig. 4.3a.

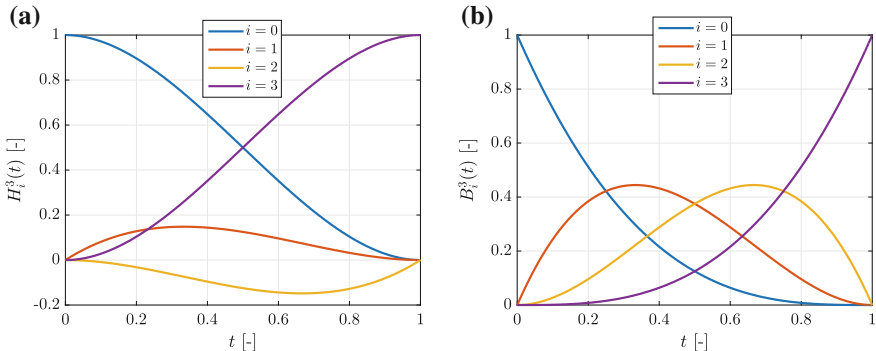


Fig. 4.3 The interpolating polynomials used for **a** Hermite and **b** Bézier spline construction

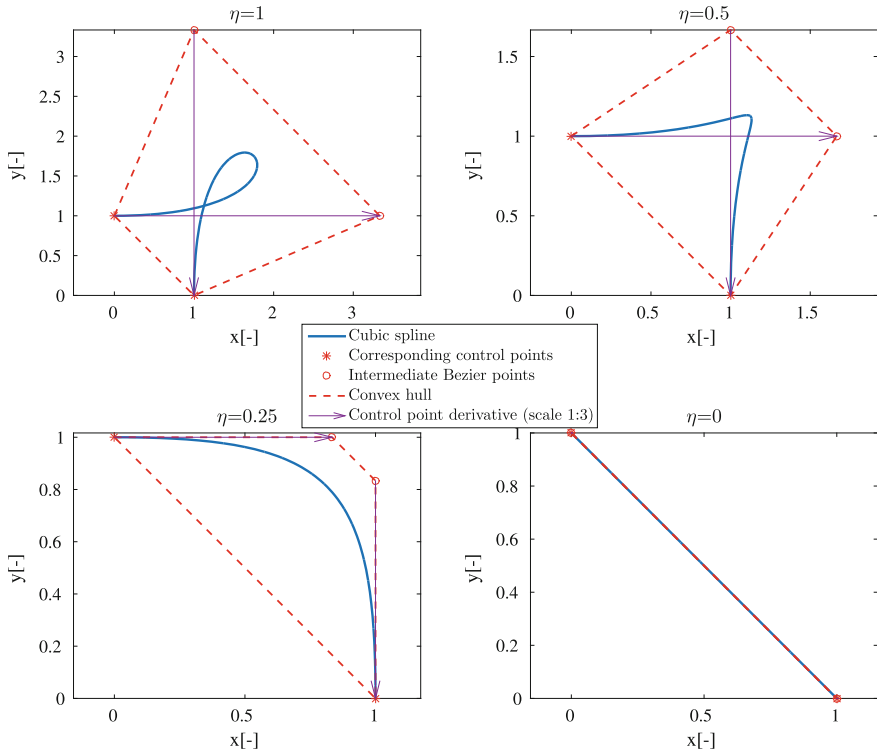


Fig. 4.4 Effect of curve tightening and illustration of convex hull, using various values of η in Eq.(4.20) and the following control points: $\mathbf{p}_0 = (0, 1)$, $\mathbf{p}_1 = (1, 0)$, $\mathbf{m}_0 = \eta(10, 0)$, $\mathbf{m}_1 = \eta(0, -10)$

The Bézier and Hermite curve are simply different representations of the same curve. The difference lies in whether the intermediate Bézier points or the control point derivatives are defined. The two are related by the following equations:

$$\begin{aligned}\mathbf{b}_{3i} &= \mathbf{p}_i \\ \mathbf{b}_{3i+1} &= \mathbf{p}_i + \frac{1}{3}\mathbf{m}_i \\ \mathbf{b}_{3i+2} &= \mathbf{p}_i - \frac{1}{3}\mathbf{m}_{i+1} \\ \mathbf{b}_{3i+3} &= \mathbf{p}_{i+1}\end{aligned}\quad (4.18)$$

These identities are graphically represented in Fig. 4.4, where a number of Hermite/Bézier curves is shown. In, addition, the corresponding intermediate points and control point derivatives are shown, indicating the relation between the two.

In case the derivatives are known at each point, the above procedure will yield a unique result for the cubic interpolant between any two points, as a cubic spline has four degrees of freedom. In practice, however, the values of the derivatives may not be specified *a priori*. A relatively simple method, which will ensure only C^1 continuity, is to use finite differences to approximate the derivatives at the control points. The type and order of approximation used is a matter of preference. As a result, this will not yield a unique spline, but the shape will instead depend on the choice of method for approximating the derivatives. For first-order central difference:

$$\mathbf{m}_i = \frac{1}{2}(\mathbf{p}_{i+1} - \mathbf{p}_{i-1}) \quad (4.19)$$

Additional methods for constructing splines, such as the C^2 cubic spline presented by Press et al. (2007), can be used. However, the method presented here has the advantages that local changes in the control points have only local influence in the shape of the spline, which greatly simplifies the physical interpretation of the influence of the position of a point on a vehicle's shape.

For the above procedures for determining the derivatives at the control points, it is also possible to impose the values at a number of control points, while determining the others from one the numerical methods. This can be advantageous when, for instance, the behaviour on part of the curve is known *a priori* and can be imposed.

It can also be used to insert a ‘kink’ (C^1 discontinuity) at the position of a control point. This is done at control point i by imposing that $\mathbf{m}_i = 0$. At a control point itself, it can be seen from Eqs. (4.13)–(4.17) and Fig. 4.3a that only the value of \mathbf{p}_i influences the position of the spline at $u = 0$, but that the derivative at $u = 0$ is only affected by \mathbf{m}_i . Since the spline definition is symmetric, the same holds at $t = 1$ on the previous spline segment for \mathbf{p}_{i+1} and \mathbf{m}_{i+1} . So, by imposing a zero derivative at a control point, the consecutive spline segments will not be forced to be C^1 continuous at their connection.

4.2.3 Avoiding Self-intersection and Concavity

When generating splines from random control-point positions and/or derivatives, splines that are self-intersecting or concave may be obtained. In the context of entry vehicle shape generation, this yields non-physical designs that must not be part of the feasible-design space. A method of avoiding such self-intersections is presented in this section.

The appearance of self-intersection and concavity is caused by excessively large derivatives at the control points. A method of modifying the spline in Eq. (4.19) can be used, in which a parameter η is used to tighten or loosen a spline. This is done as follows by modifying the first-order central difference approximation for the control point derivative:

$$\mathbf{m}_i = \frac{1}{2}(1 - \eta)(\mathbf{p}_{i+1} - \mathbf{p}_{i-1}) \quad (4.20)$$

For $\eta = 0$, this can be seen to reduce to Eq. (4.19). By varying the value of η , the curve can be made ‘looser’ or ‘tighter’. One illustration of this is given in Fig. 4.4. By decreasing the value of η , both the self-intersection and the concavity can be removed. To apply this method in a consistent manner, a method of determining the value of η that will modify the spline curve so as to remove the unwanted behaviour is needed. This is achieved by exploiting the equivalence of the Bézier and Hermite definition of a cubic spline, given by Eq. (4.18), as well as the convex-hull property.

From Eq. (4.18), it can be seen that the auxiliary Bézier points lie on the lines passing through \mathbf{p}_i and \mathbf{p}_{i+1} , with slopes \mathbf{m}_i and \mathbf{m}_{i+1} , respectively. As a result, it follows that by varying the value of η in Eq. (4.20), the location of the auxiliary points on these lines can be controlled.

To analyze whether self-intersection and concavity will occur, two straight lines are defined, one by \mathbf{p}_i and \mathbf{b}_{3i+1} and one by \mathbf{p}_{i+1} and \mathbf{b}_{3i+2} . The point of intersection between these two lines will be denoted \mathbf{p}_{int} . Now, the following theorem is used

Theorem 4.4 *A cubic Bézier spline segment will be both non-self intersecting and convex if:*

$$\begin{aligned} \mathbf{b}_{3i+1} &\text{ lies between } \mathbf{p}_i \text{ and } \mathbf{p}_{int} \\ \wedge \\ \mathbf{b}_{3i+2} &\text{ lies between } \mathbf{p}_{i+1} \text{ and } \mathbf{p}_{int} \end{aligned}$$

Now, using the unmodified values of the control point derivatives, derivative amplification factors c_i and c_{i+1} are determined that would cause the auxiliary points to both lie on the point \mathbf{p}_{int} , so that the curve will be at the limit of concavity. Since the tightening will only be applied to a spline in two dimensions in this work (keeping the third component constant over the curve), the rest of the derivation is performed for splines with only two dependent variables, x and y :

$$\mathbf{p}_i + c_i \mathbf{m}_i = \mathbf{p}_{i+1} + c_{i+1} \mathbf{m}_{i+1} \quad (4.21)$$

$$\begin{pmatrix} x'_i & -x'_{i+1} \\ y'_i & -y'_{i+1} \end{pmatrix} \cdot \begin{pmatrix} c_i \\ c_{i+1} \end{pmatrix} = \begin{pmatrix} x_{i+1} - x_i \\ y_{i+1} - y_i \end{pmatrix} \quad (4.22)$$

$$\begin{pmatrix} c_i \\ c_{i+1} \end{pmatrix} = \frac{1}{x'_{i+1}y'_i - x'_iy'_{i+1}} \begin{pmatrix} -y'_{i+1} & x'_{i+1} \\ -y'_i & x'_i \end{pmatrix} \cdot \begin{pmatrix} x_{i+1} - x_i \\ y_{i+1} - y_i \end{pmatrix} \quad (4.23)$$

Having obtained the values for c_i and c_{i+1} , Eq. (4.18) and Theorem 4.4 can be used to determine whether the spline will be self-intersecting or concave. If either of the values is smaller than $\frac{1}{3}$, the Bézier auxiliary point will not satisfy this condition. In such a case, the control-point derivative is scaled, so that the auxiliary point \mathbf{b}_{3i+1} now coincides with point \mathbf{p}_{int} as follows:

$$\mathbf{m}_{i,new} = 3c_i \mathbf{m}_{i,old} \quad (4.24)$$

and similarly for \mathbf{m}_{i+1} .

4.3 Hermite-Spline Surfaces

To be used for the description of vehicle surfaces, the concepts presented in the previous section need to be generalized to a surface. This involves the use of two independent variables (denoted here u and v), so that, instead of mapping a straight line segment to a space curve, a rectangular flat surface is mapped to a general curved surface in space. For this, an approach similar to the construction of Bézier curves is applied. Piecewise bivariate interpolation is used to obtain the Bézier surface $\mathbf{b}^{m,n}$ from $m \times n$ points $b_{i,j}$.

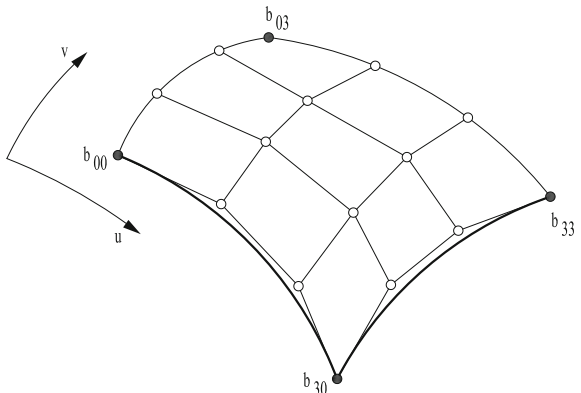
Here, the discussion will be restricted to bicubic surfaces ($m = n = 3$). For the construction of the Bézier spline surface, generalizing Eq.(4.11), 16 Bézier points are required, of which only 4, namely the corner points, are specified. An illustration of the required Bézier points, as well as a piecewise linear interpolation between these points, is given in Fig. 4.5.

We use bicubic Hermite-spline patches, which will yield a surface that is C^1 over the boundaries of the patches. This form is used as it makes the generation of the surfaces geometrically more intuitive. The bicubic-spline patch is written in Hermite form as follows:

$$\mathbf{x}(u, v) = \sum_{i=0}^3 \sum_{j=0}^3 \mathbf{h}_{i,j} H_i^3(u) H_j^3(v) \quad (4.25)$$

With the matrix of coefficients $\mathbf{h}_{i,j}$ a generalization of Eq.(4.13) as follows, for $0 \leq u, v \leq 1$:

Fig. 4.5 Points required for generation of a bicubic Bézier surface. Also indicated are piecewise linear interpolations between the points and the Bézier curves at two of the edges



$$[\mathbf{h}_{i,j}] = \begin{bmatrix} \mathbf{x}(0, 0) & \mathbf{x}_v(0, 0) & \mathbf{x}_v(0, 1) & \mathbf{x}(0, 1) \\ \mathbf{x}_u(0, 0) & \mathbf{x}_{uv}(0, 0) & \mathbf{x}_{uv}(0, 1) & \mathbf{x}_u(0, 1) \\ \mathbf{x}_u(1, 0) & \mathbf{x}_{uv}(1, 0) & \mathbf{x}_{uv}(1, 1) & \mathbf{x}_u(1, 1) \\ \mathbf{x}(1, 0) & \mathbf{x}_v(1, 0) & \mathbf{x}_v(1, 1) & \mathbf{x}(1, 1) \end{bmatrix} \quad (4.26)$$

To evaluate the above matrix, the first step is to create the curves that bound the surfaces, which can be done using the concepts described in the previous section. The level of continuity of the curves that this produces will be passed over to these curves on the surface, but not necessarily to the entire surface. Having done this over the entire geometry that is to be described, one has obtained a ‘net-like’ structure that divides the surface into patches with in general four boundaries, two in u and two in v direction. Also, 12 of the 16 coefficients in the above matrix are now known, as the derivative at the control point in both u and v direction were needed for generating the curves (if they are created in Hermite form). At the control points, the equation for the definition of the surface is now known, since the only Hermite polynomial that is used that is non-zero at this boundary is H_0^3 or H_3^3 , for start and end points of the cubic, respectively.

The additional information that is required for forming the spline surface patch are the cross derivatives \mathbf{x}_{uv} , also termed twists. A number of ways in which to determine these twists exist. Here however, a simple finite-difference approach will be used for their determination. This means that at a control point not at the boundary of the control net, the following will hold for equally-spaced control points in u and v direction:

$$\frac{\partial^2 \mathbf{x}}{\partial u \partial v} \approx \frac{1}{u_{i+1} - u_{i-1}} \left(\left(\frac{\partial \mathbf{x}}{\partial v} \right)_{i+1,j} - \left(\frac{\partial \mathbf{x}}{\partial v} \right)_{i-1,j} \right) \quad (4.27)$$

$$\frac{\partial^2 \mathbf{x}}{\partial u \partial v} \approx \frac{1}{v_{j+1} - v_{j-1}} \left(\left(\frac{\partial \mathbf{x}}{\partial u} \right)_{i,j+1} - \left(\frac{\partial \mathbf{x}}{\partial u} \right)_{i,j-1} \right) \quad (4.28)$$

In the case where the first derivatives in the above have been evaluated using first-order finite differences, as in Eq. (4.19), both of the above relations will evaluate to the same twist value. If this is not the case, the average of the two values can be taken. Details on the choice of derivative determination in the vehicle parametrization are given in Sect. 5.2.1. C^1 continuity of the surface over the shared boundaries of the patches is ensured if the curves that define that edges of each patch at the boundary are generated from the same coefficients, i.e., when they are the same curve.

Chapter 5

Vehicle Geometry

This chapter will describe the external geometry of the vehicle shapes that we use for the optimization. Their parametrization will be defined and (interdependent) constraints on the various shape parameters will be given. In Sect. 5.1, we will present the parameterization of a capsule shape. Subsequently, a winged vehicle shape will be described in Sect. 5.2. Finally, the surface discretization method used for the aerodynamic analysis will be described in Sect. 5.3.

Before moving on to the discussion of the specific shape parameterizations, a note on the representation of the parameter values in the implementation of the optimization is crucial. Specifically, we do not use the physical parameter values directly to represent the shape, but use a type of normalized parameters instead, where all shape parameters are by definition between 0 and 1. We take this approach to allow for shape-independent minimum and maximum parameter values. So, for a physical parameter x (a nose radius R_N , for instance), its value is determined from its minimum and maximum allowable values, denoted x_{min} and x_{max} respectively, and a scaling parameter r_x between 0 and 1. It is the set of such parameters r_x which are the normalized shape parameters. The value of the physical x is then determined from its internal representation r_x as follows:

$$x = x_{min} + r_x(x_{max} - x_{min}) \quad (5.1)$$

It is the set of these parameters r_x that span the parameter space that is used in the optimization. This facilitates the use of inter-parameter dependencies of minimum and maximum shape values. That is, regardless of other shape parameters, the range of allowable values for a given parameter is always between 0 and 1. The physical shape influence that this parameter maps to may vary, though. For instance, a given value of the parameter r_{R_N} can map to different values of R_N , depending on the current minimum and maximum nose-radius values.

For example, the value of r_{R_N} defines the size of the nose radius of the capsule shape by defining it relative to its minimum and maximum values. For $R_{N,min} = 0.5$ m, $R_{N,max} = 1.0$ m and $r_{R_N} = 0.3$, we get $R_N = 0.65$ m. In some cases, discussing

the behaviour of the value of r_x will be more illuminating than discussing the value of x , as its value is by definition between 0 and 1. Therefore, it is made much more transparent whether the parameter is at, or near, its minimum or maximum value.

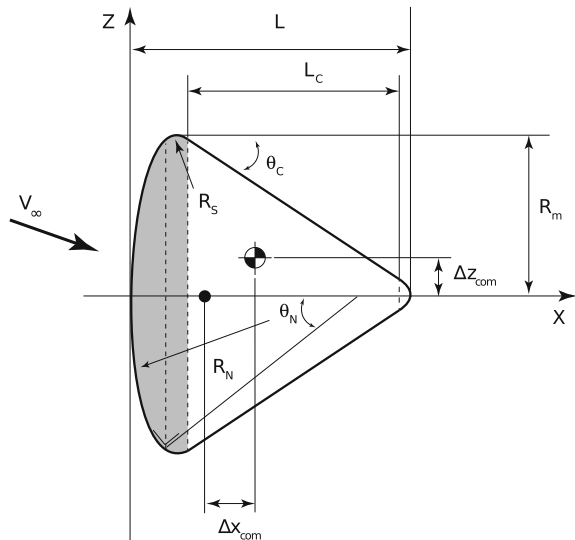
5.1 Analytical Parameterization

A number of vehicle shapes can be defined by a combination of analytical surfaces. The analytical shape that will be discussed here is shown in Fig. 5.1. It is an approximate parameterization of, among others, the Apollo capsule. As can be seen, it consists of four matched analytical geometries, a sphere segment, a torus segment, a conical frustum (i.e., a cone with the top cut off) and a spherical segment, further explained in Fig. 5.2. Although no unique set of parameters exists for defining this shape, five independent parameters are required for defining it. Since the shape is axisymmetric, the full surface geometry is defined by the top half of cross-section shown in Fig. 5.1. The parameters that are chosen for the shape definition for this study are:

- Nose radius R_N
- Side radius R_S
- Rear cone half-angle θ_c
- Mid radius R_m
- Rear conical part length L_c

The parameter L_c is chosen here, instead of the capsule length L , due to the simplicity of the constraint on it from other vehicle parameters, to be discussed shortly.

Fig. 5.1 Schematic representation of capsule re-entry vehicle shape (Ridolfi 2013), with shape parameters and division in analytical shapes indicated



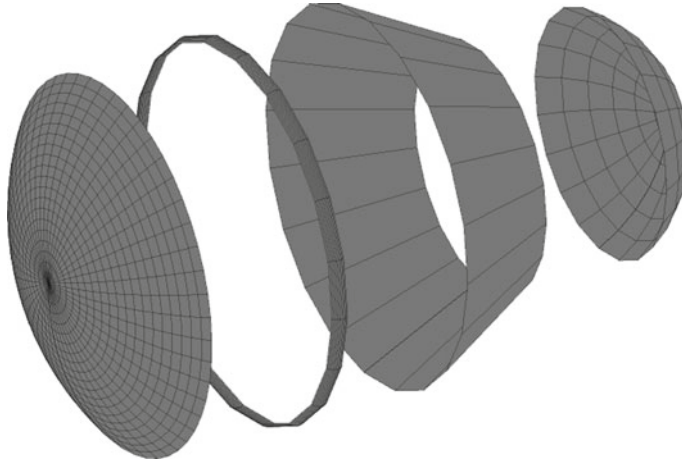


Fig. 5.2 Exploded view of capsule shape showing distinction between constituent analytical shapes

The cross-sections and defining parameters of the constituent analytical shapes can be seen from Fig. 5.3. The relations between the parameters of the capsule and the parameters of these analytical sub-shapes can be derived by simple geometrical relations, which are given below.

For the nose sphere:

$$R_{sp1} = R_N \quad (5.2)$$

$$\sin(\theta_{sp1,max}) = \frac{R_m - R_S}{R_N - R_S} \quad (5.3)$$

The parameters of the toroidal connection between the nose sphere and the rear cone are:

$$\theta_{t,min} = \theta_{sp1,max} \quad (5.4)$$

$$\theta_{t,max} = \theta_c \quad (5.5)$$

$$R_{t,1} = R_S \quad (5.6)$$

$$R_{t,2} = R_m - R_S \quad (5.7)$$

For the connection to the cone:

$$R_{c,1} = R_m (1 - \cos \theta_c) \quad (5.8)$$

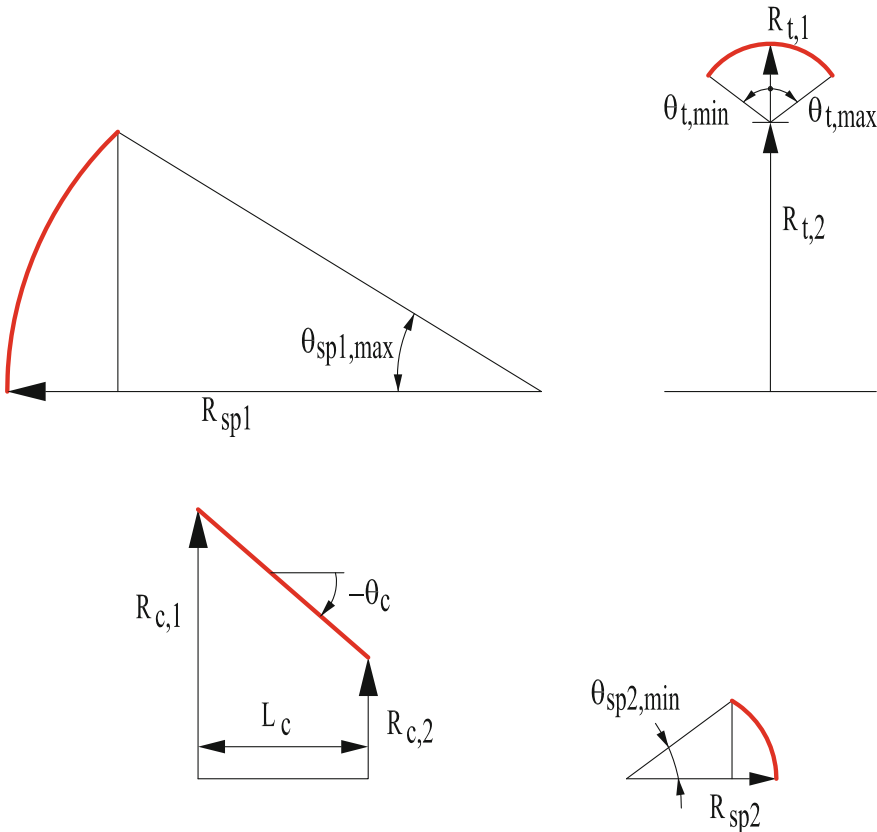


Fig. 5.3 Schematic representation of capsule shape with constituent shape parameters

For the rear sphere:

$$\theta_{sp2,min} = \frac{\pi}{2} - \theta_c \quad (5.9)$$

$$R_{sp2} = \frac{(R_{c,1} - L_c \tan \theta_c)}{\cos \theta_c} \quad (5.10)$$

The total length L of the capsule now follows from

$$L = L_{sp1} + L_t + L_c + L_{sp2} \quad (5.11)$$

$$L_{sp1} = R_N (1 - \sin \theta_{sp1,max}) \quad (5.12)$$

$$L_t = R_S (\sin \theta_{t,min} - \sin \theta_{t,max}) \quad (5.13)$$

$$L_{sp2} = R_{sp2} (1 - \sin \theta_c) \quad (5.14)$$

Table 5.1 Minimum and maximum shape parameter values

Parameter	Minimum value	Maximum value	Comments
R_N	3.0 m	7.0 m	—
R_S	0.02 m	0.40 m	—
θ_c	-60°	-5°	—
R_m	2.0 m	2.0 m	Value is fixed
L_c	0.2 m	2.0 m	Upper bound constrained by Eq. (5.16)
$\frac{\Delta x_{cog}}{L}$	-0.05	0.10	—
$\frac{\Delta z_{cog}}{h}$	0.0	0.10	—

When generating a capsule shape, the constraints on the minimum and maximum values of the parameters are inter-dependent. That is, in addition to constraints imposed on each variable *a priori*, the choice of R_N and θ_c influence the available choices of R_m and L_c . When generating the variables in the order described above, the following constraints are to be observed:

$$R_m < R_N \quad (5.15)$$

$$L_c < \frac{R_m - R_S (1 - \cos \theta_c)}{\tan \theta_c} \quad (5.16)$$

The first of these is to ensure that $\theta_{sp1,max} < 90^\circ$, so $\theta_{t,min} > 0^\circ$. The second of these is to ensure $R_{c,2} > 0$. For each of the shape parameters, we impose a minimum and maximum value, which we summarize here in Table 5.1. As discussed in Sect. 7.3.2, the value of R_m is kept fixed.

In addition to the vehicle's external shape, the internal mass distribution of the spacecraft can also be varied. Although we do not consider the internal layout of the vehicle in any detail here, it will be partially included by allowing a variation of the center of mass. This center-of-mass variation is well known to be an important factor in the capsule's behaviour, since an offset of the center of mass in z direction allows the vehicle to be trimmed at a non-zero angle of attack, thereby causing it to fly at a non-zero L/D . In addition, the x -position of the center of mass can be used to further modulate the moment curve, increasing the range of possible trim angles. This is advantageous for decreasing the load factor and maximum heat flux, as well as increasing the length of the flight path of the vehicle, thereby increasing its footprint size. From the examples given by Hirschel and Weiland (2009), the value for the offset of the center of mass can all be seen to be non-zero. The x - and z -positions of the center of mass are parameterized by first determining the centroid of the volume enclosed by the shape and parameterizing the lateral and longitudinal offset of the center of mass from this position. These parameters are $\Delta x_{com}/L$, the

offset along the centerline, normalized with the vehicle length, and $\Delta z_{com}/h$, the local offset in vertical direction, normalized with the local radius of the vehicle shape, h . The center-of-mass position is the only deviation from the axial symmetry of the capsule.

Due to the lack of a general mass model for a capsule-shaped vehicle, we make a simple constant-density approximation. That is, it is assumed that all capsules which are generated have one and the same uniform density, which is then multiplied by the vehicle volume to obtain the mass. Although this will introduce an error, due to the different average vehicle densities for different vehicle shapes, no model to account for these effects was found during this study. The value of the capsule density is based on the Apollo capsule, which has a mass of 5,470 kg (Hirschel and Weiland 2009) and a volume of 20.02 m³, obtained using a vehicle mesh and the method described in Sect. 5.3. This leads to a vehicle density of 273.29 kg/m³.

It should be noted that in a more multidisciplinary optimization, where shape, trajectory and system characteristics (for instance) are concurrently analyzed and/or optimized, the models and methods presented here can also be used to do the performance analysis by using system models to derive properties such as mass and center of mass.

5.2 Winged Vehicle Parameterization

Having presented the capsule-shape parameterization, we move on to the definition of a winged-vehicle shape, for which a much wider freedom in possible shape parameterizations exists. We present one possible shape definition here, in which the vehicle is generated using a Hermite spline surface (see Sect. 4.3) for the wings and fuselage and a sphere segment for the fuselage nose. For the body flap, a single rectangular plate is used. The general shape is based on the HORUS-2B reference vehicle, shown in Fig. 5.4.

This section will describe the parameterization of the fuselage and wings separately, followed by a discussion on how these two have been matched. Subsequently, the mass model that is used for the winged vehicle is described. Due to the complex nature of this section, a worked out example of the generation of a single winged vehicle shape, going from the associated parameters to the vehicle shape, is given in Appendix B.

5.2.1 Fuselage

The fuselage shape is defined by a spline surface, which is comprised of an (approximated) sphere segment for the nose and a free-form spline surface defining the rest of the fuselage. We choose to keep the nose spherical, as this shape will be able to optimally distribute the extreme thermal loading that it encounters during entry. As

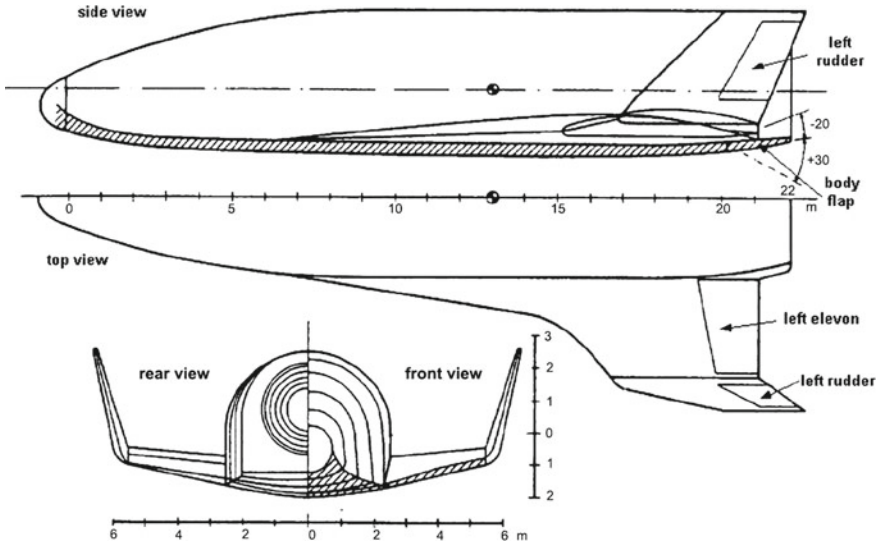


Fig. 5.4 The HORUS-2B vehicle, developed by MBB (Ridder and Mooij 2011)

an added advantage, in such a parameterization the known nose radius can be directly used in the calculation of the heat flux.

The nose segment is fully defined by two parameters, namely R_N and θ_N . These correspond to the capsule parameters R_{sp1} and $\theta_{sp1,mas}$ in Fig. 5.3, as the winged vehicle nose is parameterized identically to the capsule nose region. We define our axes as follows: by definition the nose point lies at $y = 0$ and $z = 0$ and the transition between the nose and remaining fuselage defines the point of $x = 0$. The x -axis in the longitudinal direction, the y -axis in lateral direction and the z -axis in upward direction.

The spline-surface geometry is defined by N_c cross-sectional areas perpendicular to the vehicle longitudinal axis (see Figs. 5.5 and 5.6), each of which is in turn defined by N_p points (with N_p equal for all contours). A schematic representation of the cross-sections and side view of a representative shape is given in Fig. 5.5. The N_p points on the N_c cross-sections are used to generate splines in two independent directions (lateral and longitudinal), which are subsequently used to generate the spline surface control point net. An example is shown in Fig. 5.6, where the longitudinal and lateral splines are shown in red and blue, respectively.

The u -direction of the spline surface is in longitudinal direction, with $u = 1$ denoting the interface with the nose and $u = i$ denoting the i^{th} cross section. The v direction is the lateral direction, with $v = 1$ denoting the top point of a contour and $v = j$ denoting the j^{th} point, when moving clockwise along a contour, viewed from the front of the vehicle (see Fig. 5.5). When discussing separate splines of the spline-surface control-net, ‘spline i ’ will denote the spline defining the shape of the i^{th} cross-section (i.e., with $u = i$).

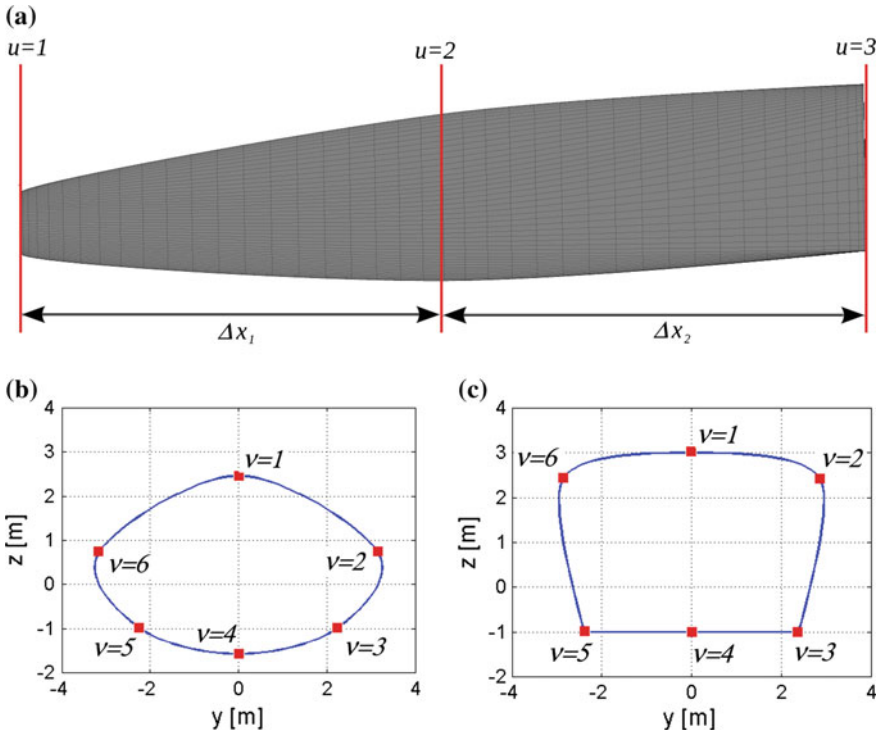


Fig. 5.5 Representation of fuselage parameterization with $N_c = 3$ and $N_p = 6$. **a** Side view indicating location of cross-sectional splines. **b** Spline curve of middle cross-section ($u = 2$) with control points. **c** Spline curve of rear cross-section ($u = 3$) with control points

The first contour of the spline surface (i.e., at $u = 1$ in Fig. 5.5a) is fully defined by the location and shape of the nose segment, with the control-point location and derivatives chosen to best approximate a circle (leading to an error of $<0.5\%$ for only 6 control points). The location of the other cross-sections is defined by parameters Δx_i , with $i = 1..N_c - 1$, which are the distances between cross-sections i and $i + 1$.

Each cross-section is symmetrical about its vertical centerline and two control points on each cross-section lie in the xz -plane. One of these defines the top and one of these the bottom of a cross-section, so that $N_p/2 + 1$ control points per cross-section are needed, imposing N_p to be even. This is illustrated in Fig. 5.5 for $N_p = 6$. The points on cross-section i are labeled as $\mathbf{p}_{i,j}$ (with components $x_{i,j}$, $y_{i,j}$ and $z_{i,j}$).

The challenge in defining the free-form fuselage-parameterization lies in the connection between the shape parameters r_x and the locations of points defining each of the cross-sections. It is not possible to freely assign a value to the y - and z -positions of each of the spline-surface control points and use this as input to the vehicle geometry generator. The vast majority of these would yield vehicle shapes with non-physical or undesirable characteristics, such as strong concavities. Therefore, the input parame-

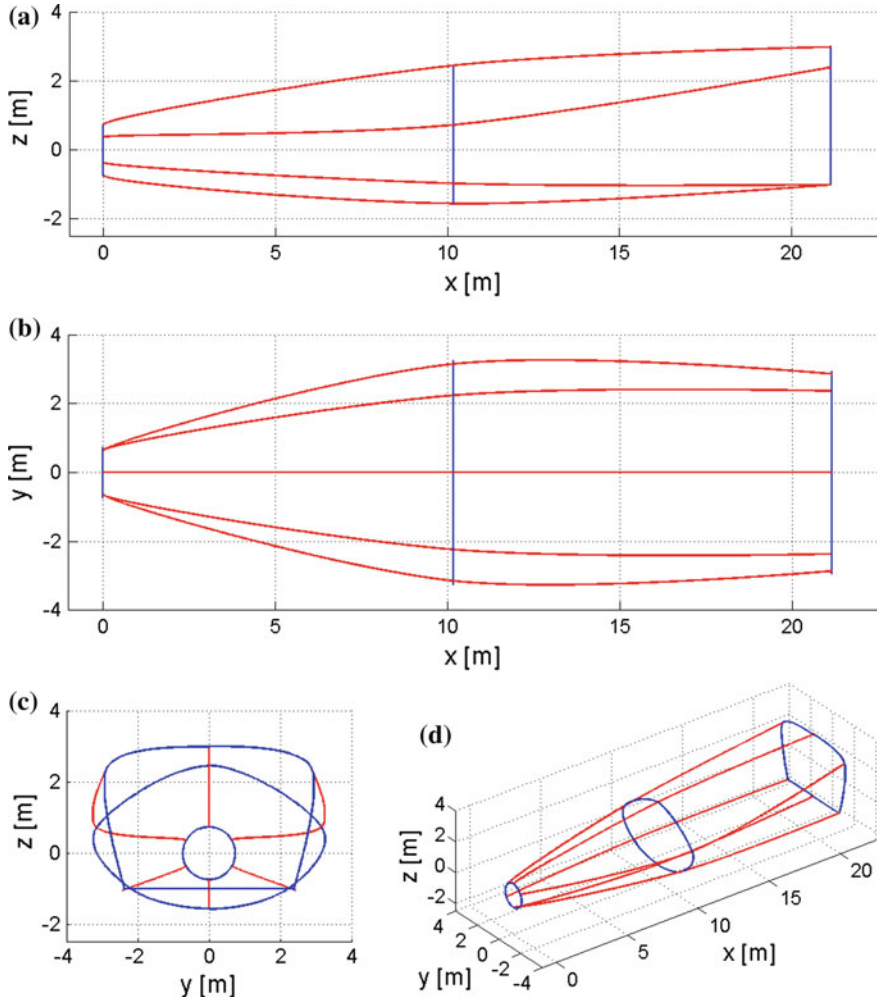
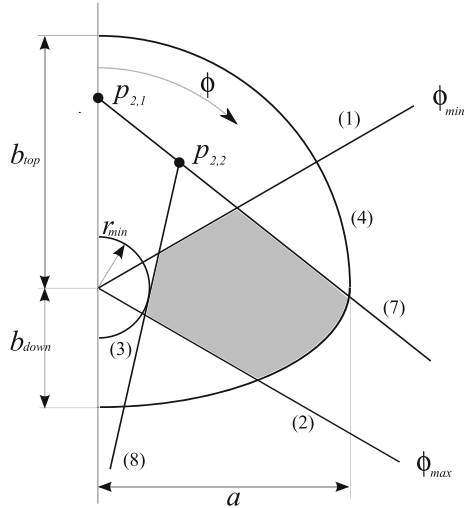


Fig. 5.6 Spline-surface control net for representative vehicle

ters r_x , see Eq. (5.1), need to be translated to control-point locations in such a fashion that they will result in an acceptable shape, while retaining sufficient freedom in possible shapes. To facilitate this, eight constraints have been developed on the location of a control point on a given cross-section. These constraints are based on broad limits for keeping the fuselage shape within reasonable bounds and the desirability of convexity and the requirement of non-intersection of the spline-surface control net. A representative case of the constraints is shown in Fig. 5.7. We will now describe the rationale and implementation of each of these constraints in detail.

Fig. 5.7 Schematic representation of constraints on selection of fuselage control point, for third point on second cross-section ($p_{2,3}$) for $N_p = 6$



We start by dividing the yz -plane (in which the contour is to be defined) into N_p parts spanning equal ranges of the angle ϕ (see Fig. 5.7) and the j^{th} control point on the contour is required to lie within the $(j - 1)^{\text{th}}$ segment (with the first point at $y = 0$). This will ensure that the control points will be reasonably distributed over the plane and prevent them from clustering, which would result in unrealistic vehicle shapes. The constraints are defined by two lines that bound the allowable angular area, shown in Fig. 5.7:

(1) Line $\phi \geq \phi_{\min}$, with:

$$\phi_{\min} = \frac{2\pi(j-1)}{N_p} \quad (5.17)$$

(2) Line $\phi \leq \phi_{\max}$, with:

$$\phi_{\max} = \frac{2\pi j}{N_p} \quad (5.18)$$

The remaining freedom of the control point location is its location in this angular range, defined by its y - and z -coordinates, for which additional constraining factors are required.

To keep the fuselage size in y - and z -direction within reasonable bounds, a minimum and maximum shape envelope is defined, which roughly represents the minimum and maximum height and width of the vehicle. It should be noted that the size of these shape envelopes depends on the type of vehicle/mission under consideration. We will give a general formulation, as well as provide numbers for our specific analysis case. The first of these constraints, constraint (3), defines the minimum vehicle size as follows:

(3) The point must lie outside a circle with radius r_{min} . The constraint on the minimum allowable radius is set at twice the radius of the first contour, which was matched to the nose sphere. Additionally, an absolute minimum radius a_{min} is imposed, which we have set to 1.0 m, to prevent the fuselage from growing too thin for vehicles with very small R_N and/or θ_N , so:

$$\sqrt{y^2 + z^2} > r_{min} \quad (5.19)$$

$$r_{min} = \max(a_{min}, 2R_N \sin \theta_N) \quad (5.20)$$

The maximum outer shape envelope is not chosen as a circle, due to some observations of typical entry vehicle shapes. Firstly, the fuselage bottom is typically flatter than the fuselage top. Secondly, vehicle shapes such as the X-38 and X-33 are much wider than they are high to produce a ‘lifting body’, whereas no vehicles are observed where the opposite is true. Although the parameterization should not restrict itself to known shapes, these shapes should form the starting point of the parameterization. It has been chosen to define separate radii for the width a_{max} and the minimum and maximum values of z : b_{down} and b_{top} (see Fig. 5.7), respectively. This naturally leads to a double ellipse shape, with the top and bottom constraining curves being separate ellipse segments, quantified by the following condition:

(4) The point must lie inside double ellipse with semi-major axis a , chosen here as 4 m, and semi-minor axes b_{top} and b_{down} (i.e., different semi-minor axes for top and bottom half), chosen here as 3.5 and 2.0 m, respectively.

$$\left(\frac{y}{a_{max}}\right)^2 + \left(\frac{z}{b_{top}}\right)^2 \leq 1 \quad (5.21)$$

$$\left(\frac{y}{a_{max}}\right)^2 + \left(\frac{z}{b_{down}}\right)^2 \leq 1 \quad (5.22)$$

Additional constraints on the allowable region arise from the desirability of (nearly) convex shapes of the fuselage cross-section. It has been chosen to relax the convexity constraint on the entire fuselage spline surface somewhat to broaden the class of possible shapes. Instead, only the splines defining the control net of the spline surface are required to be convex.

Constraints relating to longitudinal convexity (i.e., in increasing x -direction) are imposed. For $i = 2$ (i.e., first contour after match with nose segment, see Fig. 5.5), this is imposed by smoothly connecting a conical frustum to the nose segment and imposing that the entire cross-section spline at $i = 2$ lies inside the circle defined by this frustum at x_2 . For higher values of i , the convexity constraint is handled separately for each point j on the contour. For each point j , a sphere of $r_{max,c}$ inside which the point must lie is defined as follows. A line through points $(i - 1, j)$ and $(i - 2, j)$ (i.e., same index j on previous two contours) is created and continued to the current value of x . The radius $r_{max,c}$ is then defined as the distance from the origin to this line at $x = x_i$, defined by constraint (5) as follows:

(5) The point must lie inside a circle of radius $r_{max,c}$, with:

$$r_{max,c}|_{i=2} = R_N \sin \theta_N + \frac{\Delta x}{\tan \theta_N} \quad (5.23)$$

$$r_{max,c}|_{i>2} = r_{i-1,j} + (r_{i-1,j} - r_{i-2,j}) \frac{\Delta x_{i-2}}{\Delta x_{i-1}} \quad (5.24)$$

As an additional constraint from longitudinal convexity, it is required that control points on future cross-sections (i.e., with higher values of i than the current point) can satisfy constraint (5). To this end, a line is drawn from the point (i, j) to the circle of radius r_{min} (constraint 3) at $\phi = \phi_{i,j}$ on the rearmost contour of the vehicle. A value $r_{min,c}$ is defined as the distance of this line from the origin at $x = x_i$. Constraint (6) is then imposed:

(6) Point must lie outside circle of radius $r_{min,c}$:

$$r_{min,c} = r_{i-1,j} - (r_{i-1,j} - r_{min}) \frac{\Delta x_i}{\sum_{k=i-1}^{N_c-1} \Delta x_k} \quad (5.25)$$

For lateral convexity, the constraints take the form of two lines, see Fig. 5.7. A line L_1 through the previous two control points (or a horizontal line at $z = b_{top}$ for $j = 2$) is generated. The convexity constraint then follows from:

(7): The point must lie at greater value of ϕ (at a given r) than line L_1 .

Additionally, a point may not be chosen in such a manner as to reduce to zero the area of the allowable region due to convexity constraints for future points on the cross-section. To avoid this, a line L_2 through the previous control point tangent to the circle of radius $r_{min,c}$ or that defined by constraint (6), whichever dominates, is generated. The final constraint is then defined by:

(8): The point must lie at smaller value of ϕ (at a given r) than line L_2 .

Imposing these eight constraints leads to an area bounded by line segments, circle arcs and ellipse arcs. For the definition of each spline-surface control point on a cross-section, two shape parameters are required, one for the y - and one for the z -position. A physical position of the points from these shape parameters is obtained with Eq. (5.1). The minimum and maximum values of z in the bounded area, illustrated in Fig. 5.7 by the shaded area, are used first to determine the z -value of the point from:

$$z_{i,j} = z_{min} + r_{z,i,j} (z_{max} - z_{min}) \quad (5.26)$$

The value of $y_{i,j}$ is then generated similarly from the minimum and maximum values of y of the enclosing area at the generated value of $z_{i,j}$.

The control-point derivatives of the cross-section splines are determined by central finite differences. If the resultant spline is non-convex or self-intersecting due to a large control-point derivative, this derivative is rescaled to tighten the spline (see

Sect. 4.2.3). The derivatives in longitudinal direction at the first cross-section are obtained from smooth matching with the nose-sphere. Those at the remaining sections are again obtained from central differences (or backward difference for the rear contour).

By using this algorithm and specifying values for a , b_{top} and b_{down} , as well as a nose sphere shape, the fuselage shape can be defined from a set of shape parameters r to define the positions of each of the control points. In addition to the nose sphere, however, the fuselage must interface correctly with the wings and the body flap. The interface with the wings is discussed in Sect. 5.2.3, but modifies the shape of the wings based on the shape of the fuselage, and not vice versa. The interface with the body flap, though, poses a requirement on the fuselage shape, namely that there is a flat section on the bottom of the final contour onto which the flap can attach. Such a flat bottom is essential to ensure effectiveness of the body flap. The shape parameterization is modified such that the value of $z_{N_c, N_p/2+1}$ (i.e., the bottom control point of the rearmost contour) is no longer chosen freely, but is instead chosen to be equal to $z_{N_c, N_p/2}$. By additionally imposing $\dot{\mathbf{p}}_{N_c, N_p/2} = \mathbf{0}$, the bottom part of the rear contour between the final two control points will be straight and parallel to the y axis, as shown in Fig. 5.5c. The body flap attachment is shown in Fig. 5.8.

In summary, the fuselage shape is generated by the following steps:

1. Generate nose sphere segment from parameters R_N and θ_N .
2. Generate values for longitudinal position of cross-sectional splines of $\Delta x_1.. \Delta x_{N_c-1}$.
3. Generate first contour cross-section from nose-sphere segment.
4. Generate middle vehicle contours ($i = 2..N_c - 1$) as follows:
 - i Determine minimum and maximum values of z - value of contour top point; generate top contour point from associated parameter value.
 - ii For the second through the $(N_p/2)^{th}$ point, determine constraining curves. From these curves, determine bounding shape for the control point. From

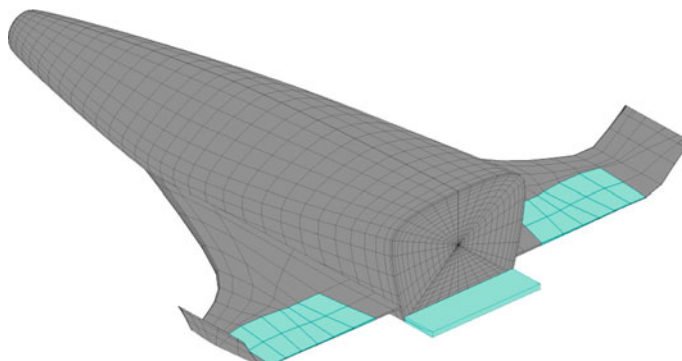


Fig. 5.8 Full vehicle configuration with control surfaces indicated in cyan, note that the hinge line of the elevons is not perfectly straight, as discussed below

- associated parameters, determine the control point's y and z location, denoted by $y_{i,j}$ and $z_{i,j}$.
- iii Determine minimum and maximum values of the z -value of the contour bottom point; generate bottom contour point from associated parameter value.
5. Generate the rear vehicle contour as follows:
 - i Determine the minimum and maximum values of the z -value of the contour top point; generate top contour point from associated parameter value.
 - ii For the second through the $(N_p/2)^{\text{th}}$ point, determine constraining curves. From these curves, determine the bounding shape for the control point. From associated parameters, determine control-point locations.
 - iii Take the bottom contour-point z -value equal to the $(N_p/2)^{\text{th}}$ control point z -value.
 6. Generate splines in u -directions from splines at the first through the $(N_c)^{\text{th}}$ cross-section.
 7. Generate the u -derivatives at first contour from interface with nose sphere.
 8. Set the u -derivatives at rear contour to zero.
 9. Set the v -derivatives on points 3 and 4 at rear contour to zero.
 10. Generate remaining control-point derivatives and twists using central finite-difference method.

We show examples of cross-sectional splines and resulting fuselage shapes for $N_c = 3$ and $N_p = 6$ in Fig. 5.9, where the bounding shapes for each control point are also shown for illustrative purposes.

The algorithm described here is valid for any value of N_c and N_p . Although an increase in these two values will generally lead to an increase in the possible shapes that can be generated, it will also lead to an increase of the number of independent variables and therefore the dimension of the search space when used in an optimization process. As such, increasing the value of N_c by one will increase the dimension of the search space by N_p and vice versa. To minimize this dimension, while retaining the functionality to generate a wide variety of shapes, N_c is therefore chosen at 3 and N_p at 6 in our optimizations. This leads to 13 independent variables for the definition of the fuselage, notably the values of Δx_1 , Δx_2 , R_N , θ_N , $z_{2..3,1..4}$ (with the exception of point $z_{3,4}$) and $y_{2..3,2..3}$. The full list of vehicle shape parameters (including the fuselage) is shown in Table 5.2, including the *a priori* and interdependent parameter-value constraints.

5.2.2 Wings

Having defined the fuselage shape, we will now discuss the parameterization and creation of the wing shapes of the vehicle. As with the fuselage shape, the wing shape is chosen to be symmetrical, so that the shape of the left wing equals that of

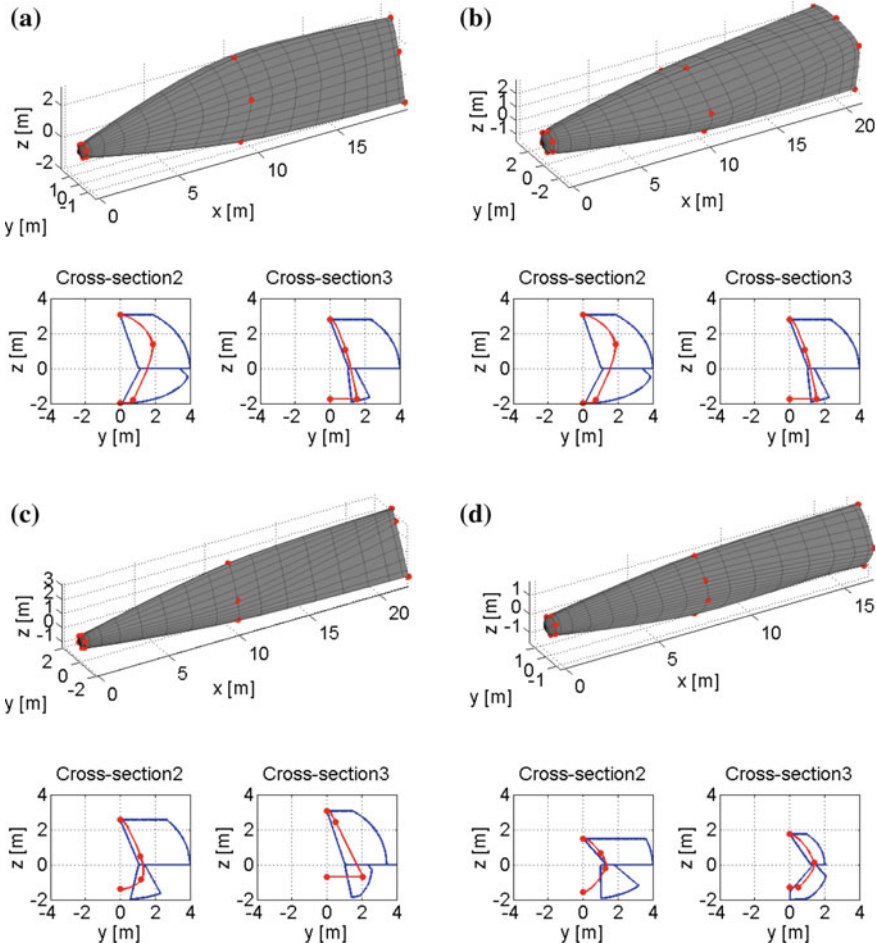


Fig. 5.9 Examples of four generated fuselage shapes with $N_c = 3$ and $N_p = 6$, with control point locations at all three cross-sections indicated. Constraining regions for spline surface control points, generated control points and resulting cross-section splines are indicated in separate figures for 2nd and 3rd cross-sections

the right wing. The wing is parameterized according to two sets of parameters, one defining the airfoil shapes and one defining the planform shape. Figures 5.10 and 5.11 show the parameterization of the wing, including the two independent directions of the wing shape u and v . The shape of the wing is defined by its cross-sectional shape (in u -direction) and the planform shape (in v -direction). Additionally, an elevon is inserted in the rear of each wing, shown in Fig. 5.8.

We will first discuss the parameterization and discretization of the airfoil. To limit the number of parameters that are required, a number of simplifying assumption is made on the airfoil cross-sectional shape:

Table 5.2 Minimum and maximum winged-vehicle shape parameter values

Parameter	Minimum value	Maximum value	Comments
R_N	0.4 m	1.0 m	—
θ_N	22.5°	77.5°	—
$\{y_{2..3,2..3} \cup z_{2..3,1..4}\} \setminus \{z_{2,4}\}$	See Sect. 5.2.1	See Sect. 5.2.1	—
$\Delta x_{1,2}$	7.0 m	12.0 m	—
R_{LE}	0.20 m	0.40 m	—
θ_{LE}	see Eq. (5.27)	30°	—
L_w	$0.35L_{fus}$	$0.8L_{fus}$	L_{fus} denotes total fuselage length
L_{mid}	$0.25L_w$	$0.6875L_w$	—
t_{mid}	R_{LE}	0.6 m	—
$x_{w,2}$	0.4	0.6	—
$x_{w,1}$	0.2	$0.9 \frac{x_{w,2}}{x_{w,1}}$	—
$x_{w,3}$	$x_{w,1}$	$0.9 \frac{x_{w,3}}{x_{w,1}}$	—
$x_{w,4}$	0.05	$0.9 \frac{x_{w,4}}{x_{w,1}}$	—
$y_{w,1}$	4.0 m	8.0 m	—
$y_{w,3}$	$\frac{y_{w,1}}{4}$	$\frac{y_{w,1}}{3}$	—
Δx_f	0.0 m	$x_{w,4}$	—
θ_f	45°	90°	—
L_{bf}	0.25 m	2.0 m	Body flap length must always be smaller than body flap width
f_{El}	0.5	0.95	$= L_{el}/x_{w,3}$

- Each airfoil cross-section of the wing is defined by the same shape, but scaled to accommodate the local chord length. That is, for each cross-section at $v = 0, 1, 2, 3$, the airfoil shape is the same, but all its linear dimensions are scaled by the same constant (to be defined in the planform parameterization).
- The airfoil shape is uncambered and symmetrical about the horizontal surface. Since the upper airfoil surface will not contribute much to the hypersonic force and moment coefficients (see Sect. 3.1.2), adding degrees of freedom to changing the shape of this surface is not deemed to be efficient.

The airfoil shape is now fully defined by the following parameters, shown in Fig. 5.10. This parameterization is roughly based on the PARSEC wing parameterization (Sobieczky 1998):

Fig. 5.10 Airfoil shape parameterization, with spline control points indicated in red

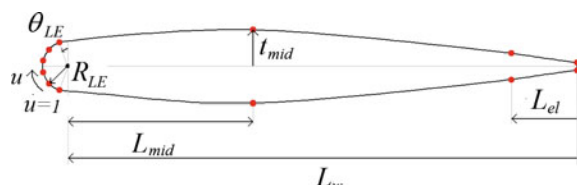
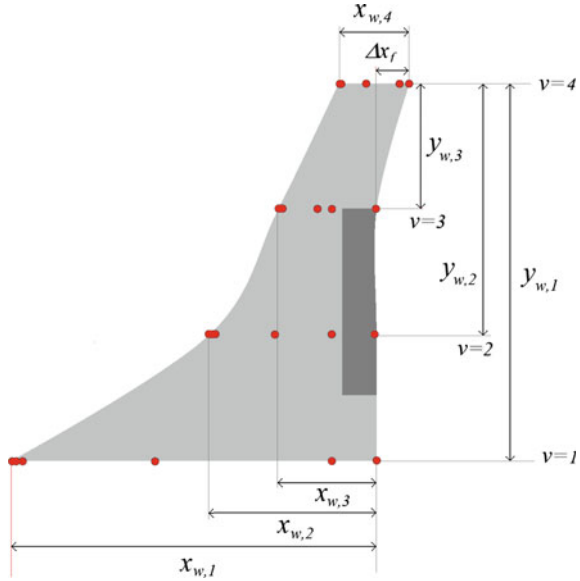


Fig. 5.11 Wing planform parameterization, with spline control points indicated in red, prior to winglet bending



- Leading edge radius R_{LE} .
- Angular range of circular nose section θ_{LE} .
- Total length of airfoil L_w , omitting circular leading edge.
- Position of middle control point L_{mid} .
- Airfoil thickness at middle control point t_{mid} .
- Length of elevon L_{el}

For the region between the leading edge and L_{mid} to be convex, the following inequality must be satisfied:

$$\tan \theta_{LE} > \frac{t_{mid} - R_{LE} \cos \theta_{LE}}{L_{mid}} \quad (5.27)$$

which is the limiting case where the nose-sphere segment is connected to the midpoint by a straight line.

The planform shape is parameterized in such a manner as to be able to approximate the wing shape of vehicles such as HORUS, the Space Shuttle, Hermes, HOPE-X, etc. For our parameterization, winglets are used for lateral control, as opposed to a vertical tail, such as on HORUS, Hope and HERMES. We create the winglets by bending the top of the wing upwards, shown in Fig. 5.12. Since we do not consider lateral control, only lateral stability, we do not include rudders on the winglets.

Figure 5.11 shows the parameters on which the wing planform shape is based, prior to the bending of the winglets. The spline control points are also shown for clarity. It can be seen that four wing cross-sections are defined. The scaling of the airfoil at each of these is determined from the ratio of $x_{w,i}$ to $x_{w,1}$. As a consequence,

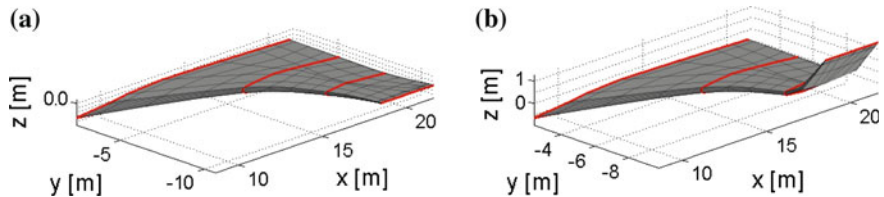


Fig. 5.12 Wing shape with locations of splines at $v = 1, 2, 3, 4$ indicated, **a** before bending, **b** after bending

the chord length and cross-section shape at each of these four locations is defined by the airfoil shape defined above, which is used directly at the first cross-section, and the parameters $\frac{x_{w,i}}{x_{w,1}}$, for $i = 1, 2, 3$, which define the scaling factor at the other cross-sections. The total span of one wing, prior to bending is defined by the parameter $y_{w,1}$, while the span of the region that is bent is defined by the value of $y_{w,3}$. We choose the distance between $v = 1$ and $v = 2$, and the distance between $v = 2$ and $v = 3$ to be equal (so that $y_{w,1} - y_{w,2} = y_{w,2} - y_{w,3}$). The angle by which the wing tip is swept upwards, as well as the sweep back of this tip, are both parameters, while the radius of curvature of the bend is fixed. The sweep-back is defined by the parameter $\frac{\Delta x_f}{x_{w,4}}$.

In total, the wing is defined by a Hermite-spline surface, the control net of which is defined by four Hermite splines each representing the same airfoil shape, scaled by the local chord length, with each contour consisting of 12 control points (shown in Fig. 5.10 in red). The first six control points approximate a circular section. Two control points define the rear of the airfoil, two define the overall shape between the nose and the rear and two define the elevon position.

The location of the knots defining the elevon position cannot be scaled along with the rest of the spline, since the elevon should ideally have a straight hinge line. To approximate this, the position of this control point is re-determined following the scaling of the spline. Its position and derivative are chosen in such a manner as to cause a minimal change in the overall shape of the spline.

The length of the elevon L_{ev} is parameterized by a value of f_{el} , which represents the fraction of the distance between $x_{3,7}$ and $x_{3,9}$ that is to become an elevon:

$$L_{ev} = \frac{x_{w,3}}{x_{w,1}} (L_w - L_{mid}) f_{el} \quad (5.28)$$

Summarizing, the wing generation algorithm is the following:

1. Generate all wing shape parameters from associated parameters and minimum and maximum values, such as those from Table 5.2.
2. Generate basic airfoil spline for each contour with appropriate scaling:
 - i Generate leading edge spline segments, which approximate a circle.

- ii Determine remaining control-point locations, excluding elevon-front control points.
 - iii Determine elevon-front control-point locations from current contour-scaling value and given (fixed) elevon length.
3. Generate splines at $v = 2, 3, 4$ from unprojected airfoil spline.
 4. Determine derivatives and cross-derivatives as spline-surface control points.
 5. Bend wing tip upwards.
- Finally, the wing is mated to the fuselage using an algorithm that will be discussed in the next section.
- 6 Determine translation of airfoil spline for proper positioning prior to precise matching to fuselage:
 - i Determine x -translation from requirement that trailing edge should be flush with fuselage rear.
 - ii Determine z -translation from required smallest difference between the value of z between fuselage and wing over entire wing.
 - iii Determine y -translation from the projection of the front point of the leading edge onto the fuselage.
 7. Project airfoil spline onto fuselage according to algorithm of Sect. 5.2.3.

5.2.3 Fuselage-Wing Interface

Using the methods described in the previous two sections, separate wing and fuselage shapes can be generated. However, to generate a complete vehicle, these two shapes must be combined into a single shape by mating the fuselage with the two wings. Firstly, this requires a relative position of the wing(s) w.r.t. the fuselage to be defined, i.e., a distance offset between a reference point on the wing and a reference point on the fuselage. Secondly, either the wing or fuselage shape must be locally deformed to allow for the two shapes to be smoothly attached, without gaps or intersections. We assume no rotations of the wing shape w.r.t. the fuselage shape, such that their local x , y and z axes are oriented in the same directions.

We start by defining the relative position of the wing and fuselage. For the longitudinal relative position (i.e., x -position) of the wing, the rear of the wing is chosen to be flush with the rear of the fuselage, shown clearly in Fig. 5.8. Next, we determine the z -translation of the wings, i.e., how ‘high’ or ‘low’ on the fuselage the wings will be attached. As a first criterion for this translation, we require that the bottom-most point of the entire vehicle will be on the fuselage bottom, not the wing bottom. We impose this to allow the large freedom of the fuselage shape to be fully exploited. To achieve this, we identify the point on the wing which, when moving the wing downward, will be the first location on the wing to be the lowest point on the whole vehicle. This point we denoted $x_{w,zmin}$. When moving the wing downwards,

$x_{w,zmin}$ is the location where the wing will first entirely obscure the bottom of the fuselage (assuming that the left and right wing are connected by some means). The placement in z -direction of the wing w.r.t. the fuselage is then performed so that the z -distance of the fuselage and wing at $x_{w,zmin}$ becomes a certain given ‘buffer’ value, which we set equal to the airfoil parameter t_{mid} . Finally, after the translations in x - and z -direction, we define the relative position in y -direction (laterally) by which to translate the wing. This is done by defining that the front point of the wing root lies exactly *on* the fuselage.

However, the wing attachment is not yet finished, since the fuselage and wing are not smoothly matched. Since the wing side that is to be attached is defined in the xz -plane and the fuselage to which it is to be attached has some general, doubly curved shape, we must deform either the wing or fuselage (or both) to attain a smooth attachment. Here, we choose to deform only the first cross-section of the wing (at the local $v = 0$) to be smoothly matched to the fuselage. We achieve this deformation by moving the spline control points at $v = 0$ in y -direction in such a manner that they lie directly on the wing. We take this approach so as not to compromise the airfoil shape, as well as to retain transparency between the shape parameters and the actual shape of the wing.

We approach this matching slightly differently for the control points on the leading edge of the wing, though, since we want the matching between the wings and fuselage to be done in a manner that leaves the leading edge radius unchanged. This is desirable, since the leading edge heating is imposed as a constraint on the vehicle (see Sect. 6.3.2). As this heating is proportional to the value of R_{LE} (see Sect. 3.4.1), it is useful in the optimization to have R_{LE} directly relatable to a single parameter, if possible. Not only will this make the meaning of the parameter more transparent and simplify the leading-edge calculations, it will also produce more realistic vehicle shapes and provide a smoother mapping between parameter space and constraint space.

To achieve the leading-edge matching without changing the value of R_{LE} , we modify the splines of the wing in v -direction (spanwise) along the leading edge. Specifically, depending on whether the root point of this spline is outside or inside the fuselage, we either extend the spline further onto the fuselage or shorten it to lie on the fuselage. An example of the front view of the wing is shown in Fig. 5.13. In this figure, the blue line represents the contour of the fuselage onto which the wing is to be projected. It can be seen that the top and bottom of the wing lie on the fuselage already, since their matching is achieved by a simple y -translation of the relevant control points, as discussed above. For the leading edge, however, the pictures to the left and right in Fig. 5.13 show the situation before and after the leading-edge matching. As shown in these figures, the part of the leading edge that is inside the fuselage (red area to the right of the blue curve in Fig. 5.13a) is removed to obtain the matching without deforming the leading edge. Similarly, the spanwise splines of the parts of the leading edge that lie outside the fuselage are extended without deforming the shape, finally resulting in the shape shown in Fig. 5.13b, where the wing is smoothly matched to the fuselage.

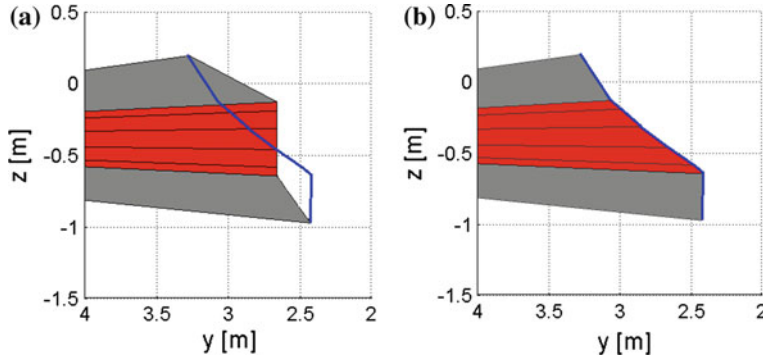


Fig. 5.13 Front view detail of wing matching. *Red* indicates wing leading edge, *grey* indicates wing top and bottom, *blue* indicates fuselage yz-shape at wing interface. **a** Before leading-edge match **b** After leading-edge match

5.2.4 Mass Model

To evaluate the performance of the entry vehicle, a model for the vehicle mass is required. Due to the greater structural complexity of a winged entry vehicle, compared to an entry-capsule, the use of a constant density assumption is not desirable. In addition, the added mass caused by the wings is a factor that makes the cost of lifting (and typically reusable) entry vehicles prohibitive. This trade-off between increased lift and increased mass, and therefore cost, is an important driver in the design of such vehicles. To more accurately assess the performance of these vehicles, an empirical sizing tool, the Hypersonic Aerospace Sizing Analysis (HASA), documented by Harloff and Berkowitz (1988), is used. The tool was created for the preliminary evaluation of both size and mass of hypersonic vehicles, including orbital entry vehicles. Examples of previous applications of this tool in the design optimization of hypersonic vehicles can be found in, for instance, Tsuchiya et al. (2007). Although the sizing part of the tool is not used in this study, the sizes that are obtained from the parameterization are used as input for the mass estimation part of the tool. The relations that are used in the tool will now be presented. It should be noted that the correlations, as presented here, use imperial units, not SI units as input (i.e., ft., lbs., psi).

The mass of the fuselage W_{fus} is estimated from the following relation:

$$W_{fus} = 0.341 C_{mf} \left[\left(\frac{L_b n_{max}}{D_{b_e}} \right)^{0.15} q_{dyn,max}^{0.16} S_{fus,tot}^{1.05} \right] \quad (5.29)$$

where L_b is the length of the fuselage, n_{max} is the ultimate load factor, $q_{dyn,max}$ is the maximum dynamic pressure, $S_{fus,tot}$ is the total fuselage surface area, C_{mf} is a modifying factor and D_{b_e} is the effective body diameter, which is determined from:

$$D_{b_e} = \sqrt{\frac{V_{tot}}{L_b \frac{n}{4} \eta_V}} \quad (5.30)$$

Here, V_{tot} is the fuselage volume, n equals 2 and η_V is the volumetric efficiency. The modifying factor C_{mf} is taken at 1.12 after the information in the HASA document.

The total mass of the wings W_w is determined from the following equation:

$$W_w = 0.2958 C_{mf} \left[\left(\frac{W_{emp} n_{max}}{1000} \right)^{0.52} S_w^{0.7} AR^{0.47} \left(\frac{1 + \lambda}{\frac{l}{c}} \right) \left(0.3 + \frac{7}{\cos(\lambda_{1/2})} \right) \right]^{1.07} \quad (5.31)$$

where S_w is the total planform area of the wings when connecting the wings together through the fuselage, AR is the wing aspect ratio, λ is the wing-taper ratio and $\lambda_{1/2}$ is the mid-chord sweep angle. It should be noted that the aspect ratio is to be determined from the value of S_w as:

$$AR = \frac{b^2}{S_w} \quad (5.32)$$

where b represents the total wing span of the vehicle. It can be seen that the wing mass is expressed as a function of the total empty vehicle mass W_{emp} , so that the final solution for the wing and total mass are to be solved iteratively. In the wing mass equation, it can be seen that an increase in wing thickness means a decrease in wing mass, which seems counterintuitive. However, data from Udin and Anderson (1991), where a mass estimation tool for a subsonic wing is described, indicate that this is most likely due to the additional required mass to withstand the bending moment.

The relation for the TPS mass is the following:

$$W_{TPS} = W_{TPS} (S_w + S_{fus,bot} + S_{cs}) \quad (5.33)$$

where W_{TPS} is an average value for the TPS mass per unit area, which will be assumed constant for all vehicles. $S_{fus,bot}$ is the area of the fuselage bottom directly exposed to the flow, which is not taken into account in the value of S_w by connecting the wings through the fuselage. The value of W_{ins} that is used in Harloff and Berkowitz (1988) for orbital entry vehicles is 3 lbs/ft², which will also be used for the approximations here.

The mass of the vehicle subsystems can also be approximated using relations from HASA, the masses of the landing gear, hydraulics, avionics and electrical systems are approximated from:

$$W_{gear} = 0.00916 W_{emp}^{1.124} \quad (5.34)$$

$$W_{hydr} = 2.64 \left(\frac{(S_w + S_{cs})q_{dyn,max}}{1000} \right)^{0.334} (L_b + b)^{0.5} \quad (5.35)$$

$$W_{avcs} = 66.37 W_{emp}^{0.361} \quad (5.36)$$

$$W_{elect} = 1.167 W_{emp}^{0.5} L_b^{0.25} \quad (5.37)$$

where S_{cs} denotes the surface area of the control surfaces and b the wing span. A relation for payload and equipment mass is also included in HASA but since an entry without payload will be considered, the former of these is not included. The form of the correlation for the equipment weight appears to be wholly inappropriate for the size of the entry vehicles that will be considered here, since it produces a minimum value of 10,000 lbs. However, the mass of the equipment of the examples listed by Harloff and Berkowitz (1988) is about 1–2 %, so that neglecting this contribution is admissible.

Since HASA was designed for the analysis for relatively large vehicles (150–400 ft. in length), the geometry information from the HORUS-2B vehicle (MBB-Space 1988; Mooij 1995) is used to obtain an empty mass estimate using the HASA relations. The resultant mass is 13,538 kg, whereas the vehicle empty mass is 18,394 kg. The discrepancy is relatively large when compared to the examples in the HASA document. To improve the mass estimations for the winged entry vehicles, a correction factor, equal to the relative error in the HORUS mass estimate, is used for the generated vehicles.

During the analysis of the performance of the winged-vehicle shape, it was found that allowing the center of mass of the vehicle to vary from the nominal position decreased the number of feasible solutions significantly. Since this number is only around $\sim 10\%$ (see Sect. 9.1), it was decided to keep the center of mass position fixed. The centroids of the various contributions to the mass were calculated and the center of mass is taken as the mass-weighted average of these points.

5.3 Meshed Surfaces

For the aerodynamic analysis methods described in Sect. 3.3, a paneled surface mesh is required. The geometry input file format that is used is the Langley Wireframe Geometry (LaWGS) Format (Craiden 1985). It bases the definition of a wireframe on a discrete number of points that make up an object, the entire configuration can then be defined from an arbitrary number of these objects. Objects may be defined in a (right-handed Cartesian) global coordinate system, or a local coordinate system, where the specification of the translation and rotation from the local to global coordinate system must be given. In addition, a mirror symmetry about the xy -, xz - or yz -plane may be defined in either local or global coordinates for an object.

A single object is composed of a number of contours that are in turn composed of a number of points, where the number of points on each contour must be equal. By connecting each point to both neighboring points on the same contour and connecting

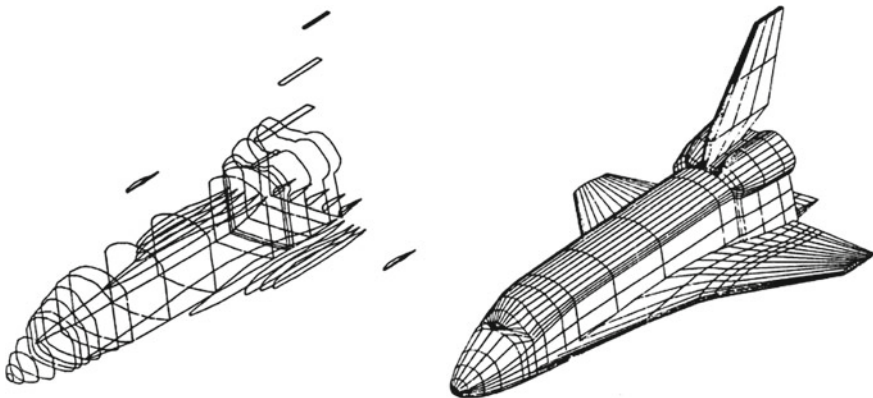


Fig. 5.14 Space Shuttle wireframe model from Langley Wireframe Geometry Standard, note the difference in the formation of fusiform and planar geometries (Craiden 1985)

points with the same indices on subsequent contours, a wireframe of quadrilaterals is obtained. An example of a resulting wireframe for the Space Shuttle is shown in Fig. 5.14. A downside of this mesh format is that, since a plane is defined by three points, the use of four points for a panel may cause the points defining them to not lie exactly on the panel. To define a panel from the four points $\mathbf{p}_{i..i+1,j..j+1}$, a panel normal $\hat{\mathbf{n}}_{i,j}$, centroid $\bar{\mathbf{p}}_{i,j}$ and area $A_{i,j}$ are determined as follows:

$$\bar{\mathbf{p}}_{i,j} = \frac{\mathbf{p}_{i,j} + \mathbf{p}_{i+1,j} + \mathbf{p}_{i,j+1} + \mathbf{p}_{i+1,j+1}}{4} \quad (5.38)$$

$$\mathbf{n}_{i,j} = (\mathbf{p}_{i+1,j+1} - \mathbf{p}_{i,j}) \times (\mathbf{p}_{i+1,j} - \mathbf{p}_{i,j+1}) \quad (5.39)$$

$$A_{i,j} = \frac{1}{2} |\mathbf{n}_{i,j}| \quad (5.40)$$

$$\hat{\mathbf{n}}_{i,j} = \frac{\mathbf{n}_{i,j}}{|\mathbf{n}_{i,j}|} \quad (5.41)$$

From this definition, the normal vector can be seen to be defined from the two cross vectors of the panel. In the case where these two cross vectors intersect, all four points will lie on the panel. In other cases, however, the effective panel is ‘translated’ so that its centroid coincides with the centroid as determined above. The area of the panel is determined from the area of an ‘effective’ parallelogram. For the computations performed for the aerodynamic coefficients (see Sect. 3.3), the exact shape of the panel is irrelevant, but a ‘concentrated quantity of area’, located according to the centroid and oriented according to the normal, is used instead. For the panel shadowing, though, a watertight mesh is important to prevent spurious results. However, since the panel-shadowing algorithm projects all panels onto the yz -plane, all points of a panel will always lie in the same plane.

To retain consistency, two main types of geometries and an associated recommended manner of defining them in LaWGS are discussed in Craidon (1985), ‘fusiform’ and ‘planar’ objects. Fusiform objects, such as a fuselage or engine nacelle, should contain contour lines starting at the nose and ending at the rear, with the first point on each line the one with lowest z -location and successive points given in a clockwise manner (when viewed from the front). For planar bodies, such as wings or tails, a contour should start at the trailing edge and should define the ‘bottom’ first. An example of a wireframe model, which shows the differentiation between fusiform and planar geometries, is given in Fig. 5.14.

To convert a spline surface, or an analytical surface, to a meshed surface, two mesh-precision settings need to be determined. The number of contours n_c and the number of points per contour n_{pt} must be defined. The first and second independent variables are then divided into a corresponding number of sections. For instance, for a spline surface with $1 \leq u \leq 5$ and $1 \leq v \leq 4$, for $n_c = 9$ and $n_p = 5$, the mesh points are those at the following values of the independent variables: $u = 1, 3/2, 2, \dots, 5$ and $v = 1, 7/4, 5/2, \dots, 4$. The first contour then corresponds to the points taken at $u = 0$ and the given values of v , the second contour to $u = 1/2$ and the given values of u , etc. For surfaces where the curve obtained by fixing a single independent variable is closed, for instance for the fuselage when fixing the value of v , this closure is taken into account when determining the location of the mesh points.

From the vehicle mesh, the total surface area and internal volume, S and V , are determined as follows:

$$S = \sum_{i=0}^{n_c-1} \sum_{j=0}^{n_{pt}-1} A_{i,j} \quad (5.42)$$

$$V = \frac{1}{3} \sum_{i=0}^{n_c-1} \sum_{j=0}^{n_{pt}-1} ((\bar{\mathbf{p}}_{i,j} - \mathbf{p}_{ref}) \cdot \hat{\mathbf{n}}_{i,j}) A_{i,j} \quad (5.43)$$

The first of these relations is self-explanatory, but the second requires some more explanation. For the calculation of the volume, a pyramid, with its apex at point \mathbf{p}_{ref} , is formed for each panel, the volumes of which are then summed. The bases of the pyramids are formed such, that they are perpendicular to the vector $(\bar{\mathbf{p}}_{i,j} - \mathbf{p}_{ref})$. The area of the base is a fraction of the panel area. This fraction is obtained from the dot product inside the summation.

Chapter 6

Optimization

This chapter will deal with the optimization process that is used for this study. We will address both the general problem of (design) optimization and the specific shape optimization problem for a capsule and winged vehicle. First, Sect. 6.1 will present a number of basic concepts of both single- and multi-objective optimization. Subsequently, the optimization algorithm used here, a Particle Swarm Optimization (PSO), will be discussed in Sect. 6.2. Finally, Sect. 6.3 will give an overview of the implementation of the design problem that we concern ourselves with here, providing the definition and rationale for the objective and constraint functions that are used.

6.1 General Concepts

In this section, we discuss some of the basic concepts of global optimization that are relevant to the problem at hand. Extensive discussion on both the fundamentals and implementation of optimization problems are given by, e.g., Wahde (2008) and Deb (2000). First the definition of a problem of optimizing a single function will be discussed in Sect. 6.1.1, followed by a discussion on how to extend the relevant concepts to multi-objective optimization in Sect. 6.1.2.

6.1.1 Problem Statement

In optimization, the goal is to find the best possible solution for a certain physical problem. To be able to quantitatively compare different solutions, the performance or cost of the solution is formulated mathematically, as a function $f(\mathbf{x})$, where the vector \mathbf{x} denotes the position in the solution or search space. The solution space of a problem spans all values of the independent variables that are considered in the

optimization. The number of independent variables, denoted n_s , is the dimension of the search space S . When the function f is to be maximized, it is typically termed a fitness function, and higher fitness denotes a better solution. When a minimum is sought, it is termed a cost function and the lower the cost, the better the solution. More generally, it is termed the objective function.

It should be noted that any minimization problem can always be turned into a maximization problem, and *vice versa*, by transforming the function f into $-f$ (or $1/f$ if $f > 0 \forall \mathbf{x}$). The single-objective optimization problem can, for this reason, be cast in the following form without loss of generality:

$$\min_{\mathbf{x}} f(\mathbf{x}) \quad (6.1)$$

In the above, we have placed no explicit limitations on the search space S , and implicitly assume the search space to be \mathbb{R}^{n_s} . Practical problems, however, are typically accompanied by both inequality and equality constraints, which can be put in the following form:

$$g_i(\mathbf{x}) \leq 0, \quad i = 1, \dots, p \quad (6.2)$$

$$h_j(\mathbf{x}) = 0, \quad j = 1, \dots, q \quad (6.3)$$

These $p+q$ additional functions limit the domain in \mathbb{R}^{n_s} where the solution is allowed to be. The \geq sign in Eq. (6.2) can be used instead of \leq without loss of generality for the same reason that a maximization problem can be cast into the form of a minimization problem. When defining the constraints, it is important that S does not become empty, i.e., that the complete set of constraints do not result in an empty search space.

For the problem that is analyzed in this study, the parameters that span the solution space are the associated parameter values of the shape r_x (see beginning of Chap. 5). Each of these parameters is chosen such that the unit interval $[0, 1]$ is its unconstrained range. As such, the unconstrained solution space is spanned by the n_s -dimensional unit-hypercube in \mathbb{R}^{n_s} , where $n_s = 6$ for the capsule shape and $n_s = 29$ for the winged vehicle. The objectives and constraints that are used in both problems are discussed in Sects. 6.3.1 and 6.3.2. Since no equality constraints are considered, they need not be considered any further.

6.1.2 Multi-objective Optimality

For complex optimization problems, where the objective function cannot be expressed as a single function, the concept of multi-objective optimization arises. To achieve this, Eq. (6.1) is generalized to allow for multiple cost functions:

$$\min_{\mathbf{x}} (f_1(\mathbf{x}), \dots, f_m(\mathbf{x})) \quad (6.4)$$

This formulation makes for a significantly more complex and ill-posed optimization problem, since the different objective functions will generally compete with another one (if they do not, some can be eliminated). This means that, for a certain change in \mathbf{x} , a decrease in one of the cost functions may result in an increase in another cost function. Consequently, the question arises how to define the optimal solution to the concurrent minimization of multiple functions. One option is to combine the objectives into a single ‘weighted total’ function by introducing a new single objective function $F(\mathbf{x})$:

$$F(\mathbf{x}) = \sum_{i=1}^m w_i f_i(\mathbf{x}) \quad (6.5)$$

where the weights w_i are chosen based on the problem at hand. This has the advantage that the problem is now simplified to a single problem of the type defined by Eq. (6.1), using the objective function $F(\mathbf{x})$. Such an approach has a number of downsides, however, one of which is clearly how to determine the weights w_i that are to be used. Typically, there will not be a single ‘correct’ choice for these weights (if there were, the problem would in essence *be* a single objective problem). This means that the choice of weights will, in general, influence the optima that are found.

Instead, it is often desirable to keep the multi-objective nature of the problem intact, which leads to the concept of Pareto optimality. A solution \mathbf{x}^* is said to be Pareto optimal, if there does not exist another value of \mathbf{x} for which at least one of the cost functions f_i improves without worsening one or more of the others. That is, moving away from a Pareto-optimal solution means that at least one objective function will worsen. This is related to the concept of dominance. If a vector \mathbf{x}^* dominates another vector \mathbf{x} (denoted as $\mathbf{x}^* \preceq \mathbf{x}$), the following condition holds (e.g., Price et al. 2005):

Definition 6.1 $\mathbf{x}^* \preceq \mathbf{x}$ if and only if the following two conditions hold:

$$\begin{aligned} \forall k \in \{1, \dots, m\} : f_k(\mathbf{x}^*) &\leq f_k(\mathbf{x}) \\ \exists k \in \{1, \dots, m\} : f_k(\mathbf{x}^*) &< f_k(\mathbf{x}) \end{aligned}$$

so that the dominating vector is at least as ‘good’ in all cost functions f_i and better in at least one. Now, a solution is said to be Pareto optimal if it is not dominated by any other solution. The set of solutions that are Pareto optimal is called the Pareto front. This Pareto front is typically represented in objective space, which is the space spanned by all possible values that the objective functions f_i can take.

Alternatively, a solution may be represented in solution space. The values of the decision vectors that give rise to the objective function values that span the Pareto front are said to be a Pareto optimal set. The mapping between the two is determined from Eq. (6.4). The shape that a Pareto front can take is very general, and it need not be convex, nor continuous (see Fig. 6.1). In fact, one of the downsides of using

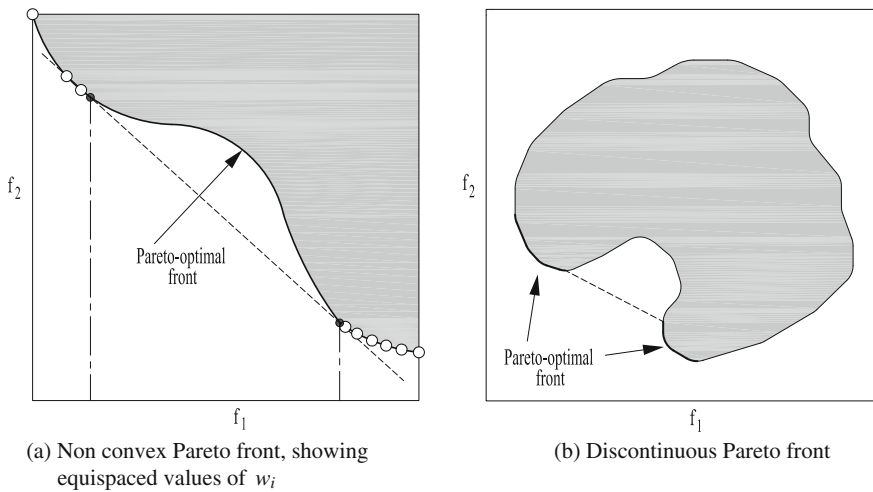


Fig. 6.1 Typical non-continuous Pareto fronts

the weighted sum method of Eq. (6.5) is that it is unable to represent the non-convex parts of a Pareto front by any choice of the weights (Deb 2005). This is illustrated in Fig. 6.1a, which shows such a Pareto front, as well as the points on it obtained when using the weighted sum method with equispaced values of w_i in Eq. (6.5).

6.2 Particle-Swarm Optimization

The choice of optimizer for a given problem can often include a significant amount of trial-and-error, as an optimizer that performs well for one type of problem may not be a good choice for a different type. The optimization method that is used in this study is the Particle Swarm Optimization (PSO) method, which is a direct method for solving global optimization problems, similar in general approach to genetic algorithms. Since it is not our goal here to perform a comparative analysis of different optimizers, we only discuss the PSO algorithm, as it provides robust results for the problem at hand. Other global optimizers include Genetic Algorithms (GA), and Differential Evolution (DE) algorithms (e.g., Wahde 2008; Deb 2000; Price et al. 2005). We provide an overview of the PSO method in Sect. 6.2.1, followed by a discussion of the manner in which constraints are handled in Sect. 6.2.2. Finally, we discuss the relevant aspects of extending the PSO algorithm to multi-objective problems in Sect. 6.2.3.

6.2.1 Method Overview

PSO is based on a model for the flocking behaviour of birds, where the behaviour is abstracted so that each bird now represents a ‘particle’ in the solution space. These particles are initialized randomly with a position \mathbf{x} and a velocity $\mathbf{v}(=\dot{\mathbf{x}})$. The method was first proposed by Kennedy and Eberhart (1995), where the basics of the method are discussed.

The particles that are initialized each represent a possible solution. After initialization, they are allowed to move around the search space at their current velocity, with their velocities being updated based on a social component and a personal (or cognitive) component. The personal component is included by letting each particle ‘remember’ what was the best location in the search space where it has been. The social component is included by allowing the different particles to communicate with one another, so that they can let each other know what has been their personal best. In this manner, each particle has a ‘personal best’ and a ‘group best’. The group best may be based on the entire swarm, a predetermined set of particles that communicate with one another or some neighborhood of each particle (Wahde 2008).

The personal and group best are used to update the velocity of each particle i from the j^{th} to the $(j + 1)^{th}$ iteration as follows:

$$\mathbf{v}_i^{j+1} = \omega \mathbf{v}_i^j + c_1 q \frac{\mathbf{x}_i^{pb,j} - \mathbf{x}_i^j}{\Delta t} + c_2 r \frac{\mathbf{x}_i^{gb,j} - \mathbf{x}_i^j}{\Delta t} \quad (6.6)$$

Here, the pb superscript represents the personal best and sb represents the global (or social) best, and Δt represents the ‘time’ difference between two iterations. q and r are both random numbers from $U(0, 1)$. The coefficients c_1 and c_2 are coefficients that indicate the influence of the personal and social bests, and are termed the self confidence and swarm confidence parameters, respectively. In a paper by Coello Coello et al. (2004) that describes a multi-objective PSO method (discussed below) these confidence parameters are omitted entirely, implicitly taking a value of 1.

A divergence of the solutions is possible if the velocity increases in such a fashion that the particles do not ‘settle’ near an optimum after a given number of iterations. There are several additional ways of avoiding such an occurrence, one of which is to impose a maximum velocity, v_{max} , on each velocity component (or on a norm of the velocity). Alternatively, the inertia weight $\omega(<1)$ in Eq. (6.6) may be used to prevent the velocity from diverging, which is the approach that we take here.

The parameters ω , c_1 and c_2 are not necessarily constant, since initially exploration of the solution space is more important than exploitation of current knowledge of the best solution. This concept of exploration vs. exploitation is common in optimizers such as PSO and GA, in that initially the search space should be explored to identify regions of higher performance. The greater the number of iterations, though, the greater the chance that the regions in which the global optimum could lie are properly identified. Having identified these regions, it is important to exploit this knowledge

by doing a more refined search of these regions. In PSO, this quality can be achieved by letting the values of ω , c_1 and c_2 vary as the number of iterations increases.

6.2.2 Handling of Constraints

Expanding the concepts of a PSO to problems involving constraints can be done in several manners. One typical method is the use of penalty functions, so that the objective function becomes less favorable when a constraint is violated. This will cause the evolution of the solutions to favor non-constraint-violating solutions. Mathematically, this can be done by modifying the (single) objective function as follows:

$$F(\mathbf{x}) = f(\mathbf{x}) + \sum_{j=1}^p R_j \langle g_j(\mathbf{x}) \rangle + \sum_{k=1}^q r_k |h_k| \quad (6.7)$$

where the $\langle a \rangle$ operator returns 0 if a is positive (constraint not violated) and $|a|$ if it is negative. The terms R_j and r_j denote the multipliers of the inequality constraints g_j and equality constraints h_j , respectively. This approach, however, has the obvious disadvantage of requiring a user-defined values of R_j and r_j .

Additionally, adding the penalty functions changes the objective function in such a manner that, depending on the magnitude of the penalty parameter, the optimum of $F(\mathbf{x})$ may not be close to the *true* constrained optimum of $f(\mathbf{x})$. That is, $F(\mathbf{x})$ might behave radically different from the true solution, showing local optima where none exist, clouding the physical interpretation of the solution. This is similar to the ambiguity that would be introduced by combining multiple objective functions into a single objective function through the use of Eq. (6.5).

An alternative method for constraint handling that avoids the need for user-defined parameters is the ‘feasible over infeasible’ method. It is based on the following three principles that are employed when ‘selecting’ what is the personal and global best:

- Solutions that do not violate any constraints (feasible solutions) are always favored over those that do violate constraint(s) (infeasible solutions).
- For comparing two feasible solutions, the solution with better objective function is favored (same as unconstrained case)
- For comparing two infeasible solutions, the solution with the least constraint violation is preferred

6.2.3 Multi-objective PSO

A number of approaches for modifying PSO to handle multi objective optimization problems are available. An overview of a number of approaches, as well as a short introduction to PSO in general, is given by Reyes-Sierra and Coello Coello (2006).

We use an algorithm that is a modification of the Multi Objective Particle Swarm Optimization (MOPSO) method described in Coello Coello et al. (2004), the Double Grid-MOPSO (DG-MOPSO) method presented, implemented and applied by Castellini (2012), Castellini and Lavagna (2012).

The MOPSO algorithm uses the same paradigm for optimization as the single-objective PSO described in Sect. 6.2.1. However, to include the concept of Pareto-optimality, the MOPSO method uses a so-called archive, which is a set of the Pareto-optimal solutions that have been found by the optimizer. The maximum size of the archive is set by the user, with new Pareto-optimal solutions replacing old ones.

To initialize the multi-objective algorithm, two additions to the PSO scheme are used. Firstly, the non-dominated initial solutions become the initial entries of the archive. Secondly, the explored objective space is divided into a number of n_S -dimensional boxes (or hypercubes in our specific case), which will be used to prevent crowding of the solutions, by limiting the number of solutions that are allowed to populate a given hypercube at any given iteration. Crowding is the phenomenon where one region in objective space contains a large number of the Pareto optimal solutions in archive, while other regions contain much less solutions in the archive. We stress that this does not mean that no true Pareto-optimal solution exist in these weakly explored regions, only that they have not been found by the optimizer. Crowding can be caused by premature convergence to one region of the objective space, or the fact that it may be easier to find solutions in a certain region. Other approaches to prevent crowding include the Tabu-search method described by Tan et al. (2003).

The optimization iterations are performed similarly to the one-dimensional PSO scheme, with the following modifications:

- Updating the velocity vector occurs using Eq. (6.6), but obviously some sort of modification is required for defining what constitutes the personal and global bests. The global best is a solution that is selected using the following selection scheme. Each hypercube that contains solutions in the repository is assigned a fitness value of x divided by the number of those solutions that it contains. The value of x may be chosen as any value > 1 , Coello Coello et al. (2004) use a value of 10. Following this, a roulette-wheel selection-procedure (discussed below) is employed to choose a hypercube from which to choose the leader. If more than one repository solution is in the selected hypercube, one is selected randomly. The personal best solution is chosen based on Pareto dominance, so that if the current solution dominates the current personal best solution, it replaces it. If the personal best dominated the current solution, no modification is made. In case neither of the two dominate the other, one is chosen randomly. In this fashion, the entire population's position and velocities are updated.
- If any solutions outside of the region of the objective space currently covered by the hypercubes are found, the grid is adapted so that it now covers the full range

of solutions that have been found. After each iteration, the repository is updated as follows. Any solution that has been found that is not dominated by a solution in the repository is added to it. If any solutions currently in the repository are dominated by this new solution, they are discarded. In case the repository reaches its maximum prescribed size, selection of the non-dominated solutions that are to be kept is performed, based on the amount solutions with which they share a hypercube. This last aspect prevents crowding of the solutions in the repository.

For roulette-wheel selection, the relative fitness functions of each individual j , defined as follows, are calculated:

$$\phi_j = \frac{\sum_{i=1}^j f_i}{\sum_{i=1}^n f_i} \quad (6.8)$$

A random number r is then taken from $U(0, 1)$ and the individual with the smallest j for which $\phi_j < r$ is chosen. In this manner, individuals with a higher fitness function will have a higher chance of being selected, as they ‘span’ (i.e., the interval $\phi_{j+1} - \phi_j$) a larger portion of the ‘roulette wheel’ than individuals with low fitness.

The MOPSO optimizer that has been described was can show very fast convergence, preventing it from finding the entire Pareto front, as the search space had not been fully explored before convergence. For this reason, a mutation operator can be applied to the problem. To stimulate initial exploration, the mutation operator should strongly promote exploration in the initial phase of the optimization, while its influence should reduce as the number of iterations increases.

The mutation is applied as follows. Each particle has a probability p_{mut} of being selected for mutation. If a particle i is selected for mutation, a mutation law is applied for each independent variable value $p_{i,j}$ of particle \mathbf{p}_i . A variable r_j is randomly taken from $U(0, 1)$ and a pre-defined variable η is used to mutate the values as:

$$p_{i,j,mut} = p_{i,j} + \delta_j (x_{j,max} - x_{j,min}) \quad (6.9)$$

$$\delta_j = \begin{cases} (2r_j)^{\frac{1}{1+\eta_{mut}}} - 1 & \text{if } r_j < 0.5 \\ 1 - (2(1-r_j))^{\frac{1}{1+\eta_{mut}}} & \text{if } r_j \geq 0.5 \end{cases} \quad (6.10)$$

As was mentioned before, it is possible and indeed advantageous to have the various parameters of the PSO algorithm vary as the number of iterations increases to change from exploration to exploitation of the solution space. This is implemented in the optimizer by letting the parameters vary linearly with the number of iterations. Since the number of iterations is set prior to the optimization initialization, this allows for a linear determination of the value of each parameter at a given iteration number. The values of these parameters, at the first and last iteration, are given in Table 6.1.

Table 6.1 Default settings for MOPSO algorithm used in simulations

Variable	Initial value	Final value
Inertia parameter ω	0.5	0.2
Self-confidence parameter c_1	1.7	1.0
Swarm-confidence parameter c_2	1.0	1.7
Mutation probability p_{mut}	0.5	0.1
Mutation distribution parameter η	0	5
Number of outer grid bisections $n_{gr,out}$	4	4
Number of inner grid bisections $n_{gr,in}$	1	1

6.3 Shape Optimization

This section will describe the specifics for the problem of shape optimization that is considered in this work. Specifically, the performance functions and constraints will be defined and explained in Sects. 6.3.1 and 6.3.2, respectively. The permissible constraint function values will be further evaluated in the Monte-Carlo analyses, which are discussed in Sects. 8.1 and 9.1 for the capsule and winged vehicle, respectively.

6.3.1 Performance Criteria

The choice of performance criteria is the main driver in steering the particles in the swarm during the optimization, since they determine what represents optimal behaviour. As this study represent a conceptual analysis, and not the full design of a specific vehicle, we define objectives that give a good indication of the general quality of a re-entry vehicle.

The function of an entry vehicle is to safely bring a cargo from a (super-)orbital velocity to a subsonic/supersonic velocity inside the atmosphere of a Solar System body (in our case Earth). Depending on the type of vehicle, such vehicles may be reused or purpose-built for a single entry. Capsule-shaped entry vehicles are typically not re-used and the entry capability is used for sample return or astronaut transport. For this reason, it is advantageous to maximize the useful volume of such a capsule. A measure for the quality of a capsule in this respect is the volumetric efficiency, which is defined as follows, (e.g., Theisinger and Braun 2009):

$$\eta_V = 6\sqrt{\pi} \frac{V}{S^{3/2}} \quad (6.11)$$

This quantity is a measure for the structural mass fraction that is required for a certain aeroshell volume. It is a scaled ratio of volume and surface area, so maximizing η_V amounts to minimizing the surface area for a certain internal volume. The value is

normalized in such a manner that $\eta_V = 1$ for a sphere, which is its maximum possible value. For the capsule-shape vehicles, we use the volumetric efficiency as one of the objectives.

In the development of space vehicles, mass is always an important design driver, since the mass strongly drives the launch cost. Especially for winged entry vehicles, where additional structural mass is required for the lifting surfaces and its TPS, vehicle masses can increase in such a manner that it makes the project economically infeasible. For the winged vehicle, we use a bottom-up model for the mass of a given shape, where the design parameters are used to determine the mass based on empirical relations, as detailed in Sect. 5.2.4.

Since the mass is used as an objective function for the winged vehicle, considering the volumetric efficiency as an objective for the winged vehicle in addition to the mass produces an ‘overlap’ in the objective functions. Instead, the fuselage volume of the winged vehicle will be optimized directly. The volume of the fuselage is a measure for the amount of payload that the vehicle can take into orbit, as well as the flexibility regarding the addition of internal systems, such as a propulsion system. By considering both the mass and volume directly, the cost of the mission, in part driven by the mass and the potential benefit in terms of economic or scientific return, can be more directly assessed.

For the capsule, mass optimization is partially included in the volumetric efficiency objective, as opposed to the case of the winged vehicle. This is in contrast to the winged vehicle, where the wing mass or shape would hardly be included in the determination of η_V , making the use of η_V less suitable for winged vehicles.

To include the vehicle mass in the capsule optimization, we note that a strong driver for the total mass is the total mass of the TPS. Although empirical correlations for the TPS mass based on the total heat load Q exist, their use would require an iterative process when determining the trajectories. This is because m is required as input to the trajectory propagation, which in turn produces the value of Q , from which the value of m_{TPS} can then be determined. Taking such an approach would greatly increase the computational effort of the problem at hand, making it undesirable for our conceptual analysis.

For this reason, the TPS mass of the capsule will be indirectly included in the optimization by using the stagnation-point heat load Q_s as an objective function. The heat flux and heat load over the majority of the region containing a thick TPS are typically strongly related to the heat flux and load at the stagnation point, so that a high value of Q_s indicates a high value of m_{TPS} . Although the corner heating is also of influence on the total TPS mass (see Sect. 3.4.2), the area of this region is relatively small compared to the nose region. Additionally, the heating along the toroidal segment that constitutes the corner is relatively low over the majority of the azimuthal angle, further limiting the required TPS mass due to corner heating. For these reasons, we only consider the stagnation point heat load as a minimization objective.

A third objective function for both the winged vehicle and the capsule stems from the flexibility of an entry vehicle in performing an entry. For fully ballistic, uncontrolled vehicles, the entire trajectory is fully defined from the initial conditions. For

a controlled vehicle, the aerodynamic characteristics of the vehicle may be modified to influence the trajectory that the vehicle will take. By doing so, the TAEM interface location can be varied, allowing a greater variety in the landing sites that can be reached from a given entry point. Thus, unforeseen circumstances in orbit insertion or de-orbiting can be mitigated. Also, the mission profiles that can be flown are automatically increased by having a greater possible range. Although targeting of a TAEM interface is not included in this study, measuring this flexibility is done by optimizing the ground track length s_g .

Summarizing, the objective functions for the capsule-shaped vehicle are:

- Stagnation-point heat load Q_s
- Volumetric efficiency η_V
- Ground track length s_g

For the winged vehicle, the objective functions are:

- Total vehicle mass at entry m_e
- Fuselage volume V_{fus}
- Ground track length s_g

An alternative third objective function will be considered in addition to the ground track length for the winged vehicle. The guidance scheme that is used to determine the commanded angle of attack (Sect. 2.3.2) was previously used for an experimental vehicle gathering measurement data at a constant heat rate (Mooij and Hänninen 2009). The amount of data that can be gathered increases with the amount of time flown at this reference heat rate. For this reason, the optimization when considering time at reference heat rate $t_{q_{ref}}$ instead of total ground track length s_g will also be performed. By doing so, the vehicle's mission is in essence changed from a generic re-entry vehicle to a specific mission to gather data related to thermophysical effects that occur at high heat rates.

6.3.2 Constraints

For the vehicle to safely re-enter the atmosphere, a number of conditions need to be met. In the optimization, these conditions are quantified in the form of constraints. Two constraints that will be used for both winged and capsule-shaped vehicles are the following, which are typical in the analysis and optimization of an entry vehicle:

- Maximum stagnation-point heat flux q_s , determined from Eq. (3.77), so:

$$\left(\max_{t_i} q_s \right) \leq q_{s,max} \quad (6.12)$$

That is, the maximum value of q_s from all time steps t_i should be smaller than $q_{s,max}$

- Maximum load factor n_{tot} , which is the maximum total aerodynamic deceleration experienced by the vehicle, determined from the following equation (assuming the vehicle side force to be zero; Sect. 3.2):

$$n_{tot} = \frac{\sqrt{D^2 + L^2}}{mg} \quad (6.13)$$

$$= \frac{q_{dyn}B}{g} \sqrt{1 + \left(\frac{L}{D}\right)^2} \quad (6.14)$$

Using this, the constraint equation is formulated as follows:

$$\left(\max_{t_i} n_{tot} \right) \leq n_{tot,max} \quad (6.15)$$

The aerodynamic coefficients vary only marginally over the trajectory for a capsule (see Sect. 7.2.2). This, along with the form of Eq. (6.14), leads to the fact that the point of maximum load factor will be very close to the point of maximum dynamic pressure q_{dyn} . For this reason, considering the q_{dyn} -constraint separately for capsule-shaped vehicles is unnecessary. For winged vehicles, however, the aerodynamic coefficients vary much more due to the greater range of α at which the vehicle flies, as well as the changing values of the control-surface deflection δ_{bf} and δ_e . This means that the load factor and dynamic pressure are not nearly as closely related. Additionally, the dynamic pressure becomes more important as a separate entity due to the presence of the control surface, the hinge moments of which are strongly dependent on the dynamic pressure. This constraint is expressed as:

$$\left(\max_{t_i} q_{dyn} \right) \leq q_{dyn,max} \quad (6.16)$$

Specific to the capsule vehicle is the constraint on the location of the stagnation-point. As discussed in Sect. 3.4.2, having the stagnation-point lie on the vehicle shoulder will increase the maximum heat transfer substantially. The Newtonian approximation will give a stagnation-point location that is more in the direction of the shoulder than the true stagnation-point. For this reason, a constraint requiring the stagnation-point location to always lie on the nose region of the capsule is imposed. This is reinforced by the information given by Crowder and Moote (1969), and Robinson and Wurster (2009). The constrained is expressed as follows:

$$\left(\max_{t_i} \Delta\theta_s \right) \leq 0 \quad (6.17)$$

where $\Delta\theta_s$ denotes the angular difference between the stagnation-point location and the angular position of the transition from spherical to toroidal section, so (see Fig. 5.3):

$$\Delta\theta_s = \theta_s - \theta_{sp1,max} \quad (6.18)$$

Related to this constraint on the capsule shape is a constraint on the maximum heat flux in the corner region. An empirical relation for this quantity was derived in Sect. 3.4.2. The magnitude of this heat flux is a factor >1 of the stagnation-point heat flux, so that it is likely that the TPS type or layout at this location will be different and a higher heat flux can be withstood. Consequently, the constraint on the value of $q_{cor,max}$ will be different from $q_{s,max}$. It is expressed as:

$$\left(\max_{t_i} q_{cor} \right) \leq q_{cor,max} \quad (6.19)$$

Similarly, the winged vehicle has an important heating consideration in addition to the stagnation-point heating, namely the leading edge heating, as was discussed in Sect. 3.4.1. In the same manner as the other heating constraints, it is formulated as:

$$\left(\max_{t_i} q_{LE} \right) \leq q_{LE,max} \quad (6.20)$$

The product of dynamic pressure and angle of attack is a first-order measure for the bending moment that is exerted on the vehicle. The bending load constraint will be extended to be generalized for vehicles of varying shapes, namely by taking into account the length of the vehicle. This choice follows from the fact that a longer vehicle with equal forces exerted on it will, all other things being equal, experience a large bending moment, linearly related to the length (which in our study is a variable quantity). The following will be used to limit the bending moments on winged vehicles:

$$\left(\max_{t_i} \left(q_{dyn} \cdot \alpha \frac{L}{L_{ref}} \right) \right) \leq (q_{dyn} \cdot \alpha)_{max} \quad (6.21)$$

where the maximum allowable value of $q_{dyn}\alpha$ is referenced to a given vehicle length. The value of L_{ref} will be taken at 25 m, the length of the HORUS vehicle.

In addition to constraints arising from loads on the vehicle, a number of criteria regarding stability and controllability must be satisfied. For the control schemes employed in the simulations here (Sect. 2.3.3), controllability can be measured by trimmability. Specifically: is the vehicle capable of achieving a trimmed state within the given control bounds. For the capsule-shaped vehicle, this means that:

$$(\forall t_i : \exists |\alpha_{tr}| \leq \theta_N) \quad (6.22)$$

That is, α_{tr} (which is passively achieved) should be such that the value of $\Delta\theta_s$ remains within the constraint set by Eq. (6.17). However, these two constraints will produce the same results when using the Newtonian streamline approximation, so that only a single one needs to be considered.

For the winged vehicle, the controllability amounts to:

$$(\forall t_i : (\exists (\delta_e, \delta_{bf}) : C_m = 0)) \quad (6.23)$$

For an analysis of the stability of the vehicle, the values of a number of stability derivatives will be analyzed. These matters were discussed in Sect. 2.2.3. The derivatives C_{m_α} , C_{l_β} and C_{n_β} are considered.

For a capsule-shaped vehicle, though, the rotational symmetry means that a change in angle of attack and a change in angle of sideslip have similar effects on the vehicle. Since the aerodynamic characteristics of the capsule are the same for any given total angle of attack, regardless of the separate contributions of the angles of sideslip and attack, C_{m_α} and C_{n_β} need not be analyzed separately. In addition, due to this symmetry, the value of C_l in the total angle of attack reference system will always be zero, so that no analysis of this value is required. Due to the limited control capability of capsule-shaped vehicles, it is required that:

$$(\forall t_i : C_{m_\alpha} < 0) \quad (6.24)$$

For winged vehicles, though, the shape is not axisymmetric, so that the above simplifications cannot be applied for the stability analysis and all three stability derivatives will be considered separately. For the pitch-moment derivative, it is typically required that Eq. (6.24) holds. However, it is noted by Hirschel and Weiland (2009) that this is not the case for most winged re-entry vehicles in the hypersonic regime at moderate ($< 20^\circ - 25^\circ$) angles-of-attack, where the GNC system is used to actively stabilize the vehicle. In line with the characteristics of previous winged entry vehicles, the following is enforced:

$$(\forall t_i : \text{If } \alpha_i > 25^\circ : C_{m_\alpha} < 0) \quad (6.25)$$

For the lateral stability derivatives, literature values of the Space Shuttle (Rockwell International 1980) and HORUS (MBB-Space 1988) indicate that both C_{l_β} and C_{n_β} are negative, so that a disturbance in β will cause moments correcting the disturbance. Also, these constraints are used in the shape-optimization effort described by Johnson et al. (2007). As such, the following constraints are imposed:

$$(\forall t_i : C_{l_\beta} < 0) \quad (6.26)$$

$$(\forall t_i : C_{n_\beta} < 0) \quad (6.27)$$

The above is a conservative approach in the design of the vehicle. If the Monte-Carlo simulation shows them to be very restricting, modifications of these criteria could be considered.

As a final constraint for the capsule shape, the length of the vehicle will be limited. Due to the manner in which it is parametrized, a small absolute value of θ_c and a large value of L_c can lead to very large total vehicle lengths. This is due to the fact

that the radius of the rear spherical cap will become very large. The length of the capsule will be limited, so, using Eq. (5.13), the length of a capsule is determined and the following constraint is imposed:

$$L < L_{max} \quad (6.28)$$

Summarizing, the following constraints are used for the capsule-shaped vehicle:

- Maximum stagnation-point heat flux.
- Maximum corner heat flux.
- Maximum load factor.
- Stagnation-point location/trim angle of attack.
- Pitch stability.
- Total vehicle length.

For the winged vehicle, the following constraints are used:

- Maximum stagnation-point heat flux.
- Maximum leading-edge heat flux.
- Maximum load factor.
- Maximum dynamic pressure.
- Length-weighted dynamic-pressure angle-of-attack product.
- Trimmability.
- Static pitch stability for $\alpha > 25^\circ$.
- Static roll stability.
- Static yaw stability.

In addition to these indirect constraints, explicit constraints on the minimum and maximum allowable values of the shape parameters are directly imposed. For the capsule and winged-vehicle shapes, these constraints are summarized in Tables 5.1 and 5.2, respectively.

Chapter 7

Simulator Design

This chapter will describe how the methods discussed in the previous chapters are implemented and tested. First, the layout of the simulation software will be discussed in Sect. 7.1. Subsequently, we discuss the verification and validation of the simulation code in Sect. 7.2, based on literature data for the Apollo and Space Shuttle vehicle shapes. Finally, the various settings of the simulation and optimization code are discussed and the rationale behind the selection of the values is given in Sect. 7.3.

7.1 Simulation Code

This section will give a breakdown of the implementation of simulation code that is required for the problem at hand. The process by which the theoretical considerations presented in the previous chapters have been put together to analyze the aerodynamics of a vehicle, propagate its trajectory and evaluate its quality, will be described. A single analysis of a vehicle shape performance (i.e, mapping a single set of shape parameters to objective and constraint functions) is termed a function evaluation. This function evaluation is performed sequentially during the Monte Carlo analyses (Sects. 8.1 and 9.1) and optimization (Sects. 8.2 and 9.2) that are described in subsequent chapters. The top-level flow of the function evaluation is shown in Fig. 7.1.

Although the code architecture used for the capsule and winged vehicles is largely the same, there are differences in the options that are used in the two cases (shadowing, control-surface deflections, mass estimation method, etc.). For this reason, the internal workings of the separate blocks shown in Fig. 7.1 will be discussed separately where necessary. In flow diagrams that follow, red will indicate action taken or information passed only in the case of the winged vehicle, with green indicating this for the capsule shapes vehicle.

Figures 7.2 and 7.3 show the generation of the geometries. Both receive the minimum and maximum allowable values of the shape parameters and the associated parameters r_x (see Chap. 5; Eq. (5.1)). The mathematical models that are used to

Fig. 7.1 Top-level flow for evaluation of a vehicle shape

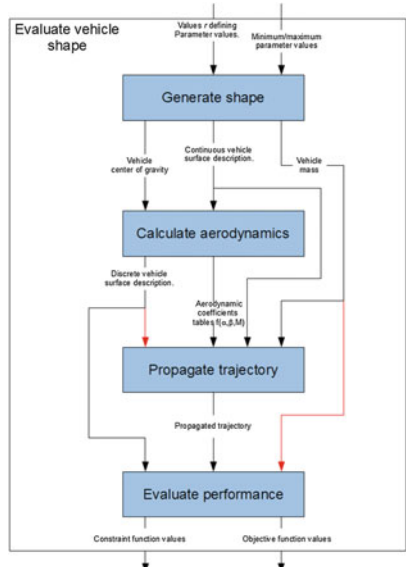
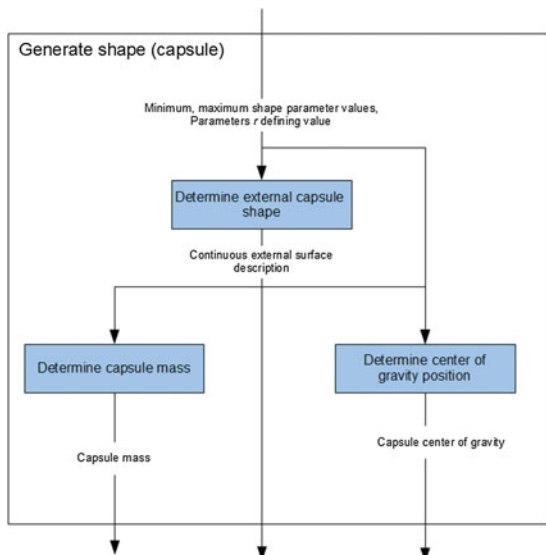


Fig. 7.2 Top-level flow for generation of capsule shape



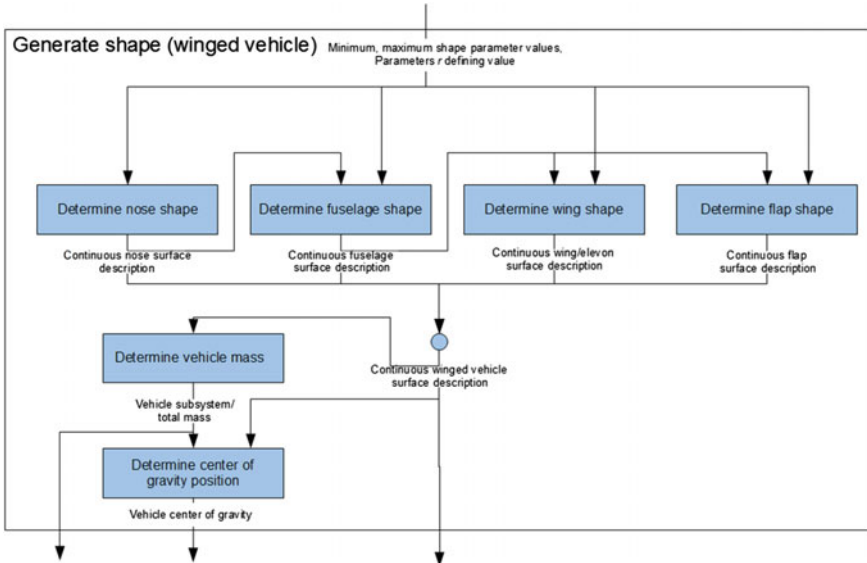
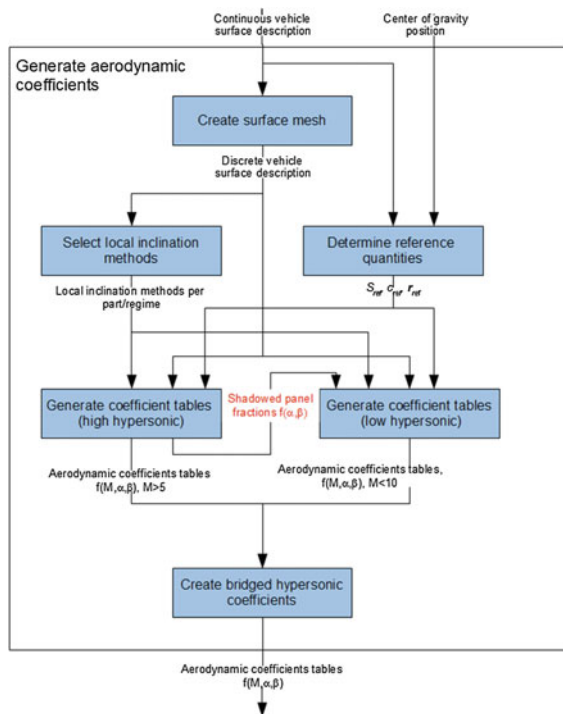


Fig. 7.3 Top-level flow for generation of winged vehicle shape

generate the capsule and winged vehicle are discussed in Sects. 5.1 and 5.2, respectively. Having generated the vehicle's shape, its aerodynamic characteristics are generated. The top-level flow of this is shown in Fig. 7.4. Prior to the generation of the coefficients, the continuous surface description is discretized by a set of panels, as described in Sect. 5.3. From this discretized surface, the aerodynamic methods are selected, as discussed in Sect. 3.3.2. Additionally, the vehicle's aerodynamic reference quantities (c_{ref} , S_{ref} and \mathbf{r}_{ref}) are determined directly from the undiscretized vehicle description. The moment reference point is chosen to equal the center of mass, which is assumed constant during entry. For both the winged and capsule-shaped vehicles, the reference length is chosen as the total vehicle length. The reference area S_{ref} of the capsule is chosen as the circle with radius R_m , and the wing-planform area continued through the fuselage in the case of the winged shape.

Having determined the reference quantities and aerodynamic methods, two databases are generated, a low and high hypersonic database. In the case of the winged vehicle, where shadowing is used, the shadowed panel fractions are passed from the high hypersonic generator, which is called first, to the low hypersonic generator. This is done to save computation time, since the shadowed fractions are independent of Mach number. Having generated the low- and high-hypersonic coefficients, the results are merged by the method described in Sect. 3.2. This yields the final database of aerodynamic coefficients, including control increments for the winged vehicle shape, as a function of Mach number M , angle of attack α and angle of sideslip β , which is included for the numerical computation of the static stability derivatives in Eqs. (2.50) and (2.51).

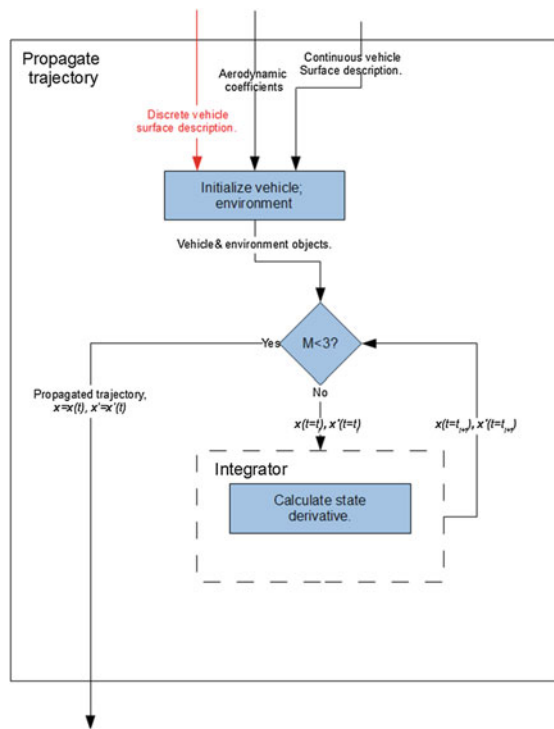
Fig. 7.4 Top-level flow of aerodynamic coefficient generation



Following the generation of the aerodynamic coefficients, the vehicle's trajectory can be simulated. The top-level flow of this process is given in Fig. 7.5. The first step is the initialization of the objects and variables that are used in the trajectory propagation. In addition to the vehicle geometry and aerodynamics, which were created in the previous steps, the following elements are initialized:

- Environment, consisting of:
 - Atmosphere model
 - Gravity model
 - Central body shape model
- Guidance Navigation and Control (GNC) System, consisting of:
 - Navigation system
 - Guidance system
 - Control system (winged vehicle only)
- Additional vehicle subsystems:
 - Control surfaces (winged vehicle only)
 - Thermal Protection System (performs heat-flux analyses)
- Vehicle initial conditions

Fig. 7.5 Top-level flow of trajectory propagation



The implementations used for the Guidance Navigation and Control subsystems in this work are all ‘ideal’. This means that the Navigation system, which is to determine the vehicle’s state, determines the vehicle state exactly. For the guidance system, ideal means that the commanded vehicle attitude is assumed to be attained exactly and immediately, if permissible given the angle-rate constraints (see Sect. 2.3.3). More details on the guidance schemes for the two types of vehicle are given in Sect. 2.3. The capsule-shaped vehicle employs ideal control, as described in that section, in that the angle of attack is assumed to always equal the trimmed state of the vehicle. The exact means by which the bank angle is modulated is neglected. For the winged vehicle, control-surface deflections are computed such that trim the vehicle at the commanded angle of attack. Again, ideal control is used, indicating that the control surfaces can exactly achieve the required deflection.

The state vector used during trajectory propagation is different for the winged and capsule-shaped vehicles, since the stagnation-point heat load is used as an objective for the capsule, but not the winged vehicle. Since the heat load is obtained by integration of the heat flux, it is included in the state vector. The ground-track length is also included in the state. This leads to the following state vectors for the winged and capsule-shaped vehicles:

$$\mathbf{x}_{capsule} = \begin{pmatrix} x_I \\ y_I \\ z_I \\ \dot{x}_I \\ \dot{y}_I \\ \dot{z}_I \\ Q_s \\ s_g \end{pmatrix} \quad \mathbf{x}_{winged} = \begin{pmatrix} x_I \\ y_I \\ z_I \\ \dot{x}_I \\ \dot{y}_I \\ \dot{z}_I \\ s_g \end{pmatrix} \quad (7.1)$$

Note that stagnation point heat load is not integrated as a state vector for the winged vehicle, only because it is not directly considered as a constraint or objective. Consequently, the state derivatives, the calculation of which is shown in Fig. 7.6, are the following for the two types of shapes:

$$\dot{\mathbf{x}}_{capsule} = \begin{pmatrix} \dot{x}_I \\ \dot{y}_I \\ \dot{z}_I \\ \frac{F_{g,I,x} + F_{a,I,x}}{m} \\ \frac{F_{g,I,y} + F_{a,I,y}}{m} \\ \frac{F_{g,I,z} + F_{a,I,z}}{m} \\ q_s \\ V_R \cos \gamma \left(\frac{R}{h+R} \right) \end{pmatrix} \quad \dot{\mathbf{x}}_{winged} = \begin{pmatrix} \dot{x}_I \\ \dot{y}_I \\ \dot{z}_I \\ \frac{F_{g,I,x} + F_{a,I,x}}{m} \\ \frac{F_{g,I,y} + F_{a,I,y}}{m} \\ \frac{F_{g,I,z} + F_{a,I,z}}{m} \\ V_R \cos \gamma \left(\frac{R}{h+R} \right) \end{pmatrix} \quad (7.2)$$

When requesting aerodynamic coefficients at values of α , β and M , the coefficients are determined from the database using multilinear interpolation. The maximum angle of attack is known before trajectory propagation due to the imposition of an ideal guidance system and the angle of sideslip is constrained to zero for all cases. This means that it is not possible for the angles of attack or sideslip to be outside the range of the database points. The lower bound of the Mach number is also known, as this defines the end of the propagation. For high Mach numbers, it is possible that the Mach number exceeds the maximum value in the database. However, due to the Mach number independence principle, taking the value of the coefficients at the maximum value of M in the database is permissible.

7.2 Model Validation

This section will present the validation of the aerodynamics code, as well as an assessment of the effect on the performance and constraint values of the trajectories. The Apollo capsule and the Space Shuttle are used for this purpose, as they represent typical vehicle shapes of the two classes of vehicles that are to be considered in the optimizations. Extensive theoretical and experimental work has been performed for

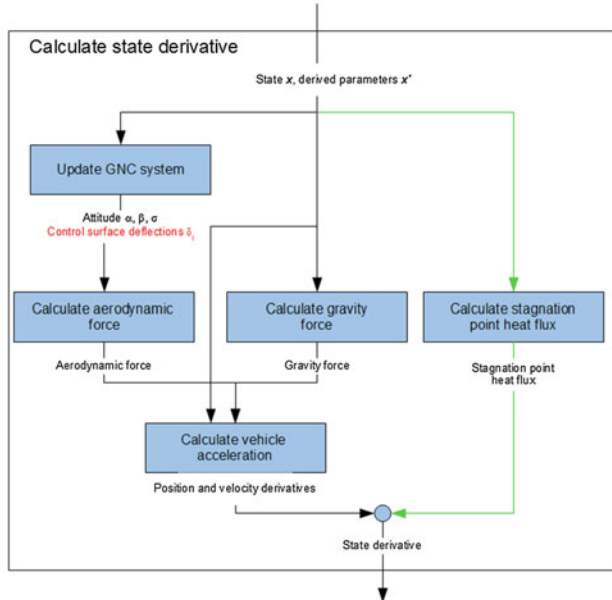


Fig. 7.6 Top-level flow of state derivative calculation

these vehicles by, among others, Underwood and Cooke (1982), Rockwell International (1980), Maus et al. (1983), North American Aviation (1965), Hillje (1969), Lee and Goodrich (1972), Crowder and Moote (1969), Lee (1972), and Dirkx and Mooij (2011).

7.2.1 Aerodynamics

The largest degree of physical-model simplification in the optimization is in the aerodynamic model (Chap. 3). Any inaccuracies in the mathematical model will influence the location of the Pareto-optimal solution in both decision and solution space. Therefore, the general magnitude of the errors must be ascertained to be able to make a judgment on the fidelity of the optima that are found. In this section, the aerodynamic coefficients produced by the methods described in Sect. 3.3.2 are compared to available aerodynamic databases and the influence on the discrepancies is analyzed.

Apollo

The geometry of the Apollo capsule has been modeled with the parametrization given in Sect. 5.1, with the shape parameters from Hirschel and Weiland (2009):

$$R_N = 4.694 \text{ m}, R_m = 1.956 \text{ m}, R_S = 0.196 \text{ m}, \theta_c = 33^\circ, L_c = 2.662 \text{ m}$$

Aerodynamic coefficients were then generated and compared to the data from wind-tunnel testing given by North American Aviation (1965). The relevant reference quantities are:

$$S_{ref} = 39.441 \text{ m}^2, c_{ref} = 3.9116 \text{ m}, \mathbf{r}_{com} = (1.0367, 0, 0.1369) \text{ m}$$

where the axes are defined as in Sect. 5.1.

Figure 7.7a and b show the drag and lift coefficients of the Apollo capsule that we generate compared to the wind-tunnel results. Clearly, the results coincide quite well with the wind-tunnel data. The most important difference between the two is the over-prediction at $M = 10$. At this Mach number the contribution of the expansion pressure coefficient is very small, as the vacuum pressure coefficient is very close to zero. Consequently, the results are almost fully defined by the compression pressure distribution. From Fig. 3.6, it can be seen that the Modified Newtonian method gives the lowest value of the pressure coefficient at a given inclination angle of the methods used. Since this method is used on all compression surfaces at $M = 10$ and still produces an axial force that is too high, this indicates that no suitable local inclination method exists that can produce sufficiently low results here. This is likely due to the fact that the streamlines pass through a shock wave at an angle somewhat lower than 90° . This results in a lower stagnation pressure coefficient, which will in turn result in a lower pressure coefficient from Eq. (3.53), as discussed in Sect. 3.3.1.

The pitch moment coefficient for the Apollo capsule is shown in Fig. 7.7c, where it can be seen that the results coincide very well with the wind-tunnel data. For us, it is important that the trimmed α and consequent L/D are well predicted. From the figure, it can be seen that the value of α_{trim} is off by about 1° for $M_\infty = 10$ and 0.1° for $M_\infty = 3$. The resulting errors in L/D , which are due to errors in both force and moment coefficients are $\sim 10\%$ in both cases. These discrepancies are well acceptable for a conceptual-design effort. Their influence on the trajectories of the capsule will be discussed in Sect. 7.2.2.

A comparison between the streamlines that are obtained from the Newtonian approximation and the results of an Euler (inviscid) solution are shown by Bohachevsky and Matos (1965), where significant differences between the two are observed. Despite the fact that there is a significant difference in the shape of the streamline pattern, most notably in the curvature of the streamlines, the effect on the force and moment coefficients is minimal for the case shown here. However, if the streamline pattern that follows from the pressure distribution calculated here would be used for the determination of viscous effects, the boundary-layer thickness and the flow velocity component derivatives would show more significant discrepancies to actual values. This is an indication of the fact that, although the method here is quite accurate for inviscid calculations, extending the method to viscous analysis would require critical evaluation of the underlying inviscid calculations.

A discrepancy between the wind-tunnel data obtained for Apollo pre-flight and the actual in-flight coefficients is shown by Crowder and Moote (1969) and discussed by

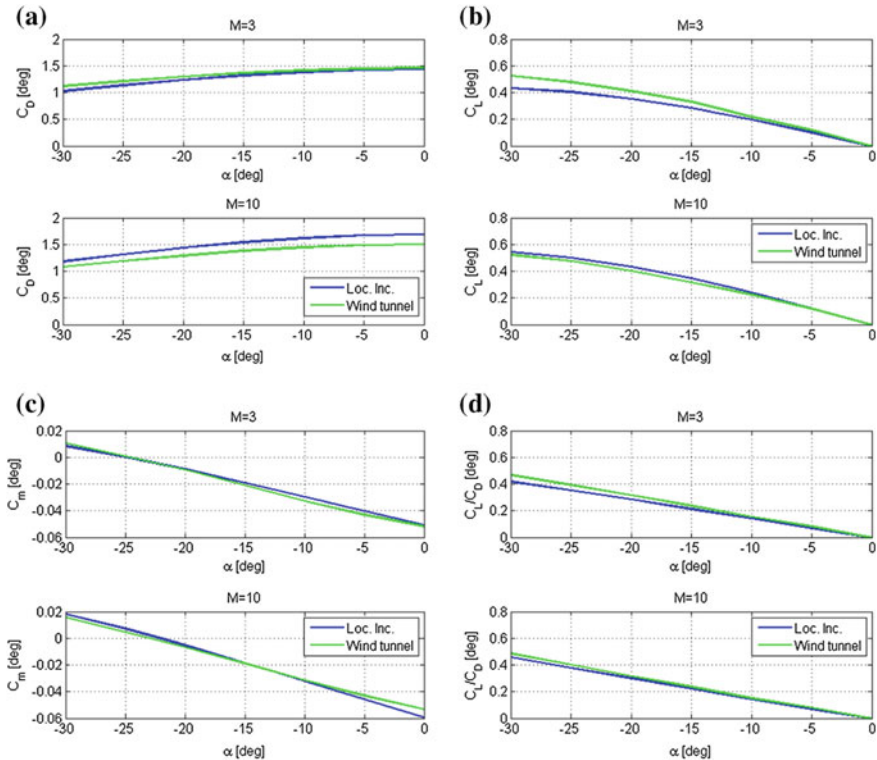


Fig. 7.7 Aerodynamic coefficients for Apollo command capsule. **a** Drag coefficient, **b** Lift coefficient. **c** Moment coefficients and **d** Lift over Drag

Schneider (2006). A difference of $\sim 15\%$ is observed at Mach 36, which is postulated to be caused by real-gas effects, since the effect appears to scale with freestream velocity instead of Reynolds or Mach number. The Mach numbers that are expected to occur in the entries from LEO, which will be considered here, have a maximum of 25–30. As a result, real gas effects are not expected to have significant effects on the aerodynamic forces and moments.

Space Shuttle

Aerodynamic coefficients of the Space Shuttle have been generated using the methodology outlined in Sect. 3.3. Here, we show the comparison with coefficients obtained from wind-tunnel data documented in (Rockwell International 1980). Although these data are known to contain some discrepancies when compared to flight data, they comprise a comprehensive and consistent set of data that can be used to compare the coefficients generated here at more data points than could be done using only flight data. The reference quantities of the coefficients are:

$$S_{ref} = 249.9092.441 \text{ m}^2, c_{ref} = 12.0579 \text{ m}, \mathbf{r}_{com} = (21.356, 0, 0.8224) \text{ m}$$

with the Orbiter nose as origin, positive x -direction rearwards and positive z -direction upwards.

The analysis is performed using the default method selection criteria given in Sect. 3.3.2. When comparing the lift and drag coefficients from Fig. 7.8, it can be seen that this method predicts these coefficients quite well. In addition, for low Mach numbers where a non-Newtonian method is used as the compression method, the accuracy of the method selection yields results that are superior to a modified Newtonian approach. The effect of shadowing on the longitudinal force coefficients is minimal, however.

The moment coefficients differ more strongly from the database values, though, as shown in Fig. 7.9b. However, there is a known discrepancy between the wind-tunnel data and flight data, consistently giving underpredicted values of the moment coefficients at high Mach numbers (Maus et al. 1983). The difference between the flight and wind-tunnel coefficients are shown here in Fig. 7.9b. Since the results produced in the present study show an over-prediction of the coefficients at $\alpha > 20^\circ$, they likely approximate the actual coefficients more closely than can be seen from the figures here.

The effect of shadowing is more noticeable for the moment coefficients than the longitudinal force coefficients. For high Mach numbers, it seems to cause the moment curve to better approximate the flight-measured curve. The pitch moment at high angle of attack and low Mach numbers is adversely affected the most strongly by the shadowing. However, since the vehicle considered here will not fly at this combination of variables, this error will not propagate to a difference in trajectory results.

The stability derivatives of the lateral coefficients for small sideslip angles, which are important in the analysis of the vehicle stability during re-entry, can be seen in Fig. 7.10. Here, the effect of the shadowing is very clear in the case of the side force and yaw moment. They cause the overall trend of the coefficients to be followed quite

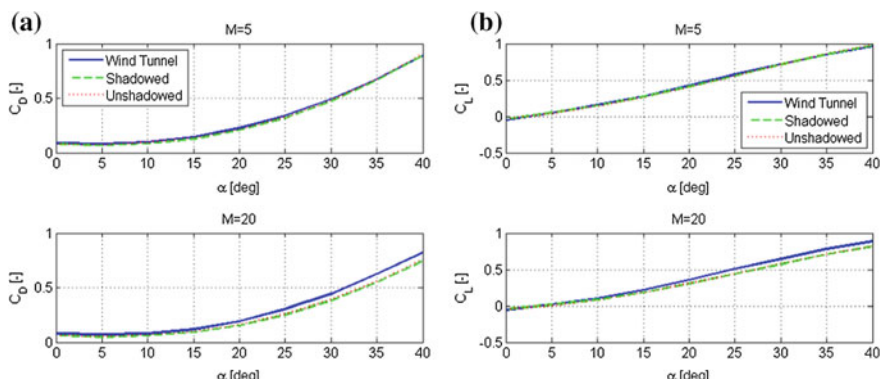


Fig. 7.8 Lift and drag coefficients produced for the Space Shuttle with and without shadowing compared to wind-tunnel data

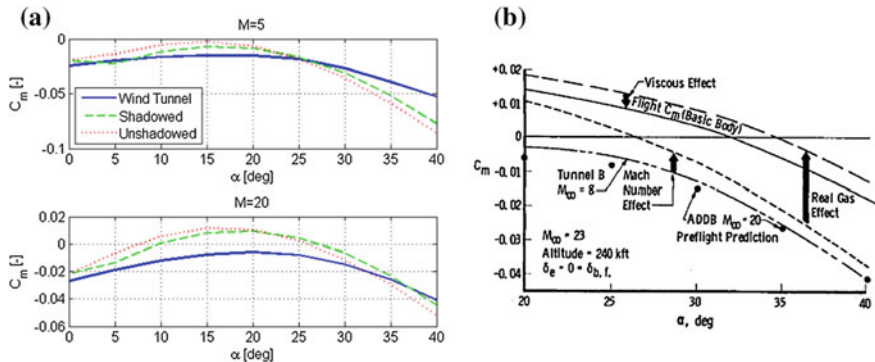


Fig. 7.9 Moment coefficients for the Space Shuttle. **a** Results generated here with and without shadowing compared to wind-tunnel data and **b** Wind-tunnel data compared to flight data (Maus et al. 1983)

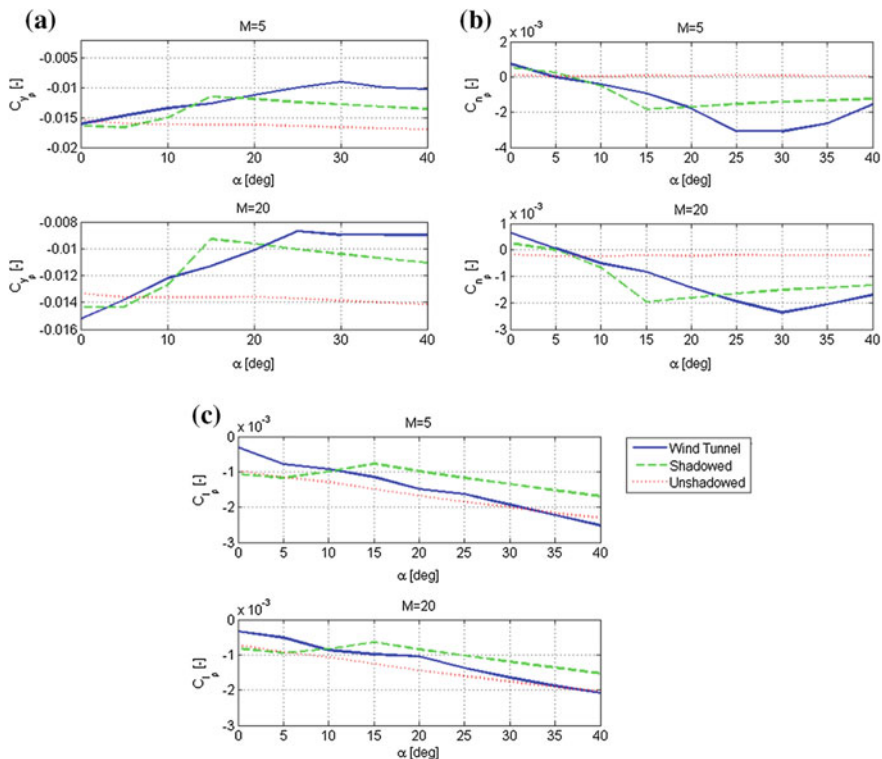


Fig. 7.10 Stability derivatives produced for the Space Shuttle with and without shadowing compared to wind-tunnel data

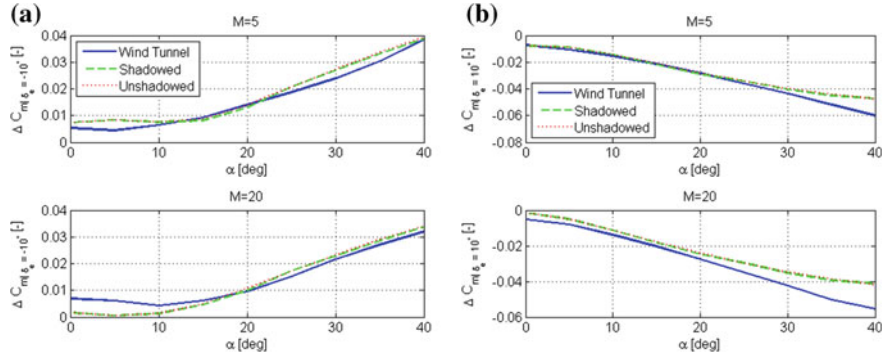


Fig. 7.11 Elevon moment increments produced for the Space Shuttle compared to wind-tunnel data

well, as opposed to the case without shadowing, where no such trend can be observed. In the case of the roll moment derivative shown in Fig. 7.10c, the influence of the shadowing is not quite as clearly positive, causing the coefficients to be somewhat underpredicted instead of overpredicted in most cases. This will, however, result in a more conservative estimate of the vehicle stability.

For the control increments, proper prediction of the pitch moment increments are the primary objective for this study, since these values determine the deflection of the control surfaces required to trim the vehicle. The resulting lift and drag increments can be $\sim 10\%$ of the total lift and drag and should not be neglected. The control derivatives shown in Figs. 7.11, 7.12 and 7.13 indicate that the predictions for the elevon increments are reasonably good, with lift increments having the lowest accuracy, showing differences of up to about 0.01.

The body flap increments shown in Figs. 7.14, 7.15 and 7.16 show greater discrepancies, however, for positive deflections. This can be caused by a number of factors. Firstly, for low deflection angles, the body flap will be fully engulfed in the fuselage boundary layer, reducing the body flap effectiveness. For higher deflection angles, the compression shock that will occur on the ramp between the fuselage and shock wave will cause an increase in surface pressure on the body flap. This effect is not observed as strongly on the elevon, where a similar ramp effect is expected to occur. Due to the smaller size of the wings, the boundary layer will be less thick on the elevons, reducing its effect on the control increments. Since a positive body-flap deflection is required for Space-Shuttle trim, these errors in the moment increment prediction will result in an over-prediction of the required body flap deflection. The effect on the performance of the Shuttle will be discussed in the next section.

Concluding, it can be said that the longitudinal force coefficients show excellent agreement with wind-tunnel data. The pitch moment coefficients are reasonably well predicted, but show substantial discrepancies in some regions. To properly predict the side force and yaw moment coefficients, using shadowing is necessary, although this slightly decreases the accuracy of the yaw-moment coefficients. Elevon

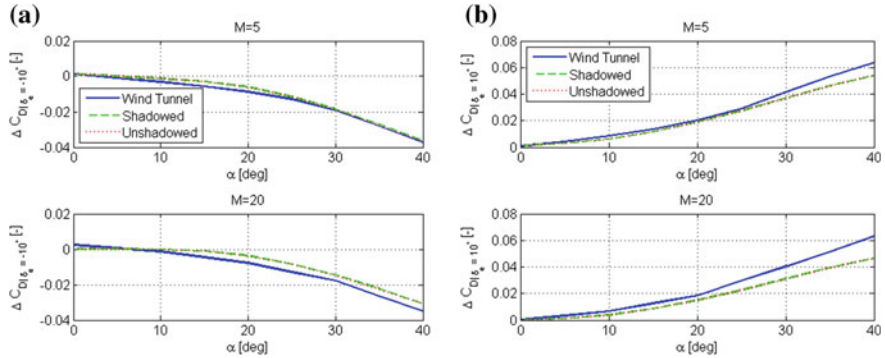


Fig. 7.12 Elevon drag increments produced for the Space Shuttle compared to wind-tunnel data

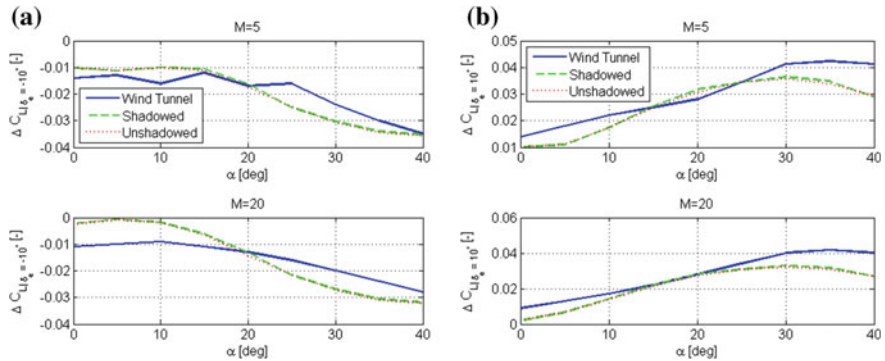


Fig. 7.13 Elevon lift increments produced for the Space Shuttle compared to wind-tunnel data

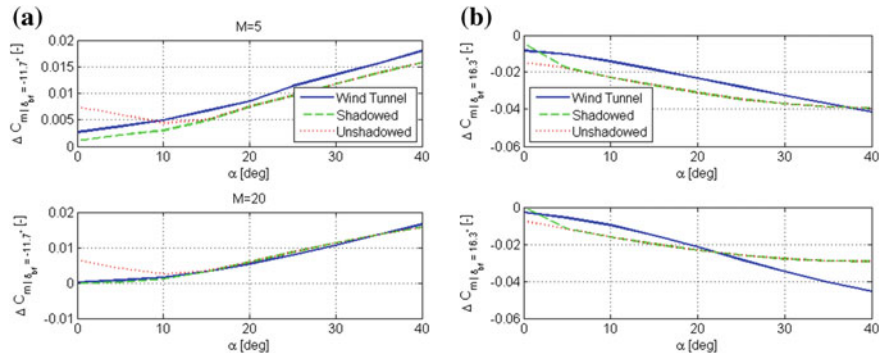


Fig. 7.14 Body flap moment increments produced for the Space Shuttle compared to wind-tunnel data

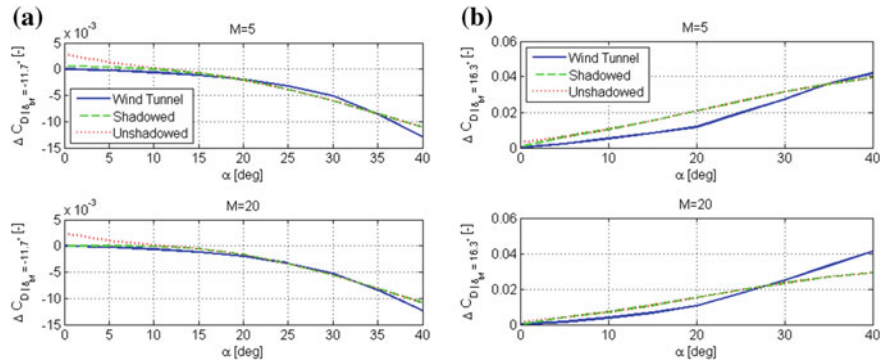


Fig. 7.15 Body flap drag increments produced for the Space Shuttle compared to wind-tunnel data

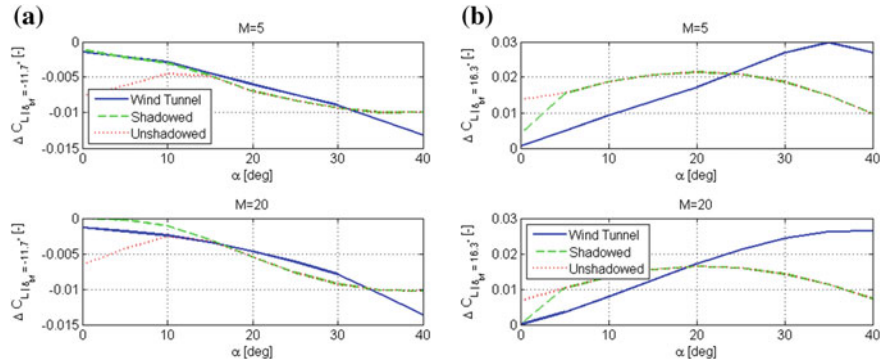


Fig. 7.16 Body flap lift increments produced for the Space Shuttle compared to wind-tunnel data

increments are better predicted than body flap increments. The body-flap moment and lift increments show the largest deviations, especially at high angle of attack and Mach numbers.

7.2.2 Vehicle Trajectories

This section will describe the entry trajectories that have been calculated for the Apollo-shaped capsule and the Space Shuttle-shaped vehicle. The results obtained here are not meant to resemble the actual entry profiles of these vehicles. Instead, they are used to assess the influence of errors in the aerodynamics on trajectory simulation, using the guidance law and environment assumptions discussed in Sects. 2.1 and 2.3. The trajectories were integrated using a Runge-Kutta 4th-order fixed step-size integrator with a step size of 0.1 s.

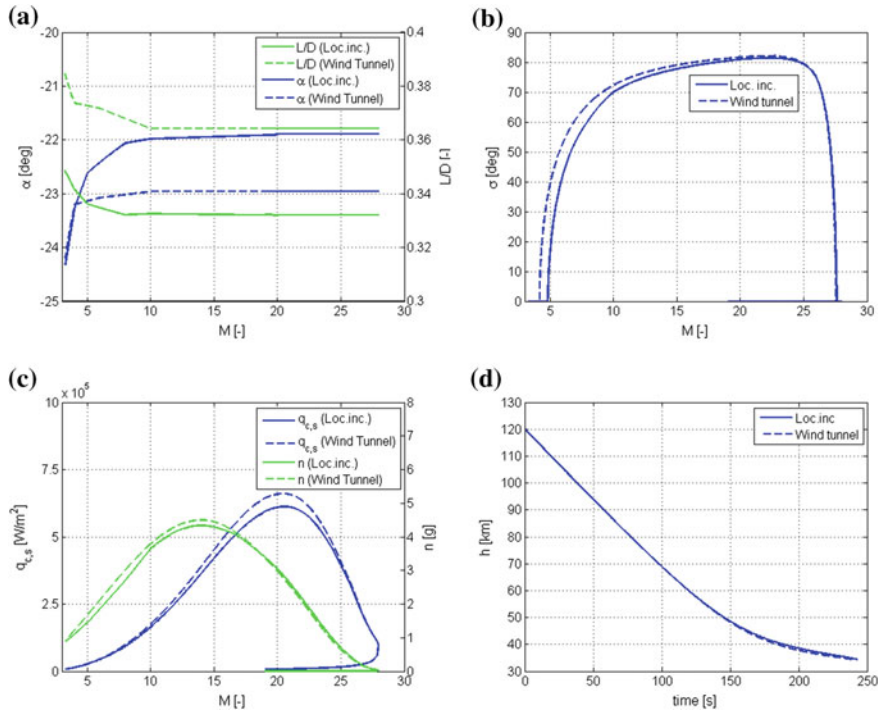


Fig. 7.17 Re-entry trajectory profile of capsule shape. **a** Lift over drag and trimmed angle of attack. **b** Bank angle. **c** Stagnation-point heat rate and total g-load and **d** Altitude

Capsule Trajectory

In this section, the results of the Apollo trajectory propagation using the wind-tunnel database from North American Aviation (1965) are compared to those that are obtained from the aerodynamic analysis methods in Sect. 3.3. The difference between the coefficients was discussed in the previous section.

Figure 7.17 shows the entry trajectory of the capsule, using the following initial conditions:

$$h = 120 \text{ km}, \tau = 225.5^\circ, \delta = -23.75^\circ$$

$$V_R = 7.83 \text{ km/s}, \gamma = -4^\circ, \chi = 49.6^\circ$$

$$m = 4532 \text{ kg.}$$

It can be seen from Fig. 7.17a that the trimmed angle of attack remains approximately constant for the initial part of the re-entry, owing to the near Mach number independence of Eq. (3.53). The gradual increase in the value of α , and resultant decrease in L/D , is due to the bridging between the low and high hypersonic regime

Table 7.1 Comparison of results for performance criteria of Apollo to be used in optimization

	Wind tunnel	Local inclination	% Percentage difference
Stagnation-point heat load	49.232 MJ/m ²	53.06 MJ/m ²	+7.7754
Ground track length	1425.6 km	1430.2 km	+0.3227

for the aerodynamic coefficients. The trimmed angle of attack changes more substantially for $M < 10$ than $M > 10$, as the independence principle is longer valid at low angles of attack. The change in trimmed angle of attack is slightly larger when using the local inclination methods than when using the wind-tunnel data. The difference in L/D between the two cases is roughly constant (≈ 0.03) over all angles of attack, though. This difference is acceptable for a conceptual design stage, though, as will be discussed shortly. Bank-angle modulation is required during part of the entry, as shown in Fig. 7.17b. In the absence of this modulation, a small skip in the trajectory was observed.

The figures show that the trajectories produced using the wind-tunnel coefficients and the ones generated here are very similar, which was to be expected from the discussion in the previous section. Since the L/D is somewhat overpredicted, the vehicle's range and stagnation-point heat load are also overpredicted. These values are shown in Table 7.1, and it is clear that the results are of sufficient accuracy for conceptual design studies. The error in the vehicle's range is very small, owing to the limited lifting capability of the vehicle. The error in stagnation-point heat load, although substantially higher than for the range, is still acceptably low at about 7.5%.

Shuttle-Shape Trajectory

Figure 7.18 shows the trajectory of the Space Shuttle geometry using the guidance algorithm discussed in Sect. 2.3. The following initial conditions are used:

$$h = 120 \text{ km}, \tau = 225.5^\circ, \delta = -23.75^\circ$$

$$V_R = 7.83 \text{ km/s}, \gamma = -1.5^\circ, \chi = 49.6^\circ$$

$$m = 75000 \text{ kg}$$

The following constraints are imposed on the attitude angles:

$$10^\circ < \alpha < 40^\circ, |\dot{\alpha}| < 2^\circ/\text{s}, |\sigma| < 80^\circ$$

The heat rate, which is set at a reference value of 500 kW/m², is properly tracked, even without the inclusion of control gains. In addition, it can be seen that the heat rate tracking stops being possible once α reaches 10 degrees. At this point the constant heat rate can no longer be tracked, see Eqs. (2.42)–(2.44), since the required drag computed from Eq. (2.45) becomes so low that it is impossible for the vehicle to

attain. Also, it is clear that the bank-angle modulation successfully prevents the vehicle from skipping out of the atmosphere before the heat-rate peak.

Figure 7.18b shows that the body flap is capable of trimming the Shuttle throughout most of the entry, as was to be expected. The actual deflections during the initial phase of the STS-1 entry correspond reasonably well to our results, as can be seen

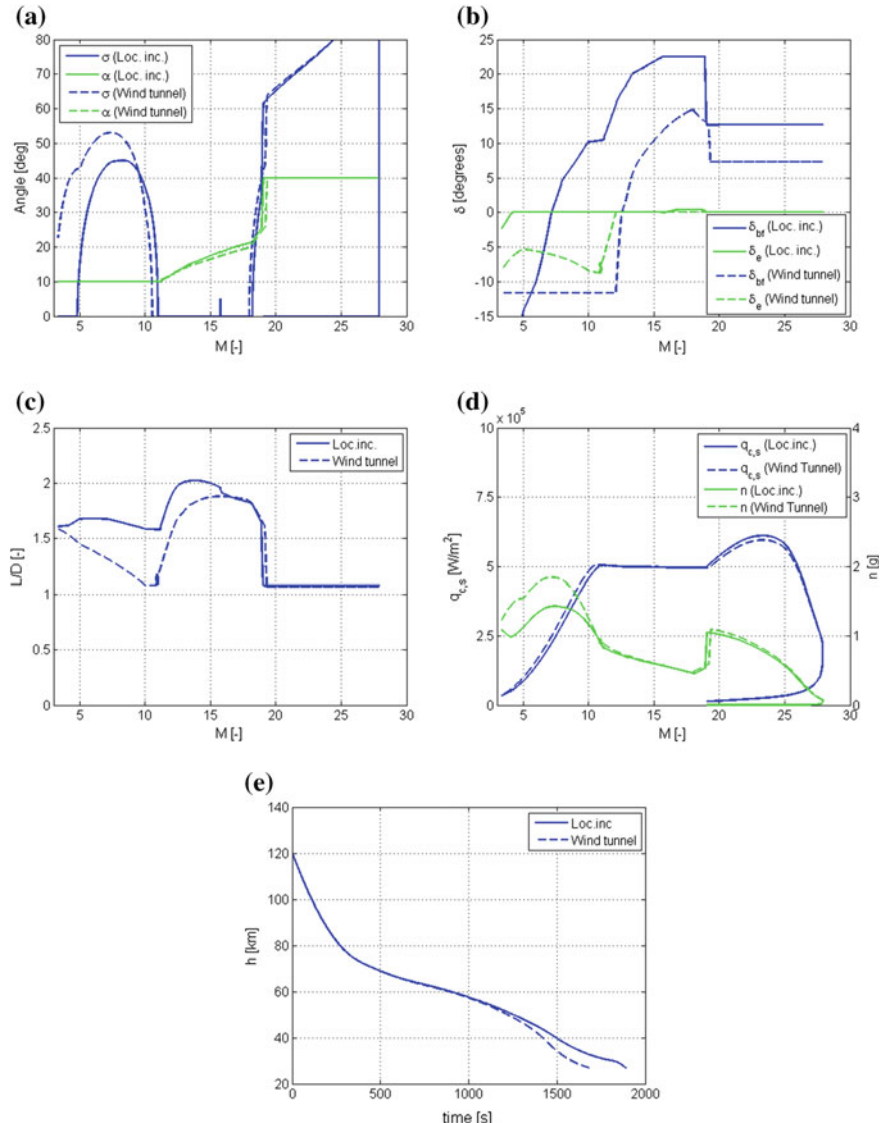


Fig. 7.18 Space Shuttle re-entry trajectory profile. **a** Angles of attack and bank. **b** Control-surface deflections. **c** Lift over drag. **d** Stagnation-point heat rate and total g-load and **e** Altitude

from comparing to Fig. 7.19. Due to the different control schemes used in the actual flight and our simulations, this only holds for high Mach numbers, where the α profile is similar (\approx constant at 40°). It may appear curious that trim is achieved by a downward deflection of the body flap, which will cause a negative pitch moment increment, in light of Fig. 7.9. However, this is due to different centers of mass during the wind-tunnel tests and re-entry. In the wind-tunnel tests, the center of mass is approximately 24 in. more forward than during the entry of STS-1 (Underwood and Cooke 1982). This change causes the center of pressure to lie in front of the center of mass, instead of behind, as was the case during the wind tunnel tests, causing a positive untrimmed pitch moment.

The relatively large discrepancy in the behaviour of the control-surface deflections for the two simulations is caused by the stacking of a number of errors. Namely, the over-prediction of the pitch moment at moderate angles of attack, along with the under-prediction of the body flap effectiveness, cause the required control-surface deflections to show relatively large differences during the nose-down maneuver. This is especially noticeable after the nose-down maneuver is initiated. Before this occurs, when $\alpha = 40^\circ$ and the Mach number is high, the pitch moment difference is relatively small. After the initiation of the nose-down maneuver, though, the lower angle of attack causes the influence of the control surface deflections on L/D to increase, in turn differently affecting the trajectories of the vehicle. This can be clearly seen in the L/D curves of the two vehicles, which coincide well up until about Mach 16, at which $\alpha \approx 20^\circ$.

The effect on the performance criteria is shown in Table 7.2. Despite the discrepancies in the L/D curves, the difference in the ground track length is limited to about 7.5 %. The error in the stagnation-point heat load, although higher, is also an acceptably low at 10 %. This shows that despite the complexity of the Space-Shuttle

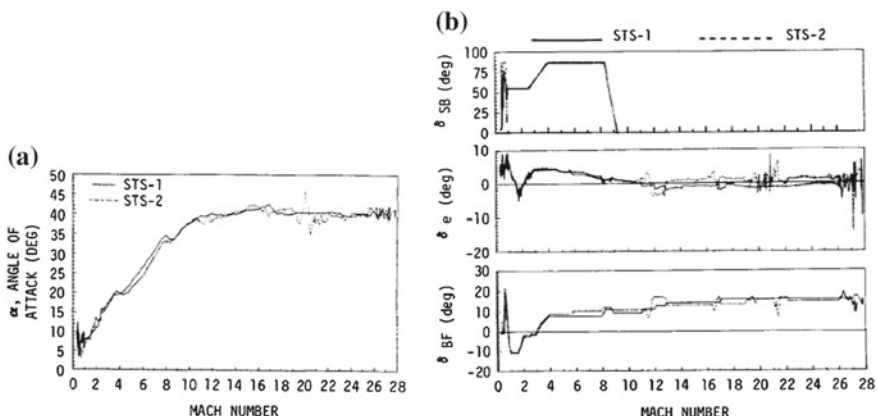


Fig. 7.19 Selected re-entry conditions for STS-1 and STS-2 from Underwood and Cooke (1982). **a** Angle-of-attack profile and **b** Control-surface deflections

Table 7.2 Comparison of results for performance criteria of the Space Shuttle to be used in optimization

	Wind tunnel	Local inclination	% Percentage difference
Stagnation-point heat load	698.9 MJ/m ²	762.9 MJ/m ²	+9.160
Ground track length	9608 km	10288 km	+7.0776

shape and the resulting errors in the aerodynamic coefficients, vehicle performance is still predicted to a level of accuracy acceptable at a conceptual design stage.

7.3 Simulation Settings

In this section, we summarize the settings used for the simulation results presented in subsequent chapters. First, the settings that are common to both vehicle types are discussed in Sect. 7.3.1, followed by discussion on settings specifically for the capsule and winged vehicle shapes in Sects. 7.3.2 and 7.3.3, respectively.

7.3.1 General

Here, the general settings for the simulations are presented. Although many of the settings have been mentioned in previous chapters, this section will serve as a summary for quick reference.

- Integrator Runge-Kutta 4th order, fixed step size integrator with step size of 1.0 s (note that we used a smaller step size in the previous section).
- Forces (Sect. 2.2.2): Aerodynamic and gravity forces only.
- Aerodynamics model (Sect. 3.3): The hypersonic local inclination methods, with the methods selected according to the algorithm described in Sect. 3.3.2. The low hypersonic regime is chosen to run from $M = 3$ to $M = 12$, while the high hypersonic regime is chosen to run from $M = 5$ to $M = \infty$. Shadowing is only used for the winged vehicle, due to the axisymmetry and the convexity of the defining curve of the capsule shapes.
- Gravity model (Sect. 2.1.2): Only terrestrial gravity, no third body perturbations. The J_2 term due to flattening is included. Values from the EGM96 gravity model (Vallado 2007) have been used, so that, for the entries of Eq. (2.9):
 - Central body term: $\mu = 398600.47 \cdot 10^9 \text{ m}^3/\text{s}^2$
 - First spherical harmonic term in $J_2 = 1.082626683553 \cdot 10^{-4}$
 - Reference radius $R_e = 6378.137 \text{ km}$

- Atmosphere model (Sect. 2.1.3): US 1976 Standard atmosphere model, giving density ρ , pressure p and temperature T as a function of altitude h . In addition to these values, the values of the speed of sound a and the specific gas constant R are given.
- Wind model: no wind.
- Central body characteristics (Sect. 2.1.1):
 - Angular velocity: $\omega_p = 7.29211538 \cdot 10^{-5}$ rad/s around polar axis (z_R axis), rotation axis and rate assumed constant.
 - Oblate spheroid central body shape, equatorial radius $R_e = 6378.137$ km (same as for gravity model).
 - Flattening $f = 1/298.257$

7.3.2 Capsule

For the capsule-shaped vehicle, an ideal guidance and control system is used, so that the commanded attitude angles (α, β, σ) are assumed to be achieved instantaneously by the vehicle. The guidance algorithm is described in Sect. 2.3.1, summarizing:

- Angle of attack α from the pitch trim condition: $C_m = 0$. If multiple trim points exist, the trim point with $C_{m_\alpha} < 0$ (pitch stable) is chosen.
- Angle of sideslip β equals zero during entry.
- Bank angle σ from condition that $\dot{\gamma} \leq 0$. This condition is only imposed after the lift term in Eq. (2.31) becomes the dominant term.

Since no specific mission is used for the analysis of the vehicle, the choice of initial conditions is partly arbitrary. However, using values that are known to be realistic for a re-entry vehicle is advisable. For this reason, the initial conditions are chosen to be the following:

$$\begin{aligned} h_E &= 120.0 \text{ km}, \tau_E = 225.5^\circ, \delta_E = -23.75^\circ \\ V_E &= 7.83 \text{ km/s}, \gamma_E = -2.0^\circ, \chi_E = 49.59^\circ. \end{aligned}$$

The minimum and maximum values of the shape parameters have been chosen based loosely on the data from Hirschel and Weiland (2009) and are given in Table 5.1. The value of the base radius R_m has been fixed to prevent shapes that are very different from being nearby one another in objective space. Although this could be considered too strong a simplification, by doing so the general trend in capsule-shape objective and constraint-function behaviour can be much better evaluated. It is not the purpose of this work to optimize a capsule for a very specific mission, but to identify overall trends in the influence of the shape. The other linear parameters can then be seen as a ratio of it compared to R_m .

7.3.3 Winged Vehicle

For the determination of the control surfaces of the winged vehicle, the following limits on the deflections are chosen:

- Body flap deflection limits: $\delta_{bf,max} = 20^\circ$, $\delta_{bf,min} = -20^\circ$.
- Elevon deflection limits: $\delta_{e,max} = 25^\circ$, $\delta_{e,min} = -25^\circ$.

The deflection limits were chosen based on data from the Space Shuttle (Rockwell International 1980) and HORUS (MBB-Space 1988). The minimum and maximum deflections of the Shuttle control surfaces are substantially smaller than those of HORUS. For downward body-flap deflections, it is known that shock-wave boundary-layer interactions can lead to excessive heating, so that its maximum value is chosen conservatively at 20° . This is smaller than the value of 22.5° for the Shuttle and 25° for HORUS. Similarly to HORUS, maximum upward and downward deflection are chosen to be equal. The maximum elevon deflection downward is chosen as 25° , which is larger than the value of 20° for the Shuttle, but smaller than the 40° value for HORUS. However, since only the longitudinal control is considered in this study, some leeway must be kept in the elevon deflections. Specifically, it must be accounted for that in realistic flights, additional deflection of the elevons will be needed to provide lateral control. The maximum upward elevon deflection is again taken equal to the downward deflection.

As for the capsule-shaped vehicle, the choice of initial conditions is not dictated by a specific mission profile. However, it is again useful to use conditions that are realistic, and the same values, with the exception of the flight path angle, are chosen to be equal to the capsule-shaped case. The initial conditions are chosen to be the following,

$$h_E = 120.0 \text{ km}, \tau_E = 225.5^\circ, \delta_E = -23.75^\circ$$

$$V_E = 7.83 \text{ km/s}, \gamma_E = -1.5^\circ, \chi_E = 49.59^\circ.$$

The reference heat rate is chosen at 700 kW/m^2 , which is the same as the maximum stagnation-point heat rate of the Space Shuttle. This indicates the need for correct knowledge of thermophysical phenomena at this heat flux. This choice will be evaluated in Sect. 9.1, where a Monte-Carlo analysis is performed for the winged vehicle. The choice of the minimum and maximum values of the shape parameters are shown in Table 5.2.

Chapter 8

Shape Analysis - Capsule

This chapter will show and discuss the optimization results of the capsule-shaped vehicle using the models and methods described in the previous chapters. First, a 1,000 solution Monte Carlo analysis is presented in Sect. 8.1. There, the influence of the parameters and constraints on the performance of the capsule solutions will be presented and a rationale for the constraint-function values that are chosen for the optimization is given. Subsequently, the optimization results will be presented in Sect. 8.2, including results of both two and three dimensional Pareto fronts. Finally, Sect. 8.3 will give some concluding remarks regarding the capsule optimization.

8.1 Monte Carlo Analysis

For the preliminary analysis of the capsule-shaped vehicles, 1,000 solutions were randomly generated. The settings from Sect. 7.3 were used for the analyses.

The values of the constraint functions are plotted in histograms in Fig. 8.1, with the corresponding scatter plots given in Figs. 8.2–8.7. The values of the stagnation-point heat flux shown in Fig. 8.1a lie in the range that was to be expected from experience of previous LEO entry studies using low L/D vehicles. A significant variation in maximum stagnation-point heat fluxes is observed here, with a factor of nearly 3 difference between the minimum and maximum values. The behavior of the maximum shoulder heat flux can be seen to have a similar distribution, with the notable difference that the ‘tail’ of the distribution at high fluxes is more stretched out. This is due to the fact that the shoulder heat flux is calculated as a geometry-dependent multiple (generally roughly between 1 and 2) of the stagnation-point heat flux (see Sect. 3.4.2).

It can be seen from Fig. 8.2 that the greatest variability in the heat fluxes are due to changes in the nose radius and the rear cone angle. Although the influence of the nose radius is obvious from Eq. (3.77), the influence of the rear cone angle warrants some more discussion. The influence of the cone half-angle is felt in the heat flux, since an increase in absolute cone angle will generally mean an increase in

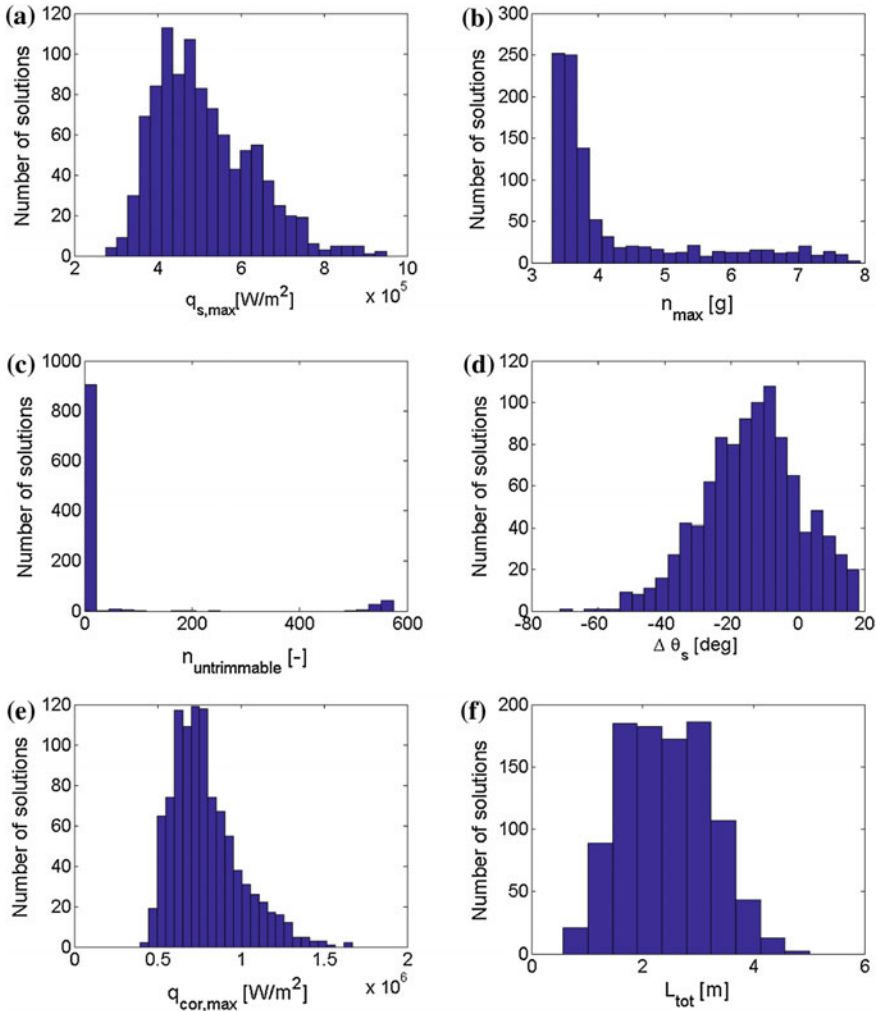


Fig. 8.1 Histograms of constraint function values for 1,000 randomly generated capsule shapes (stability constraint not shown; all solutions were found to be stable)

volume and therefore mass of the capsule. The frontal area that is seen by the flow is hardly, if at all, affected by a change in θ_c . Therefore, the ballistic coefficient (see Eq. (2.36)) will increase and as a result, the maximum heat flux will occur deeper in the atmosphere at a higher density, leading to an increase in maximum heat flux. It is interesting to note that the influence of the corner radius on the corner heating is not as pronounced (see Fig. 8.6) as may have been expected. The data presented in Sect. 3.4.2 showed that the side radius is of lower influence on $q_{\text{cor},\max}$ than the angle of attack at which the capsule flies. We stress, however, the results for the corner

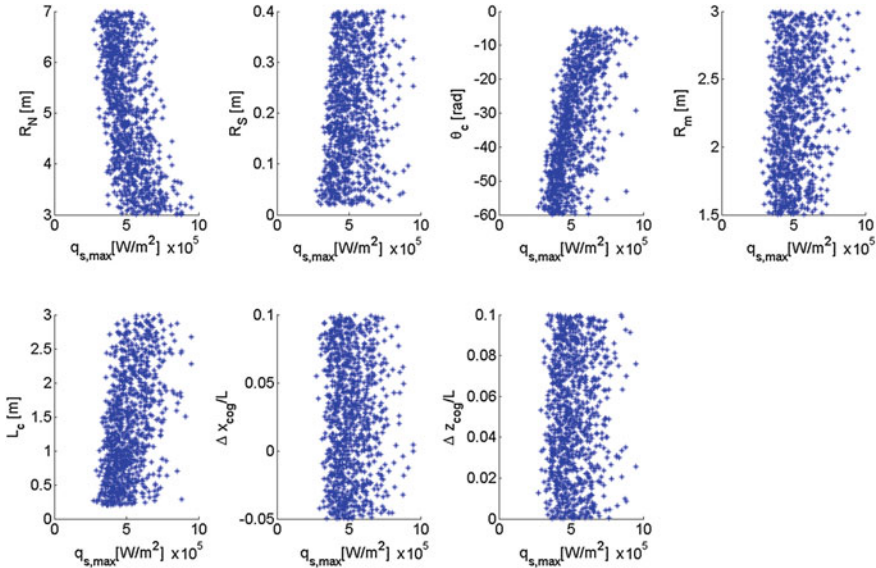


Fig. 8.2 Scatter of shape parameters against maximum stagnation-point heat flux

heating should be treated with caution, since the empirical procedure on which they are based was generated using a limited data set.

The maximum load factor values, which are shown in Fig. 8.1b, show that most solutions have a maximum load factor below 4.5, with values as high as 8 occasionally occurring, but much less frequently. It can be seen from Fig. 8.3 that the variation in the load factor is primarily influenced by the location of the center of mass in z -position. This is due to the direct relation between this value and the trimmed angle of attack. Since a vehicle flying at greater angle of attack will experience increased L/D , the vehicle's trajectory will be even less like a ballistic entry in such cases (and more like, but still far from, a gliding one). The figure shows a rationale for giving capsule-shaped vehicles a small center of mass offset, since this small deviation strongly reduces the load factor.

It can be seen from Fig. 8.1c that most shapes that are analyzed have their trim point within the allowed range, with about 10 % having more than one time step during the numerical integration at which no trimmed condition can be found. The behavior (aside from the peak at 0) is bi-modal, with one peak around 100 time steps, and one peak around 550 time steps. This behavior is due to the trend of the aerodynamic coefficients of the capsule with Mach number (see Sect. 3.1.2). At high Mach numbers, the aerodynamic coefficients are almost invariant, while for lower Mach numbers, this Mach-number independence breaks down. The two peaks that are observed are due to untrimmability at low Mach numbers and untrimmability at all Mach numbers, respectively. The trend observed in Fig. 7.7c shows that for lower Mach numbers, the magnitude of the trimmed angle of attack increases. This indicates

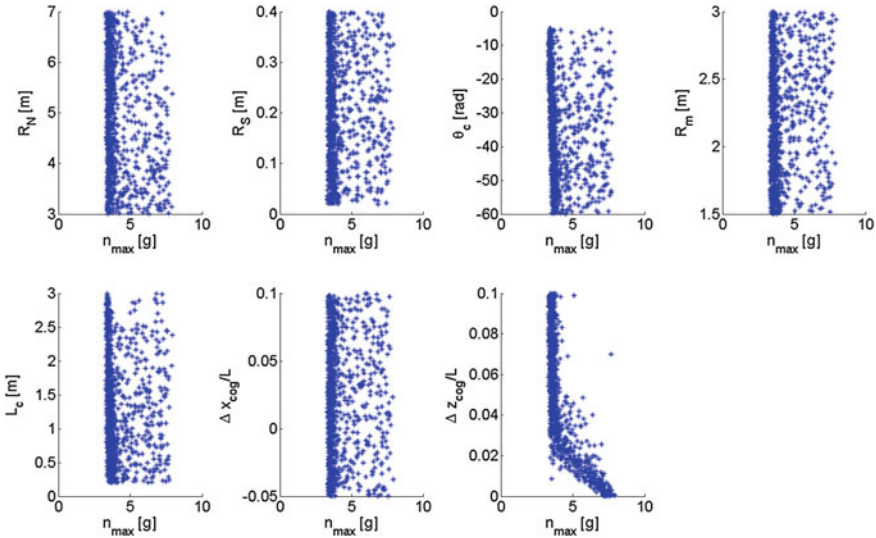


Fig. 8.3 Scatter of shape parameters against maximum load factor

that if a vehicle is untrimmable at high Mach numbers, so that $|\alpha_{tr}| > |\alpha_{max}|$, this will also be the case for low Mach numbers. The opposite is not true, however. From Fig. 8.4, it can be observed that untrimmability is correlated with high values of θ_c and z_{cog}/h . For high θ_c , the moment coefficient behavior differs from the trend observed for the Apollo capsule, since the flow directly hits the rear body even at moderate angles of attack. The influence of the center of mass position on the trimmability is due to the fact that a high center of mass offset in z -direction typically means a high magnitude angle of attack trim condition.

The behavior of the Newtonian stagnation-point location can be seen in Fig. 8.1d, from which it can be seen that for the majority of cases the stagnation point will still lie on the front heat shield. For about 25 % of cases, though, this will not be true ($\Delta\theta_s > 0$). A large variation of possible values is observed in the angular location of the stagnation point, with a range of nearly 90° seemingly possible. This is, however, a bit misleading since the value that is shown is measured starting from the angular transition location between the nose sphere and the toroidal segment (see Eq. 6.18). Since this point is itself dependent on the vehicle's shape parameters, part of the observed variability in the stagnation-point location is due to this change. The data are presented in this manner, though, since a deviation from this transition point is considered to be the relevant quantity in determining a constraint violation of this type, as discussed in Sect. 6.3.2. The dependencies on R_m and R_N that are observed in Fig. 8.5 were to be expected from Eq. (5.3), as these are important for determining the angular transition point between the spherical and toroidal segments. The dependency on z_{cog} that is observed is due to the previously noted dependency of α_{tr} on its value, which is of course of influence on the stagnation point location.

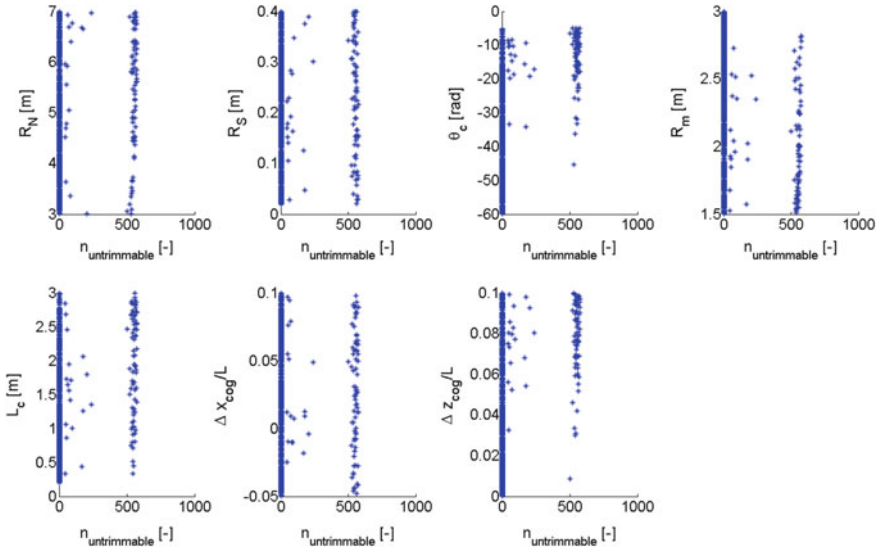


Fig. 8.4 Scatter of shape parameters against number of untrimmable time steps

All capsule shapes that are analyzed are stable. Although some capsules may have two trim points, of which one is unstable (Sect. 2.3.1), the guidance algorithm is such that if a stable trim point exists, this point is chosen as the trim point. For untrimmable shapes, the angle of attack with the lowest pitch moment value is selected as the commanded angle of attack. At these points, the algorithm does not analyze the stability of the trim point, since the vehicle is untrimmed and the solutions can be said immediately to be infeasible. It is possible, however, that unstable configurations exist for certain combinations of the shape parameters, so this constraint will be kept in the optimization. It is likely from the results presented here, though, that an occurrence of its violation is rare.

Finally, the vehicle lengths are plotted in Fig. 8.1f. It can be seen that there is a relatively uniform distribution of lengths between about 1.5 and 3 m, with outliers as small as 1 m and as large as 5 m (Fig. 8.7).

The 1,000 random capsule are plotted in objective space in Fig. 8.8. The results are presented as a three dimensional scatter, as well as projected onto the planes for clarity. The variability in all three performance criteria is sufficient to warrant their inclusion as cost functions in the optimization procedure. Optimality in stagnation-point heat load and ground-track length are strongly competing criteria, as was to be expected. Similarly, increased volumetric efficiency is at the expense of a higher stagnation-point heat load. This due to the fact that a vehicle with higher volumetric efficiency will have a lower ratio of frontal area over volume, which in turn means a higher ballistic coefficient and higher heat rate. The volumetric efficiency and ground-track length, however, do not compete strongly, in the sense that a higher value of s_g generally means a higher value of η_V . This is most likely due to the fact

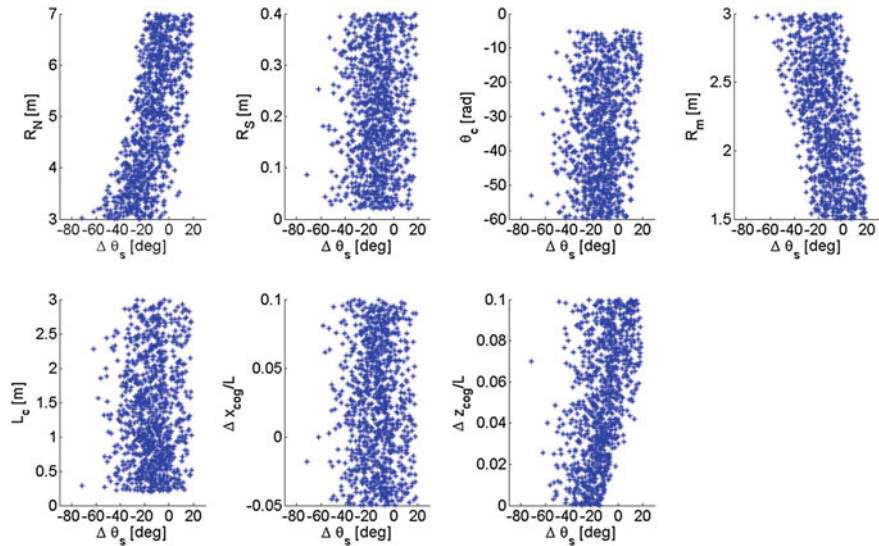


Fig. 8.5 Scatter of shape parameters against stagnation-point location

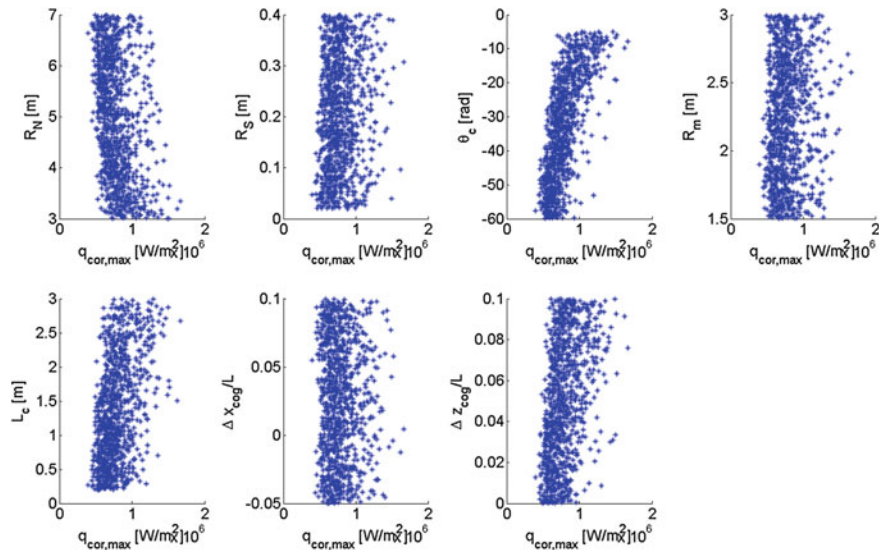


Fig. 8.6 Scatter of shape parameters against maximum corner heat flux

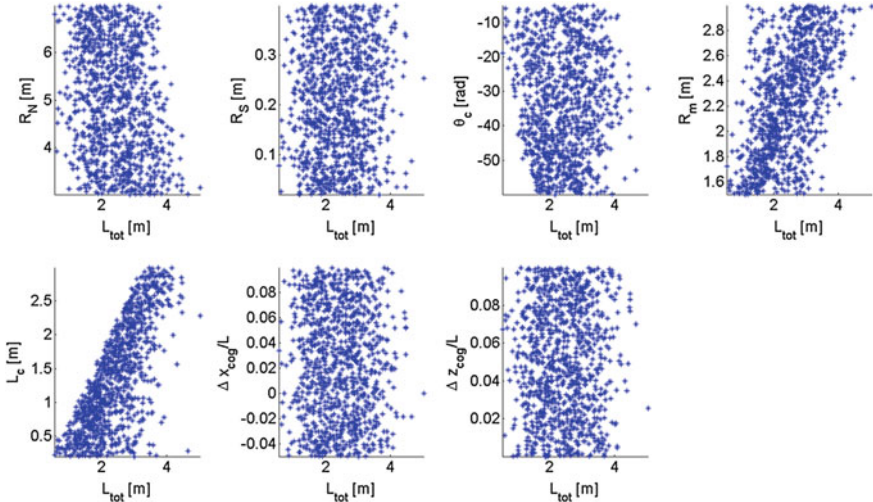
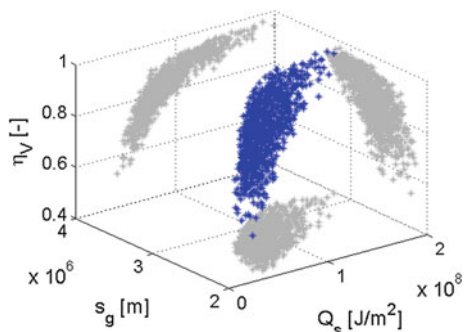


Fig. 8.7 Scatter of shape parameters against vehicle length

Fig. 8.8 Scatter of Monte Carlo solutions in performance space (blue), projected onto planes (grey)



that vehicles with higher η_V and higher mass will be less affected by the aerodynamic forces. Consequently, the deceleration peak will occur later in the trajectory. As a result, the vehicle will fly at the large initial velocity for a longer period of time and therefore have a longer ground-track length. In addition, the decrease in flight-path angle that occurs near the end of the trajectory is delayed by this, further increasing its ground-track length.

To assess the effect of changing the constraint values on the feasible solutions in performance space, the infeasible solutions are plotted in Figs. 8.9, 8.10 and 8.11 for a number of constraint values. The constraints for θ_s and $n_{uncontrollable}$ will not be included in this analysis, since the permissible constraint value is fixed from physical considerations. It can be seen from Figs. 8.9 and 8.11 that the stagnation-point and corner heat flux constraint have a large overlap in which solutions they constrain, as was to be expected. The load factor constraint mostly affects solutions with high η_V , as can be seen from Fig. 8.10.

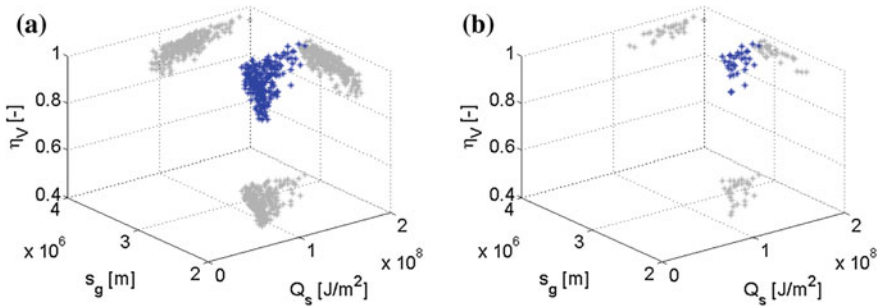


Fig. 8.9 Solutions from Monte Carlo analysis that violate the constraint for $q_{s,max} = \mathbf{a}$ 600 kW/m^2 , **b** 750 kW/m^2

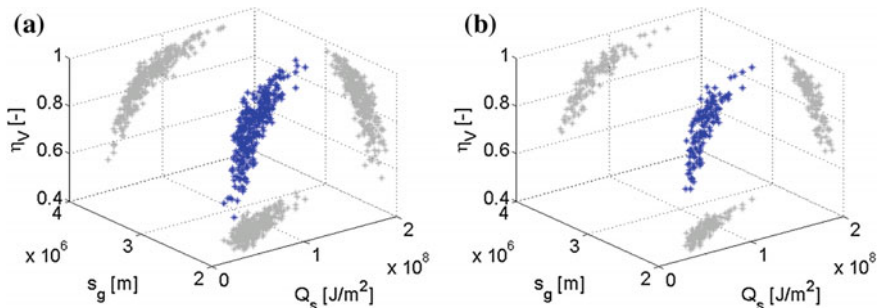


Fig. 8.10 Solutions from Monte Carlo analysis that violate the constraint for $n_{max} = \mathbf{a}$ 4 g , **b** 6 g

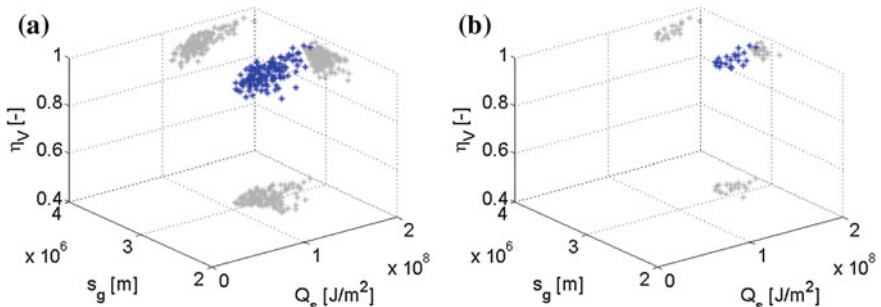


Fig. 8.11 Solutions from Monte Carlo analysis that violate the constraint for $q_{cor,max} = \mathbf{a}$ 1000 kW/m^2 , **b** 1300 kW/m^2

The results obtained here for the constraints are used to guide the selection of the permissible constraint function values. This is done in such a manner that the constraints are not chosen in a manner that they become inactive or overly restrict the search space, while keeping the values within physically realistic ranges. The final baseline constraints chosen for the capsule optimization are the following:

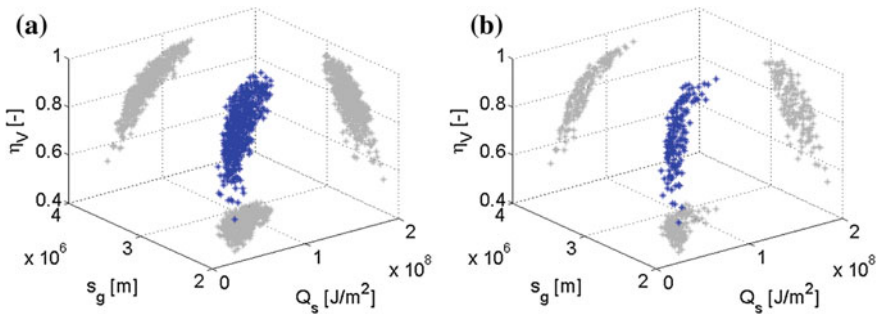


Fig. 8.12 Solutions of Monte Carlo simulation that are **a** Feasible and **b** Pareto optimal

- $q_{s,max} < 700 \text{ kW/m}^2$
- $q_{cor,max} < 1,000 \text{ kW/m}^2$
- $\Delta\theta_s < 0^\circ$
- $n_{tot} < 5 \text{ g}$
- $L_{tot} < 4 \text{ m}$

Figure 8.12a shows the constrained results of the Monte Carlo analysis and Fig. 8.12b shows the Pareto optimal solutions of the constrained Monte Carlo results. Out of 1,000 solutions, 446 are feasible, of which 141 are Pareto optimal. Figure 8.13 shows the Pareto fronts when considering each of the combinations of two objective functions. For optimization of Q_s and s_g , 35 of the solutions are Pareto optimal, for Q_s and η_V 36 are Pareto optimal and for s_g and η_V 7 are Pareto optimal. The comparatively small number of Pareto optimal solutions in the final case is due to the fact that the general trends for s_g and η_V are similar, as discussed previously in this section.

8.2 Optimization

The optimization procedure discussed in Chap. 6, with the settings for a function evaluation given in Sect. 7.3 and the constraint function values determined in the previous section will now be used to generate the Pareto fronts for the capsule shape. First, each of the combinations of the three objective functions will be used to generate three two-dimensional (in objective space) Pareto fronts in Sect. 8.2.1, followed by the full three-dimensional Pareto front in Sect. 8.2.2.

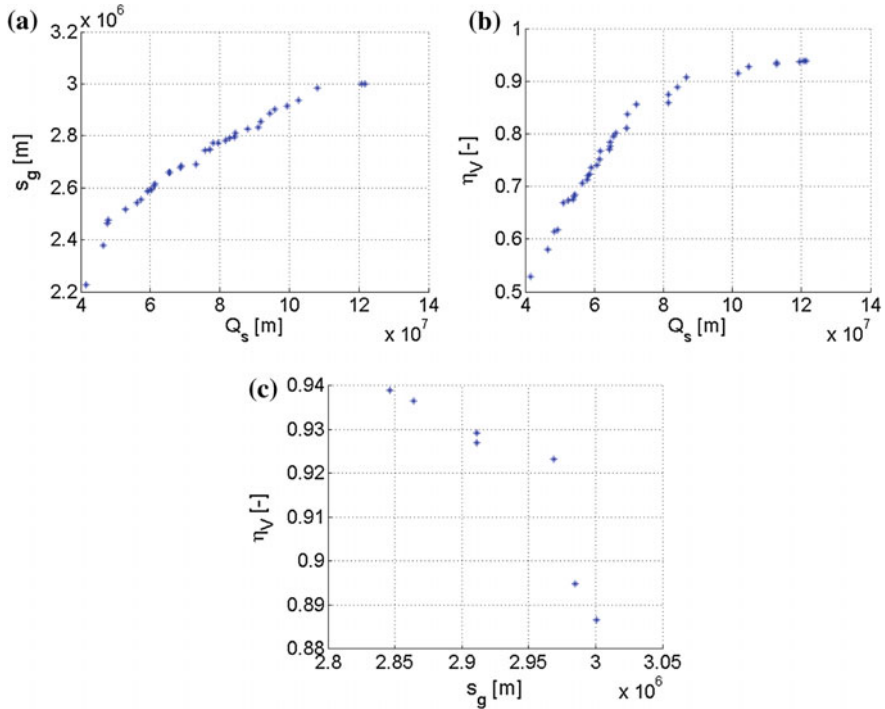


Fig. 8.13 Pareto-optimal results of Monte Carlo simulation for two objective functions

8.2.1 Two-Dimensional Analysis

Here, the two-dimensional optimizations will be discussed for each combination of the three objective functions. The Pareto fronts that have been found are presented, colored by shape-parameter value and constraint-function value, as well as the trimmed angle of attack, L/D at high hypersonic velocities and capsule volume.

Range Versus Heat Load

The Pareto front for the optimization of s_g and Q_s is shown in Figs. 8.14, 8.15 and 8.16. The front appears to be smooth and continuous over the whole range of objective-function values, with two prominent discrepancies. Firstly, there is a region of sparse solution density at high s_g and Q_s . The low density of solutions here is due to the very specific combination of parameter values that can form an optimal solution that does not violate any constraints. This can also be observed in Fig. 8.17, where five capsule shapes on the Pareto front are shown. Here, the shape for maximum heat load and range can be seen to differ substantially from the neighboring shape, most prominently in the rear body shape and size.

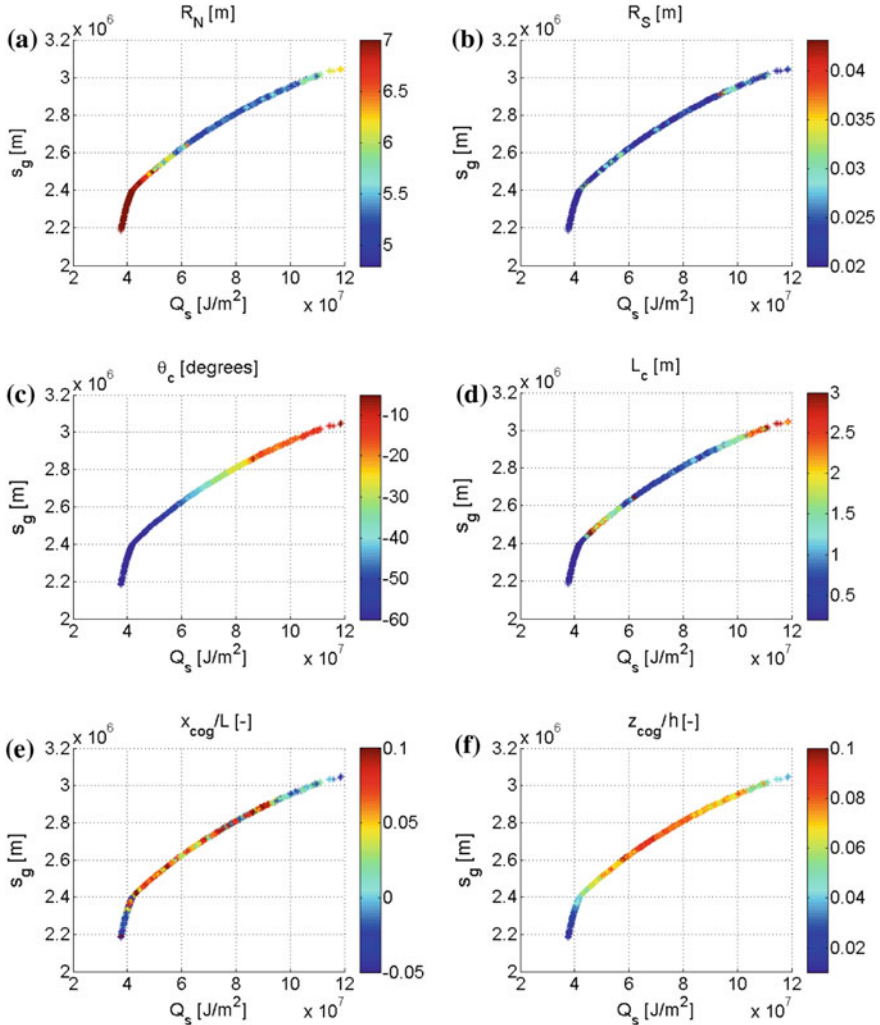


Fig. 8.14 Pareto optimal solutions for optimization of range and stagnation-point heat load, colored by shape parameter values

The second notable feature on the Pareto front is the ‘kink’ at $s_g \approx 2.4 \cdot 10^6$ m. The cause of this effect can be seen from Fig. 8.15c, in which the value of the constraint function $\Delta\theta_s$ is shown. The value can be seen to increase rapidly between the minimum value of s_g and the position of the kink, at which it reaches its maximum allowable value of zero. Figures 8.14f and 8.16a show an associated increase in $\Delta z_{cog}/h$ and $\alpha_{tr,M=20.0}$, while the nose radius can be seen from Fig. 8.14a to be at its maximum value up to this point. The fact that the nose radius decreases following this point is due to Eq. (5.3), which shows that a decrease in nose radius increases the

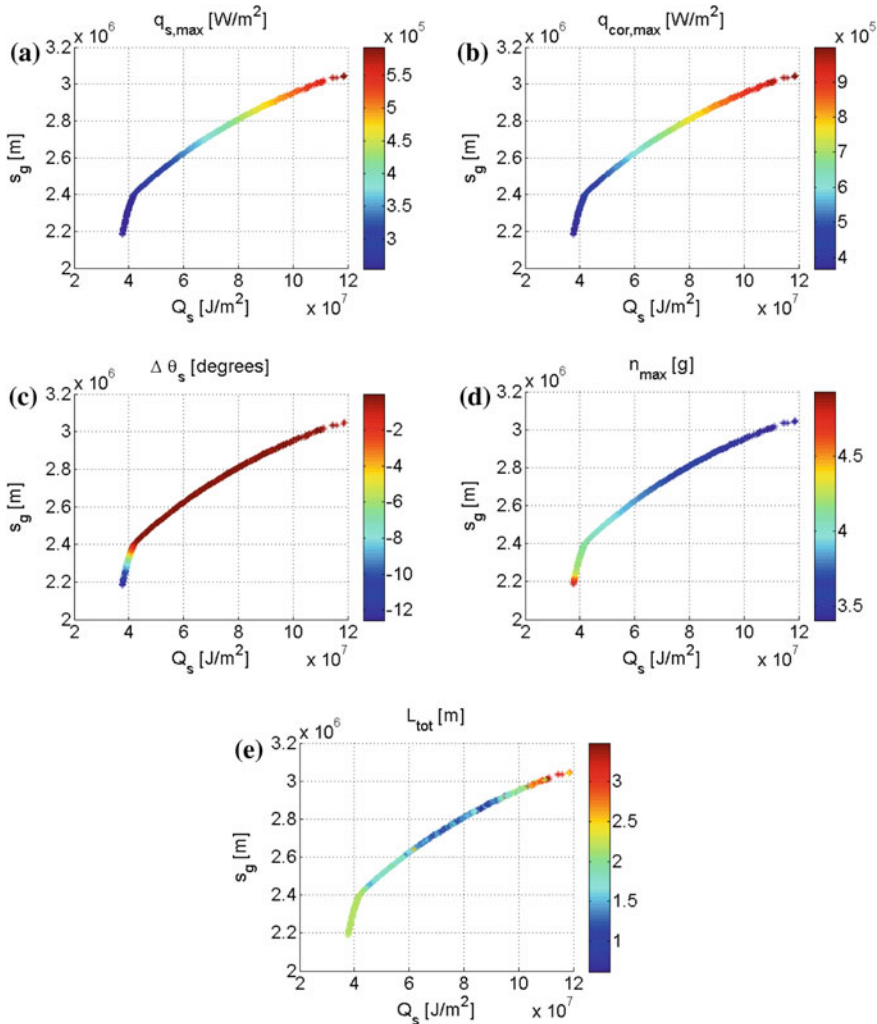


Fig. 8.15 Pareto optimal solutions for optimization of range and stagnation-point heat load, colored by constraint function value

angular position of the nose-to-torus transition. This gives more leeway for the angle of attack to increase, causing an increased range, without violating the constraint on $\Delta\theta_s$. In doing so, however, the stagnation heat flux and heat load increase due to the decrease in R_N . This in turn causes the sudden change in the slope of the curve defining the Pareto front. This can also be seen in Fig. 8.17 by comparing the capsule shape of minimum Q_s and the shape just following the kink. Clearly, there is very little change in the external vehicle shape over this initial region of the front. The modulation in vehicle behavior is achieved largely by a change in center of mass.

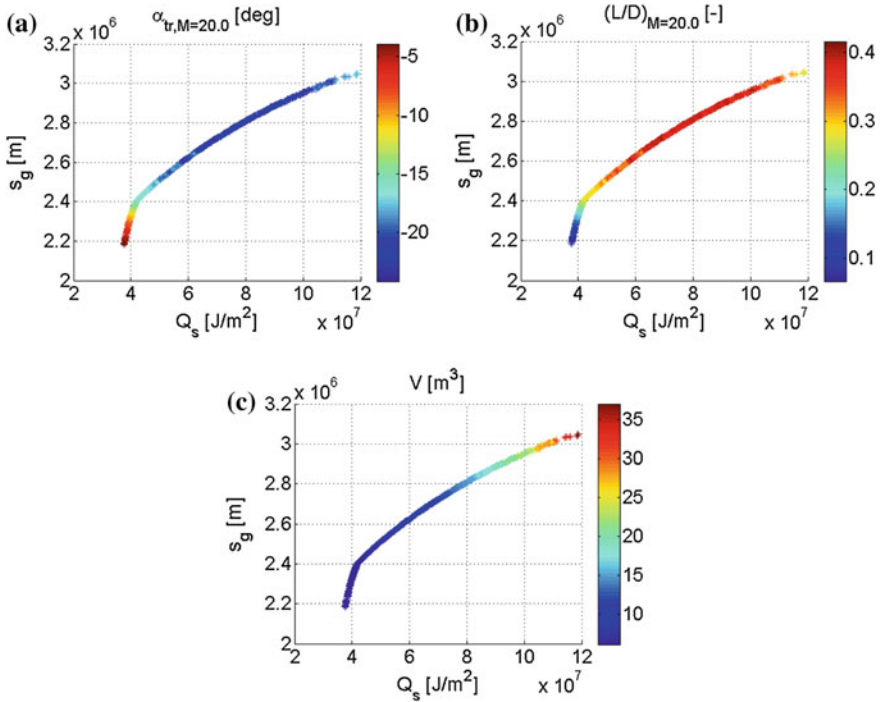


Fig. 8.16 Pareto optimal solutions for optimization of range and stagnation-point heat load, colored by selected vehicle characteristics

Following the kink, the rear cone half angle increases from its minimum value of -60° to its maximum value of -5° at high heat-load and range, as seen in Fig. 8.14c. As previously discussed, this is due to the fact that an increase in θ_c causes an increase in vehicle mass and as a result an increase in both range and stagnation-point heat load. This increase in volume can also be clearly seen in Fig. 8.16c. In fact, the vehicle's volume, and therefore mass, can be seen to increase continuously and (following the kink) reasonably uniformly for increasing range and heat load.

At the minimum values of both the range and heat load, the load factor appears from Fig. 8.15d to be the constraining factor, as it reaches its maximum value of 5 here. Also, the position of the center of mass in x - and z -direction are near their minimum values (see Fig. 8.14e, f), respectively, to minimize the trimmed L/D (Fig. 8.16b). This minimized L/D reduces the range of the vehicle.

The value of R_S can be seen from Fig. 8.14b to be low everywhere on the Pareto front. An increase will firstly decrease the corner heat flux and secondly increase the volumetric efficiency. Since the latter is not considered in this two-dimensional optimization case, this influence of the side-radius is not considered by the optimizer. The corner heating can be seen from Fig. 8.15b to be near its maximum value near the maximum values of s_g and Q_s , which an increase in R_S would mitigate somewhat.

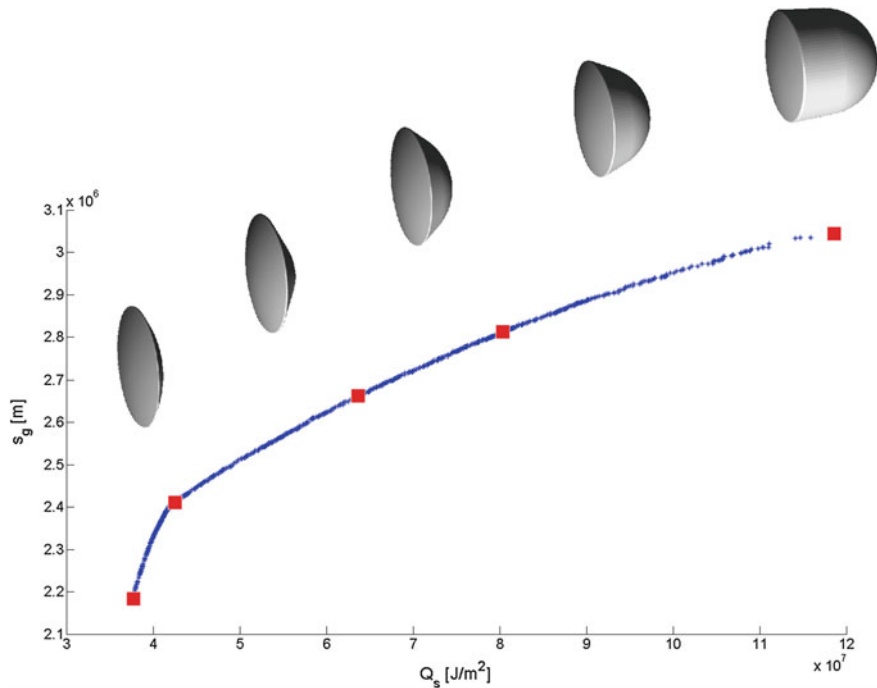


Fig. 8.17 Representation of evolution of capsule shape along $s_g - Q_s$ Pareto front

However, when regarding Fig. 8.14b, it can be seen that no Pareto-optimal solution for the highest values of s_g exist with high values of R_S . Such an increase in R_S would also increase the value of $\Delta\theta_s$, which would in turn require the vehicle to fly at a lower absolute value of α , yielding a decrease in s_g . This case is a good example of how an optimizer can automatically perform a trade-off between conflicting modifications to the vehicle.

Some peculiar behavior is observed in the Pareto-optimal solution for the region of highest objective function values. An increase in range is caused by an increase in both L/D and mass over the majority of the front. In this region of high Q_s and s_g , however, a decrease of L/D is observed, combined with a steep increase in capsule volume. Although less efficient from the viewpoint of minimizing the heat load, this appears to be the only manner for the optimizer to find solutions that do not violate the constraints on $\Delta\theta_s$ and $q_{cor,max}$ in this region. It must be noted though, that due to the simplicity of the mass prediction, the precision of these solutions is uncertain.

Summarizing, the following general conclusions for capsule-shape optimality can be drawn from the $m - s_g$ optimization:

- The mass of the vehicle is strongly related to the position on the Pareto front.

- The stagnation-point position constrains the optimal shape over the majority of the Pareto front, being inactive only for low range and mass. To comply with this constraint, the vehicle nose radius must be reduced and the side radius is kept low.
- Both stagnation-point heat flux and corner heat flux are (close to) active for the solutions of maximum range and mass.
- The normal-load constraint limits the lowest values of s_g and Q_s on the Pareto front.
- Although an increase in z_{cog}/h will increase L/D and thereby s_g , its value must decrease for high values of range for the solutions to remain compliant with the constraints.

Volumetric Efficiency Versus Heat Load

The Pareto fronts of the optimization with respect to η_V and Q_s are shown in Figs. 8.18, 8.19 and 8.20. Although a kink in the Pareto front (as was observed in the previous case) is absent here, it can be seen that the Pareto front has a region of high curvature around $Q_s = 80 \text{ MJ/m}^2$. Near this region, a number of shape parameters begin to show aberrant behaviour. Most noticeably, from Fig. 8.18b, the value of R_S moves very suddenly from its minimum to its maximum value. A high value of R_S will increase η_V , so that it was to be expected that its value would be high for regions of high η_V . The sudden increase in R_S can be seen from Fig. 8.18c to be accompanied by an anomaly in the behavior of θ_c : a sudden decrease in θ_c by about 10° is observed after the angle reaches close to its maximum value at about 85 MJ/m^2 . Upon close inspection of the two curves, it can be seen that the increase in R_S occurs at a slightly higher value of η_V than where the value of θ_c becomes very high. An explanation for this is the following: both an increase in R_S and θ_c increases the value of η_V . However, a high value of θ_c decreases the value of Q_s , while a high value of R_S increases it. Therefore, the Pareto optimal solutions will have a low value of R_S and a high value of θ_c , until θ_c reaches its maximum value and R_S must be increased to extend the Pareto front to regions of higher η_V . This can also be seen in Fig. 8.21, where five capsule shapes are shown and the three of lower heat load show a very sharp corner and the two of higher heat load show a very round corner, with no transitional behavior in R_S . The trimmed angle of attack (see Fig. 8.20a) can be seen to decrease relatively rapidly in this region, when compared to the area of low η_V and Q_s . This will also cause the maximum stagnation-point heat flux to increase more rapidly, as will be discussed shortly.

The value of R_N is kept at its maximum value for the majority of the Pareto front. This is with the exception of high values of η_V , where a low value of R_N is necessary, since for the extreme case of $\eta_V = 1$, the capsule equals a sphere, on which $R_m = R_N = 2 \text{ m}$ (since R_m is fixed).

Similarly, the value of L_c is kept low, to decrease the vehicle mass and therefore heat load. However, for the highest values of η_V , a moderate value of L_c is required to approximate the shape of a sphere in a Pareto-optimal manner.

Due to the relatively small absolute angle of attack, the stagnation-point heating constraint has a greater influence than the corner heating constraint. The stagnation-

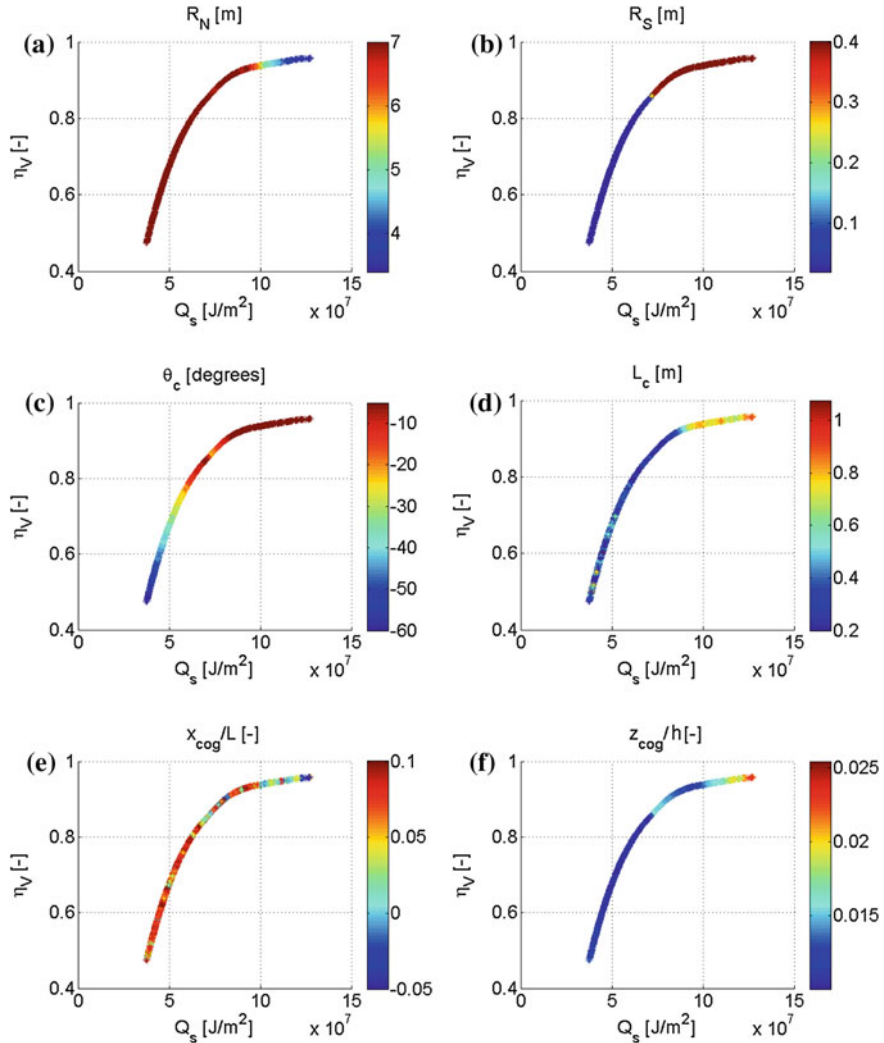


Fig. 8.18 Pareto optimal solutions for optimization of volumetric efficiency and stagnation-point heat load, colored by shape parameter values

point heating reaches its maximum allowable value at high Q_s . The corner heating, though, reaches a maximum value of approximately 930 kW/m^2 , below its maximum permissible value. This can be explained by the decrease in R_N , which is in turn caused by the desire for increased η_V .

The load factor is on or near its maximum value of 5 g over almost all of the Pareto front. This is due to the fact that, as previously discussed, a low L/D causes a short trajectory and a resultantly low value of Q_s , but increases the load factor.

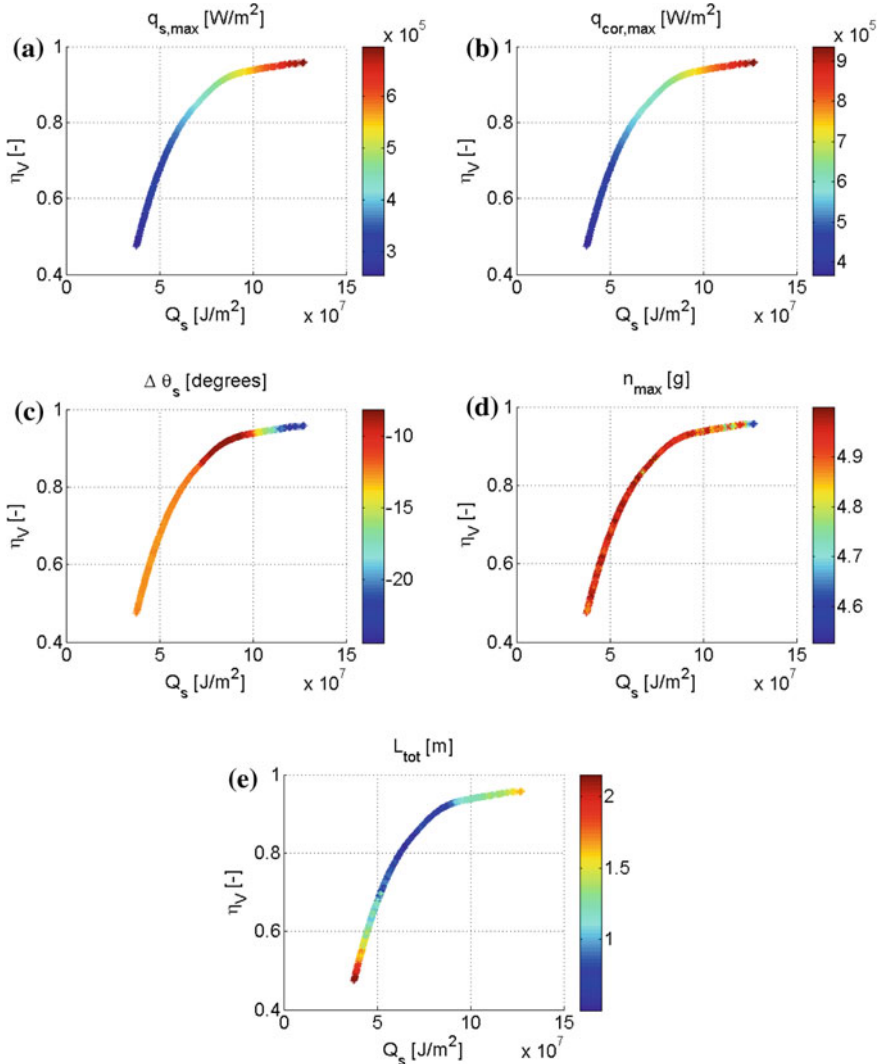


Fig. 8.19 Pareto optimal solutions for optimization of volumetric efficiency and stagnation-point heat load, colored by constraint function value

Since the range is not considered in this optimization run, the decrease in L/D is not disadvantageous to the s_g objective, as in the previous section (s_g - Q_s optimization). In this case, the load factor is the constraining quantity over most of the front. The capsules of high η_V have a greater volume, and therefore a greater mass. Consequently, the value of L/D must increase to keep the value of n below n_{\max} , increasing Q_s . This can be seen from Fig. 8.18e, f to be achieved by variation of the center of mass. Although at low values of Q_s , the influence of x_{cog}/L is insufficient to show

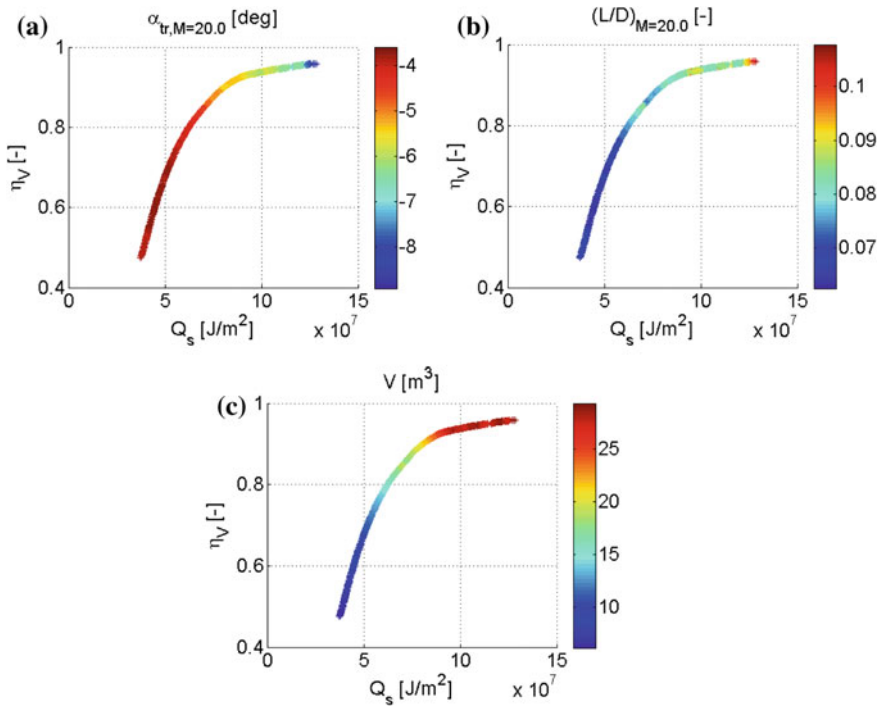


Fig. 8.20 Pareto optimal solutions for optimization of volumetric efficiency and stagnation-point heat load, colored by selected vehicle characteristics

any real trend in its value over the front, at high values of η_V , a clear decrease of its position can be seen. The value of z_{cog}/h can be seen to remain well below its maximum allowable value of 0.1 over the entirety of the front. The effect of this can be seen in Figs. 8.19c and 8.20a: the angle of attack remains relatively close to zero and therefore the stagnation-point location constraint is not active anywhere on the front. Only at the very highest values of η_V do the thermal constraints become the constraining factor.

The following summarizes the main results of this optimization set:

- The load factor is constraining over the majority of the Pareto front, as range is not considered; a lower value z_{cog}/h and therefore of L/D causes a lower flight time and lower stagnation-point heat load. Modification of the center of mass position is used to remain on or near the load factor constraint.
- To comply with the load factor constraint, it is advantageous to keep the corner radius low. However, for high values of η_V , its value is increased to its maximum value on the Pareto front.
- Thermal constraints limit the high m , high η_V region of the Pareto front.

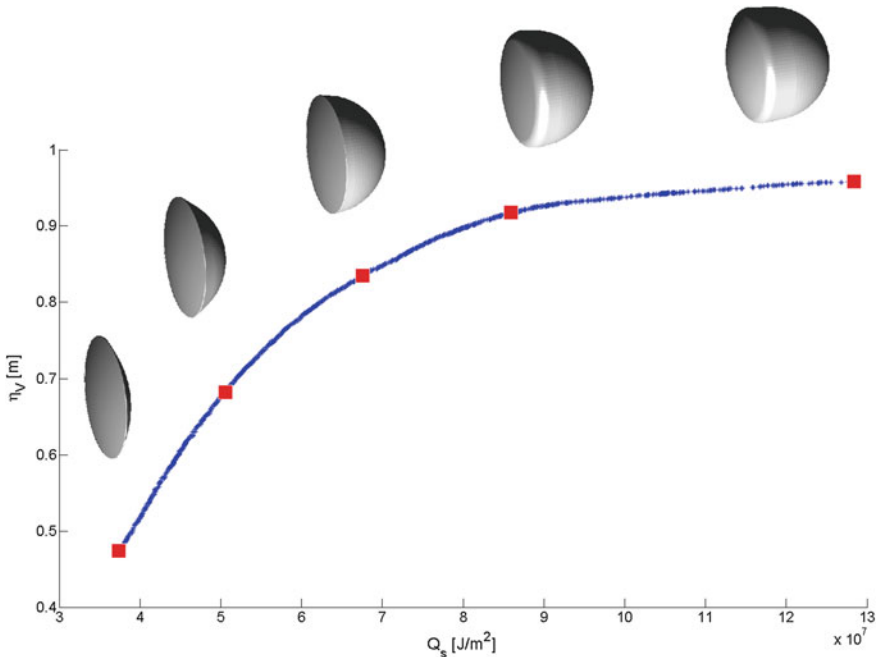


Fig. 8.21 Representation of evolution of capsule shape along $\eta_V - Q_s$ Pareto front

Range Versus Volumetric Efficiency

The Pareto front for optimization w.r.t. to s_g and η_V exhibits significantly different behavior from the two fronts discussed previously. Foremost, the extent of the front in objective space is relatively small, when compared to the values of s_g and η_V that occur in the other Pareto fronts. This is due to the comparatively similar vehicle characteristics that lead to a high η_V and s_g , notably a relatively large size. As discussed previously, for a low stagnation-point heat load, the vehicle mass should be low, so both θ_c and L_c should be low. However, since Q_s is not considered here as an objective, these influences do not drive by the optimizer. We show the parameter values, constraint function values, and selected performance criteria in Figs. 8.22, 8.23 and 8.24, respectively.

From Fig. 8.22c, it can be seen that the rear cone angle is near its maximum value of -5° on the entirety of the Pareto front. Such values increase the volume and therefore mass of the vehicle, increasing the range. Also, the shape will more closely approximate a sphere, increasing the volumetric efficiency. The vehicle length L_c can be seen from Fig. 8.22d to increase from its minimum value to higher values for the high s_g region of the front. Although this will decrease the volumetric efficiency, as can be deduced from regarding the shapes shown in Fig. 8.25, the mass (and therefore range) will be increased.

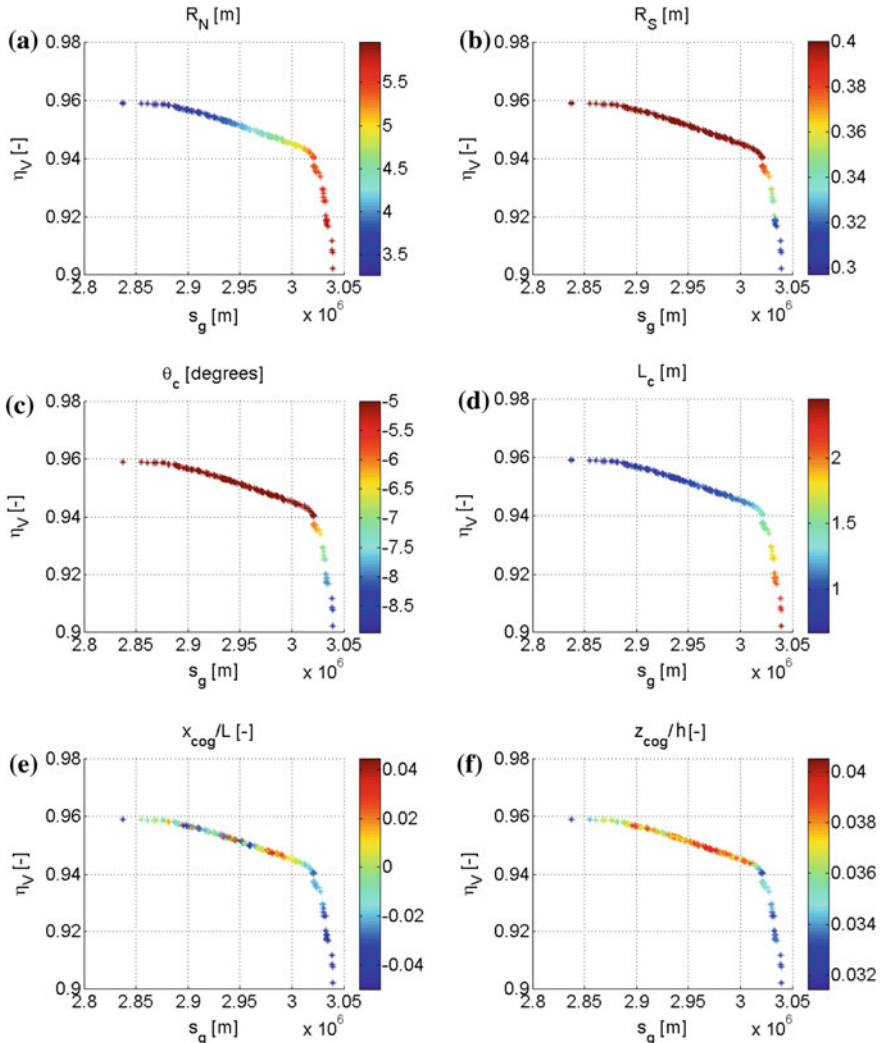


Fig. 8.22 Pareto optimal solutions for optimization of volumetric efficiency and range, colored by shape parameter values

Two kinks can be seen in the front, one near $s_g = 2.88 \cdot 10^6$ m and one near $s_g = 3.02 \cdot 10^6$ m. The latter of these can be seen to be associated with a deviation of R_S from its maximum value, at which it is for all values of s_g smaller than that at this kink. Additionally, for all values greater than that at the kink, the $\Delta\theta_s$ constraint is active. The activation of this constraint is the driving factor behind this kink in the front. The behavior of the Pareto-optimal solutions, however, is also driven by the corner-heating constraint, which is at its maximum value on almost all of the Pareto

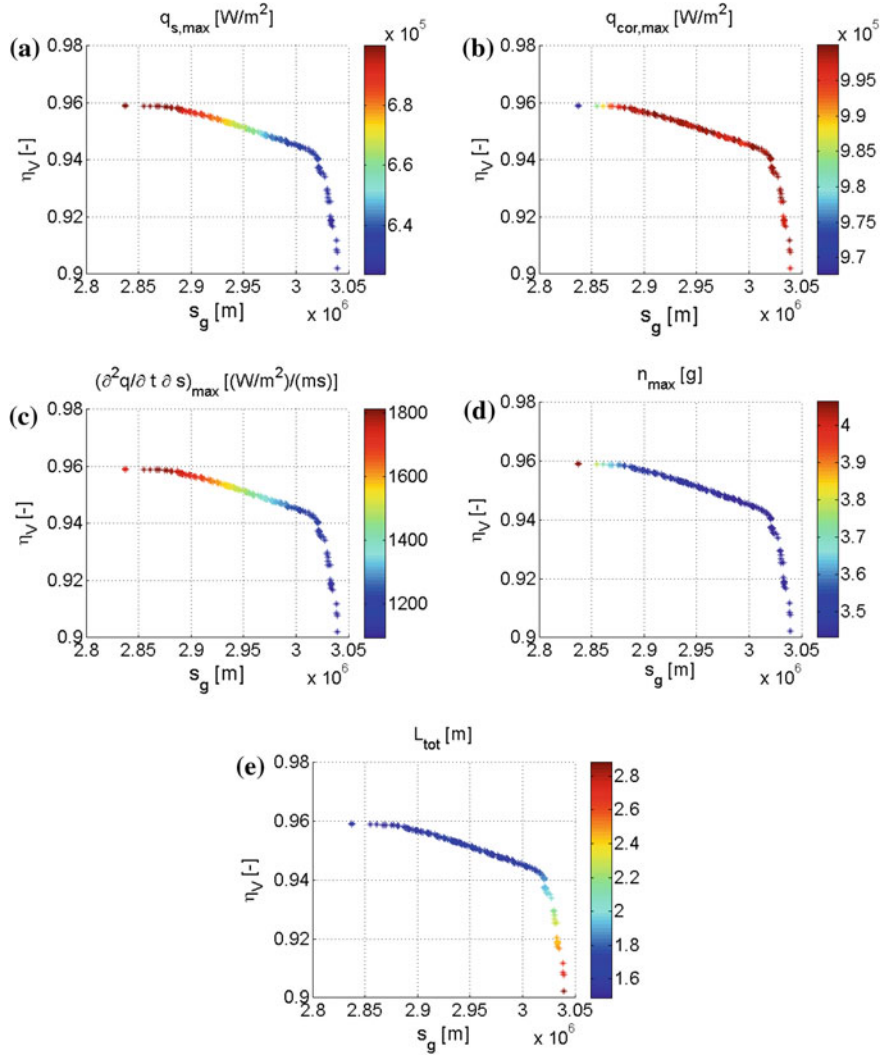


Fig. 8.23 Pareto optimal solutions for optimization of volumetric efficiency and range, colored by constraint function value

front. Since a higher absolute trim angle of attack positively influences the range, but negatively influences the corner heating, other measures are taken to compensate for this. Here, this can be primarily seen to be an increase in the nose radius, which will decrease the stagnation-point heating and therefore the corner heating. Also, the cone half-angle decreases slightly, although the variations in the other parameters are such that the mass still increases with increasing range. This change is mostly due to an increase in L_c . However, the increase in range for these solutions is at the

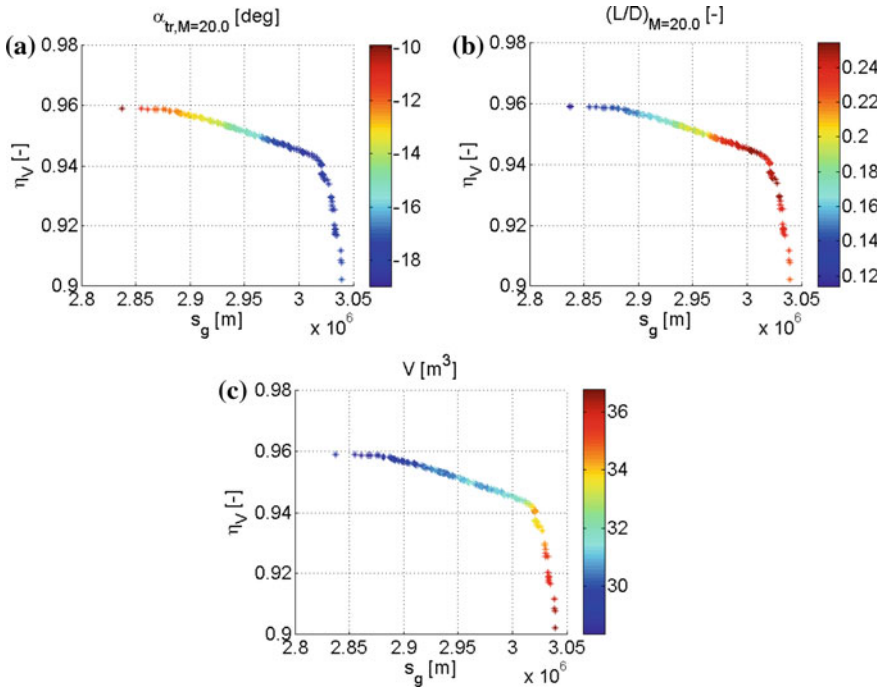


Fig. 8.24 Pareto optimal solutions for optimization of volumetric efficiency and range, colored by selected vehicle characteristics

expense of a substantial loss in volumetric efficiency. Regarding the shapes shown in Fig. 8.25, the vehicle shape for high range can be seen to differ relatively strongly from the other four shapes that are shown, much less closely resembling a sphere (for which $\eta_V = 1$).

For maximum η_V solutions, R_S and L_c are at their maximum and minimum values, respectively, and a change in these values is therefore unable to increase η_V . The value of R_N is near, but not on, its maximum value here, although a decrease to its minimum value would further increase η_V . However, the stagnation-point heating can be seen to be on its maximum value on the nearly horizontal part of the Pareto front, making a further decrease in R_N impossible. This limit the possibility of the volumetric efficiency increasing further.

Although both the maximum corner and stagnation-point heat rates are near their maximum values over the entire Pareto front (Fig. 8.23) the trend in their behavior is opposite. Specifically, the direction of increasing $q_{cor,max}$ is the direction of decreasing $q_{s,max}$. The cause for this is a change in the ratio of the two, the reasons for which are threefold. Firstly, the value of R_S decreases with increasing s_g , increasing the ratio. Secondly, the magnitude of the value of α_{tr} increases for increasing s_g (Fig. 8.24), also increasing the ratio between the heat fluxes. Thirdly, the ratio of R_m/R_N decreases for increasing s_g , also increasing the ratio. The fact that the heat

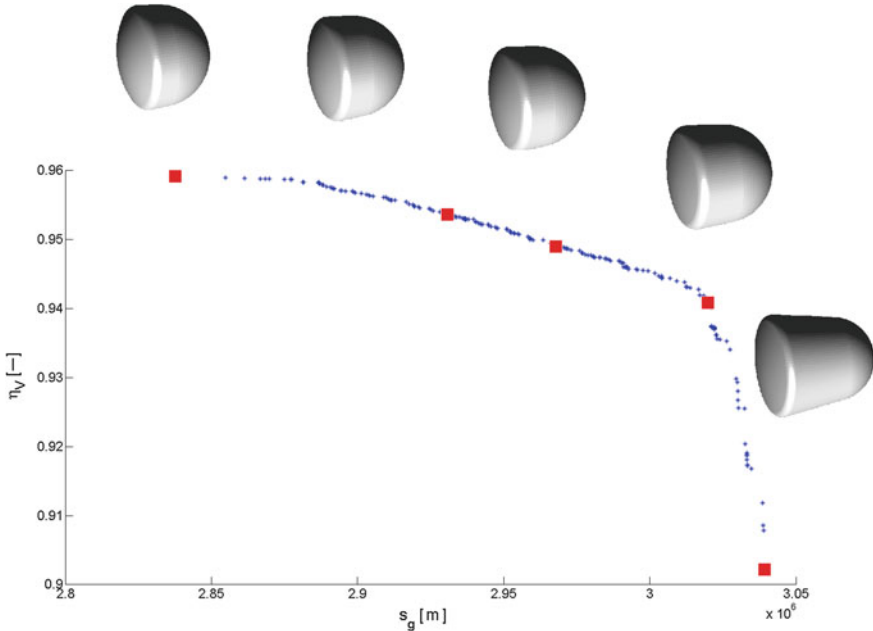


Fig. 8.25 Representation of evolution of capsule shape along $\eta_V - s_g$ Pareto front

rates are near their maximum values over the entire front is related to the fact that optimization of the heat load is not included in this case, so that phenomena that influence the heat load and rate similarly are not used by the optimizer to steer to a region of lower maximum heating.

The kink in the front around $\eta_V = 0.96$ is due to an inability by the shape to reach values significantly higher values of η_V (the front is nearly horizontal here). The left-most shape in Fig. 8.25 corresponds to this shape. It can be seen that only R_N is not on its boundary value here, which, as indicated previously, is due to the stagnation-point heating constraint. For reference, the shape of $\eta_V = 0.96$ is the left-most shape shown in Fig. 8.25, which can be seen to resemble a sphere with a ‘flattened side’ where the heat shield is.

Overall, the behaviour of this two-dimensional Pareto front can be summarized as follows:

- The range and volumetric efficiency are only weakly competing criteria, when compared to the other two two-dimensional optimization cases discussed in this chapter. As a result, this Pareto front is relatively sparsely populated and contains shapes with extremely high s_g , η_V and Q_s .

8.2.2 Three-Dimensional Optimization

Having evaluated the Pareto fronts of the three combinations of objective functions, the full Pareto front in three dimensions will be discussed to see how the two-dimensional optimal behavior carries over to the three-dimensional case. Due to the extra dimension in the Pareto front, the number of Pareto-optimal solutions that is found is significantly larger than in the two-dimensional case. This is because there is a greater chance that a given solution is ‘good for something’. The Pareto fronts are presented differently from the two-dimensional fronts: only the projections on the three planes are shown. The full front in three dimensions, as well as the projections onto the planes, is given in Fig. 8.26.

A first feature that can be observed is that the general shape of the Pareto fronts of two dimensions is correctly identified, with one small exception. The region of highest s_g in the concurrent s_g and η_V optimization is not identified by the three-dimensional optimization. This region was not identified in the two-dimensional optimization until a relatively late iteration. This shows the difficulty in finding this region, caused by the relatively sudden change in a number of parameters needed to identify this. Although this shows a shortcoming in the process, the region that is not identified is one that gives a marginal increase ($\approx 1\%$) in s_g at the expense of a relatively large decrease in η_V ($\approx 7.5\%$).

The sudden change in R_S that was observed in the η_V versus Q_s optimization can also be clearly seen in the three-dimensional front. The ‘band’ that runs across the front bisecting it into a region of high and a region of low R_S can be seen to pass through the s_g versus η_V front, on which a rapid change in R_S was indeed also observed. Although less apparent, the increase to near maximum θ_c , followed by a

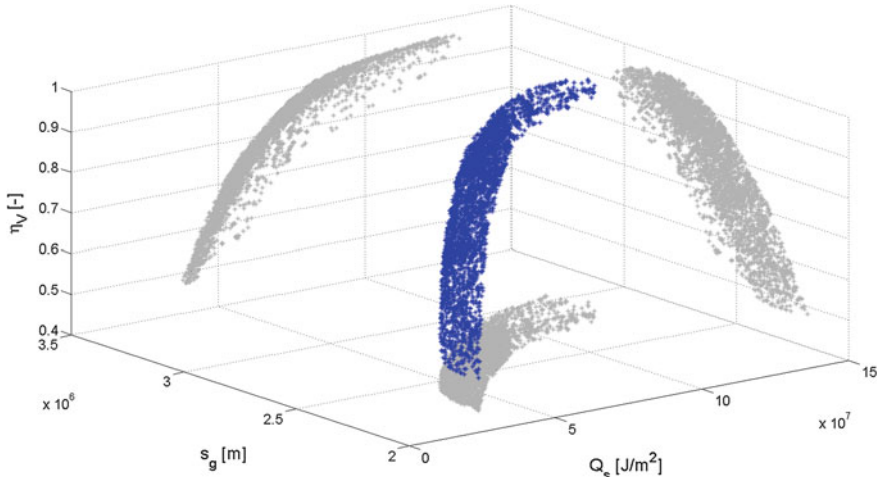


Fig. 8.26 Pareto front of benchmark results, plotted in the three objective functions, and projected onto the three objective planes

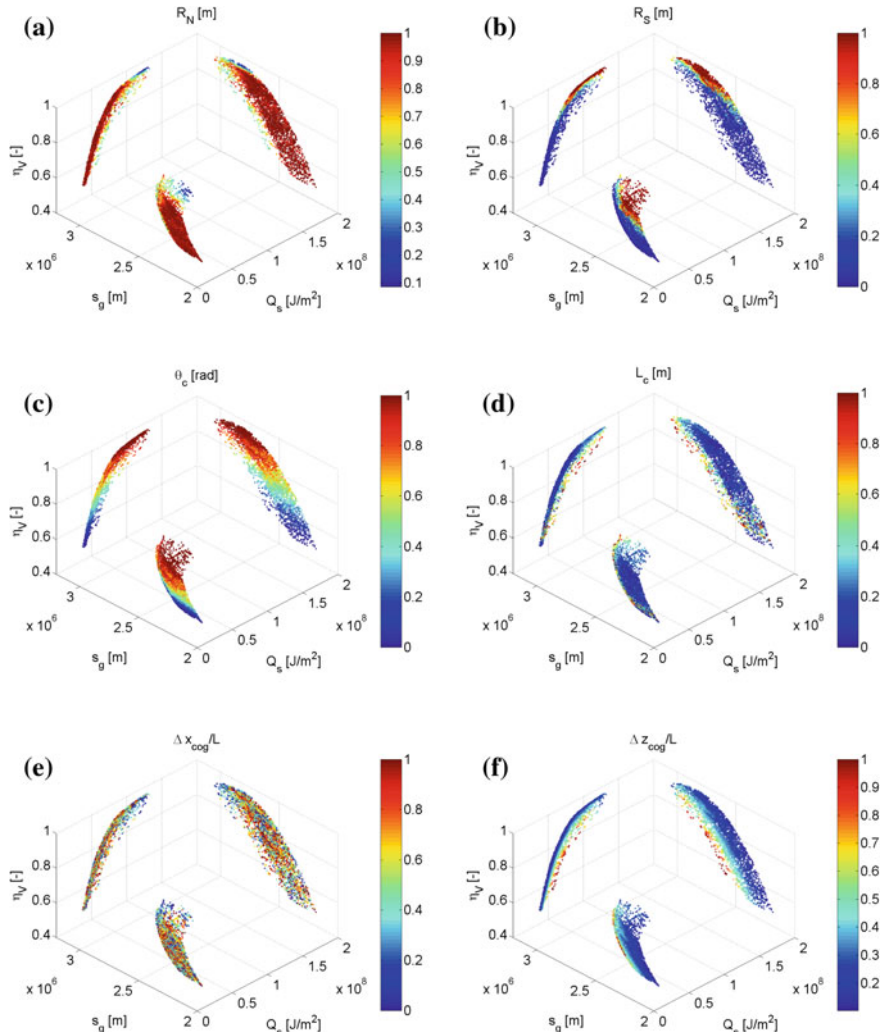


Fig. 8.27 Scatter plots of shape parameters, projected onto the three objective-function planes

small drop in its value that was theorized to be the cause of the sudden change in R_S can also be seen in three dimensional fronts.

The value of R_N can be seen to be at its maximum value over the majority of the three dimensional front, a feature that could not be identified when regarding the two-dimensional optimizations alone. It can be seen that the $s_g - Q_s$ front in the three dimensional projection has a very small band along the two-dimensional front of these two objectives, where R_N is not on or near its maximum value. Although this band is what is identified in Fig. 8.14a, the sudden increase in R_N very close to this band could not have been predicted from the 2 dimensional optimization.

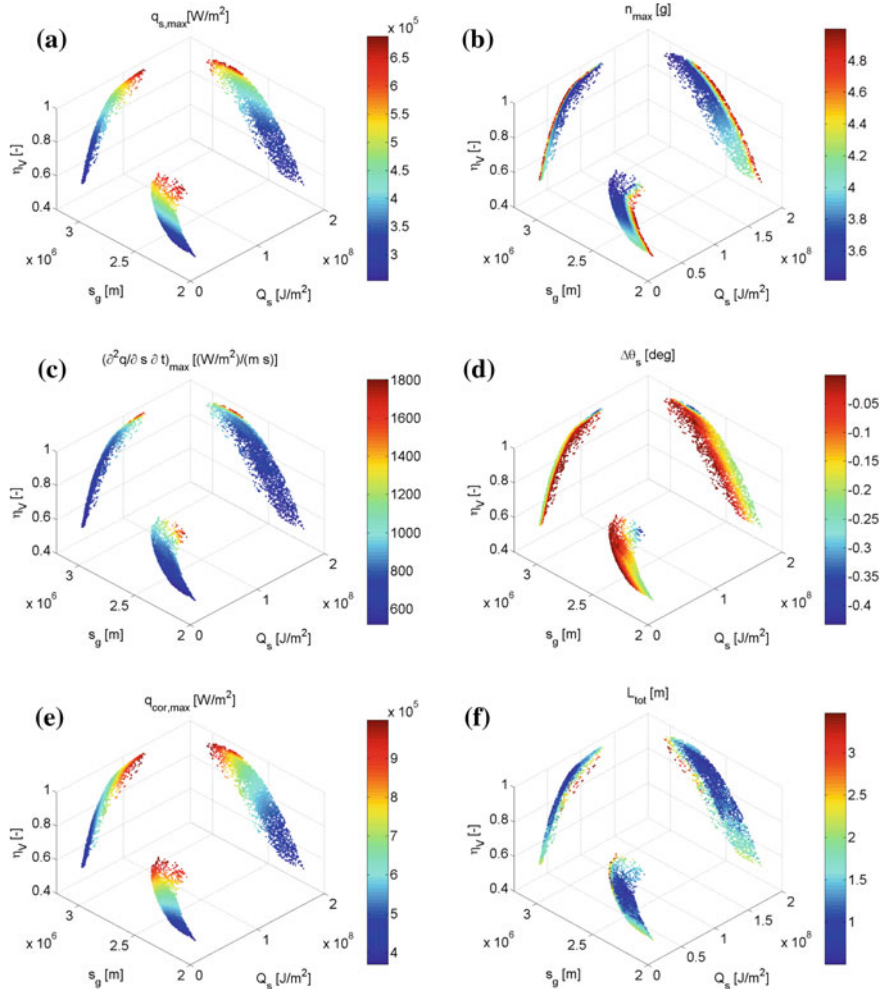


Fig. 8.28 Scatter plots of constraint function values, projected onto the three objective-function planes

Similarly, the value of the load factor has a band of around the maximum value of 5 g along the $\eta_V - Q_s$ Pareto front (Fig. 8.28). It decreases to a value of around or lower than 4 very rapidly when moving away from this band, though. These effects show the need to perform a three-dimensional optimization, as opposed to three separate two-dimensional optimization (combined with some sort of interpolation). As clarification, consider the case where a capsule is being designed for which η_V and Q_s are the primary objectives. If a two-dimensional optimization is performed, a high-load-factor capsule will be the likely result. The designers could choose to

accept a slight decrease in the main objectives for a substantial improvement in the load factor, though.

Although the three-dimensional Pareto front is filled relatively well with solutions, a region of greater sparsity is observed. This can be seen best in the projections of s_g versus η_V and Q_s versus η_V on the rightmost portion of the front for given η_V . From Fig. 8.27d, f, these solutions can be seen to correspond to the points on the two-dimensional front of Q_s versus s_g . This indicates that the Pareto optimal solutions have a stagnation-point heat load that is relatively much higher than that of the ‘nearly’ Pareto optimal solutions. This again indicates that, when considering only two objective functions, the decisions that can be made in a design process are limited by neglecting additional objectives. In this case, a solution very near to, but not on, the s_g - Q_s Pareto front can have a much higher volumetric efficiency than those that are on the s_g - Q_s front. Also, the solutions on this front show different behavior in solution space than those near it in objective space. Namely, the values of L_c , R_N and z_{cog}/h change rapidly from on, to nearly on, the s_g - Q_s front.

Now, from comparing the three dimensional to the previously discussed two-dimensional optimizations, the following can be concluded:

- The three-dimensional optimization is largely able to reconstruct the two-dimensional Pareto fronts.
- Three dimensional optimization shows features in objective space that could not have been reproduced by the combination of the two-dimensional results. Particularly:
 - The range versus heat load front differs strongly from the nearby solutions in objective space. This indicates the benefit of choosing a ‘slightly non-Pareto-optimal’ solution w.r.t. these two objectives if volumetric efficiency is of even slight interest.
 - The normal load is very high on the η_V - Q_s front, but decreases sharply when moving away from the front. Again, this indicates the usefulness of choosing a ‘slightly non-Pareto-optimal’ solution w.r.t. these two objectives if decreasing the normal load is of interest.
- The Pareto front is ‘bisected’ in the value of R_S , with associated ‘wiggle’ in the value of θ_c , for reasons discussed with the η_V - Q_s results.

8.3 Concluding Remarks

In this chapter, the results of the optimization of the capsule-shaped vehicle were presented. Here, a number of key features will be reiterated.

It has been shown that the behavior in both objective and solution space of the Pareto-optimal solutions is quite smooth, with the notable exception of the x -position of the center of mass. This is due to the very limited influence of this parameter on the performance, which causes the convergence of this parameter to the optimal solutions

to be slow. Its influence is limited to a change in angle of attack due to a change in pitch moment, which is in turn caused by a (small) change in the moment arm of (small) normal aerodynamic force. This is further reinforced by the fact that a clearer trend can be observed in the two-dimensional fronts than in the three-dimensional front. The z -position of the center of mass, though, strongly influences the solutions due to the fact that it is determining for the moment arm of the (large) axial force.

In the optimization results, the stagnation-point heat load was found to compete strongly with both of the other objective functions, so that, generally, an increase in one of them would also increase the stagnation point heat load. The volumetric efficiency and vehicle range objectives drive the optimizer to similar regions of the solution space, as it is advantageous for both objectives to have a relatively large vehicle. Nevertheless, there remains significant competition between the two objectives, especially in the more extreme values in objective space.

The optimization clearly showed that the mass of the vehicle is the main driver behind increasing the range of the vehicle. This is due to the fact that a vehicle of higher mass, but similar frontal area, will have a high ballistic coefficient, so that it is less strongly affected by the aerodynamic force. This will in turn cause the vehicle to retain a greater fraction of its kinetic energy for a longer time during the beginning of the entry, so that it covers a larger range.

Also, it was observed that the maximum load factor decreases sharply when moving away from the $Q_s\text{-}\eta_V$ Pareto front. The normal load is the constraining factor for the low range/low heat load solutions, as these shapes typically fly at a low absolute angle of attack to reduce the L/D and thereby reduce the total flight time. For the $Q_s\text{-}\eta_V$ optimization, the load factor is near its maximum prescribed value on the Pareto front, since the range objective, which should normally drive the optimizer towards an increased L/D and decreased normal load, is not included here. A strong decrease in normal load (from 5 g to about 3.5–4 g) can be achieved by moving slightly away from the two-dimensional $Q_s\text{-}\eta_V$ front onto the three-dimensional front and allowing higher range solution to dominate lower range solutions. This means that, if a low normal load is of even limited interest, the capsule shape should not be optimized for volumetric efficiency and heat load alone.

Similar to the previous point, the vehicle shape changes substantially when moving slightly away from the $s_g\text{-}Q_s$ front. A number of parameters, namely the z -position of the center of mass, the nose radius and the vehicle length change very strongly when moving slightly away from this two-dimensional front. The volumetric efficiency increases strongly when moving over the three-dimensional front. This indicates that changes in these parameters cause a marginal improvement in range and heat load for a relatively large penalty in volumetric efficiency. This means that, if volumetric efficiency is of interest in a vehicle design, range and heat load should not be the only objectives in an optimization effort.

The previous points show that the three-dimensional Pareto-optimal behavior cannot be fully deduced from the combination of two-dimensional Pareto-optimal behaviors. Especially the two-dimensional front of heat load and range shows strongly different behavior in solution space to the nearby ‘nearly two-dimensionally Pareto-optimal’ solutions in objective space, as discussed in the previous point. Also, the

normal load is at its maximum value on most of the $Q_s - \eta_V$ two-dimensional front and decreases strongly when moving away from this front. This behavior shows the use for performing a multi-dimensional optimization.

Finally, we found that the vehicle side-radius takes either its minimum or its maximum value on the three dimensional Pareto front. The side radius changes very suddenly over a very thin band of solutions in objective space in which the transition takes place. This change is accompanied by a similarly near-discrete change in the absolute value of θ_c . This anomaly stems from the stronger influence of the rear cone angle on the volumetric efficiency, so that this value is increased to its absolute minimum before increasing the side radius. The limited influence of the side radius on vehicle performance causes the parameter to change very strongly over nearby solutions in objective space.

Concerning the constraint function values and influence, thermal constraints (stagnation-point heat flux and corner heat flux) are active for high range/high volumetric efficiency. This is due to the fact that the flight time is long for high-range solutions, which leads to a large heat load. Also, the fact that high volumetric efficiency solutions have a small nose radius, increasing the stagnation-point heat flux, is of influence. The load factor constraint is only active for low heat-load solutions, due to the fact that these vehicles fly at a low absolute angle of attack to minimize lift over drag and thereby flight time. However, this also increases the load factor. The stagnation-point location constraint is active for the high-range solutions. This is due to the fact that the vehicle flies at a high absolute angle of attack here to increase L/D , causing the stagnation point to lie closer to the corner. Finally, the vehicle length, as limited here, was found to be the constraining factor for any of the solutions on the Pareto front, likely due to the fact that other constraints are active before the length constraint.

As a final note, it is interesting to compare the shapes plotted on the Pareto fronts in Figs. 8.17, 8.21 and 8.25. In particular, there is a clear difference between the typical shapes of the Apollo and ARD capsule and the optimal capsule shapes that we obtain here. The shapes shown in our figures more closely resemble the Soyuz entry capsule, which has a higher volumetric efficiency. However, in the results presented here, we have not included any considerations of internal systems/cargo volume requirements, which would undoubtedly constrain the search space. Such an approach, which would employ MDO methods and models, would be the natural extension of our approach.

Chapter 9

Shape Analysis - Winged Vehicle

This chapter will present the results of the optimization of the winged entry vehicle, for which the parameterization is given in Sect. 5.2. The settings for the simulations were given in Sect. 3. As an example, we show several views of a typical winged-vehicle shape in Fig. 9.1, for which we describe the generation in great detail in Appendix B.

A Monte Carlo analysis is performed to gain some insight into the behaviour of the solutions and to finalize the choice of parameters and allowable constraint-function values. This analysis is presented in Sect. 9.1. Subsequently, Sect. 9.2 presents the results of the optimization. Finally, Sect. 9.3 will present a number of general concluding remarks concerning the optimization.

9.1 Monte Carlo Analysis

This section will show the results of the Monte Carlo simulation of 1,000 randomly generated winged vehicles. By randomly varying the shape-parameter values, we get an overview of how the mapping from parameter to objective space behaves. Also, it provides us with insight into the behaviour of the constraint functions, aiding us in the selection of realistic and practical constraint-function values. The presentation will be different from that of the Monte Carlo analysis for the capsule shape, as given in Sect. 8.1, since the number of shape parameters is much larger here. Consequently, presenting scatter plots of the constraint and objective functions for all parameters is not an efficient manner of presenting the results. For all combinations of parameters and objectives/constraints, the correlation coefficients will be presented, with the behavior of selected parameters discussed in more detail. Interpretation of these coefficient should be done with caution, since a correlation does not imply a dependence. However, it is deemed an efficient manner of gaining insight into the behavior of the vehicle's performance.

Due to the interdependent nature of how the values of parameters r_x translate into physical parameters x (see Chap. 5), especially for the fuselage, it is expected

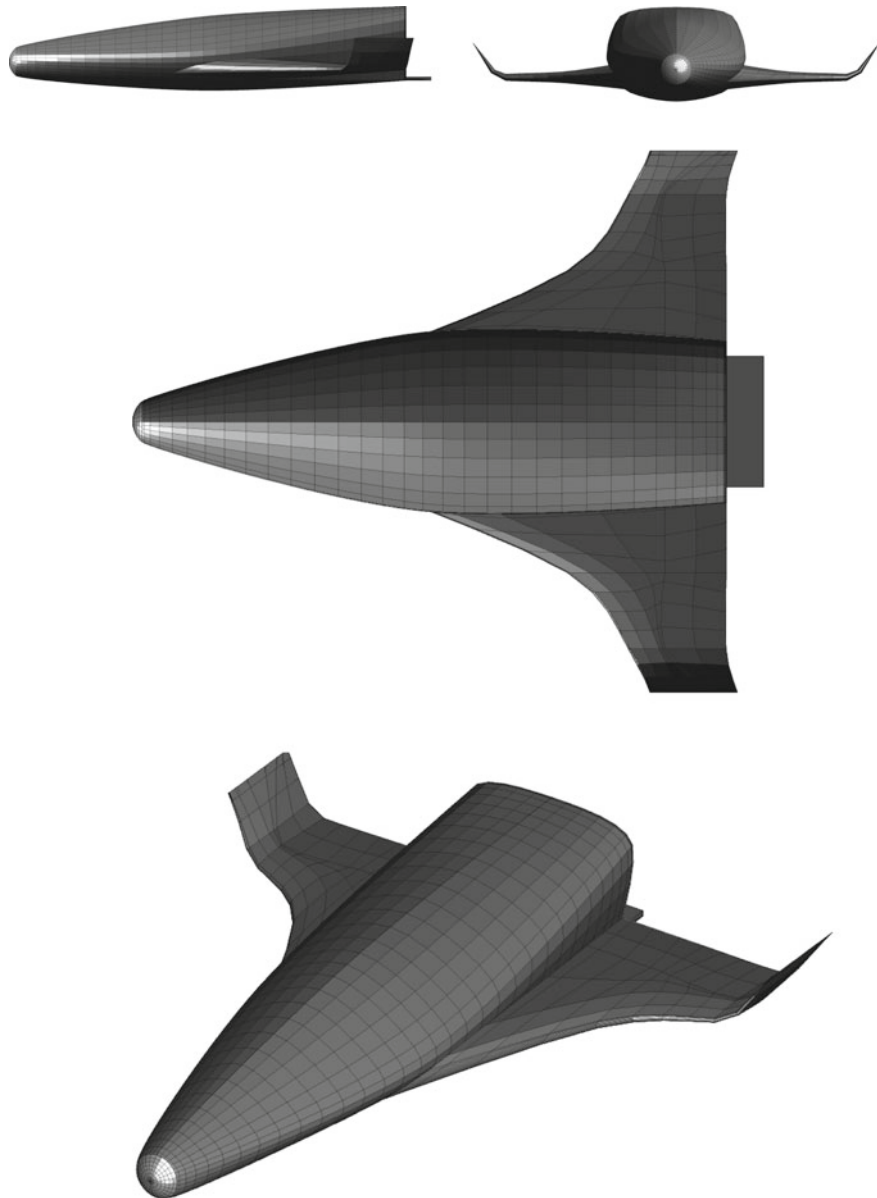


Fig. 9.1 Several views of a representative winged-vehicle shape (see Appendix B for details on generation)

that there will be less strong trends between the parameters and constraints, as well as between parameters and objectives. Moreover, the number of parameters that contribute to the final performance is significant, so that different combinations of parameter values can result in specific physical behaviour, in a manner which may not be immediately obvious from a Monte Carlo analysis.

Histograms for the behavior of the constraint functions are shown in Fig. 9.2. The correlation coefficients between parameters and constraints/objectives given in Table 9.1. These correlation coefficients are computed from the data sets using standard statistical tools discussed by e.g., Dekking et al. (2005). The yaw and roll constraints are omitted from the results presented in this section, as it was found that the randomly generated vehicles rarely (<5 %) violate these constraints and they are rarely the only active constraint. In general, the constraint and objective functions lie in the range that is to be expected based on data from past and current entry vehicle analyses. We will now elaborate on some features of the constraint-function behaviour.

The maximum stagnation-point heat flux lies mostly between 600 and 1200 kW/m² (Fig. 9.2a), which corresponds well to the range of maximum entry heat fluxes for existing vehicles, as shown in detail by Hirschel and Weiland (2009). In light of these results, the reference heat flux that was chosen (700 kW/m²) appears to be a reasonable choice, as most vehicles reach this value, with relatively small overshoot.

The maximum heating at the leading edges is slightly lower than that at the stagnation point, but the values can be seen to be quite similar. This was to be expected from data from, for instance, the Space Shuttle. Despite the fact that the leading edge is allowed to reach a radius of curvature half that of the nose, the maximum leading-edge heating that is found to occur is about 700 kW/m². This is due to the fact that in addition to the dependency on freestream density and velocity and the radius of curvature, the value of $q_{LE,max}$ is also dependent on the shape of the leading edge. Specifically, the wing sweep angle reduces the heating at the leading edge. This is because the maximum value of Eq. (3.4) will depend on the values of x and Λ over the leading edge. These dependencies are shown in Table 9.1, where a clear correlation between both $\frac{x_{w,2}}{x_{w,1}}$ and $\frac{x_{w,3}}{x_{w,1}}$ and the value of $q_{LE,max}$ can be seen. The sign is different for these correlations. This is counterintuitive, as it would be expected that a large value for both of these ratios would result in a low value of Λ and a resultant large value of q_{LE} . However, interdependencies must be considered when interpreting the correlations. Here, this is due to the fact that the maximum value of $\frac{x_{w,3}}{x_{w,1}}$ is determined by the value of $\frac{x_{w,2}}{x_{w,1}}$ (see Table 5.2). Consequently, a large value of $\frac{x_{w,3}}{x_{w,1}}$ would decrease the expectation value of the maximum value of Λ in the region between contours 2 and 3 of the wing. Similarly, the wing leading-edge heating increases with increasing $y_{w,1}$ and decreases with L_w (although relatively weakly so). Although the former of these is intuitive, as an increase in wing 68 span decreases the sweep angle Λ .

The maximum load factors that occur during the entries are shown in Fig. 9.2c. It can be seen that the largest values that occur are similar to the lowest values found in the capsule Monte Carlo analysis (see Sect. 8.1), indicating a fundamental difference

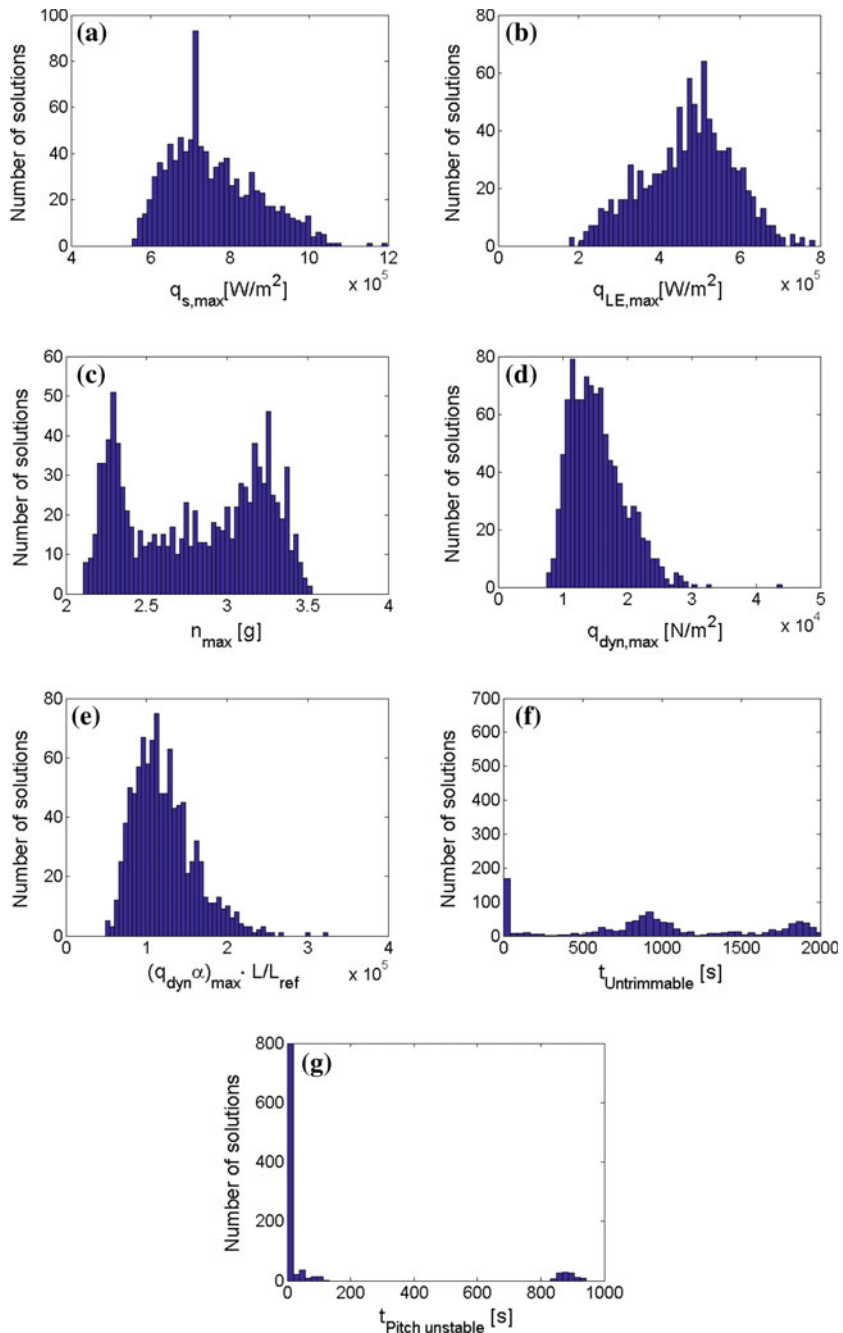


Fig. 9.2 Histograms of constraint function values for 1,000 randomly winged entry shapes (roll and yaw constrained not shown)

Table 9.1 Correlation coefficients ($\times 10$) between shape parameters and constraint/objective function values (dimensionless). Correlations >0.4 are shown in bold

	q_s, max	q_{LE}, max	n_{max}	$q_{\text{dyn}}, \text{max}$	t_{untrim}	$t_{\text{yunst.}}$	$t_{\text{xunst.}}$	$t_{\text{zunst.}}$	m	s_g	V
R_N	-8.626	0.623	-8.583	0.759	-0.992	-0.358	0.035	-0.463	2.057	-0.379	2.630
θ_N	0.417	0.090	0.951	1.219	0.237	0.506	0.167	0.279	-1.822	0.756	-2.384
Δx_1	0.349	-0.915	1.075	1.952	-0.150	0.277	-0.368	-0.157	3.283	2.078	1.227
$z_{2,1}$	1.354	0.609	0.350	2.105	-1.428	-1.179	0.342	0.454	0.394	2.388	2.853
$y_{2,2}$	-0.359	-0.285	-0.802	-1.495	1.075	1.570	-0.581	-1.826	4.984	-1.802	6.082
$z_{2,2}$	0.768	-0.185	0.870	0.669	-1.061	-0.793	-0.040	1.177	0.229	0.848	0.863
$y_{2,3}$	-2.682	-1.465	-1.323	-4.810	1.426	2.039	0.038	1.070	2.592	-5.691	3.147
$z_{2,3}$	-1.086	-0.990	-0.122	0.955	0.268	1.067	-0.777	-1.213	-0.034	-0.369	-0.359
$z_{2,4}$	0.444	0.449	-0.382	-1.136	1.103	-0.428	0.098	-0.641	0.173	-0.381	0.699
$z_{3,1}$	-0.222	0.811	-0.152	-0.441	0.025	1.163	0.093	-0.158	0.399	-0.614	0.983
$y_{3,2}$	0.210	-0.005	-0.547	-0.644	0.676	1.613	0.238	0.660	1.348	-0.367	2.368
$z_{3,2}$	-0.359	0.211	-0.476	-0.036	-0.667	-0.237	0.128	-0.478	0.179	-0.052	0.359
$y_{3,3}$	0.635	0.442	0.816	1.590	-0.964	-0.529	0.566	-0.652	0.863	1.481	0.822
$z_{3,3}$	1.714	1.044	1.380	1.315	-0.004	-1.174	0.917	-0.644	1.531	2.335	-0.480
Δx_2	0.107	-0.940	0.413	2.937	-0.207	-0.137	0.520	0.173	5.094	2.549	3.579
R_{LE}	0.467	-4.624	0.413	-0.429	-0.446	-0.960	-0.178	-0.138	-0.126	-0.103	-0.122
$t_w/2$	-0.561	-0.283	-0.616	-0.421	-0.529	-0.591	0.082	0.063	-0.533	-0.298	0.249
$x_{w,t}$	-0.245	-0.246	-0.119	0.770	1.978	0.279	0.225	-0.023	0.066	0.208	0.026
L_w	-0.388	-2.412	0.484	2.591	-1.737	-1.882	-0.183	0.413	1.598	2.314	0.148
θ_{LE}	0.918	0.481	0.552	-0.046	-0.109	-0.201	0.377	-0.211	-0.605	0.147	-0.586
$x_{w,2}$ $x_{w,1}$	0.174	-3.432	0.550	0.048	-1.039	-0.573	-0.025	0.684	0.370	0.044	-0.261
$x_{w,3}$ $x_{w,1}$	-0.325	6.410	-0.468	-1.569	-1.505	-0.045	-0.145	0.205	0.840	-1.095	-0.152
$x_{w,4}$ $x_{w,1}$	0.535	0.193	0.041	-0.109	0.912	0.102	0.485	0.470	-0.141	0.128	-0.519
$y_{w,1}$	-0.981	1.512	-0.320	-1.151	-1.008	-1.579	-0.609	0.932	3.324	-1.452	0.493
$y_{w,3}$	0.365	-0.681	0.106	0.350	0.610	0.818	-0.115	0.082	0.358	0.382	0.291
Δx_f	-0.784	0.036	-0.916	0.247	-0.240	0.218	-0.018	-0.414	0.209	-0.118	0.647
θ_f	0.057	0.055	-0.109	-0.179	-0.282	0.299	0.332	-0.820	0.560	-0.052	0.545
f_{el}	-0.380	0.150	-0.483	-0.264	-1.291	0.235	0.241	0.290	-0.357	-0.191	-0.306
L_{bf}	-0.322	-0.479	0.514	0.970	-2.870	-1.130	-0.314	0.254	0.072	0.780	-0.235

between the two types of vehicles and their respective trajectories. Comparing these to the simplified model for an equilibrium glide (Regan and Anandakrishnan 1993), the load factors that occur are larger than would be expected from this approximation. Clearly, the deviations from the equilibrium glide are important when determining the load factor, as was to be expected. It can be seen from Table 9.1 that the maximum load factor is strongly negatively correlated to the vehicle nose radius. Although this is not immediately obvious from physical considerations, a number of factors contribute to this. Primarily, it is a result of the fact that the guidance law is heat-flux-tracking based. A smaller nose radius and consequent larger heat flux causes the vehicle to begin its nose-down maneuver later in its flight, since it takes longer for the

heat flux to go back down to the reference heat flux value $q_{c,ref}$, which will influence the maximum value of the load factor. A reason for this is that the longer the vehicle flies at large angle of attack, the more kinetic energy it loses at large altitudes. When initiating the nose-down maneuver, the drag is reduced and the vehicle will subsequently have a larger velocity for a given altitude and density. Therefore, having a large maximum heat flux will reduce the maximum load factor, since these vehicles lose more energy at large altitudes and low densities.

An important parameter for a number of constraints is $y_{2,3}$, as can be inferred from Table 9.1. This parameter determines the width of the vehicle bottom on the middle contour. This parameter will have a large influence on the size and shape of the frontal area of the vehicle at large angles of attack, which is the configuration in which the vehicle initiates its entry. Since an increase in its value will result in an increase of the drag area $C_D S_{ref}$ and therefore a lower ballistic coefficient (see Sect. 2.2.3) at $\alpha = 40^\circ$, the vehicle will lose kinetic energy more quickly. As such, the vehicle will experience lower loads at larger densities, explaining the decrease in heating, dynamic pressure and normal load. Associated with these decreases in constraint functions, though, is a decrease in vehicle range, since the quick loss of kinetic energy means that the vehicle will spend less time at large velocities, thereby decreasing its range.

Similarly, an increase in dynamic pressure is observed with increasing Δx_1 and Δx_2 . Increases in both of these parameters cause the vehicle to become heavier, thereby encountering maximum dynamic pressure deeper in the atmosphere. Similarly, the vehicle's range is positively correlated with large values of these parameters. Also, the mass and volume are, obviously, strongly coupled to their values. The reason for the slight decrease in leading-edge heating is due to the fact that the wing length's maximum is a fraction of the vehicle length. This means that an increase in vehicle length means an increase in wing sweep angle.

As the vehicle width is allowed to be greater than its height, the values of y on the fuselage can, in general, be seen to have a stronger impact on the values of m and V than the values of z . Also, values of y and z on the middle contour have a larger influence than those on the rear contour. The reason for this is that the values at the middle will influence the shape of the entire fuselage, while those at the rear are only of influence on the rear half of the fuselage.

To see what the general effect of constraint-function values on the Pareto-front shape is, the feasible solutions for a number of different constraint-function values are given in Figs. 9.4, 9.5, 9.6 and 9.7. For comparison, the unconstrained scatter is given in Fig. 9.3.

Based on the experience of previous winged entry vehicles, (e.g., Hirschel and Weiland 2009), and the results here, coupled with a desire to not overly restrict the search space, has led to the following choices for the constraint function values:

- $q_{s,max} < 1,000 \text{ kW/m}^2$
- $q_{LE,max} < 600 \text{ kW/m}^2$
- $q_{dyn,max} < 25,000 \text{ N/m}^2$
- $(q_{dyn}\alpha)_{max} \frac{L}{L_{ref}} < 4,400 \text{ N}\cdot\text{rad/m}^2 (\approx 250,000 \text{ N}\cdot\text{deg/m}^2)$
- $n_{tot,max} < 3.25$

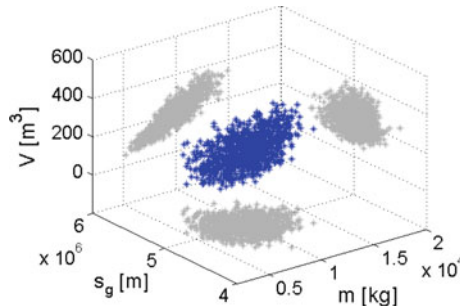


Fig. 9.3 Scatter of Monte Carlo solutions in performance space (blue), projected onto planes (red)

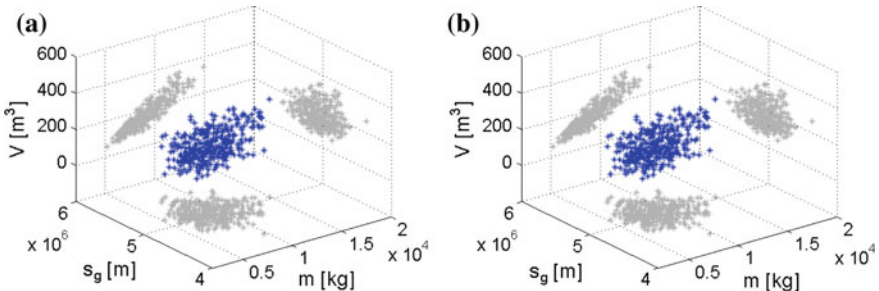


Fig. 9.4 Solutions from Monte Carlo analysis that violate the constraint for $q_{s,max} = \mathbf{a}$ 800 kW/m², \mathbf{b} 1000 kW/m²

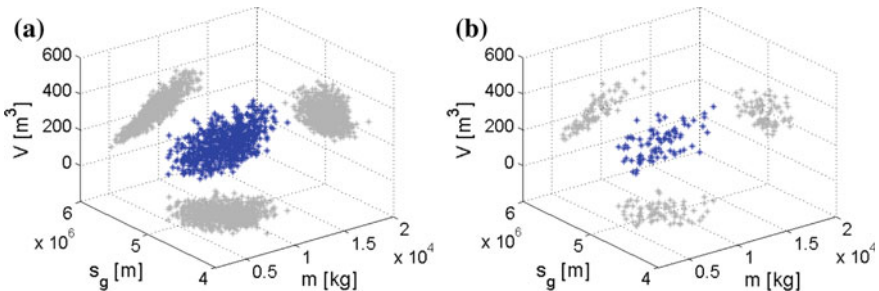


Fig. 9.5 Solutions from Monte Carlo analysis that violate the constraint for $q_{LE,max} = \mathbf{a}$ 400, kW/m², \mathbf{b} 600 kW/m²

Some of these values, namely the dynamic-pressure values, may seem to be excessive. By choosing these values, though, the behavior of the Pareto-optimal solutions over a greater portion of the objective space can be examined. Recent or near-term technological developments could allow vehicles and its contents to withstand larger loads than, for instance, the Space Shuttle. This makes the investigation of vehicles undergoing such loads of practical interest.

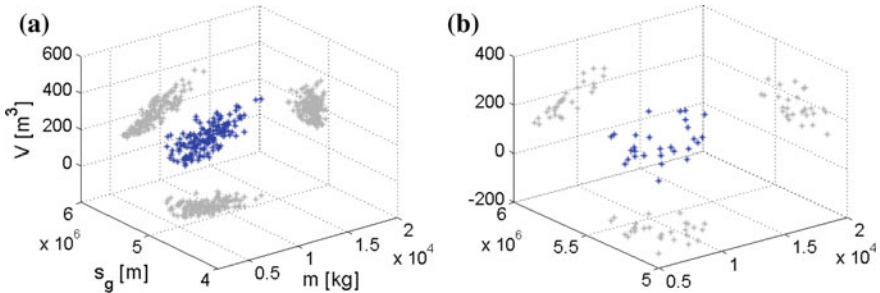


Fig. 9.6 Solutions from Monte Carlo analysis that violate the constraint for $q_{dyn,max} = \mathbf{a}$ 20,000 N/m², \mathbf{b} 25,000 N/m²

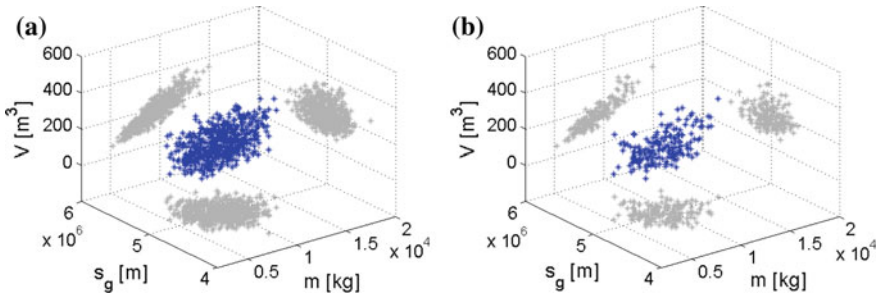


Fig. 9.7 Solutions from Monte Carlo analysis that violate the constraint for $n_{tot,max} = \mathbf{a}$ 2.75 g, \mathbf{b} 3.25 g

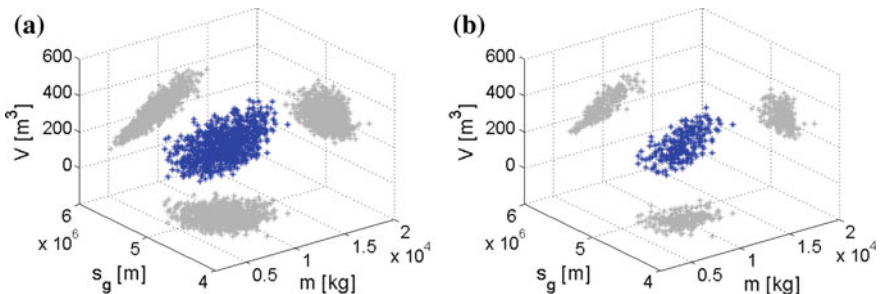


Fig. 9.8 Solutions from Monte Carlo analysis that violate the constraint for **a** Trim constraint **b** Pitch stability constraint (for $\alpha > 25^\circ$)

For completeness, the infeasible solutions when considering only one of the stability and control constraints are shown in Fig. 9.8. The trim constraint, which is the most active, can be seen to make solutions infeasible throughout the objective space, with no obvious bias in any direction. The pitch-stability constraint, however, is much more active in the low-range region of the objective space. As can be seen

from Table 9.1, the parameters most strongly correlated with pitch stability generally have opposite influences on pitch stability and range.

9.2 Optimization Results

In this section, we present the results of the shape optimization of the winged-vehicle parameterization described in Sect. 5.2, using the settings given in Sect. 7.3. First, the baseline optimization case will be discussed in Sect. 9.2.1. Subsequently, the results when considering the pitch stability constraint for all angles of attack are presented in Sect. 9.2.2. Finally, we investigate the influence of using the total time at reference heat rate instead of the ground-track length as an objective (keeping the other two objectives the same) in Sect. 9.2.3.

It must again be stressed here that all parameter values on the Pareto front are presented using the associated parameter values r_x for parameters x , as shown in Eq. (5.1) and accompanying text.

9.2.1 Baseline Optimization

We will now present and discuss the results of the optimization of the winged vehicle shape. The size of the solution space for the winged vehicle is much larger than of the capsule-shaped vehicle (29-dimensional, compared to 6-dimensional). Therefore, only the results of the three-dimensional optimization will be discussed in detail.

Nevertheless, both a run with three objective functions and three runs with each combination of two of the objectives are performed, as was done for the capsule-shaped vehicle. For the 3D (e.g. where all three objective functions are considered) optimization, 400 iterations were used, and 200 for each of the 2D (e.g. where all three objective functions are considered) optimizations. Figure 9.9 shows the 3D Pareto front, with projections onto each of the planes. In Fig. 9.10, the Pareto fronts as obtained from the 2D and 3D optimizations are compared for each of the combinations of objective functions. Each of these fronts is the Pareto front, taking into account only two of the three objectives, as obtained from the final 3D and 2D Pareto optimal solutions. The discrepancy between the Pareto fronts of $s_g - m$ and $s_g - V$ is significantly greater than the differences that were observed in the case of the capsule. This indicates that the winged vehicle shape is a much more difficult problem to optimize and that the 3D optimization has not fully converged to the boundaries of the Pareto front in 400 iterations. However, overall trends in the behavior of the parameters and constraints over the 3D fronts can clearly be observed. To get a sense of both the evolution of the Pareto front and the look of the winged vehicles, the evolution of the minimum mass winged vehicle with $s_g > 5100$ km and $V > 400$ m³ are given in Appendix D.1. In addition, the external shape of a number of solutions from the final Pareto front are shown in Appendix D.2.

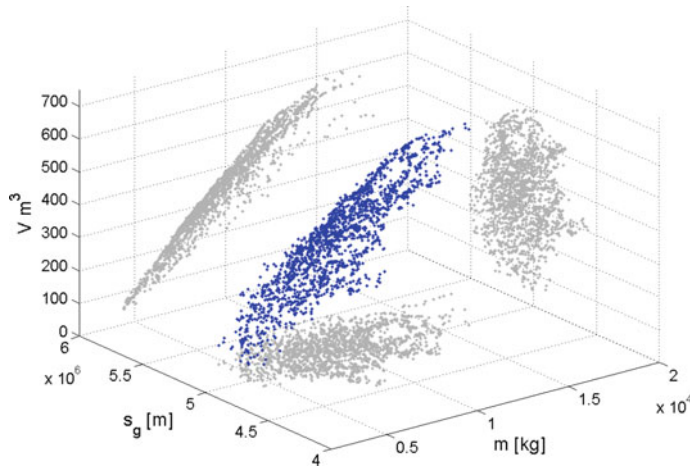


Fig. 9.9 Pareto front of benchmark results, plotted in the three objective functions, and projected onto the three objective planes

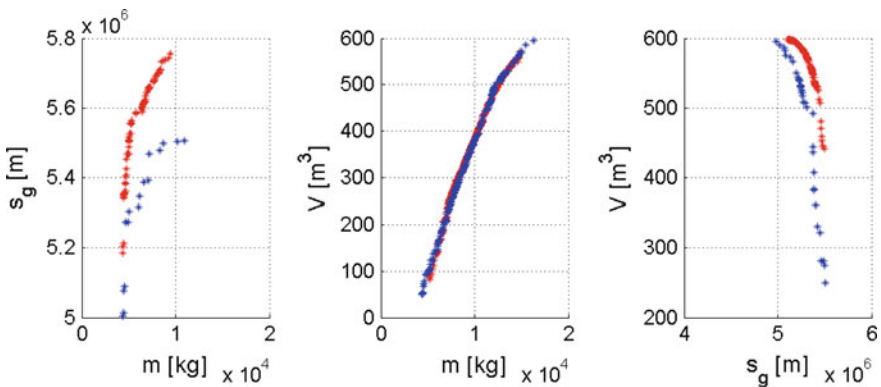


Fig. 9.10 Comparison of two-dimensional Pareto fronts obtained from dedicated two-objective optimizations (red) and three objective optimization (blue)

First, the trajectories of the optimal solutions will be analyzed, with trajectory constraints and a number of key figures of merit of the trajectories being discussed. Subsequently, the behaviour of the optimal fuselage and wing shapes will be presented.

Vehicle Trajectories

A number of quantities related to the trajectories of the Pareto-optimal solutions is shown in Fig. 9.11. Since the value of s_g is the only one of the three objectives that is influenced by the trajectory, special attention will be paid to the factors influencing this quantity. In the discussion here, the nomenclature from Sect. 2.3.2 regarding the different phases of the entry will be used. In the subsequent discussions on the winged vehicle trajectories, the term ballistic coefficient will again be used to denote the quantity B denoted by Eq. (2.36).

The relation between the total vehicle range, and the values of L/D and ballistic coefficient B during the initial phase of the entry, during which $\alpha = 40^\circ$, are shown in Fig. 9.11a, b. Although the aerodynamic coefficients are not invariant during this phase, their variations are very small (see Sects. 3.1.2 and 3.3), meriting the consideration of the value only at $M = 20$. From the figures, it can be seen that there is a relation between the initial L/D and total range and an even clearer relation between the initial ballistic coefficient and total range. The relation between the ballistic coefficient and s_g is due to the fact that this indicates that vehicles with large ballistic coefficient are less affected by atmospheric drag during the initial entry phase. Therefore, they decelerate less quickly and cover a larger range. The importance of the range covered while $\alpha = 40^\circ$, between t_0 and t_2 (see Sect. 2.3.2) can be deduced from Fig. 9.11c, d. The fraction of the range that is covered before t_2 is always greater than 0.5, with maxima around 0.675. By comparison, the range covered during the heat-rate tracking is between 0.1 and 0.25 of the total range.

Figure 9.11e, f show the velocity and density at the initiation of the heat-rate tracking, at $t = t_2$. A clear feature is visible in both of these figures, delineating a maximum V and a minimum ρ . Further investigation of these features showed that these are the solutions for which $q_{s,max} < q_{s,ref}$, so ones for which $t_1 = t_2$ and the time of heat-rate-tracking initiation coincides with the point of maximum heat rate. There is very little variation in the velocity here (~ 20 m/s), but more significant variation in the variation of the density. This result can be compared to the result for the point of maximum heat rate when making the equilibrium glide, non-rotating Earth assumption (Regan and Anandakrishnan 1993). In such a case the velocity here is always a factor $\sqrt{\frac{2}{3}}$ of the orbital velocity (assuming laminar flow), whereas the density is a function of the vehicle lift coefficient and mass. The velocity and density at which maximum heat flux occurs here is substantially different from the result of the aforementioned assumptions, though. A velocity of about 7,000 m/s is the average, whereas a value of around 6,350 m/s (depending on the exact altitude), would be expected from the simplified theory. Still, the fact that the velocity at t_1 remains mostly invariant for the shapes considered is interesting, as it shows that removing the equilibrium-glide assumption does not very strongly negate the result of invariant velocity at maximum heat transfer.

Figure 9.12 shows the constraint function values of the Pareto-optimal solutions. A very distinctive and unexpected feature can be seen in the normal-load behavior Fig. 9.12c. In this figure there is a clear demarcation of region of $n \approx 2$ and $n \approx 2.75$.

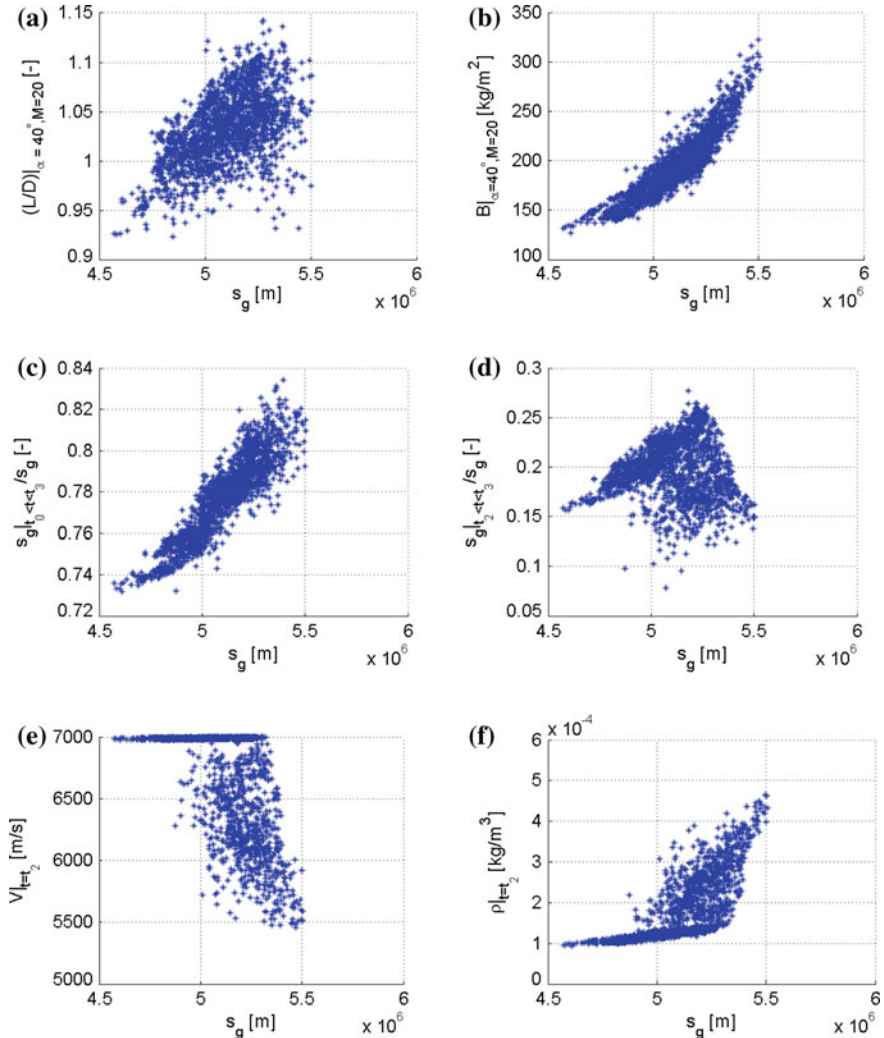


Fig. 9.11 Selected trajectory parameters of Pareto-optimal solutions. **a** Initial L/D . **b** Initial ballistic coefficient. **c** Fraction of total range traveled up until nose down maneuver complete. **d** Fraction of total range traveled during nose-down maneuver. **e** Velocity at initiation of nose-down maneuver. **f** Density at initiation of nose-down maneuver

Although the region of larger normal load appears to be less uniform, there is a clear division between the two regions. The region of large normal load roughly corresponds to large range, while low normal load range corresponds to low range. The reason for the discontinuity can be found from Fig. 9.12a. Here, the region of low normal load can be seen to correspond to a region where $q_{s,\max} < 700 \text{ kW/m}^2$: the value at which the reference heat rate was chosen. This means that the vehicle

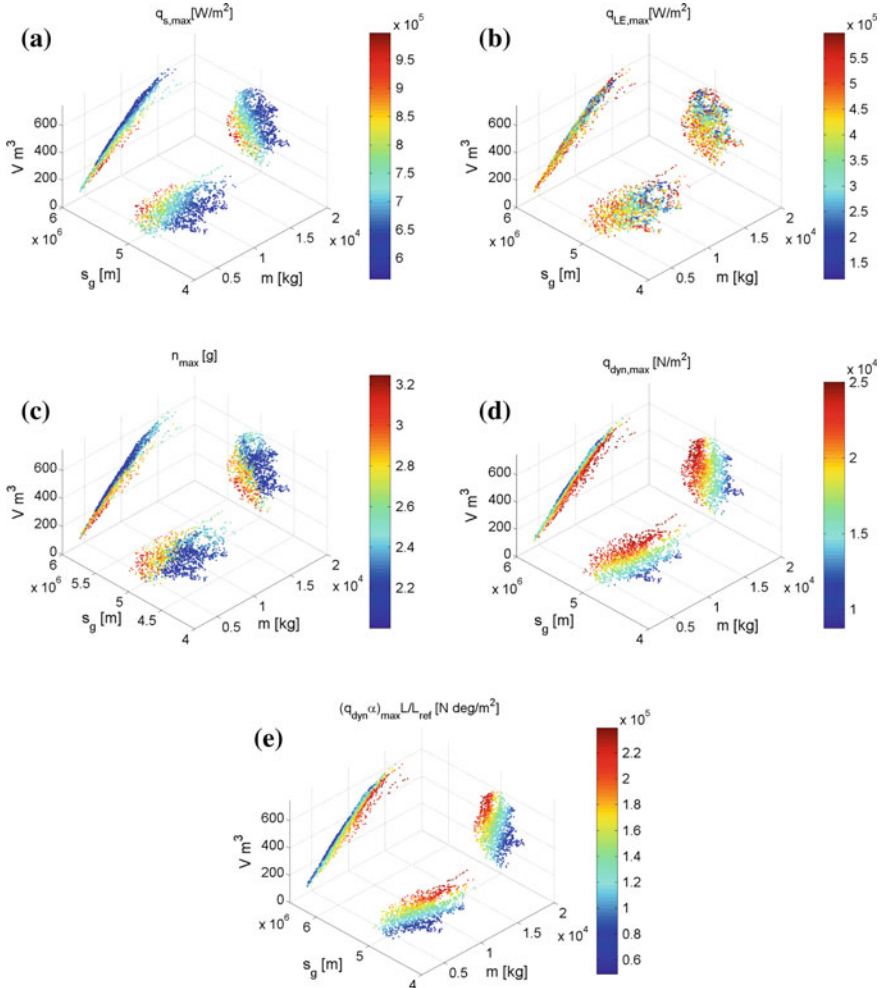


Fig. 9.12 Scatter plots of trajectory-constraint-function values, projected onto the three objective-function planes

never attains the reference heat rate and tracks its value of $q_{s,\text{max}}$. For the vehicles that do attain the reference heat rate, the point of maximum load factor is the last point in the flight in which $\alpha = \alpha_{\text{max}}$. More in-depth analysis of the vehicle shapes that result in trajectories that do not reach the reference heat rate has shown that these shapes have a smaller ballistic coefficient during the initial phase of the entry, shown in Fig. 9.11b. As such, they lose a greater amount of kinetic energy per unit time, which by itself will reduce the vehicle's range. Since the vehicle will have lost more velocity when beginning the heat-rate-tracking phase, it will, in general, be able to fly at the reference drag for a shorter period of time.

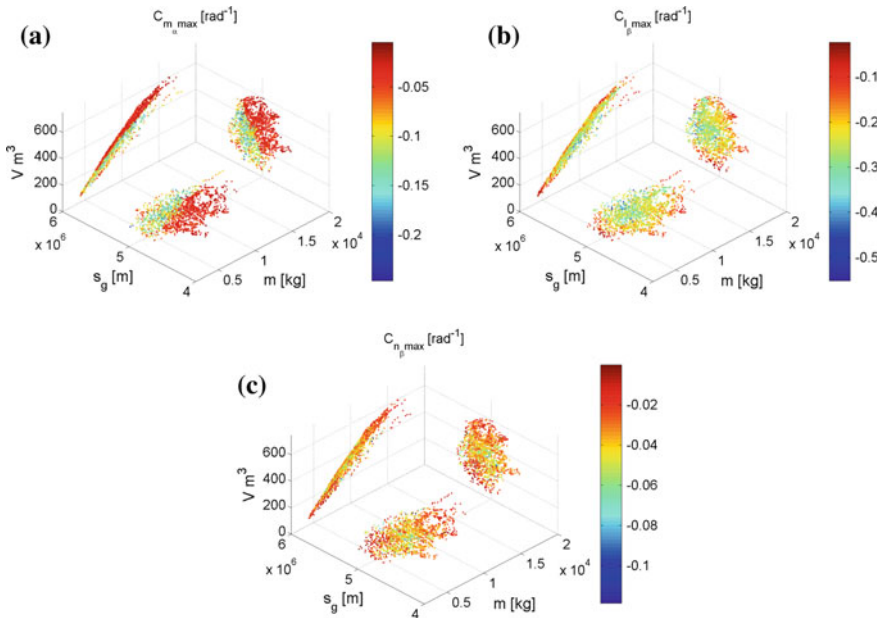


Fig. 9.13 Scatter plots of maximum values of stability derivatives, projected onto the three objective-function planes

Due to this related trend in maximum load factor and maximum stagnation-point heating, the region where these constraints are active is very similar. Specifically, they are active in the high-range, low-volume region, although the heating constraint is somewhat more closely coupled to the range than maximum load factor is. The leading-edge heating constraint is near its maximum value for the majority of the Pareto front. It becomes fully active, though, for the largest mass and volume solutions. This is caused by an increase in the value of $x_{w,3}/x_{w,1}$ here, as will be discussed shortly.

The dynamic-pressure constraint function value can be seen from Fig. 9.12d to be strongly coupled to the range of the vehicle, as a very smooth transition from low to large values is observed with increasing s_g . For the largest range solutions, the dynamic pressure is the constraining factor for the vehicle shapes. However, as mentioned earlier (see Sect. 9.1) the maximum value that is chosen for the dynamic pressure is quite large. As was to be expected, the bending-moment constraint, measured by the product of dynamic pressure and angle of attack, behaves similarly to the dynamic pressure. One exception is that, due to the fact that it is length-weighted, the values are larger for longer and therefore heavier vehicles. It can be seen that, for the maximum constraint-function values that were chosen, the constraint is not active anywhere on the front. This does not mean, however, that it can be ignored in future conceptual design studies. Changes in the guidance algorithm can cause a greater

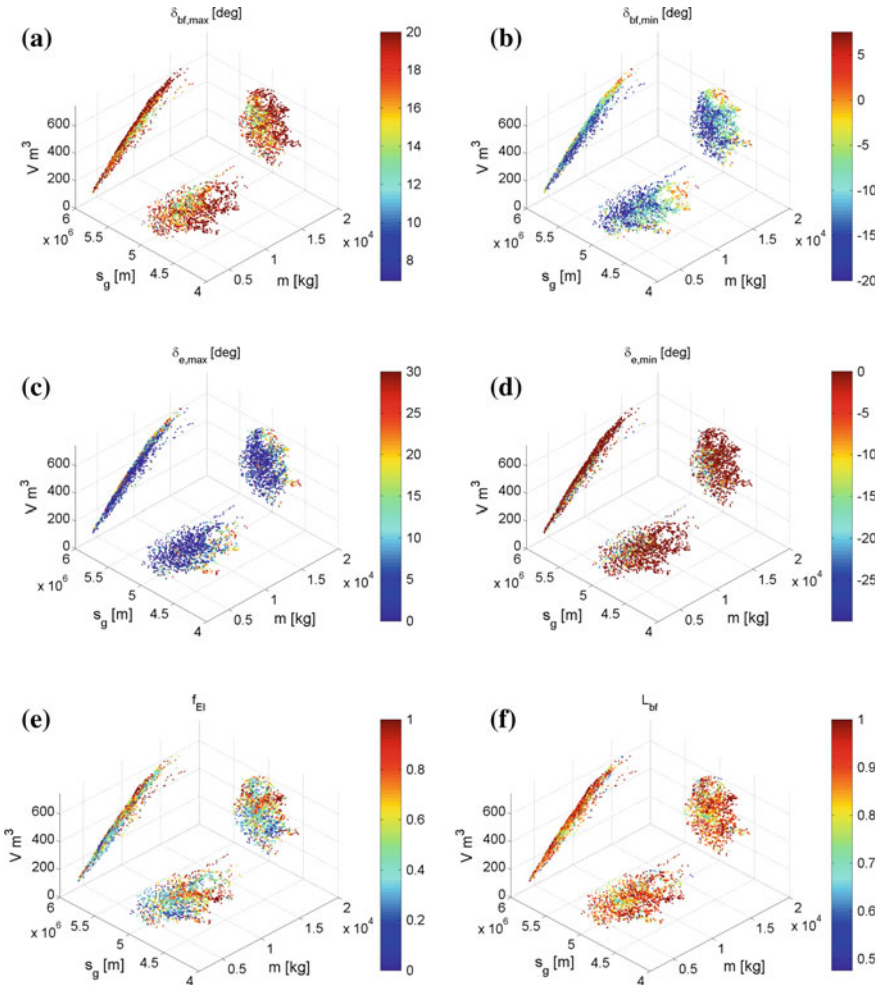


Fig. 9.14 Scatter plots of control surface properties, projected onto the three objective-function planes

variety in the angle-of-attack profile. Also, more specific vehicle requirements can lead to different maximum constraint-function values.

It can be seen from Figs. 9.13a, 9.14b, d that there is a correlation between shapes that are marginally pitch stable and those that have a large downward deflection of the control surfaces, for reasons discussed in Sect. 2.3.3. More details of this will be discussed in Sect. 9.2.2, where the optimization results for which pitch stability is required for all angles of attack, are discussed. It can be seen that both the yaw- and roll-stability constraints are nearest to their maximum permissible values for low vehicle mass and volume. This can be explained by the very flat fuselages that

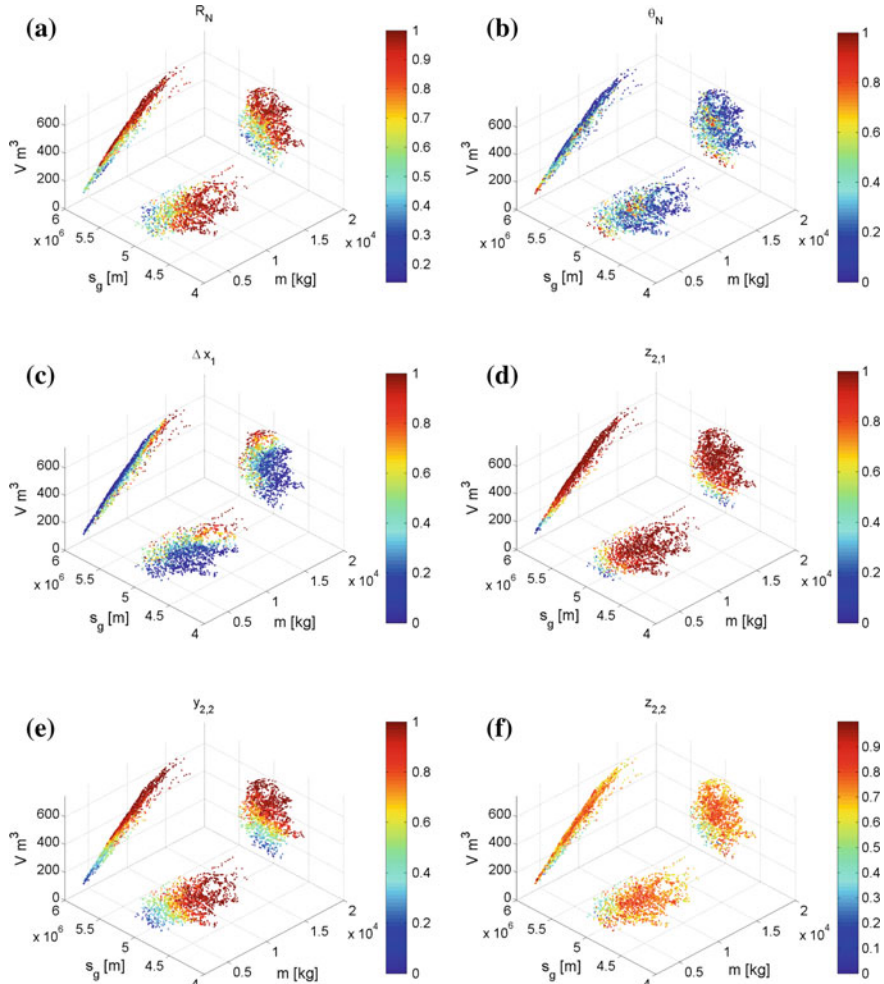


Fig. 9.15 Scatter plots of parameters r defining fuselage-shape parameters indicated in the figures, projected onto the three objective-function planes

these vehicles have. Only the correspondingly small vehicle sides can produce a restoring moment. The roll moment is not active anywhere, although it is nearly on this constraint in the low mass and volume region.

Fuselage Shape

The parameters defining the fuselage shape are shown in Figs. 9.15, 9.16 and 9.17. As discussed previously, the values of r_x instead of x are given for the fuselage points, as this makes it more insightful whether the parameter is on the edge of its allowable range.

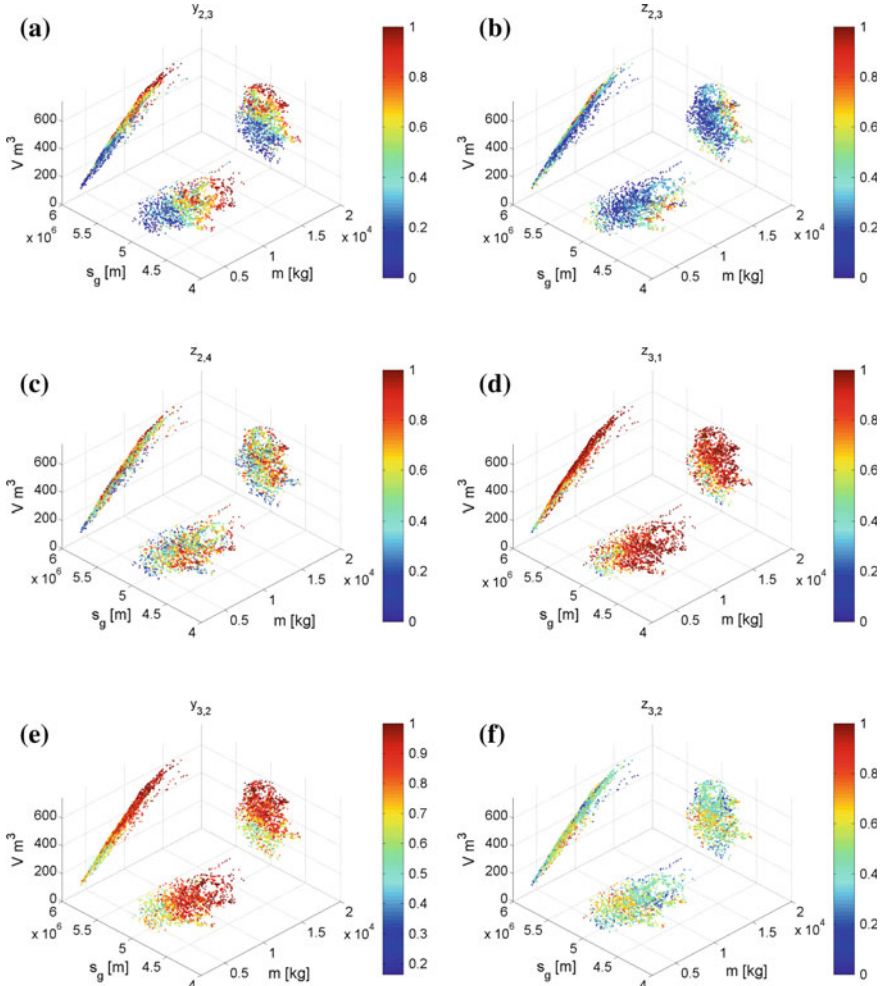


Fig. 9.16 Scatter plots of parameters r defining fuselage-shape parameters indicated in the figures, projected onto the three objective-function planes

Comparing the values of Δx_1 and Δx_2 (Figs 9.15c and 9.17c, respectively) shows that, as was to be expected, there is a trend for both of these values to increase with increasing vehicle mass and volume. It is interesting, though, that the value of Δx_2 increases more rapidly than the value of Δx_1 . Such shapes are also typically observed in existing concepts (e.g., Hermes, HOPE-X, HORUS). The value of Δx_1 is large only along the $V-s_g$ front, indicating that it increases both V and s_g . The same is true, however, for Δx_2 . It can be seen from Fig. 9.12 that none of the constraints appears to be on its maximum value across the region of large Δx_1 , nor in the region where Δx_2 is large and Δx_1 is not. This indicates that the reason for the different behavior

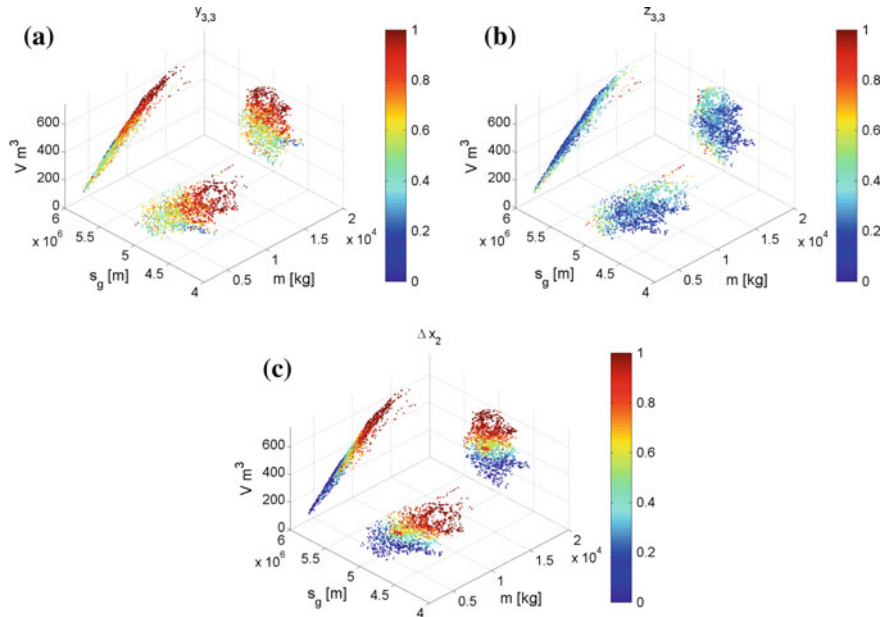


Fig. 9.17 Scatter plots of parameters r defining fuselage-shape parameters indicated in the figures, projected onto the three objective-function planes

should be found in the different influence on the objective functions. Obviously both the mass and volume of the fuselage will increase due to an increase in Δx_1 and Δx_2 . A possible reason for the different behavior, though, is that Δx_1 increases the value of m_{TPS} more strongly than Δx_2 does. In general, a larger part of the front of the vehicle will require high-temperature TPS, the area of which is increased by increasing Δx_1 . Thus, a solution with larger Δx_2 will dominate a solution of larger Δx_1 . For the large range solutions, where the value of Δx_2 is already at its maximum, however, increasing the value of Δx_1 will increase the objective functions such that they can achieve Pareto-optimality.

The behavior of the nose radius R_N (Fig 9.15a) is very similar to that of the normal load. The reason for this is that a large nose radius causes a smaller heat rate, so there is a larger chance that these vehicles will not encounter the reference heat rate.

The behavior of the points defining the fuselage surface is largely as was to be expected from their influence on the mass and volume of the vehicle. That is, a wider and larger fuselage will yield a larger fuselage volume and mass. It can be seen that for the lowest mass and volume, a number of parameters shows slightly aberrant behavior. Namely, the values of θ_N , $z_{2,1}$, $z_{2,2}$ (limited to high-range solutions) and $z_{3,1}$ show behavior that is different from most of the rest of the Pareto front. In these cases, a sudden change from a near constant value on the majority of the rest of the Pareto front is observed. In addition, a strong gradient is observed in the values of $y_{2,2}$, $y_{3,2}$ and $y_{3,3}$. The changes for each of these three parameters result in a very

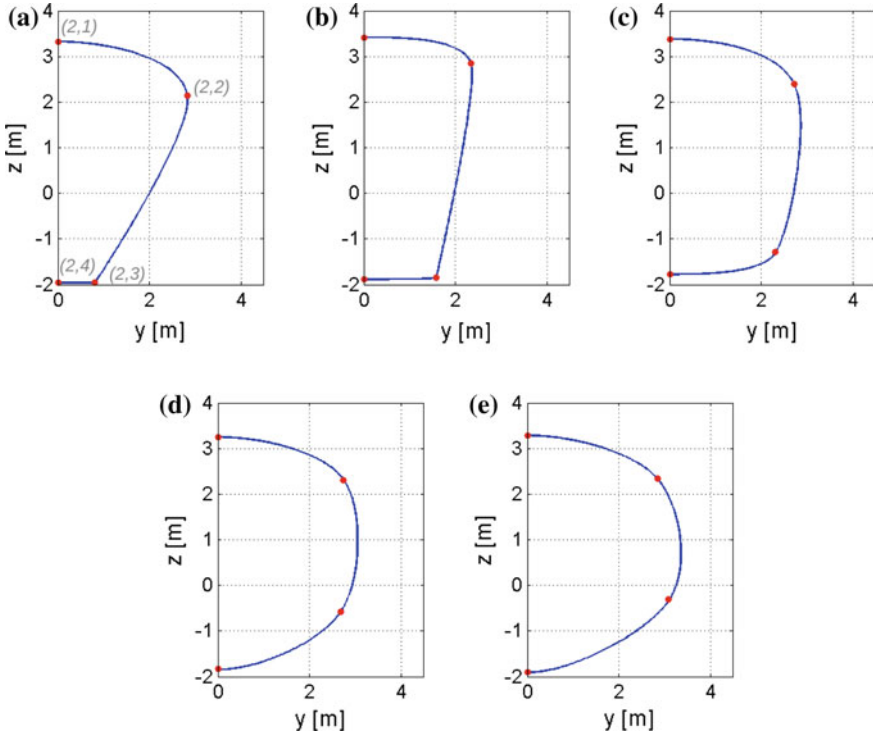


Fig. 9.18 Example of middle contour cross-sections along the Pareto front. $V = 300 \pm 1 \text{ m}^3$ for each. **a** $s_g = 5344 \text{ km}$, **b** $s_g = 5225 \text{ km}$, **c** $s_g = 5118 \text{ km}$, **d** $s_g = 5072 \text{ km}$, **e** $s_g = 4930 \text{ km}$

slender vehicle, while the changes in the three aforementioned z -values all result in a vertical slendering of the vehicle. All these changes cause the vehicle to become as thin as possible, given the parameterization. This can also be seen in Figs. 9.24 and 9.25, where the low mass and volume solutions can be seen to differ more strongly from the neighboring shapes than is the case for the other shapes. The constraints on normal load, leading-edge heat flux, and yaw and roll stability all near their maximum allowable values in this region.

The behavior of a number of variables, especially $y_{2,3}$ and $z_{2,4}$, seems to show a large degree of randomness, in that the solution does not appear to be smooth in these parameters. However, it is the values of $r_{y_{2,3}}$ and $r_{z_{2,4}}$ (see Eq. (5.1) and associated discussion) that are plotted, not the physical parameters. We omit the figures for the behaviour of the physical parameters, since their behaviour is only interesting for a limited number of (non-critical) parameters. Nevertheless, the observed behaviour is interesting, as it shows that it is likely that the optimizer has converged to its proper solution here, despite the fact that nearby solutions in objective space can differ strongly in solution space. The solutions are more smooth in their actual parameter values, though.

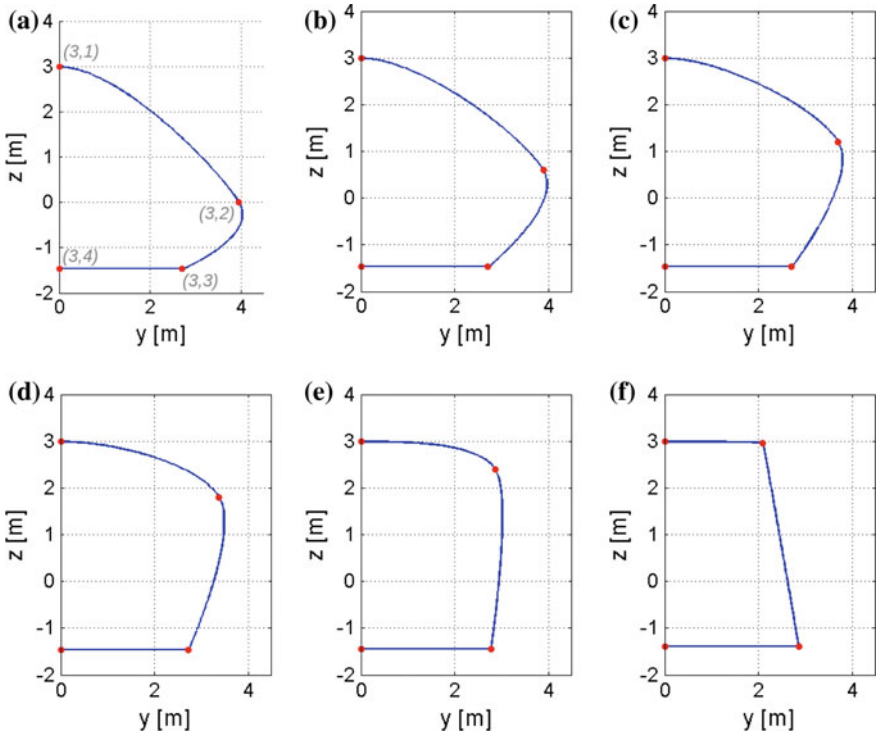


Fig. 9.19 Example of change in value of $r_{z3,2}$ on rear-contour spline shape. **a** $r_{z3,2} = 0.0$, **b** $r_{z3,2} = 0.2$, **c** $r_{z3,2} = 0.4$, **d** $r_{z3,2} = 0.6$, **e** $r_{z3,2} = 0.8$, **f** $r_{z3,2} = 1.0$

In addition to the influence of the mass and volume in driving the fuselage shape, the range can also be seen to have a clear influence for a number of parameters. Most notably, $z_{2,3}$ and $y_{2,3}$ can both be seen to decrease with increasing range, in addition to their trends with m and V . The reasons for this are related to the influence of the ballistic coefficient at large Mach number and angle of attack on the range, as discussed previously. Specifically, a flatter vehicle bottom will yield a lower ballistic coefficient and therefore a lower range. To illustrate this, the middle cross-section of a number of Pareto-optimal vehicles at $V \approx 400 \text{ m}^3$ are shown in Fig. 9.18. Here, it can be seen that for the high-range solution, the region on the vehicle bottom with large inclination is very small, whereas this region increases for decreasing range due to the associated decrease in ballistic coefficient.

The value of $r_{z3,2}$ (Fig. 9.16f) can be seen to decrease for large m and V , although an increase in its value would increase both m and V . This indicates a different reason for the parameter being steered in this direction. It affects the vehicle shape by making the rear cross-section more triangular in shape, so that the top is less flat. This has been visualized in Fig. 9.19. For this figure, the point in (normalized) objective space nearest to $V = 550 \text{ m}^3$ and $s_g = 5,000 \text{ km}$ is taken and the value

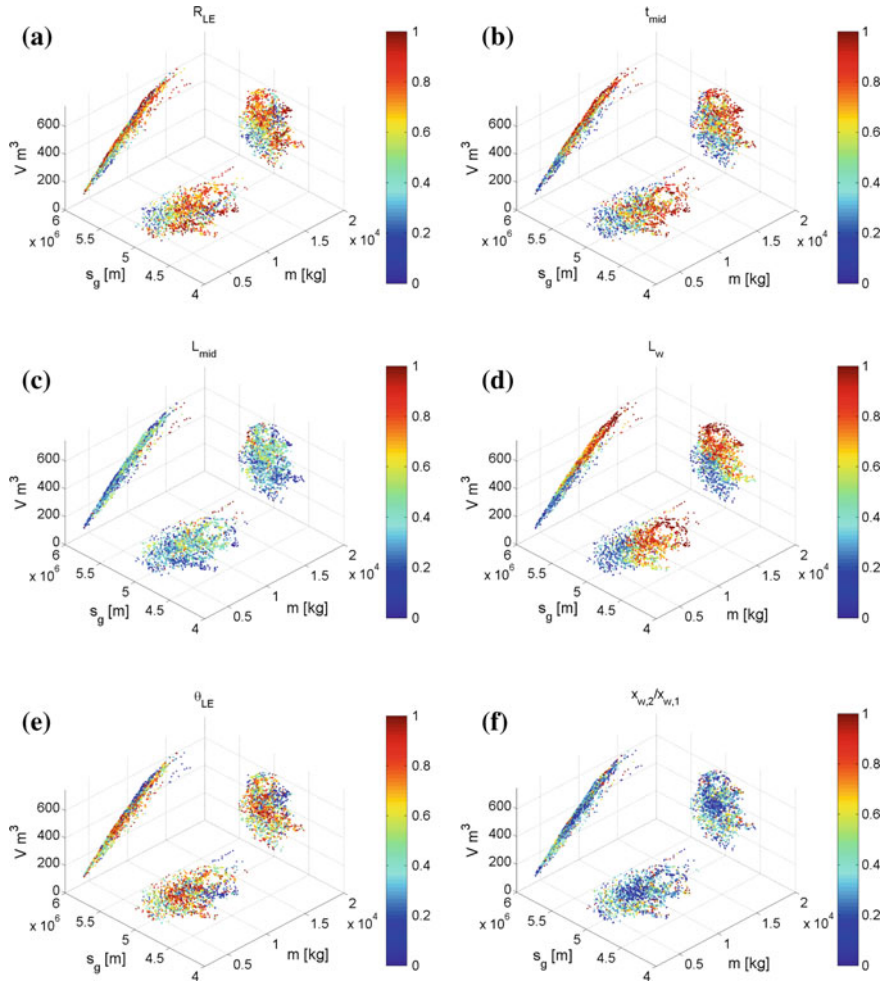


Fig. 9.20 Scatter plots of parameters r defining wing-shape parameters indicated in the figures, projected onto the three objective-function planes

of $r_{z_{3,2}}$ is changed from 0 to 1 in six steps. The rear contour spline is then shown to illustrate the effect of this change of changing this value. It can be seen from Fig. 9.17b that $z_{3,1}$ does not show the same behavior as $z_{3,2}$ on the Pareto front, so that not the entire rear cross-section is made flat. Since this behavior decreases the mass and volume and in itself affects the range very little, the cause of this behavior should be found in the constraint values. The active constraint functions here are the stability constraints, namely the yaw and pitch stability constraint (see Fig. 9.13). The yaw stability will be decreased due to this change, as pressure on the vehicle rear sides will increase the restoring strength of the yaw moment when the sideslip angle is perturbed. Although the pitch moment may seem to be hardly affected by

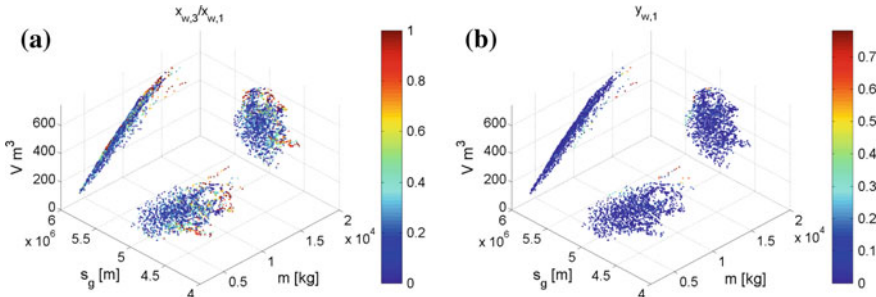


Fig. 9.21 Scatter plots of parameters r defining wing-shape parameters indicated in the figures, projected onto the three objective-function planes

this change, the shape change will cause the whole rear of the vehicle (between the mid contour and the rear cross-section) to decrease in volume. This will move the center of mass forward, increasing pitch stability. Although a concurrent decrease in $z_{3,1}$ would further increase pitch stability, the resultant decrease in yaw-stability would likely violate the yaw-stability constraint.

Wing Shape

The wing shapes that are produced by the optimizer are described by the parameter behaviour shown in Figs. 9.20 and 9.21. Unexpectedly, the wing span (defined by $y_{w,1}$) is small for all solutions (Fig. 9.21b), including those of large range. For the low-range region of the Pareto front, the wing span would be expected to be low, as an increased wing size gives an increased vehicle mass with no benefits to the fuselage volume. It would have been expected, though, that wings with a greater span would produce greater a L/D and therefore a greater range. However, the opposite can be seen from the Monte Carlo results in Table 9.1, where the span is negatively correlated with the the range, if weakly so. One reason for this is due to the increased value of $(C_{DS}_{ref})_{\alpha=40^\circ}$ that larger wings cause, which will in turn cause the ballistic coefficient in the initial phase of the re-entry to decrease, decreasing the range. However, an increase in wing size would be expected to increase the L/D of the vehicles, but we found that this is not always the case.

To further investigate this, the value of $y_{w,1}$ is varied from its minimum to its maximum for a Pareto-optimal solution of large range, to see whether such a change produces a better range. The L/D of these shapes is shown in Fig. 9.22a. The L/D for the large span vehicles is marginally larger in the initial large angle-of-attack phase and is larger in the low Mach-number phase. It is substantially smaller than that of the vehicles with low span for the intermediate phase, though. The L/D in the initial phase varies little with $y_{w,1}$ and the velocity in the low Mach-number range is such that the vehicle's range is influenced only slightly by its behavior there. Therefore, the majority of the diversity in the range due to a change in L/D occurs in this

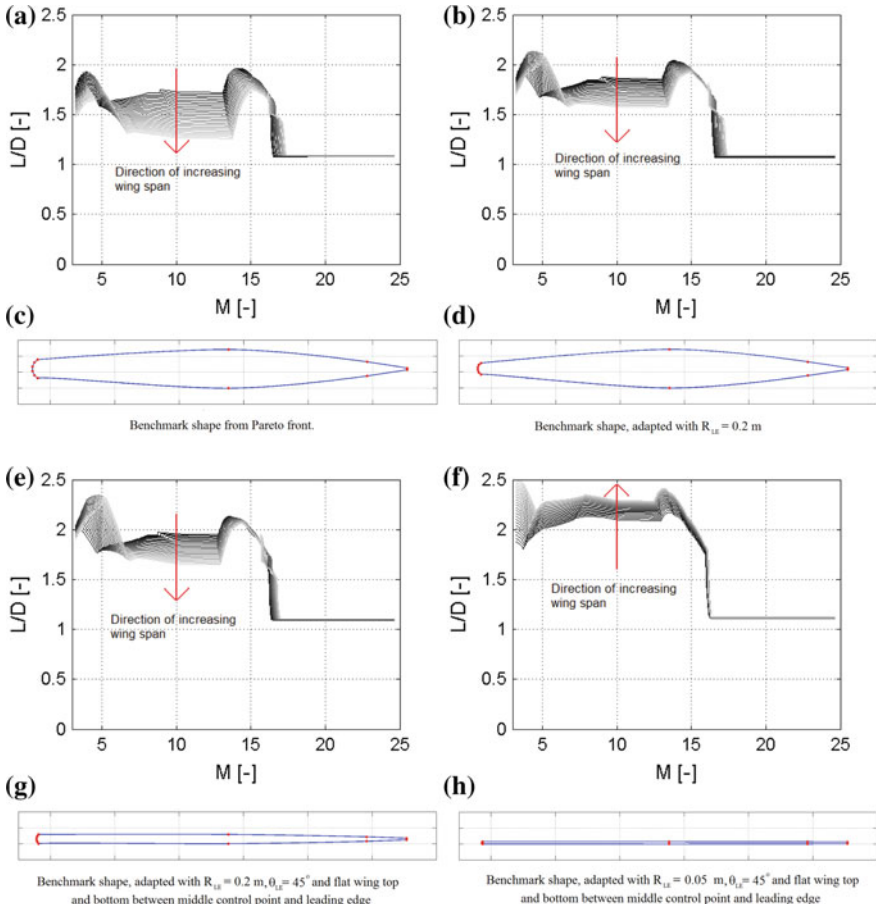


Fig. 9.22 Comparison of L/D profiles for varying values of wing span (dark-light corresponds to low-high span, arrows indicate direction of increasing wing span at medium Mach numbers), with corresponding airfoil shapes shown

intermediate region. The behavior of L/D in this region shows that a low span is preferred for a large range.

From these results, it can be deduced that, for certain shapes, the L/D at low angle-of-attack of the large span wings is smaller than that for the low wing spans and intermediate angles of attack. This is due to the fact that a change in wing width $y_{w,1}$ directly influences the wing sweep angle Λ and therefore the inclination angles at the leading edge. Similarly, since the region behind the leading edge is one of increasing wing thickness, increasing the wing span will increase the surface inclination here. Especially at relatively low angles of attack, these increases in inclination may be such that the increase in drag causes the L/D of the vehicle as a whole to decrease. To further investigate this effect, the L/D during entry for the full

range of allowable span values is plotted for a number of different leading-edge radii and wing thicknesses. Firstly, in Fig. 9.22b, the wing leading-edge is decreased to 0.2 m. In Fig. 9.22e, the wing leading edge is also decreased to 0.2 m and in addition the leading edge radius θ_{LE} is set at 45 degrees and the region between the leading edge and the center control point is set as a flat plate. Finally, Fig. 9.22f shows this same flat-plate wing, but with a leading edge radius of 0.05 m. As can be seen, only for the flat-plate wing with a leading edge radius of 5 cm do the shapes with large wing span have larger L/D . This is a very interesting result, but applies only to variations of a single vehicle shape. The same procedure was done for other shapes, with mixed results. In fact, for some shapes, the L/D increased with increasing wing span for all four of the above cases, indicating that the above cannot be seen as a general result for all winged vehicles. To ascertain how widely the above result apply, all solutions on the Pareto front were re-analyzed, but with the value of r_{y_w} (degining parameter for wing width) being 0.1 higher. The results showed that, for 10 % of all cases, the range increased due to the increased wing span. Although this may seem to indicate that the optimizer should be driven to larger span solutions for this 10 %, this is not the case. During optimization, apparently few of these solutions have been put in the Pareto archive, as they are dominated by other solutions with low span.

From the above discussion, a number of interesting conclusions can be drawn:

- Varying the shape in manners other than increasing the wing span can, in most cases, increase the vehicle's range by a given amount at a lower mass penalty than it could by an increase of the wing span.
- The L/D of most large range fuselage shapes is larger than the L/D of most small range wing shapes (for our parameterization range of parameter values).
- For a large wing span to be advantageous for the vehicle's range in a greater number of cases, the leading edge radius should be reduced to very low values, which would likely require active or ablative thermal protection.
- The flat-plate approximation should not be used to assess the influence of wings on a winged entry-shape configuration, as both the airfoil shape and leading-edge radius contribute significantly to the characteristics.

From the second of these conclusions, it can be deduced that the optimizer essentially drives the vehicle to a lifting body shape as much as possible. The third conclusion indicates that wings may not be advantageous (at hypersonic speeds) for all but very small leading-edge radii (and flat bottoms). Small leading-edge radii would produce a severe heating environment and a flat wing bottom could be disadvantageous for subsonic handling characteristics. Extensions of the approach we present could investigate the optima in a more multidisciplinary manner, taking into account the added mass and cost of an active leading-edge cooling system and subsonic aerodynamic characteristics. Especially the addition of sub- and transonic aerodynamics would be advantageous, as the added value of larger wings may be driven by stability or controllability characteristics in these regimes. Additionally, modifying the hypersonic aerothermodynamic analysis to be more accurate could influence the results found here. Also, the guidance algorithm that is used does not fully exploit the positive influence that the larger wings have between $\alpha = 10^\circ$ and 40° . Although it has been

shown that the influence of wide wings on aerodynamic characteristics at 10° angle of attack is not necessarily favorable, the results for intermediate values of α are more ambiguous. Finally, it would be very interesting to extend the work so that the optimizer can choose between different parameterizations, to find whether a winged vehicle or lifting body is an optimal choice and under what circumstances.

Although this result is interesting, the fact that it is not in line with many existing designs that are observed for winged re-entry vehicles means it should be treated with caution. Errors in the aerodynamic analysis, or incorrect wing-mass prediction, amongst others, could steer the optimizer in a wrong direction. Also, the fact that no aerodynamic performance for $M < 3$ is performed could steer the direction of the optimizer away from wider wings. Although the hypersonic regime is dominant for determining the vehicle performance, sub-, trans- and supersonic aerodynamic considerations may impose additional constraints related to, e.g., controllability. On the Space Shuttle, and to a lesser degree HORUS, the wing sizes that are observed are not as small (relative to the fuselage size), as those that are produced here as optima. For other vehicles, such as the X-30, X-33 and X-38, the shape resembles a lifting body, with small wings.

In addition to the considerations above, a number of features regarding the wing shape is observed. The wing leading-edge radius R_{LE} (Fig. 9.20a) can be seen to roughly increase with increasing mass, although this will decrease the vehicle's L/D and thereby its range, indicating that a different reason exists for this behaviour. Figure 9.12b shows the maximum leading-edge heat-rate, which decreases with increasing R_{LE} . The value of $q_{LE,max}$ decreases with increasing mass and volume, with more or less the exception of the solutions bounding the projection of the front in the $s_g - m$ plane for large m . This sudden increase in $q_{LE,max}$ can be seen from Fig. 9.21a to be correlated with a sudden increases in $x_{w,3}/x_{w,1}$ and $x_{w,2}/x_{w,1}$. Such an increase would increase the inclination angle of the leading edge, thereby increasing the heating. Although this indicates that the leading-edge heating becomes constraining here, it is not the leading-edge heating constraint that drives the wing leading edge to a lower sweep angle. This indicates that the leading-edge heating is not the factor causing the leading edge radius to become large. Instead, the cause can most likely be found in the constraints for pitch and yaw stability. Figure 9.13a, b show the values of the pitch and yaw derivative C_{m_α} and C_{n_β} . It can be seen that their values are close to zero, corresponding to marginal stability, in the region of large range/mass/volume.

The influence of the value of R_{LE} of C_{n_β} can be explained as follows. An increase in sideslip angle β will result in an increase of the inclination angle along the left wing and a decrease of the inclination angle on the right wing. As a result, the total force exerted along the left leading edge will increase, while decreasing for the right leading edge and as such cause a restoring moment. It is interesting to note that an increase in wing span would increase this restoring moment, allowing the leading edge radius to decrease. It can be seen that such behavior is not optimal for the ranges of the shape parameters used here, though. It can be deduced that the required increase in span needed to compensate for a given decrease in leading edge radius will negatively influence the vehicle's range.

The effect of R_{LE} on pitch stability is more dependent on the other shape parameters, though. The position of the leading edge in x -direction will determine whether the force on the leading edge produces a nose-up or nose-down moment. This is due to the fact that the line of action of this force, projected onto the xz -plane can pass in front of the center of mass for a far forward leading edge. This causes a nose-up moment; equivalently, when it passes behind the center of mass for a rearward leading edge, it causes a nose-down moment. In the case where it causes a nose-up moment, the arm of the force causing this moment will increase with increasing angle of attack. Thereby, the magnitude of the (negative) pitch moment will increase, resulting in a negative value of C_{m_α} .

Similarly to the wing span, the values of $x_{w,2}/x_{w,1}$ and $x_{w,3}/x_{w,1}$ (Figs 9.20f and 9.21a) are kept small over the majority of the Pareto front. The region at large mass and volume where $x_{w,3}/x_{w,1}$ is large can be seen to coincide with a region of large maximum elevon deflections (Fig. 9.14), indicating a likely reason for the increase of this shape parameter. The size of the elevons is, in part, determined by the length of the wing at $v_w = 3$ (where v_w represents the independent variable v defining the wing; see Sect. 5.2.2), which is determined by $x_{w,3}/x_{w,1}$ and L_w .

The position of the middle wing spline point, denoted by L_{mid} remains low for the majority of the Pareto front. This will not influence the aerodynamic characteristics much, when compared to the wing length or span and the influence on the mass will be next to negligible. The behavior of the thickness at the wing midpoint shows a trend apparently related to that of the normal load, possibly implying a connection between whether or not the vehicle reaches the reference heat rate. In this region, the vehicle has marginal pitch stability and a thicker wing will, in most cases, increase pitch stability, indicating a possible reason for the observed behavior. However, in a design optimization including the sub- trans- and supersonic regime, the behavior in these lower velocity regimes will most likely be more influential on the airfoil shape.

Finally, there is a strong relation between the wing length L_w and whether the vehicle reaches the reference heat rate. Namely, for low maximum stagnation-point heat flux (solutions that do not reach the reference heat flux) the value of L_w is large, whereas it is small for solutions with large maximum heat flux. Again, a likely explanation is the pitch-stabilizing effect that a longer wing has. This effect is due to the fact that the majority of the wing surface is behind the center of mass of the vehicle, so that the center of pressure of the wing is likely to lie behind the center of mass of the full vehicle. It might have been expected that a large wing length is discouraged for the same reasons that a large wing span is discouraged. However, there is one crucial difference between the influence of these parameters on the vehicle's aerodynamic characteristics. Namely, an increase in wing length increases the wing sweep angle, whereas an increase in wing span decreases it. Since an increase in wing sweep means a decrease in the inclination angle of the panels on the leading edge, an increase in wing span will increase the drag. An increase in wing length will decrease the drag, due to an associated increment of leading-edge sweep angle.

Fin Shape

The final part of the winged vehicle that is to be discussed are the ‘fins’, the wing tips that are bent upwards. By doing so, the lateral stability is influenced. Also, the ballistic coefficient is expected to be influenced by this value, as a greater bend upwards corresponds to a smaller value of the drag at large angles of attack. The four parameters that define the fin shape are shown in Fig. 9.23. It can be seen that their behavior is not as smooth as is the case for many other parameters. This indicates that either the performance and constraint functions vary relatively chaotically with their values or that the optimizer has not properly converged to its ‘true’ shape in solution space. Again, this could be due to the limited influence of the values on the performance.

The behavior of the fin bend angle θ_f is twofold. It can be seen that for large range, θ_f is typically larger. As mentioned, a large ballistic coefficient, and therefore low value of $C_D S_{ref}$ at large angles of attack, is advantageous for a large range. Since a large θ_f will do just that, its behavior with increasing range was to be expected. In addition, a large θ_f is expected to increase the yaw stability, as the vertical area at the wing tip for a θ_f of 90° will add to the restoring yaw moment upon an angle-of-attack deviation.

The behavior of the fin sweep is likely related to the pitch or roll stability. This is due to the fact that a fin sweep will not (or hardly) affect the area and pressure on the fins, so that the translational aerodynamic coefficients will not be affected directly. It is possible, though, that the translational aerodynamics will be indirectly affected by a change in control surface deflections. However, the relative influence of the fins on the pitch moment is much smaller than the relative influence on the yaw moment. Also, the region of marginal yaw stability corresponds to the region of large sweep. The pitch stability in the region of high large sweep is quite good, though, although an increase in fin sweep would increase pitch stability. This indicates that the pitch derivative is not the driving force behind the change in fin sweep, making it likely that the fin sweep increases to yaw stabilize the vehicle.

The increase in $x_{w,4}/x_{w,1}$ for the largest values of range is most likely caused by a ‘final try’ to decrease the dynamic pressure to achieve Pareto-optimal solutions that do not violate any constraints at large range. The behavior of $y_{w,3}$, on the other hand shows very little structure, possibly due to the limited range of values that it can take, limiting the influence it can have on the solutions.

The behavior of the other fin-shape parameters is more difficult to explain. In part, this is due to the apparent lack of proper convergence and in part due to the fact that the influence of the values on most performance and constraint functions is only marginal. The increase in the value of $y_{w,3}$ at large ranges could be to mitigate the dynamic-pressure constraint somewhat, as a ‘last resort’ measure. That is, although there are generally better ways to increase the range, for extreme cases an increase in $y_{w,3}$ becomes the only course of action for the optimizer to gain slight range increases.

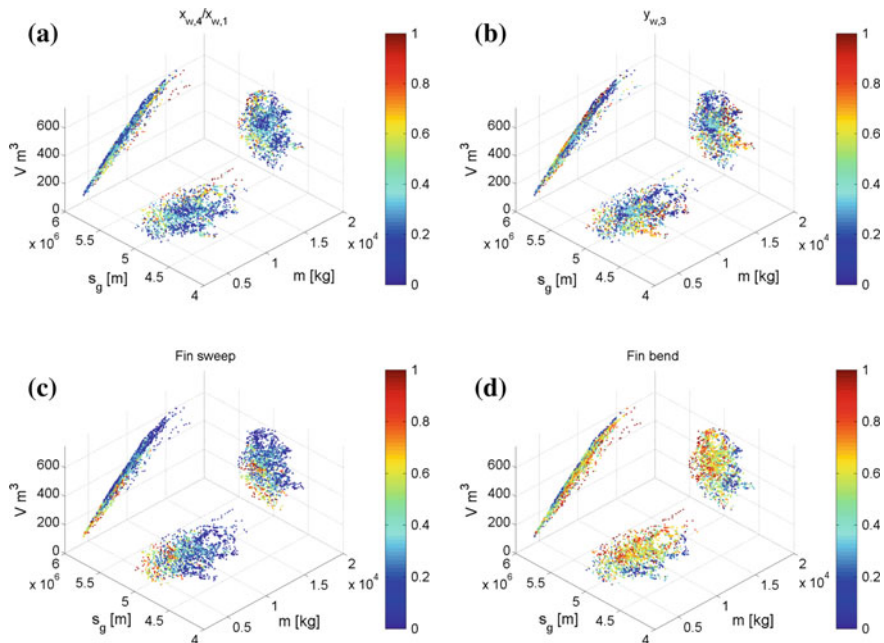


Fig. 9.23 Scatter plots of parameters r defining fin shape parameters indicated in the figures, projected onto the three objective-function planes

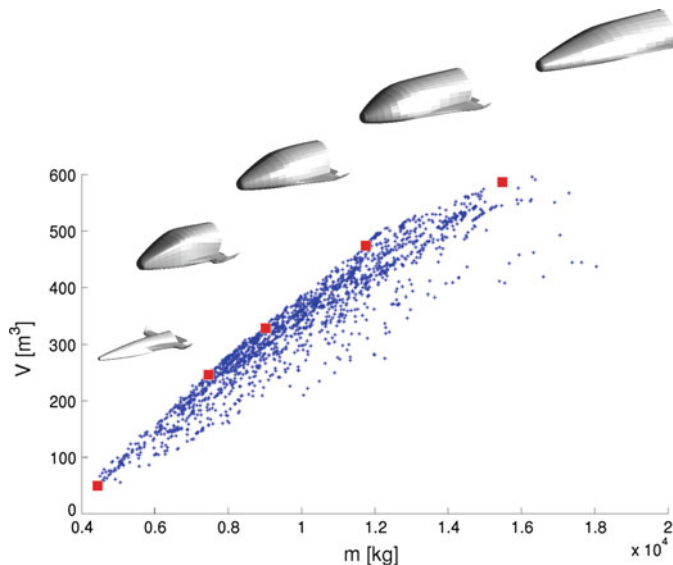


Fig. 9.24 Pareto-optimal winged shapes along mass - volume Pareto front

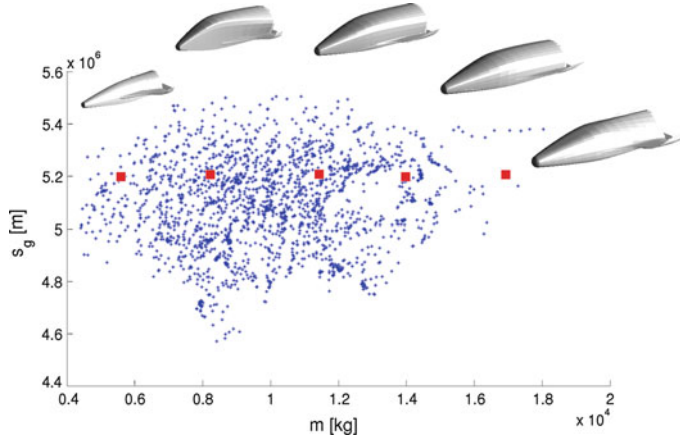


Fig. 9.25 Pareto-optimal winged shapes for increasing mass and $s_g \approx 5.2 \cdot 10^3$ km

9.2.2 Pitch-Stable Optimization

As was discussed in Sect. 6.3.2, pitch stability was not imposed on the vehicle for all angles of attack for the baseline optimization (Sect. 9.2.1), but only for $\alpha > 25^\circ$. This section will discuss the results of the optimization that was performed with the pitch-stability constraint extended to the full angle-of-attack range. Using the results presented here, a trade-off between stability and other criteria can be made.

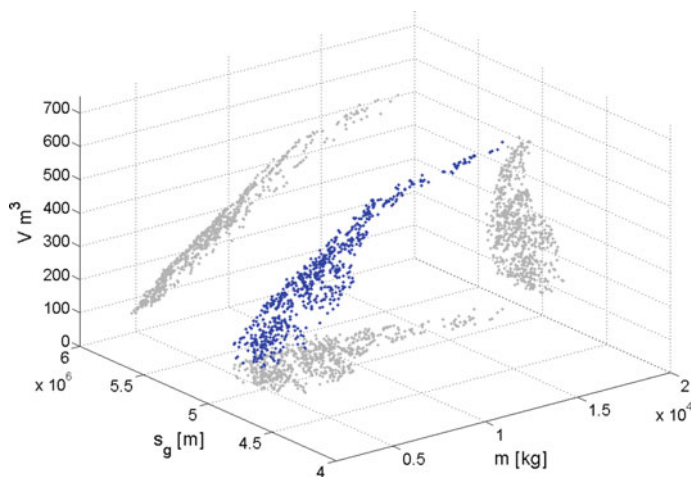


Fig. 9.26 Pareto front of pitch-stable results, plotted in the three objective functions, and projected onto the three objective planes

The projections of the Pareto optimal solutions are shown in Fig. 9.26. In addition, projections of the benchmark and pitch-stable solutions are shown in Fig. 9.27. Although it can be seen that the overall shapes of the projections are relatively similar, there is a clear decrease in attainable performance by extending the pitch-stability constraint. This is especially clear in the m - V plot, where the two-dimensional Pareto front is again clearly delineated, but has a smaller slope.

A clear difference between the benchmark and pitch-stable cases lies in the control-surface deflections that are required (from both the elevons and body flap). Histograms of the occurrences of maximum and minimum deflections are shown in Fig. 9.28. The elevons are used relatively little and the elevon size is reduced to its minimum for the majority of the benchmark Pareto-optimal solutions (see Fig. 9.14e).

The pitch-stable solutions tend strongly to maximum upward control surface deflections. As was discussed in Sect. 2.3.3, upward deflection of control surfaces serves to pitch-stabilize the vehicle. The control-surface behavior is much more strongly driven to large upwards deflections: no variations of the vehicle shape were found to be Pareto optimal that did not exhibit such deflection behaviour here. This can mean one or both of the following:

- Changes in the vehicle shape that increase pitch stability directly, negatively influence the objective functions more strongly than changes in the vehicle shape that cause an increase in the upward required control surface deflection and size of the control surface.
- No vehicle shapes exist with the current parameterization that are pitch stable over the full angle-of-attack range with control-surface deflection behavior as that of the baseline case.

A number of shape parameters show clearly different behavior w.r.t. the benchmark case, the main points of which will now be shortly discussed. We show the key parameters exhibiting different behavior in Figs. 9.29 and 9.30 for the fuselage and

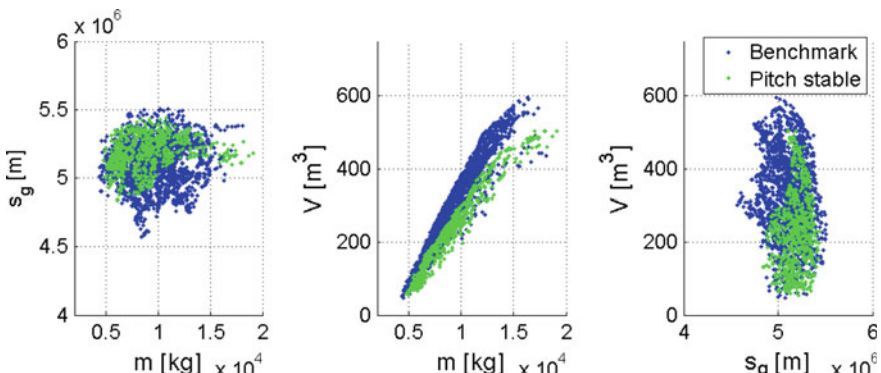


Fig. 9.27 Comparison of projections of Pareto fronts for benchmark and pitch-stable solutions

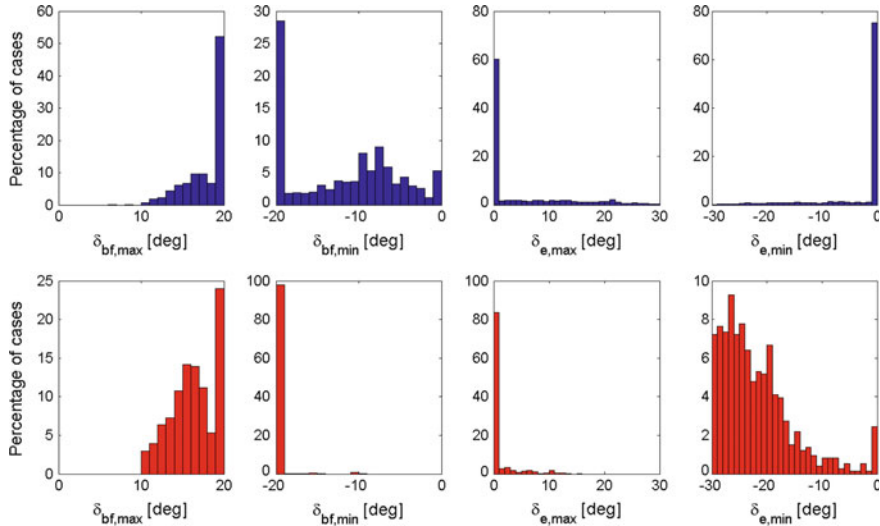


Fig. 9.28 Comparison of maximum and minimum control surface deflections for Pareto optimal solutions, blue = benchmark, red = pitch stable

wings, respectively. The plots of all parameter values and constraint functions are not given. Instead, we focus on the key differences between the two optimization cases.

For the fuselage, the main differences are in the shape of the middle contour (compared to the benchmark behavior shown in Figs. 9.15, 9.16 and 9.17). Most parameters on this middle contour, with the exception of $z_{2,3}$ and $z_{2,4}$, are smaller than for the benchmark case. The smaller values on this contour indicate a narrowed and lower cross-section, properties that will of course make the whole front of the vehicle narrower and lower. This will have two important effects on the pitch-moment properties of the vehicle:

- The total aerodynamic force on the front of the vehicle will become smaller, thereby causing the value of C_m to increase (become more positive) as the center of pressure is moved rearwards. Since this will require a more upward control-surface deflection to trim, such behavior is advantageous for pitch stability.
- The center of mass of the vehicle will move backwards, since both fuselage mass and fuselage TPS mass at the front of the vehicle will decrease. This will in part counteract the effect on the pitch moment just discussed, as the distance between the two centers is decreased, thereby requiring smaller control-surface deflections.

Although these two contributions are conflicting for the pitch stability, the results of the optimization would indicate that the former of these properties influences the pitch stability more strongly than the latter. In addition, although large upward control-surface deflections are desirable, the required deflections must not be such as to lie beyond the range of possible deflections. The second effect could aid in the trimmability of the vehicle.

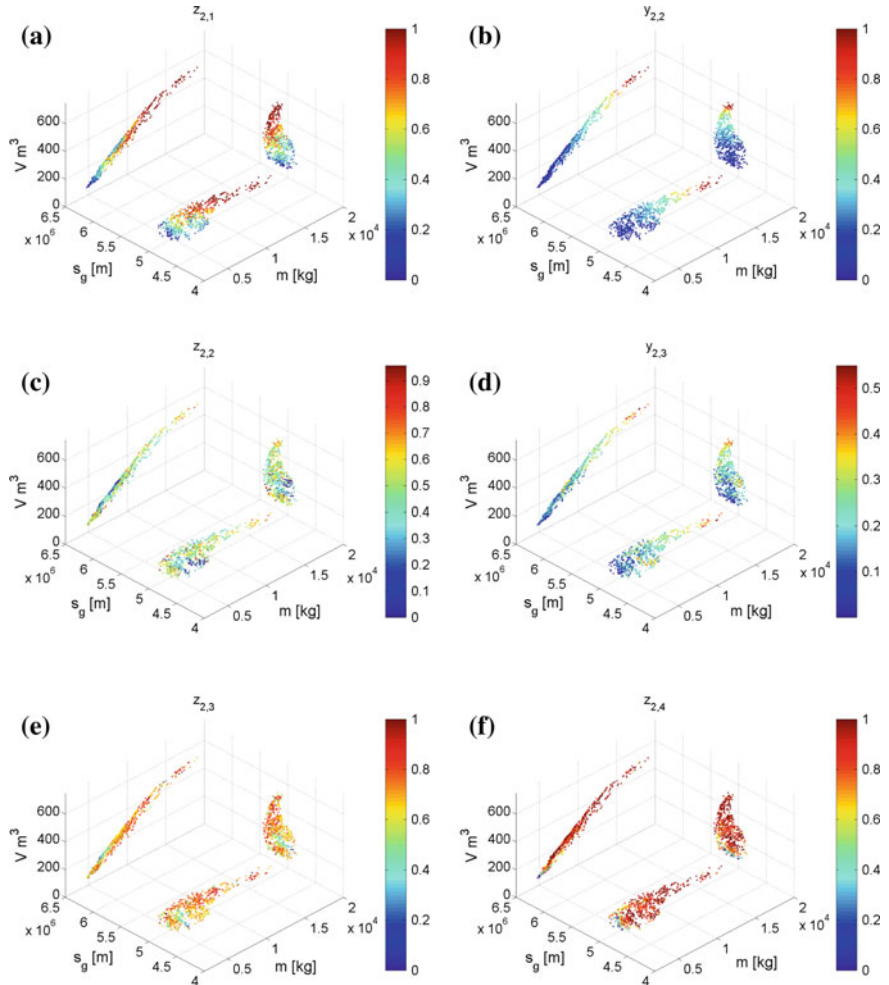


Fig. 9.29 Scatter plots of selected parameters r defining fuselage-shape parameters for pitch-stable optimization, projected onto the three objective-function planes

The different behavior of larger values of $z_{2,3}$ and $z_{2,4}$, compared to the benchmark case, indicate a less flat vehicle bottom between the vehicle front and middle contour. Since the center of mass will, for the values of Δx_1 and Δx_2 that are observed, lie behind the middle fuselage contour, this less flat bottom will result in a stronger nose down moment. Such a pitch moment must be trimmed by an upward control-surface deflection, which is desirable for pitch stability. The value of C_{m_α} of the vehicle with flush control surfaces will increase, however, as a flatter vehicle bottom will not only result in a lower value of C_m , but also a stronger reduction in C_m with α , so a larger absolute value of C_{m_α} . This is interesting, since it shows that the decrease in pitch

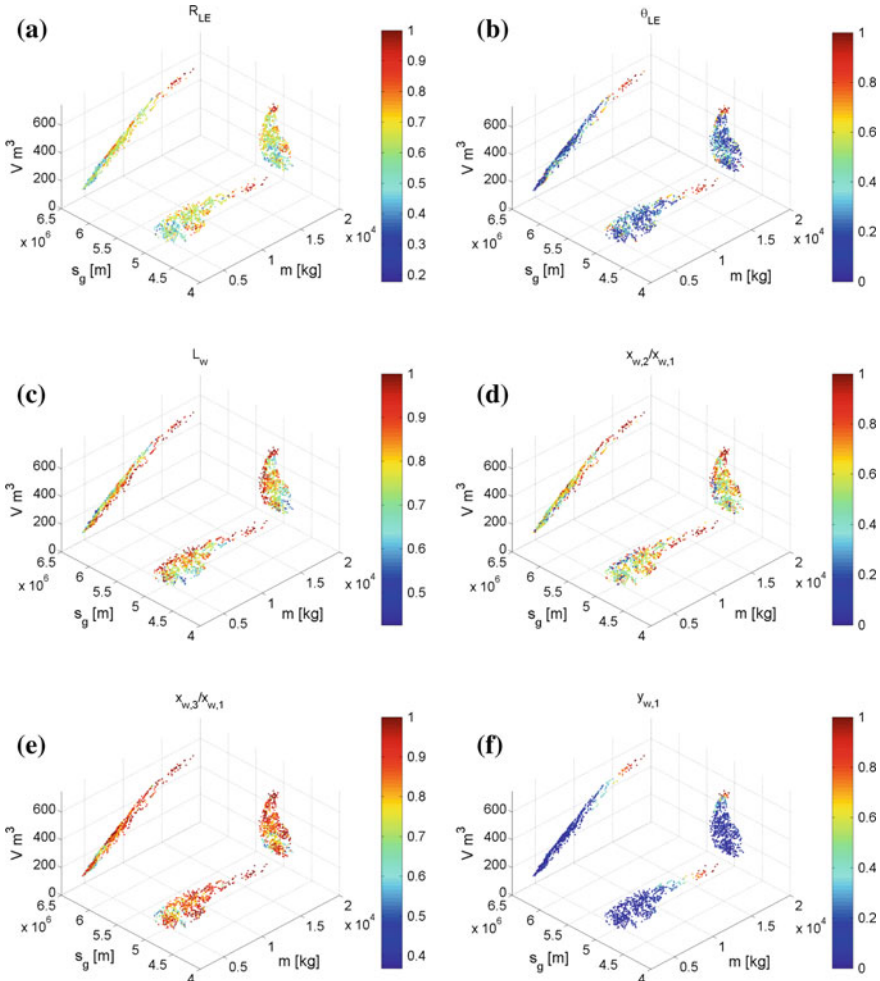


Fig. 9.30 Scatter plots of selected parameters r defining wing-shape parameters for pitch-stable optimization, projected onto the three objective-function planes

stability of the vehicle in untrimmed configuration is offset by the change in pitch stability due to the change in required control surface deflections to trim the vehicle. That is, although the untrimmed vehicles that are produced by the optimization are less pitch stable, this reduction is more than offset by the increase in stability due to the control surface deflections

The wing shape also shows some key differences compared to the benchmark case, for which the key parameters are shown in Fig. 9.30. Clearly, the value of $x_{w,3}/x_{w,1}$ is large for most solutions, as the elevon size is determined from the scaled airfoil contour at this location.

An interesting effect is noticed for R_{LE} , where the behavior along the Pareto front is clearly different to that of the benchmark case. Whereas it is increasing with increasing m and V for the default case, it is decreasing with increasing m and V for the pitch-stable case. This is possibly due to the fact that the behavior of $C_{n\beta}$ is different in the two cases. For the benchmark case, it was hypothesized that the increase in R_{LE} is in part driven by the requirement of negative values of $C_{n\beta}$. Here, however, the low-mass/high-range solutions are the most constraining from a yaw-stability point of view.

Whereas the wing length was kept small in about half the cases for the baseline case, the wings are longer for a majority of solutions in the pitch stable case. A likely explanation for this is firstly the increased elevon size, and secondly the fact that longer wings should in general increase pitch stability. For longer wings, a larger portion of the wing will be ahead of the center of mass. Consequently, a greater portion of the wing will contribute to a pitch-up moment. Since the pressure coefficient on the wing increases with increasing α ($\partial C_p / \partial \theta > 0$, see Eq. (3.51)), this larger pitch-up moment will increase with α .

A large value of the wing width is observed for the largest values of m and V for the pitch-stable case (Fig. 9.30c). Possibly no sufficient control-surface action can be created by a different set of parameters for values of m and V larger than the maximum values observed. Since the wing span is the final parameter to increase for the benefit of the possible control surface action, this again indicates that a larger wing span is undesirable for our mission and model definition.

9.2.3 Heat-Rate Tracking Optimization

The guidance law that is used has many similarities with the typical angle-of-attack modulation of general re-entry vehicles. Nevertheless, it is most likely not truly optimal for the general case considered in the benchmark optimization. Here, we discuss the results of a specific optimization in which the ground-track length objective is replaced by a time duration at reference heat rate objective. By doing so, the guidance algorithm that is used better suits the optimization; it will more closely approximate the best possible value of this objective than the best possible s_g . However, the results presented here are more specific, since they are now tailor-made to a specific mission description. Therefore, they are not as generally applicable to entry mission design as the results presented in the previous sections.

The Pareto front is shown in Fig. 9.31. The volume and mass objectives compete very little with the reference heat-rate duration objective. That is, an increase in fuselage volume or a decrease in vehicle mass will not, or hardly, decrease the maximum duration at reference heat rate that is found on the Pareto front. This in itself is an interesting conclusion, as it shows that the optimal size and mass of the re-entry vehicle are not strongly influenced directly by the requirement of maximum duration at reference heat rate. Of course, the required experimental apparatus and vehicle subsystems will impose certain requirements on the size and mass of the

vehicle. Instead of being limited by the vehicle's size, the duration at reference heat rate is constrained by the dynamic pressure and load factors constraints, as well as having a marginal stability.

The Pareto optimal solutions of both the baseline and this case, projected onto the m - V plane are shown in Fig. 9.32. It can be seen that the majority of the m - V front is hardly affected by the change of the third objective function. Only for the largest values of mass and volume do the fronts show substantially different behaviour, with the benchmark case having solutions up to higher values of mass and volume.

Figure 9.33 shows the value of the maximum stagnation-point heat rate that occurs. It is clear that the maximum value very nearly coincides with the reference heat-rate value of 700 kW/m^2 for the majority of the cases. This was to be expected, since any time spent overshooting the reference heat rate is time during which kinetic energy is lost without being at the measurement flight conditions. If this overshoot is small, this kinetic energy could be lost while performing the measurements at the reference heat rate, increasing the time that can be spent at the reference heat rate.

The majority of shape parameters show similar behavior to the benchmark case, but it is interesting to consider those parameters that show different behavior. To understand these differences, the different requirements for optimality on the vehicle's behavior for the two cases should be analyzed. For the tracking-objective case, only the time spent during the heat-rate tracking is considered, whereas for the benchmark case the range throughout the full entry (down to Mach 3) is considered. A long time spent at the reference heat rate could benefit the total range of the vehicle. However, spending a long time at this heat rate could decrease the time spent and range traveled during the other phases of the entry, decreasing the total range s_g .

A number of characteristics of the entry trajectory are plotted in Fig. 9.34 for the heat-rate tracking case. When comparing these figures to Fig. 9.11, it can be seen that some behavior is similar. The relation between initial lift over drag and the third

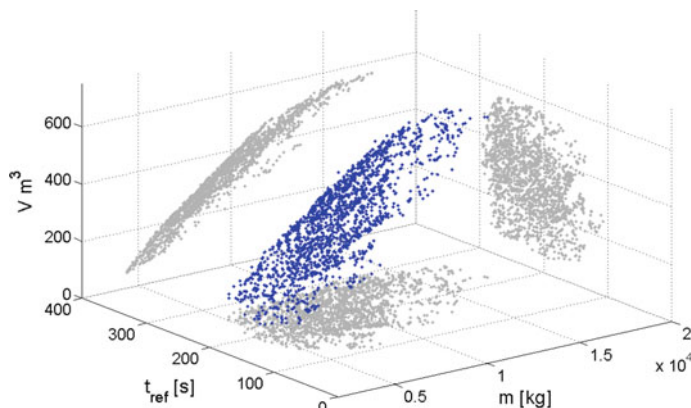


Fig. 9.31 Pareto front of heat-rate tracking objective results, plotted in the three objective functions, and projected onto the three objective planes

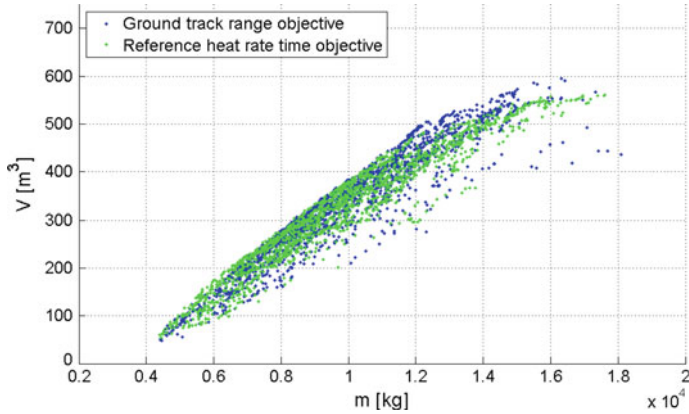
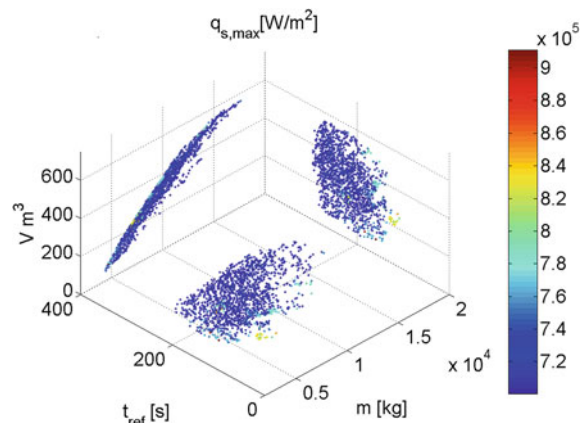


Fig. 9.32 Comparison of Pareto-optimal solutions projected onto m - V plane for benchmark and heat-rate tracking objective cases

objective function are similar. The relation between the density and velocity at the initiation of the tracking phase are clearly different, though. For the tracking-time objective, a large velocity and low density are advantageous for the objective function, whereas an opposite behavior is observed for the ground-track length objective. This indicates that for the s_g objective, it is advantageous to start the nose-down maneuver at a lower altitude and velocity, as discussed in Sect. 9.2.1. This is not a causal relation, though, but a correlated one. Vehicles with large s_g will spend a longer time at large velocities due to a lower drag in the initial phase, which is advantageous for a large range. Such behaviour will result in a later initiation of the nose-down maneuver. Although the L/D will be higher for a lower angle of attack, the flight profile of the shapes with a late nose-down maneuver decelerate slower, and therefore have a larger range. It should be noted, however, that this will not necessarily be the case

Fig. 9.33 Scatter plot of maximum stagnation-point heat transfer for tracking-time objective



for an optimal guidance law, where the vehicle is, for instance, commanded to fly at maximum L/D over a portion of the trajectory. For the heat-rate tracking objective, though, the time spent during the nose-down maneuver is what is to be optimized. The drag coefficient is typically strictly increasing with angle of attack at the attitudes considered and the required drag coefficient during the maneuver decreases with decreasing velocity. As such, a lower rate of change in kinetic energy during the nose down maneuver will result in a longer time at the reference heat rate. For a given $\alpha - C_D$ relation, the rate of change of velocity can be written as:

$$\frac{dV}{dt} \sim \rho V^2 \quad (9.1)$$

For a given nose radius, the value of $\rho^{1/2} V^3$ should be constant at a value K during the tracking phase. As such, the above dependency can be written as:

$$\frac{dV}{dt} \sim \left(\frac{K}{V^2} \right)^2 \quad (9.2)$$

so that a larger velocity at the initiation of the entry will yield a smaller rate of change of velocity and thereby a longer time at the reference heat rate. As is to be expected, and can be seen from Fig. 9.34b, this corresponds to a low ballistic coefficient at high angle of attack.

In addition to initiating the nose-down maneuver at a high velocity, additional factors influence the time that the vehicle spends at the reference heat rate. From Eq. (2.45), it can be seen that the vehicle will stop the heat-rate tracking when the required drag becomes so low that it cannot be attained by the vehicle within the prescribed attitude bounds. Due to this, a maximum value of the ballistic coefficient at low angle of attack is desirable, since this will extend the time during which the vehicle can fulfill Eq. (2.45). The requirements for small ballistic coefficient at large angle of attack and large ballistic coefficient at low angle of attack are somewhat conflicting. The range of the ballistic coefficient between $\alpha = 40^\circ$ and $\alpha = 10^\circ$ will vary for different shapes, though. This can be seen from Fig. 9.35, where the solutions with largest t_{ref} have both the lowest values of $B_{\alpha=40^\circ}$ and the highest value of $B_{\alpha=10^\circ}$.

We show a number of the shape parameters for the optimization for maximum t_{ref} in Fig. 9.36 for the fuselage. The nose radius of the solutions with maximum t_{ref} differ strongly from those of the benchmark case. This is explained by the desire of the large t_{ref} solutions to have their maximum stagnation-point heat flux at $q_{s,ref}$, so that the value of R_N is ‘tailored’ to fit this, based on the shape of the rest of vehicle.

These opposite requirements for the tracking time and ground-track length objectives will cause differences in the optimum shapes that are produced. A number of differences can be observed for the middle fuselage cross-section. The top of this cross-section, namely the values of $z_{2,1}, y_{2,2}$ and $z_{2,2}$ are hardly affected by the change in objective function, but the values defining the bottom of the vehicle vary more substantially. These parameters are important for determining the ballistic coefficient at large angles of attack. The value of $y_{2,3}$ increases faster, indicating a wider vehicle

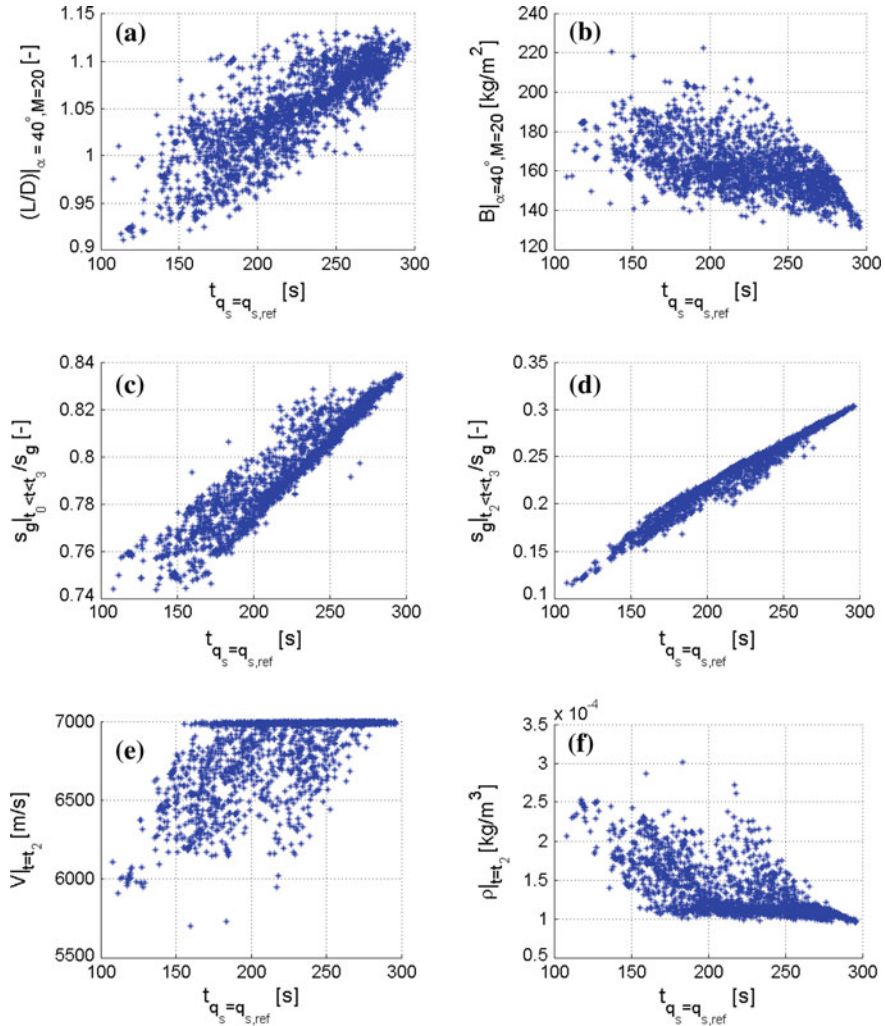
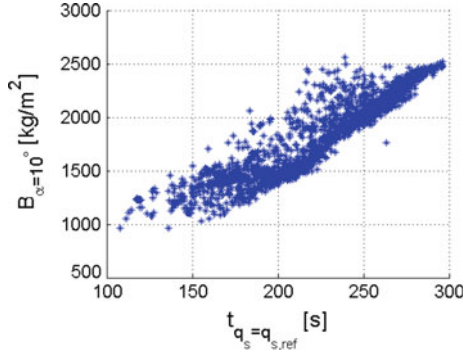


Fig. 9.34 Selected trajectory parameters of Pareto-optimal solutions. **a** Initial L/D . **b** Initial ballistic coefficient. **c** Fraction of total range traveled up until nose down maneuver complete. **d** Fraction of total range traveled during nose-down maneuver. **e** Velocity at initiation of nose-down maneuver. **f** Density at initiation of nose down maneuver

bottom and therefore a larger drag at $\alpha = 40^\circ$. Clearly, $z_{2,4}$ can be seen to decrease. For large values of t_{ref} , as was to be expected from the desirability of low $B_{\alpha=40^\circ}$.

For the rear cross-section, an opposite behavior is observed, in that the top of the vehicle is more strongly affected than the bottom. Although the value of $z_{3,1}$ behaves very similarly, the value of $y_{3,2}$ is smaller than in the ground-track range objective case. This value will not directly affect the aerodynamics at large angles

Fig. 9.35 Ballistic coefficient at end of heat tracking phase



of attack, as it will be shadowed by the wing. At low angles of attack, though, a larger value of this parameter will cause a larger cross section that the flow sees, thereby increasing the ballistic coefficient. This is only true for cases where the rear contour is ‘wider’ than the middle contour so as not to be shadowed by it, which is the case for most of the Pareto-optimal solutions, especially the large t_{ref} solutions. The value of $z_{3,2}$ becomes larger for the t_{ref} objective case, which will not affect the aerodynamic characteristics very strongly for the low values of $y_{3,2}$. However, this could be to ‘compensate’ for the loss in volume V . Alternatively, it could be caused by yaw instability, which is an issue for a large number of the Pareto-optimal solutions. Since a large value of $z_{3,2}$ means a ‘flatter’ vehicle side, the restoring yaw moment due to a sideslip perturbation will be by this.

The wing shape is also influenced by the change in objective function, with the key changes shown in Fig. 9.37. Most notably, the values of both R_{LE} and θ_{LE} are at very low values for most of the points on the Pareto front. This is due to the fact that their values, especially R_{LE} , much more strongly reduces the value of $B_{\alpha=10^\circ}$ than it increases the value of $B_{\alpha=40^\circ}$. This is due to the fact that the added region of large inclination is comparatively less influential at large angles of attack, where the rest of the wing will have a large inclination anyway, then at low angles of attack. Due to the preference for low values of $B_{\alpha=10^\circ}$, the values of R_{LE} and θ_{LE} are driven to low values.

The wing planform shape of the benchmark and t_{ref} cases show the greatest differences in the value of L_w . It increases more slowly with increasing m and V and $x_{w,2}/x_{w,1}$, which has a region of large t_{ref} , m and V where its value jumps to the maximum allowable value. The different behavior of L_w could be caused by the trade-off between large $B_{\alpha=40^\circ}$ and low $B_{\alpha=10^\circ}$. Alternatively, it could be to increase the pitch stability of the vehicle, which is marginal in this region. The aberrant values of $x_{w,2}/x_{w,1}$ could be to ‘compensate’ for this. The change in $x_{w,2}/x_{w,1}$ is accompanied by a strong decrease in $q_{LE,max}$, which was previously noted in the Monte Carlo analysis described in Sect. 9.1. If this had been the driving factor behind the change, though, the change would have occurred much less rapidly, to keep the $q_{LE,max}$ on its maximum value. In addition to these changes in $x_{w,2}/x_{w,1}$ and L_w , the value of

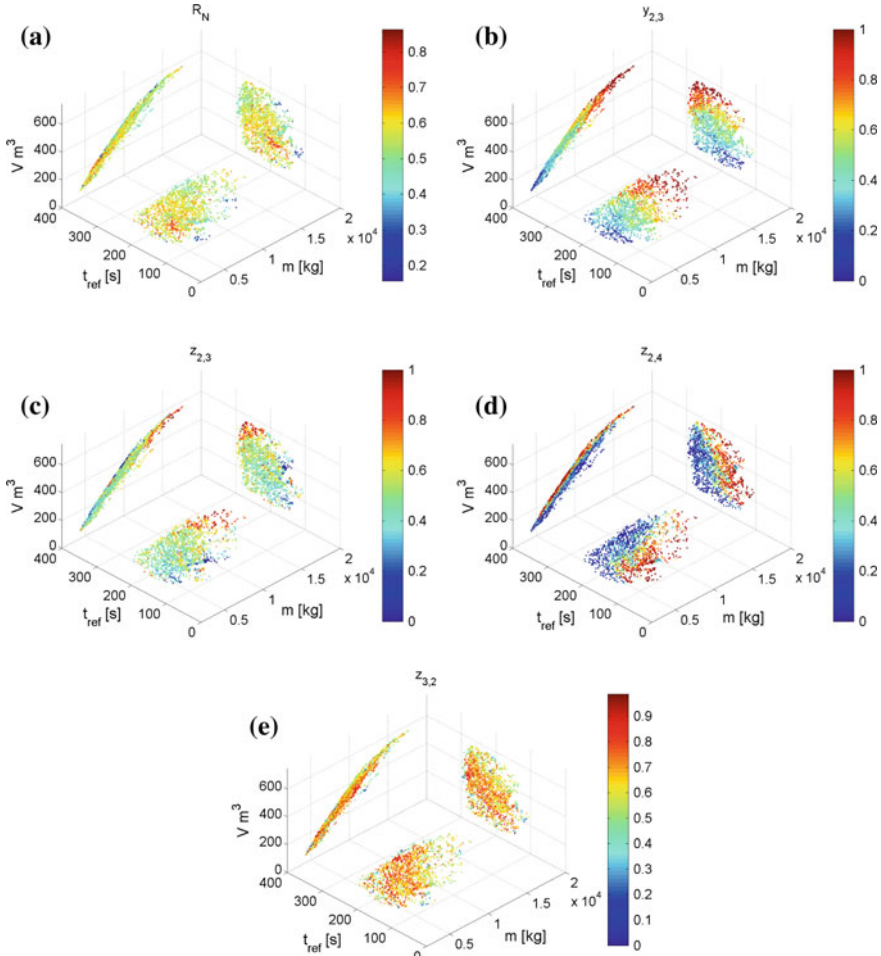


Fig. 9.36 Scatter plots of selected parameters r defining fuselage-shape parameters for heat-rate tracking optimization, projected onto the three objective-function planes

$y_{w,1}$ can be seen to increase from its minimum value only for the largest m and V . The reasons for this behavior is likely that the increase in mass due to a greater wing span is only offset by the associated increase in drag to cause a large value of $B_{\alpha=40^\circ}$ for large vehicles, where the fuselage mass itself is already large.

Finally, we note that along the maximum values of t_{ref} , all stability constraints, as well as the dynamic-pressure constraint, are at or near their maximum allowable values, indicating a broad sensitivity to the selected constraint function values.

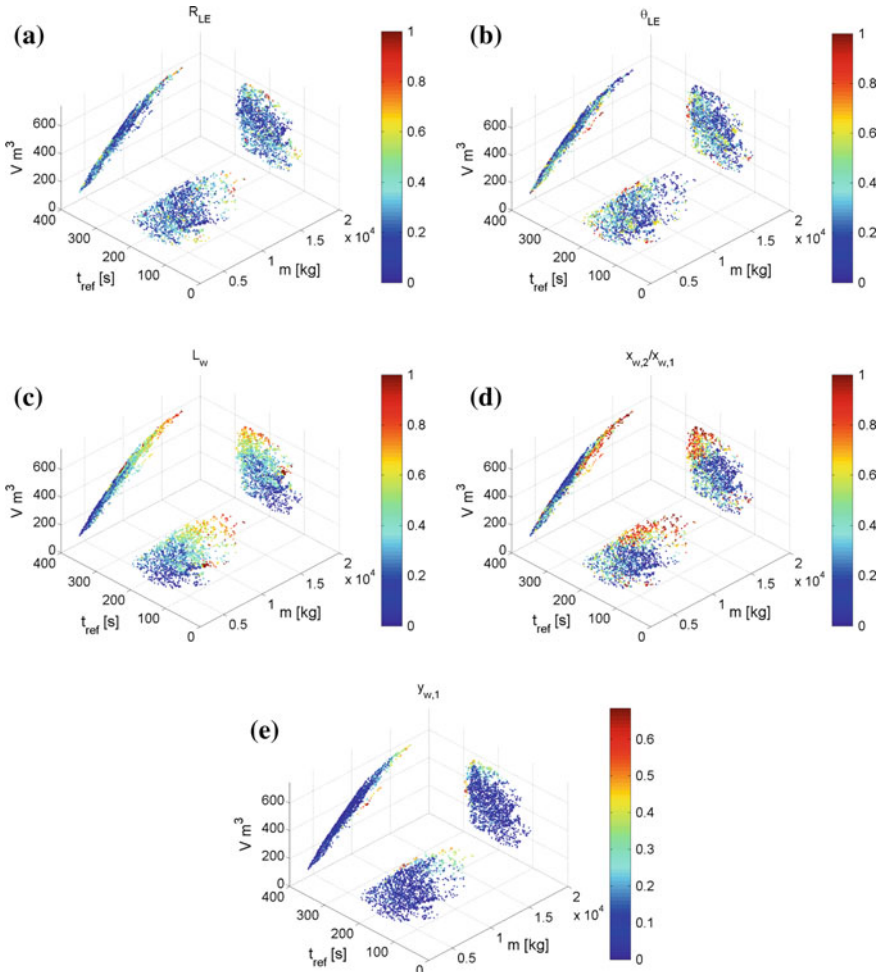


Fig. 9.37 Scatter plots of selected parameters r defining wing-shape parameters for heat-rate tracking optimization, projected onto the three objective-function planes

9.3 Concluding Remarks

In this chapter, the optimization of the winged vehicle shape was outlined, based on the models outlined in the Chaps. 2–7. We have uncovered a variety of interesting features in the behaviour of the optimal shapes, as well as the manner in which the constraint functions depend on the shapes. The optimization of a winged vehicle was performed using the same aerodynamic analysis tools as for the capsule shaped vehicle, with the addition of panel shadowing and aerodynamic analysis of the control surfaces. The winged shape consists of separately defined fuselage and wings, both

of which are generated using Hermite spline surfaces. The two are merged to form a single shape in such a manner as to keep the leading edge radius unchanged. The vehicle includes both a body flap and elevons for pitch trim. For the trajectory determination, a simple guidance law, based on tracking a reference heat flux, taken here at 700 kW/m^2 , following the heat flux peak.

Due to the interdependent nature of the various shape parameters in how a value of r_x translates into the actual parameter x (see Eq. (5.1)), behavior in a number of parameters appears to be non-smooth in the values of r , while it actually is smooth in the physical parameters. This is most notable in the $y_{2,3}$ and $z_{2,4}$ parameters. This indicates the viability of shape parameterizations with such interdependent parameters. However, we do observe a slower convergence of the optimizer compared to the capsule-shaped vehicle.

For the fuselage shape, it was observed that the distance between the front and middle contour increases more slowly than the distance between the middle and rear contour. That is, the front of the vehicle is small on a larger portion of the Pareto front than the rear part. This was found to be due to the stronger influence of the length of the vehicle front on the TPS mass. It is interesting to see that for most existing vehicles and vehicle concepts, this behavior is also observed.

A very interesting effect was observed in the optimal wing shapes, namely that for almost all vehicle shapes, the wing span was at its minimum allowable value. This indicates that there is, using the mathematical models and mission profile used here, very little use of having wide wings. The cause for this is most likely from three contributions. Firstly, an increase in wing size will decrease the ballistic coefficient at high angle of attack, decreasing the range. Secondly, larger wings mean an increase in mass without any benefit to the fuselage volume objective. Counterintuitively, the lift over drag does not necessarily increase with increasing wing size, when using the permissible wing shapes in the parameterization. The blunt leading edge, which the vehicle has to limit the leading-edge heat-flux, adds to the drag of the vehicle in such a manner that the lift over drag of the wings alone is not always superior to that of the fuselage, as the fuselage shape itself is also optimized. This problem is only exacerbated for wider wings, in which the inclination angle of the leading edge is larger due to the effective decrease in wing sweep angle. In addition to being of influence on the drag and heating characteristics, the leading edge radius was also found to influence the pitch and yaw stability of the vehicle, due to the larger moments exerted on the leading edge for larger radii. This result should be treated with caution, though. For instance, the inclusion of sub-hypersonic Mach regimes could affect the feasibility and optimality of the vehicle shape. Additionally, any advantage of having wider wings is not explicitly exploited by the guidance algorithm, since the range of ‘intermediate’ angles of attack ($10 \leq \alpha \leq 40$) is flown for a relatively short period of time. Also, a more accurate mass model could influence the optimality of larger wings.

Nevertheless, the results shown here indicate that a lifting body optimization is highly recommended. Also, allowing the optimizer to choose between different parameterizations would allow for a good comparison between a lifting body and

winged vehicle shape. Such a method could be used to allow the optimizer to choose between different low- L/D type vehicles, such as a capsule, probe, bicone etc.

When imposing the pitch stability constraint at all angles of attack, instead of only angles of attack larger than 25°, the solutions in the Pareto front showed a strong preference to large upward control surface deflections. This shows that upward body-flap deflections are the optimal manner in which to pitch-stabilize the vehicle. Although the pitch-stabilizing effect of upward control surface deflections is well known, it is interesting to see that the vehicle shapes which are produced are typically not ‘inherently’ pitch stable, but instead derive their stability from the fact that they require such control surface deflections. It was seen that the Pareto front itself was quite a bit smaller when imposing the pitch stability constraint at all angles of attack. This is especially noticeable in the $m - V$ Pareto front. It is roughly a straight line over most of its range, the slope of which is smaller in the case of the pitch stable case. From this, a trade-off can be made between decreased fuselage (and payload) volume for a given mass at the benefit of increased pitch stability.

Concerning the driving constraints, we found that the dynamic pressure constrains the Pareto front over the maximum range solutions. Stagnation point heating and load factor became active for high range/low mass/volume solutions, though. Pitch stability was found to be marginal for the shapes which do not reach the reference heat rate and both yaw and roll stability are (nearly) marginal for low mass/volume solutions, due to the small vehicle sides for these shapes, which reduces the restoring moment due to pressure on these sides.

The stagnation-point heat flux is constraining for the high range/low fuselage volume solutions. For these solutions, the nose radius is low and the vehicle retains a relatively high velocity at relatively high density, leading to high heating. Due to the fact that the guidance algorithm is based on heat-rate tracking, there is a clear relation between maximum heat rate and trajectory behavior. Namely, for maximum heat rates below 700 kW/m², the vehicle tracks its maximum heat rate, which leads to different behavior for a number of shape parameters, as well as the maximum normal load factor.

The leading-edge heating is near, but not on, its maximum permissible value for about the lower half of the Pareto front masses and volumes. For higher mass and volume, the value decreases, but it jumps to its maximum for the largest shapes. This is due to a sharp increase in the value of $x_{w,3}/x_{w,1}$, which makes part of the leading edge less swept, increasing the heating there.

There is a vast array of mathematical options for parameterizing a vehicle shape. A good alternative to the approach we have taken here is the use of NURBS, as is also done by Theisinger and Braun (2009), because these allow for local control of the vehicle shape. Alternatively, parameterization based on more clearly interpretable quantities than Bezier points could be investigated, as this allows the mathematical results to be more transparently related to the vehicle’s design. Additionally, the class/shape methods (Kulfan 2008) could be a good candidate for re-entry vehicle shape optimization. Implementation of a number of these methods for a similar vehicle configuration, coupled with the concept for giving the optimizers a choice of

parameterization, could be used to assess the comparative performance of different vehicle parameterization techniques.

As an extension of the optimization of the shape alone, the implementation of the models of this book could be coupled to models of vehicle subsystems to form a Multidisciplinary Design Optimization (MDO) tool. One such effort is described by Bowcutt et al. (2008). For instance, models for the subsystem mass and shape, as well as structural mass, could be included to get a better estimate of vehicle masses. Also, this would introduce a number of additional constraints on the shape, since all the subsystems must fit inside the vehicle, making the results produced more realistic. It would allow for a better estimation of both center of mass and inertia tensor.

Appendix A

Relative Viscous-Force Approximation

In Chap. 3, it was stated that viscous forces would be neglected in the aerodynamic analysis to simplify the analysis. In this appendix, a rationale will be given for this assumption. First-order viscous methods will be used to show that the viscous force is much smaller than the pressure force for a simple test case. This test case is a flat plate at angle of attack, which will typically experience a larger viscous force, relative to pressure forces, than a real vehicle. Therefore, if the relative viscous force on a flat plate can be shown to have a small influence on the aerodynamic coefficients, it is reasonable to assume this influence will be smaller for a realistic vehicle configuration.

The friction coefficient c_f is typically defined as follows:

$$c_f = \frac{\tau_w}{\frac{1}{2} \rho_e u_e^2} \quad (\text{A.1})$$

where, τ_w is the wall shear, e represents quantities at the boundary layer edge and u represents the velocity component tangential to the wall. For subsonic, low temperature cases, the following was derived, as reported by White (2006), for the friction coefficient of a flat plate:

$$c_f = \frac{0.664}{Re_x} \quad (\text{A.2})$$

where Re_x is the Reynolds number from Eq. (3.31), based on the running length x . It was found by Eckert (1955) that the above relation can be used for high temperature and high velocity flows by introducing a reference temperature T^* , defined as follows:

$$\frac{T^*}{T_e} = 1 + 0.5 \left(\frac{T_w}{T_e} - 1 \right) + 0.22r \left(\frac{\gamma - 1}{2} \right) M_e^2 \quad (\text{A.3})$$

By evaluating Eqs. (A.1) and (A.2) at reference quantities, the friction coefficient can be determined. The problem of determining these quantities is made complex by the presence of high temperature effects, which will have significant influence on

especially T_e , but to lesser degrees on all thermodynamic properties behind the shock wave. These high temperature effects include excitation of the vibrational degrees of freedom, gas dissociation and gas ionization. Various theoretical models exist to predict the influence of these effects on flow properties. Here, the tabulated results of Hansen (1958) will be used to approximate the high temperature characteristics of air. These results are based on the assumption of chemical and vibrational equilibrium. The values of the compressibility Z and specific heats at constant pressure and volume, c_p and c_v , as a function of local pressure p and temperature T will be used. The compressibility Z is used to correct the ideal gas law (3.1) for a change in flow composition, and a resultant change in molar mass M and specific gas constant R . Denoting the compositional properties of the gas in freestream by a 0 subscript, Z can be defined as:

$$Z(p, T) = \frac{p M_0}{\rho R T} \quad (\text{A.4})$$

By removing the assumption of a calorically perfect gas, Eq. (3.1) must be modified to the following:

$$h = \int c_p(T, p) dT \quad (\text{A.5})$$

The calculation procedure used for the friction coefficient on a flat plate at angle of attack α is the following. The shock angle β of a flat plate at angle of attack α can be determined directly from Eq. (3.23) since for a flat plate at zero sideslip angle $\alpha = \theta$ will hold. From the shock angle β , the post-shock pressure and Mach number can be determined from Eqs. (3.18) and (3.20), assuming a calorically perfect gas. Now, the simplification is made that the post-shock pressure and Mach number are uniform, also without the calorically perfect gas assumption, as such the post shock conditions can be assumed to equal the conditions at the edge of the boundary layer. To arrive at the properties of the dissociated, vibrationally excited gas, an iterative algorithm is used, using conservation of total enthalpy. The value of γ of the previous iteration (initialized at 1.4) is used to determine values of p_e and M_e from Eqs. (3.18) and (3.20). From these values, conservation of total enthalpy, from (3.14) is used, with the tabulated values from Hansen (1958) and Eq. (A.5) to determine the equilibrium composition and temperature behind the shock. The post shock velocity is obtained from conservation of linear momentum:

$$\rho V = \text{constant} \quad (\text{A.6})$$

so that the total enthalpy behind the shock wave at a temperature T_e and pressure p_e is obtained from:

$$h_T = \int_0^{T_e} c_p dT + \left(\frac{\rho_0 Z_e R_0 T_e}{p_e} \right)^2 \frac{u_e^2}{2} \quad (\text{A.7})$$

From the equilibrium composition, a new value of γ is obtained, which is used as input for the next iteration of the algorithm.

Having found the equilibrium composition, and associated values of γ_e , M_e , Z_e , p_e and T_e are obtained. From these, Eq. (A.3) can be evaluated to obtain T^* . Subsequently, Eq. (A.4) is used to obtain the value of ρ^* . Now, the Reynolds number can be evaluated at reference temperature, so:

$$Re_x^* = \frac{\rho^* u_e x}{\mu^*} \quad (\text{A.8})$$

The viscosity is evaluated at reference temperature by using the ω -law (with $\omega = 0.7$). The friction coefficient at reference temperature becomes:

$$c_f^* = \frac{\tau_w}{\frac{1}{2} \rho_* u_e^2} \quad (\text{A.9})$$

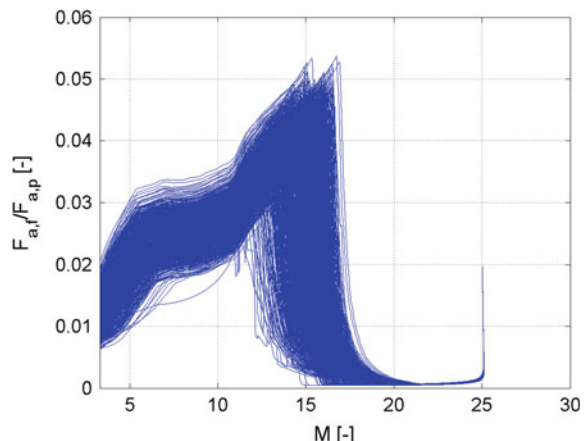
$$= \frac{0.664}{\sqrt{Re_x^*}} \quad (\text{A.10})$$

Integrating this over the running length x and dimensionalizing by (A.1), the following is obtained for the viscous force on the flat plate:

$$|\mathbf{F}_{a,f}| = \rho^* (u_e)^2 \frac{1.328}{\sqrt{Re_L^*}} L \quad (\text{A.11})$$

Comparing this to the equation for Newtonian pressure coefficient (3.51), the relative strength of the pressure and viscous forces on a flat plate can be approximated. Using a flat plate length L of 15 m, which is near the minimum length for the winged vehicles considered here, the 1,000 shapes considered in Sect. 9.1, but using an exponential atmosphere, are used. The $h - V$ profile of these vehicles is used as input for the above algorithm. The resultant ratios of viscous over pressure force on the flat plate is shown in Fig. A.1. As can be seen, the viscous force has a maximum relative strength

Fig. A.1 Ratio of viscous and pressure force for a flat plate at angle of attack, wetted on windward side only, along trajectories as in Sect. 9.1



of $<5\%$ for the majority of the trajectories, over the majority of the trajectories. Since the flat plate will have a larger relative viscous force than the vehicles which are considered here, this shows that, using first order viscous and pressure-force methods, neglecting the viscous force is justifiable.

Appendix B

Winged-Vehicle Shape Generation Example

To more clearly explain the construction of the winged-vehicle shape, this appendix will give a step-by-step example of the creation of one of these shapes. It will be clearly stated and shown with figures how the various constraints are used, which constraints are active, and how the fuselage parameters are generated from these. The randomly generated vector of associated parameters \mathbf{r}_x is found in Table B.1.

B.1 Fuselage Shape

The first step in the vehicle generation is the generation of the nose shape. From the values in Table 5.2 and the above values of the associated parameters, using Eq. (5.1):

$$R_N = 0.4 + 0.972 (1.0 - 0.4) \quad (\text{B.1})$$

$$= 0.983 \text{ m} \quad (\text{B.2})$$

$$\theta_N = 22.5 + 0.411 (77.5 - 22.5) \quad (\text{B.3})$$

$$= 49.0^\circ \quad (\text{B.4})$$

The resulting nose shape is shown in Fig. B.1.

Having generated the nose shape, the remainder of the fuselage shape is to be determined. The first step is to generate the spline curve at the first contour, which should approximate a circle to best match with the nose sphere segment. The radius of this circle R_1 of this circle is determined from the following:

$$R_1 = R_N \sin \theta_N \quad (\text{B.5})$$

$$= 0.983 \sin(49.0^\circ) = 0.742 \text{ m} \quad (\text{B.6})$$

Now, the spline that approximates a circle with this radius is generated. Figure B.2 shows the resulting spline, with its control points.

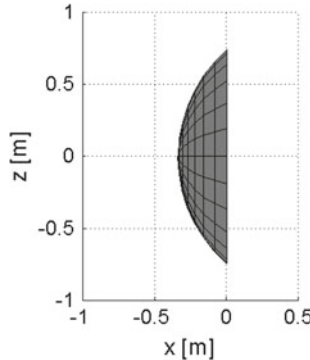


Fig. B.1 Side view of sphere segment nose shape

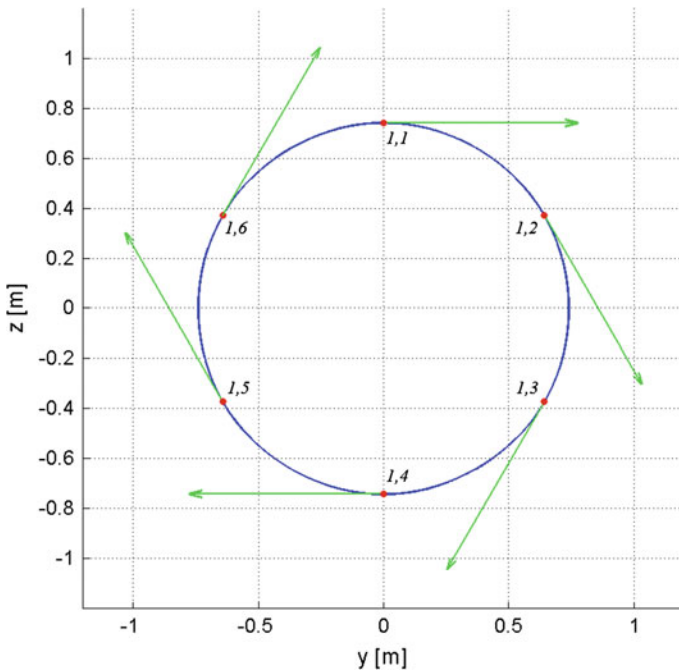


Fig. B.2 Spline at contour 1 of fuselage, which approximates a *circle*. Control point locations indicated in *red*. Control point derivative vectors indicated in *green*

The location of the second cross section is determined from the value of Δx_1 . This value is again determined from the minimum and maximum values in Table 5.2 and the associated parameter $r_{\Delta x_1}$ from Table B.1:

$$\Delta x_1 = 7.0 + 0.636(12.0 - 7.0) \quad (\text{B.7})$$

$$= 10.2 \text{ m} \quad (\text{B.8})$$

Table B.1 Associated parameters of winged vehicle used in this example

R_N	θ_N	Δx_1	$z_{2,1}$	$y_{2,2}$	$z_{2,2}$	$y_{2,3}$	$z_{2,3}$	$z_{2,4}$	$z_{3,1}$	$y_{3,2}$
0.972	0.411	0.636	0.482	0.709	0.297	0.468	0.512	0.110	0.779	0.986
$z_{3,2}$	$y_{3,3}$	$z_{3,3}$	Δx_2	R_{LE}	θ_{LE}	t_{mid}	L_{mid}	L_w	$x_{w,2}/x_{w,1}$	$x_{w,3}/x_{w,1}$
0.803	0.530	0.487	0.794	0.306	0.140	0.947	0.116	0.482	0.346	0.403
$x_{w,4}/x_{w,1}$	$y_{w,1}$	$y_{w,3}$	$\Delta x_f/x_{w,4}$	θ_f	f_{el}	L_{bf}				
0.994	0.992	0.699	0.867	0.219	0.921	0.578				

Similarly, the location of the third cross-section follows from the value of both Δx_1 and Δx_2 . Δx_2 is calculated from:

$$\Delta x_2 = 7.0 + 0.794 (12.0 - 7.0) \quad (\text{B.9})$$

$$= 11.0 \text{ m} \quad (\text{B.10})$$

Now, for the generation of the second cross-sectional spline, the algorithms described in Sect. 5.2.1 will be shown step by step.

First, the determination of the top point of this contour, $z_{2,1}$, will be explained. Since this point is at the top of the contour, its y -coordinate will be 0. The allowable region of its z -coordinate is determined by four constraint functions, two limiting the minimum and two limiting the maximum value. One of these is the outer bounding curve shown in Fig. 5.7, which is an ellipse shape. Since $z_{2,1} > 0.0$, Eq. (5.23) and not Eq. (5.24) applies for the shape of this ellipse. Since $y = 0$, the following constraint is obtained for $z_{max} = 3.5 \text{ m}$:

$$z_{2,1} \leq 3.5 \text{ m} \quad (\text{B.11})$$

The other constraint limiting the maximum allowable value of $z_{2,1}$ is expressed by Eq. (5.25). This constraint ensures that the fuselage between contour 1 and contour 2 will be convex in longitudinal direction. Evaluating the equation yields:

$$z_{2,1} \leq 0.742 \sin(49.0^\circ) + \frac{10.2}{\tan(49.0^\circ)} \quad (\text{B.12})$$

$$\leq 9.59 \text{ m} \quad (\text{B.13})$$

From these constraint function values (B.11) and (B.13), it can be seen that Eq. (B.11) limits the permissible maximum value of $z_{2,1}$.

The first constraint limiting the minimum allowable value of $z_{2,1}$, from Eqs. (5.21) and (5.22), the global minimum radius constraint, evaluates to the following:

$$z_{2,1} \geq \max(2 \cdot 0.983 \cdot \sin(49.0^\circ), 1.0) \quad (\text{B.14})$$

$$\geq \max(1.48, 1) \quad (\text{B.15})$$

$$\geq 1.48 \text{ m} \quad (\text{B.16})$$

The second constraint limiting the minimum allowable value is the requirement for the possibility of longitudinal convexity between subsequent contours. It is expressed by Eq. (5.27). Evaluating this leads to the following:

$$z_{2,1} \geq R_1 - (R_1 - r_{min}) \frac{\Delta x_1}{\Delta x_1 + \Delta x_2} \quad (\text{B.17})$$

$$\geq 0.742 - (0.742 - 1.48) \cdot \frac{10.2}{11.0 + 10.2} \quad (\text{B.18})$$

$$\geq 1.10 \text{ m} \quad (\text{B.19})$$

From constraints (B.11) and (B.13), it can be seen that the former of these is the most constraining, leading to the following for $z_{2,1}$:

$$1.48 \text{ m} \leq z_{2,1} \leq 3.50 \text{ m} \quad (\text{B.20})$$

From the value of $r_{z_{2,1}}$, the following is obtained:

$$z_{2,1} = 1.48 + 0.482 \cdot (3.50 - 1.48) \quad (\text{B.21})$$

$$= 2.46 \text{ m} \quad (\text{B.22})$$

The subsequent points, $y_{2,2..3}$ and $z_{2,2..3}$ are more complicated to generate, as bounding regions in two dimensions need to be generated from which the points are taken. The generation of all constraints, the bounding regions which result from this, and the generation of the control point locations, will now be detailed. First, the generation of point (2, 2) will be detailed. Subsequently, the same procedure will be shown, in somewhat less detail, for point (2, 3).

For $j = 2$ (and $N_{pt} = 6$), the allowable angular range from Eqs. (5.19) and (5.20) becomes:

$$0^\circ < \phi_2 < 90^\circ \quad (\text{B.23})$$

which translates into the following two equations for bounding curves:

$$y > 0 \quad (\text{B.24})$$

$$z > 0 \quad (\text{B.25})$$

Due to the second of these, the top half of the outer ellipse shown in Fig. 5.7, expressed by Eq. (5.23), is applicable. With $y_{max} = 4$ and $z_{max} = 3.5$, this becomes:

$$z^2 \leq 3.5^2 - \left(\frac{3.5}{4}\right)^2 y^2 \quad (\text{B.26})$$

$$\leq 3.5^2 - 0.766y^2 \quad (\text{B.27})$$

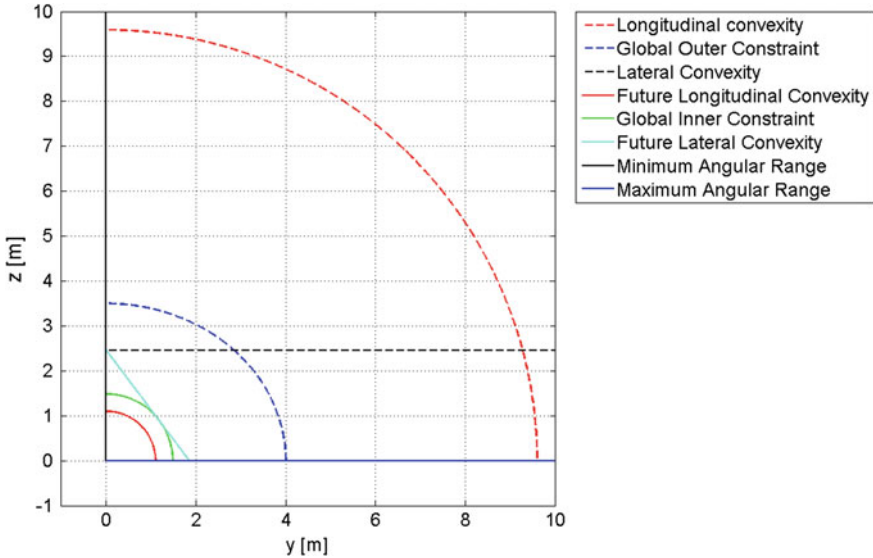


Fig. B.3 All bounding curves for point (2, 2). Curves imposing maximum values on y dashed, curves imposing minimum values full

The constraint for longitudinal convexity is the same for all j , for $i = 2$, so the right-hand side of Eq. (5.25) will be the same as in Eq. (B.12), so:

$$\sqrt{y^2 + z^2} \leq 9.59 \text{ m} \quad (\text{B.28})$$

$$z^2 \leq 9.59^2 - y^2 \quad (\text{B.29})$$

Similarly, since $r_{1,1} = r_{1,2}$, due to the fact that contour 1 is a circle, the constraint for longitudinal convexity on subsequent contours, from Eq. (5.27), has a right-hand side equal to that for $z_{2,1}$, from Eq. (B.19), so the bounding curve is the following:

$$y^2 + z^2 \geq 1.1^2 \quad (\text{B.30})$$

$$z^2 \geq 1.1^2 - y^2 \quad (\text{B.31})$$

Constraint (7) shown in Fig. 5.7 reduces to the following for $z_{2,2}$:

$$z \leq 2.46 \text{ m} \quad (\text{B.32})$$

which is used to ensure lateral convexity.

The constraint used to ensure that subsequent points on this contour can satisfy the lateral convexity constraint is shown as curve (8) in Fig. 5.7. The line through $\mathbf{p}_{2,1}$, tangent to the circle with radius R_1 is determined as follows:

$$\tan \theta_1 = 0 \quad (B.33)$$

$$\theta_1 = 0 \quad (B.34)$$

$$\sin \theta_2 = \frac{1.48}{2.46} \quad (B.35)$$

$$\theta_2 = 0.646 \quad (B.36)$$

From these, the equation for the bounding curve is found to be:

$$z - z_{2,1} = \frac{y - y_{2,1}}{\tan(\theta_1 - \theta_2)} \quad (B.37)$$

$$z = -1.33y + 2.46 \quad (B.38)$$

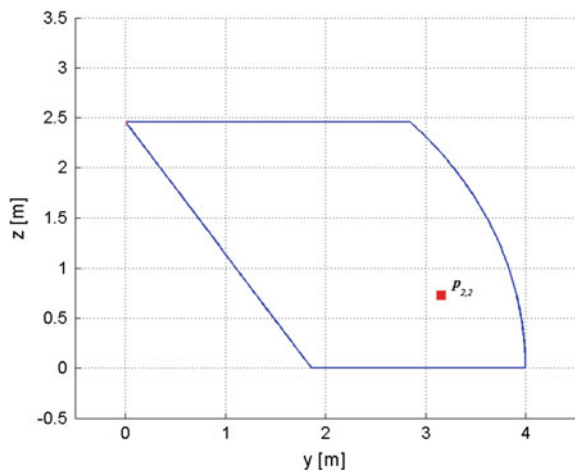
Eight bounding curves have now been determined for the position of $\mathbf{p}_{2,2}$. All of these curves are plotted in Fig. B.3, where the constraints which impose minimum values on y are drawn as full lines and constraints imposing maximum values on y are drawn in dashed lines. In this particular case, it can be seen that the longitudinal constraints are active nowhere. This is not necessarily the case for all fuselage points, though. The resulting bounding shape from which the control point is taken is shown in Fig. B.4.

From this bounding shape, the minimum and maximum possible values of $z_{2,2}$ are determined, which in this case are 0.0 and 2.46, respectively. With the value of the associated parameter $r_{z_{2,2}}$ from Table B.1, the value of $z_{2,2}$ is determined:

$$z_{2,2} = 0.0 + 0.297(2.46 - 0.0) \quad (B.39)$$

$$= 0.731 \text{ m} \quad (B.40)$$

Fig. B.4 Active bounding curves for fuselage point (2, 2), which form the bounding shape



Now, the value of $y_{2,2}$ is determined from the minimum and maximum permissible values of $y_{2,2}$ at $z = 0.731$. These values are obtained from the bounding shape as 1.31 and 3.91, respectively. Now, using the value of $r_{y_{2,2}}$ from Table B.1, $y_{2,2}$ is:

$$y_{2,2} = 1.31 + 0.709(3.91 - 1.31) \quad (\text{B.41})$$

$$= 3.12 \text{ m} \quad (\text{B.42})$$

From which the $\mathbf{p}_{2,2}$ is now fully defined.

For the subsequent control points, the evaluation of the constraint functions will not be shown in as much detail to keep the length of this example reasonable. However, since some constraints are handled differently for different values of i or j , the constraint functions which have not been used for the previous points will be shown explicitly, so that each constraint is evaluated explicitly, step by step, at least once. First point (2, 3) will be dealt with.

The angular range constraint lead to the following bounding curves for point (2, 3):

$$z < 0 \quad (\text{B.43})$$

$$y > 0 \quad (\text{B.44})$$

The global inner radius constraint becomes:

$$\sqrt{y^2 + z^2} \geq 1.48 \text{ m} \quad (\text{B.45})$$

where the value on the right-hand side is the same as for the previous points, since this constraint is constant for all control points.

The global outer constraint becomes, with $z_{min} = -2 \text{ m}$:

$$\left(\frac{y}{4}\right)^2 + \left(\frac{z}{2}\right)^2 \leq 1 \quad (\text{B.46})$$

The longitudinal convexity constraint is the same for all j when $i = 2$, so it is again Eq. (B.28). The same is true for the constraint ensuring future longitudinal convexity, so that Eq. (B.31) again holds.

Lateral convexity is handled differently for $j = 1$ and $j > 1$, so this constraint will now be handled step by step for point (2, 3). The bounding curve (shown as curve (7) in Fig. 5.7) is obtained from the positions of points (2, 1) and (2, 2). The y and z coordinates of point (2, 1) are 0.0 and 2.46. The y and z coordinates of point (2, 2) are 3.12 and 0.731. The bounding curve therefore becomes:

$$y - 3.12 \leq \frac{3.12 - 0.0}{0.731 - 2.46}(z - 0.731) \quad (\text{B.47})$$

$$y \leq -1.83z + 4.49 \quad (\text{B.48})$$

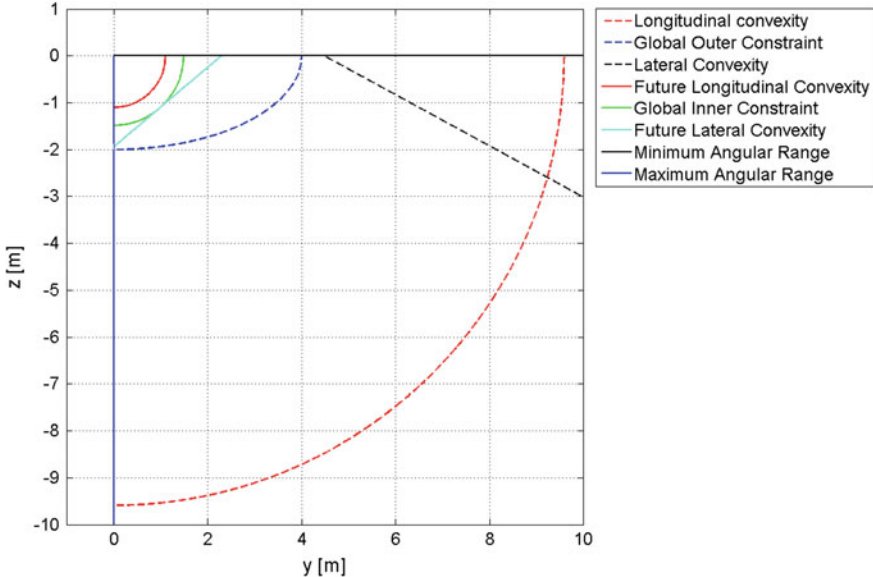


Fig. B.5 All bounding curves for point (2, 3). Curves imposing maximum values on y dashed, curves imposing minimum values full

Finally, the constraint ensuring that the subsequent control point on the contour can satisfy the lateral convexity constraint becomes:

$$y \geq 1.18z + 2.29 \quad (\text{B.49})$$

These constraints are shown in Fig. B.5. The final bounding shape from which the control point can be taken is shown in Fig. B.6.

The minimum and maximum value of z of the bounding shape are -2.00 and 0.00 m , so with $r_{z_{2,3}}$ from Table B.1:

$$z_{2,3} = -2.00 + 0.512(0.00 - (-2.00)) \quad (\text{B.50})$$

$$= -0.975 \text{ m} \quad (\text{B.51})$$

At this value of z , the minimum and maximum values of y are 1.15 and 3.45 , so, with $r_{y_{2,3}}$:

$$y_{2,3} = 1.15 + 0.468(3.45 - 1.15) \quad (\text{B.52})$$

$$= 2.24 \text{ m} \quad (\text{B.53})$$

The final point on the contour is the bottom point, $z_{2,4}$. Again, the constraint function value for the global inner constraint is similar to Eq. (B.16), only with

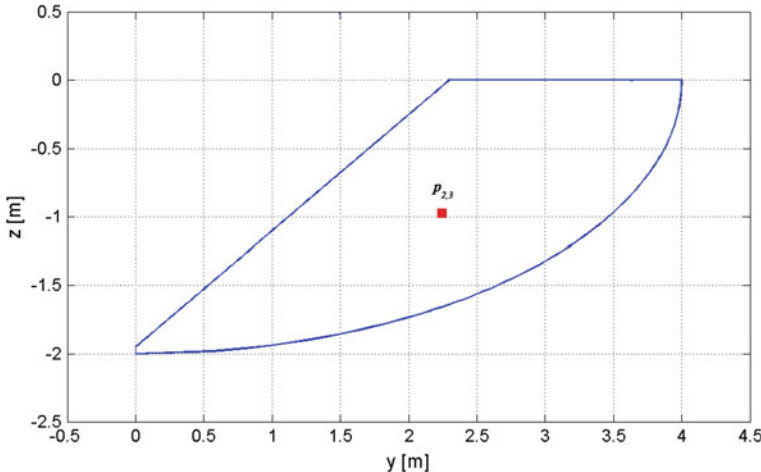


Fig. B.6 Active bounding curves for fuselage point (2, 3), which form the bounding shape

opposite sign due to the opposite signs if $z_{2,4}$ and $z_{2,1}$, so:

$$z \leq -1.48 \text{ m} \quad (\text{B.54})$$

The global outer constraint is taken from Eq. (5.24), so:

$$z \geq -2.0 \text{ m} \quad (\text{B.55})$$

The longitudinal convexity constraint values are the same for the whole contour. For $z_{2,4}$, these are expressed as:

$$z \geq -9.59 \text{ m} \quad (\text{B.56})$$

$$z \leq -1.10 \text{ m} \quad (\text{B.57})$$

From these constraint function values, the following follows:

$$-2.00 \leq z \leq -1.48 \quad (\text{B.58})$$

With $r_{z_{2,4}} = 0.110$, this leads to:

$$z_{2,4} = -1.56 \text{ m} \quad (\text{B.59})$$

Now, all control-point derivatives on the spline are determined using the first-order central difference method described in Sect. 4.2.2. When doing this, it is taken into account that the spline is closed, so that control points 6 and 1 can be considered subsequent (Table B.2):

Table B.2 Control point locations and derivatives on fuselage contour 2

Point index	y-value	z -value	\dot{y} -value	\dot{z} -value
1	0.00	2.46	3.12	0.00
2	3.12	0.731	1.12	-1.71
3	2.24	-0.975	-1.58	-1.15
4	0.00	-2.24	-2.24	0
5	-2.24	-0.975	-1.58	1.15
6	-3.12	0.731	1.15	1.71

$$\mathbf{p}'_{2,1} = \frac{\mathbf{p}_{2,2} - \mathbf{p}_{2,6}}{2} \quad (\text{B.60})$$

$$= \frac{\begin{pmatrix} 3.12 \\ 0.731 \end{pmatrix} - \begin{pmatrix} -3.12 \\ 0.731 \end{pmatrix}}{2} \quad (\text{B.61})$$

$$= \begin{pmatrix} 3.12 \\ 0 \end{pmatrix} \quad (\text{B.62})$$

$$\mathbf{p}'_{2,2} = \frac{\mathbf{p}_{2,3} - \mathbf{p}_{2,1}}{2} \quad (\text{B.63})$$

$$= \frac{\begin{pmatrix} 2.24 \\ -0.975 \end{pmatrix} - \begin{pmatrix} 0 \\ 0.246 \end{pmatrix}}{2} \quad (\text{B.64})$$

$$= \begin{pmatrix} 1.12 \\ -1.71 \end{pmatrix} \quad (\text{B.65})$$

$$\mathbf{p}'_{2,3} = \frac{\mathbf{p}_{2,4} - \mathbf{p}_{2,2}}{2} \quad (\text{B.66})$$

$$= \frac{\begin{pmatrix} 0.00 \\ -1.48 \end{pmatrix} - \begin{pmatrix} 3.12 \\ 0.731 \end{pmatrix}}{2} \quad (\text{B.67})$$

$$= \begin{pmatrix} -1.58 \\ -1.15 \end{pmatrix} \quad (\text{B.68})$$

$$\mathbf{p}'_{2,4} = \frac{\mathbf{p}_{2,5} - \mathbf{p}_{2,3}}{2} \quad (\text{B.69})$$

$$= \frac{\begin{pmatrix} -2.24 \\ -0.975 \end{pmatrix} - \begin{pmatrix} 2.24 \\ -0.975 \end{pmatrix}}{2} \quad (\text{B.70})$$

$$= \begin{pmatrix} -2.24 \\ 0 \end{pmatrix} \quad (\text{B.71})$$

To ensure that the spline which is obtained for this cross-section is both convex and non-self intersecting, the algorithm described in Sect. 4.2.3 is used. This algo-

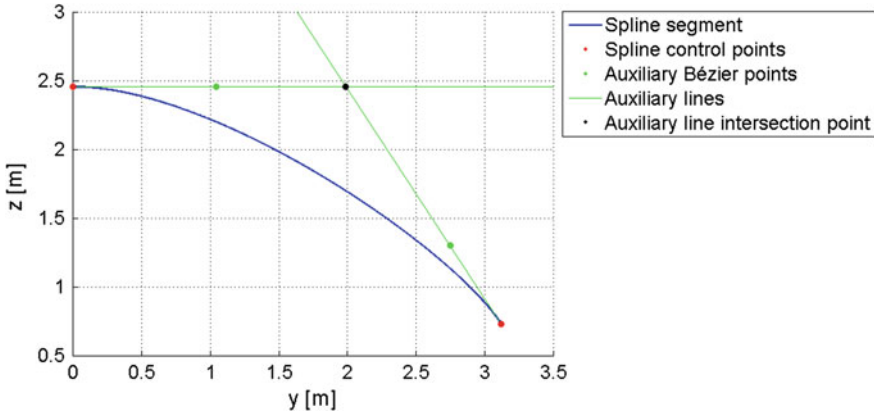


Fig. B.7 Geometric representation of algorithm used to check convexity and non-self intersection of spline segment

rithm will now be shown in detail for a single spline segment, namely the segment between the first two control points. The auxiliary Bézier points are determined from Eq. (4.18). The auxiliary lines, the intersection point between which is the main factor in identifying a self-intersection or concavity, as well as the control points, auxiliary points and spline segment, are shown in Fig. B.7. From this figure and Theorem 4.4, it can be seen that the spline segment will be convex and non-self intersecting. Mathematically, this is determined from the amplification factor equation, Eq. (4.23). The amplification factors are:

$$c_1 = 0.624 \quad (\text{B.72})$$

$$c_2 = 1.00 \quad (\text{B.73})$$

These values can be seen from Fig. B.7 to be of correct size.

The resulting spline for cross-section 2 is shown in Fig. B.8, where the control point locations and derivatives are both indicated.

The generation of the rear spline contour is done similar to the middle contour. The following differences exist between the two, though:

- The manner in which the longitudinal convexity constraint is calculated is by Eq. (5.26) instead of Eq. (5.25).
- No constraint is imposed for ‘future’ longitudinal convexity.
- The value of $z_{3,4}$ is taken equal to $z_{3,3}$.
- The control point derivatives at points (3, 3) and (3, 4) are taken equal to zero to ensure the flatness of the rear for body flap attachment.

The step-by-step calculation will not be shown here again. Instead, the bounding shapes for control points 2 and 3 on the final contour are shown in Fig. B.9. Also the procedure of calculating each derivative explicitly will not be repeated here.

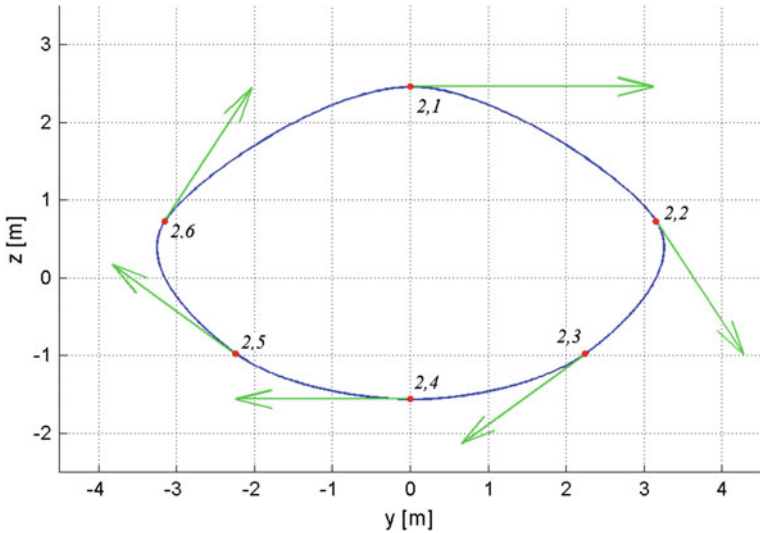


Fig. B.8 Spline defining middle fuselage contour, with control points and control-point derivatives indicated

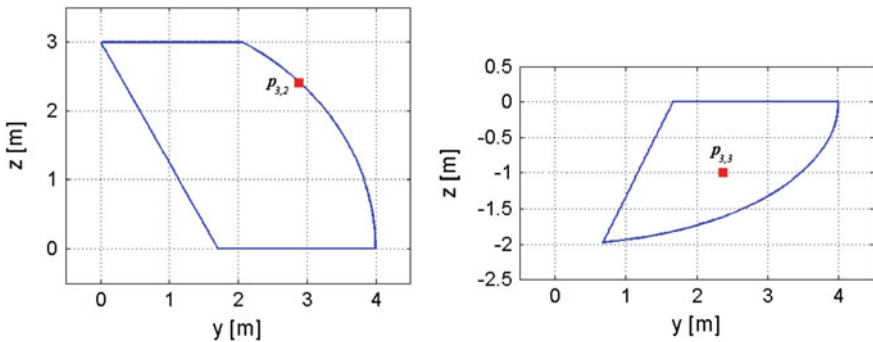


Fig. B.9 Bounding shapes for points 2 and 3 on rear contour

Instead, the resulting control point locations and derivatives of the rear contour are shown in Fig. B.10. Note that the derivatives at points (3, 3) and (3, 4) are zero by definition, due to the requirement that the spline segment between these two points be a straight line, for body flap attachment. It is interesting to note that the convexity-check algorithm modified the control point derivative at control point (3, 2) to prevent a concavity in the spline segment between points (3, 1) and (3, 2). The control point derivative was only slightly too large, with $c_2 = -0.2939$. The top of the cross-section which would have been obtained in the derivative had not been changed is shown in Fig. B.11. Note that the two axes do not use the same scale.

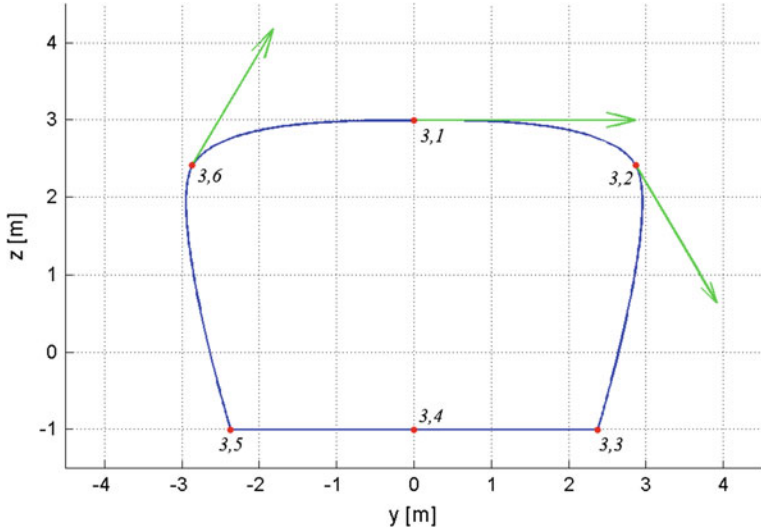
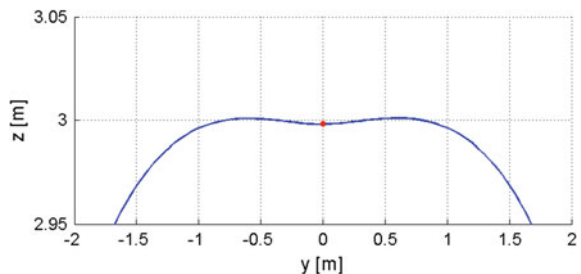


Fig. B.10 Spline defining rear fuselage contour, with control points and control point derivatives indicated. Note that the derivatives at control points $(3, 3)$, $(3, 4)$ and $(3, 5)$ equal $\mathbf{0}$

Fig. B.11 Top of third contour spline if control point derivative at point $(3, 2)$ had not been modified to remove concavity. Note the unequal scale of the axes



Having defined the three spline contours, the spline surface of the vehicle can be created. The six longitudinal splines are created by using $\mathbf{p}_{1,j}$, $\mathbf{p}_{2,j}$ and $\mathbf{p}_{3,j}$, for $j = 1..6$ from the contour splines. From these splines, as well as the splines of the cross-sections, the spline surface control net can be created. Also, the twists can be determined from Eq. (4.27) or (4.28), both of which will yield the same result. The set of cross-section contour splines, and the spline surface control net, are shown in Fig. B.12.

B.2 Wing Shape

Having generated the fuselage and shape, the wing shape can be generated. Here, first the generation of all shape parameters will be shown explicitly, followed by a step-by-step example of how the wing spline surface is generated. For the minimum and

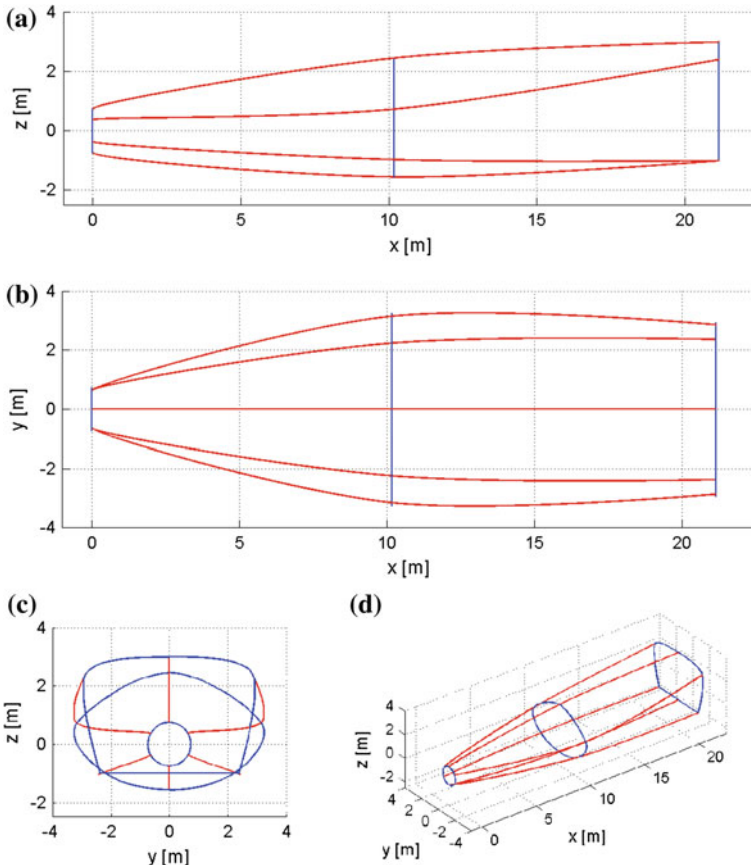


Fig. B.12 Spline surface control net for fuselage shape a) Side view, b) Top view, c) Front view, d) Isometric view

maximum values of the wing parameters, the values and equations from Table 5.2. For the associated parameter values, Table B.1 is used.

The nose radius value follows from:

$$R_{LE} = 0.200 + 0.306(0.400 - 0.200) \quad (\text{B.74})$$

$$= 0.261 \text{ m} \quad (\text{B.75})$$

With this value for the leading edge radius as minimum value for t_{mid} :

$$t_{mid} = 0.261 + 0.947(0.600 - 0.261) \quad (\text{B.76})$$

$$= 0.582 \text{ m} \quad (\text{B.77})$$

The maximum length of the wing is related to the length of the fuselage, which follows from $L_{fus} = \Delta x_1 + \Delta x_2 = 21.2$ m. This leads to a minimum wing length of $0.25 \cdot L_{fus} = 7.40$ m and a maximum length of $0.6875 \cdot L_{fus} = 16.9$ m. Consequently, the value of L_w becomes:

$$L_w = 7.40 + 0.482(16.9 - 7.40) \quad (\text{B.78})$$

$$= 12.0 \text{ m} \quad (\text{B.79})$$

The x -position of the middle control point, defined by the parameter L_{mid} (see Fig. 5.10) is determined from the following:

$$L_{mid} = L_w (0.25 + 0.116 (0.6875 - 0.25)) \quad (\text{B.80})$$

$$= 3.60 \text{ m} \quad (\text{B.81})$$

Now, the angular range of the leading edge can be determined. The minimum allowable value of this parameter, which follows from the desired convexity of the airfoil shape, is obtained from Eq. (5.29):

$$\tan \theta_{LE,min} = \frac{t_{mid} - R_{LE} \cos \theta_{LE,min}}{L_{mid}} \quad (\text{B.82})$$

$$= \frac{0.582 - 0.261 \cos \theta_{LE,min}}{3.60} \quad (\text{B.83})$$

$$\theta_{LE,min} = 5.08^\circ \quad (\text{B.84})$$

where the final step is performed using an iterative algorithm. Now, the value of θ_{LE} is determined from:

$$\theta_{LE} = 5.08 + 0.140 (30 - 5.08) \quad (\text{B.85})$$

$$= 8.57^\circ \quad (\text{B.86})$$

Having defined the parameters for the airfoil shape, the wing planform shape can be determined. For the value of $x_{w,2}/x_{w,1}$:

$$\frac{x_{w,2}}{x_{w,1}} = 0.4 + 0.346(0.6 - 0.4) \quad (\text{B.87})$$

$$= 0.469 \quad (\text{B.88})$$

From this value, the maximum value of $x_{w,3}/x_{w,1}$, which equals $0.9x_{w,2}/x_{w,1}$ can be determined to be $0.9 \cdot 0.469 = 0.422$. This leads to the following for $x_{w,3}/x_{w,1}$:

$$\frac{x_{w,3}}{x_{w,1}} = 0.200 + 0.346(0.422 - 0.200) \quad (\text{B.89})$$

$$= 0.290 \quad (\text{B.90})$$

Similarly, the maximum value of $x_{w,4}/x_{w,1}$, which equals $0.9x_{w,3}/x_{w,1}$ can be determined to be $0.9 \cdot 0.290 = 0.261$. The value of $x_{w,4}/x_{w,1}$ then becomes:

$$\frac{x_{w,4}}{x_{w,1}} = 0.0500 + 0.994(0.261 - 0.0500) \quad (\text{B.91})$$

$$= 0.259 \quad (\text{B.92})$$

The minimum and maximum wing width are fixed, so:

$$y_{w,1} = 4.00 + 0.992(8.00 - 4.00) \quad (\text{B.93})$$

$$= 7.97 \text{ m} \quad (\text{B.94})$$

The minimum and maximum values of $y_{w,3}$ (fin width) are a quarter and a third of the wing length, so 1.99 and 2.66 m, respectively. Consequently:

$$y_{w,3} = 1.99 + 0.699(2.66 - 1.99) \quad (\text{B.95})$$

$$= 2.46 \text{ m} \quad (\text{B.96})$$

The fin bend angle minimum and maximum are fixed, so:

$$\theta_f = 45.0 + 0.219(90.0 - 45.0) \quad (\text{B.97})$$

$$= 54.9^\circ \quad (\text{B.98})$$

Similarly for the value of $\Delta x_f/x_{w,4}$:

$$\frac{\Delta x_f}{x_{w,4}} = 0.00 + 0.867(1.00 - 0.00) \quad (\text{B.99})$$

$$= 0.867 \quad (\text{B.100})$$

The first step in going from this set of parameters to a wing surface is defining the airfoil spline. This spline represents airfoil shape at the root, as it would be if the algorithm from Sect. 5.2.3 would not be applied to smoothly match the wing to the fuselage. One example of such a spline, with the airfoil parameters indicated, is shown in Fig. 5.10.

For the insertion of the elevon into the wing, the elevon length is first determined from Eq. (5.30):

$$L_{el} = 0.290 (12.0 - 3.60) 0.915 \quad (\text{B.101})$$

$$= 2.22 \text{ m} \quad (\text{B.102})$$

Now the algorithm described in Sect. 5.2.2 to determine the exact position of the elevon start control point is used. A spline is formed between control points 6 and 8. The derivative at point 8 equals 0, as described in Sect. 5.2.2. The ‘temporary’ derivative of control point 6 (denoted by a tilde) now becomes:

$$\tilde{\mathbf{p}}'_{1,6} = \frac{\mathbf{p}_{1,8} - \mathbf{p}_{1,5}}{2} \quad (\text{B.103})$$

$$= \frac{\begin{pmatrix} L_w \\ 0 \\ 0.05 \end{pmatrix} - \begin{pmatrix} 0 \\ 0 \\ R_{LE} \cos \theta_{LE} \end{pmatrix}}{2} \quad (\text{B.104})$$

$$= \begin{pmatrix} 6.013 \\ 0 \\ -0.1041 \end{pmatrix} \quad (\text{B.105})$$

With the elevon positioned at $x_7 = L_w - L_{el}$ (with $x = 0$ still at the leading edge front), the following cubic polynomial is obtained, using the Hermite basis functions given in Sect. 4.2. The roots of this equation indicate the values of t where the elevon can be inserted. Since the spline runs from $t = 0$ to $t = 1$, only roots in this interval are accepted:

$$(2x_6 + \tilde{x}'_6 + 2x_8 + \tilde{x}_8) t^3 + (-3x_6 - 2\tilde{x}'_6 + 3x_8 + \tilde{x}_8) t^2 + \tilde{x}'_6 t + x_6 = x_7 \quad (\text{B.106})$$

$$- 10.75t^3 + 13.1t^2 + 6.01t - 6.16 = 0 \quad (\text{B.107})$$

A single root for $0 < t < 1$ is found for this cubic polynomial, with $t = 0.615$. The resultant location for point 7 is:

$$\mathbf{p}_{1,7} = \begin{pmatrix} 9.77 \\ 0 \\ 0.216 \end{pmatrix} \quad (\text{B.108})$$

With this, the airfoil spline is fully defined. This spline, with its control points, is shown in Fig. B.13. The next step is to put this spline in the correct position relative to the fuselage.

First, the airfoil spline as a whole is translated so that it is in the correct position w.r.t. the fuselage. The translation in x -direction is determined from the requirement

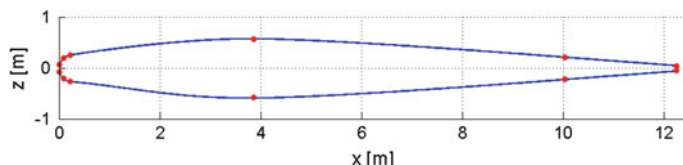


Fig. B.13 Airfoil spline which is generated, with control point locations, prior to repositioning of spline for fuselage interface

that the wing trailing edge be in line with the fuselage rear. Now, the offset in z -direction is determined. The algorithm that determines this offset is based on the idea that, for no value of x , the minimum value of z of the wing should be lower than the minimum value of z of the fuselage. In order to include a margin to assist in the smooth matching of the two parts, this is modified to the requirement that, for all x , the minimum value of z of the wing should be at least t_{mid} greater than the minimum value of the fuselage. This difference is checked at four different positions and the most constraining one is used. The following points are tested:

- (a) Transition between leading edge circle approximation and rear of wing.
- (b) Middle vehicle contour.
- (c) Point of highest thickness on airfoil spline (does not coincide with point of t_{mid}).
- (d) Rear vehicle contour (x -value coincides with trailing edge).

A side view of the fuselage and the airfoil spline, after translation x -direction, and both before and after translation in z -direction, is shown in Fig. B.14. The points where the required offset is checked are indicated in the figure, enumerated as above. The required translations in z -direction at the four points to comply with the requirement are:

- (a) -1.15 m
- (b) -0.979 m
- (c) -0.394 m
- (d) -0.429 m

These values, as well as Fig. B.14, indicate that the wing is to be moved down to go into its correct position. The required offset can be seen to be -0.394 m. Finally, the y -offset of the airfoil spline at the root is determined. This is done by imposing that

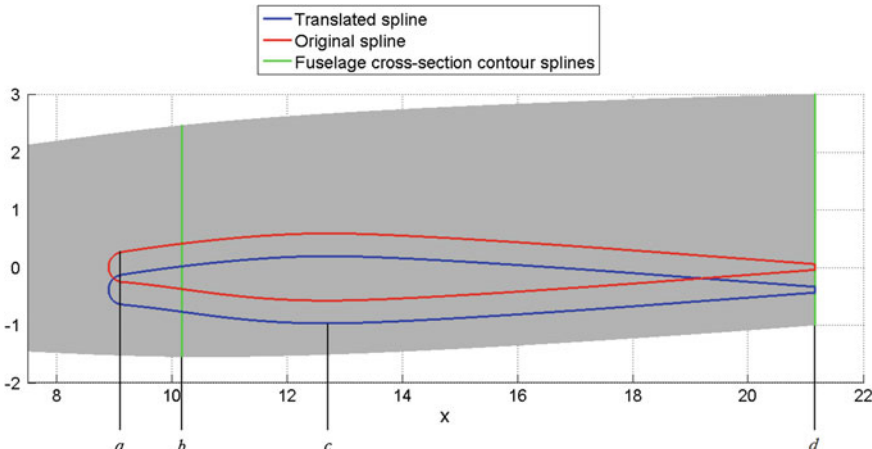


Fig. B.14 Airfoil spline before and after translation in z -direction, with four positions at which the required translation is calculated indicated

the frontmost point of the airfoil lie on the fuselage side at the given values of the x -and z -offsets. At these values, the leading edge nose is positioned at $x = 8.90$ m and $z = -0.394$ m. The interface point on the fuselage is found iteratively to be $u_{fus} = 0.89$, $v_{fus} = 1.6$, where the value of y equals 2.72 m. Consequently, the vector by which the airfoil spline is translated is the following:

$$\begin{aligned}x_{w,tr} &= 8.90 \text{ m} \\y_{w,tr} &= 2.72 \text{ m} \\z_{w,tr} &= -0.394 \text{ m}\end{aligned}$$

Having done this, the airfoil splines at $v = 2, 3, 4$ are generated. These splines are simply scaled versions of the original spline, with the exception that the position of the elevon beginning (control point 7) is re-calculated each time, so that the elevon hinge line remains straight. As with the fuselage, the control points of equal index on subsequent airfoil splines are connected to obtain the control surface net.

To finalize the control net, the wing is matched to the fuselage by using the algorithm described in Sect. 5.2.3. The points not on the leading edge keep the same values of x and z , but their y -value is modified to lie on the fuselage surface. The complex part of matching the wing to the fuselage arises when matching the wing leading edge to the fuselage, since the leading edge radius must be kept constant. This removes the possibility of simply changing the y -coordinate only of the control points. A front and bottom view of the leading edge before and after matching the leading edge is shown in Fig. B.15. The algorithm which was used to do the matching will now be shown in detail for a single point, namely the first point on the leading edge (the bottom-most point on the leading edge).

First it is checked if a suitable match point exists in front of the original point. If this is not found, a suitable point behind the original point is sought. The value of Δx_1 which is to be kept constant is shown in Fig. B.15a. The value of Δx_1 equals 0.2118. The original value of $x_{LE,1}$ is 9.13 m. Table B.3 shows the values of $\Delta x'_{LE,1}$ which are found when matching the point to the fuselage at the values of x indicated. It can be seen that the correct value of $\Delta x'_{LE,1}$ lies between the values of x at iterations 5 and 6. Following this, a bisection algorithm is used to find a closer approximation of the value of x'_1 yielding the correct value of $\Delta x'_{LE,1}$. The algorithm is considered converged here, if the accuracy of $\Delta x'_{LE,1}$ is better than $1.0 \cdot 10^{-3}$ m. The final value found is $\Delta x'_{LE,1} = 0.2124$ m at $x'_{LE,1} = 8.566$ m.

It is interesting to note that the value of $\Delta x'_{LE,1}$ at the first iteration of the algorithm can be seen from Table B.3 to be 0.4887 m, which is more than double the required value. This indicates the deficiency when keeping the x value of the leading edge points constant and only changing the y value when matching them to the fuselage.

To finalize the control net, the wing tip is bent upwards by the given value of θ_f . The cross-derivatives are then determined and the spline surface is complete. The meshes of the wing, before and after the bending of the wing tip, are shown in Fig. 5.12, with the locations of the splines at $v = 1, 2, 3, 4$ indicated (Fig. B.16).

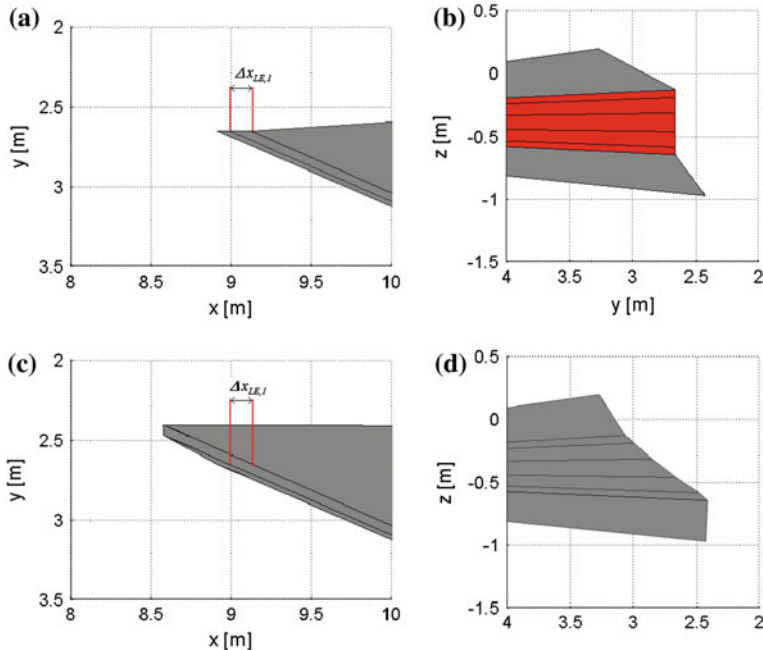


Fig. B.15 Detail of wing leading edge. **a** Before match, *bottom view*. **b** Before match, *front view*. **c** After match, *bottom view*. **d** After match, *front view*

Table B.3 Values of match point location and distance between subsequent splines in control net found by matching algorithm of point x_1 of airfoil spline to the fuselage

Iteration	x'_1 (m)	$\Delta x'_{LE,1}$ (m)
1	9.026	0.4887
2	8.926	0.4262
3	8.826	0.3652
4	8.726	0.3054
5	8.626	0.2468
6	8.526	0.1894

The final part of the vehicle which is to be generated is the body flap. The width of the flap is determined from the bottom of the fuselage rear, so from $y_{3,3}$ and $y_{3,4}(= 0)$. The value of $y_{3,3}$ equals 2.37 m, making the flap width b_{bf} 4.74 m. The maximum value of the flap length $L_{bf,max}$ follows from:

$$L_{bf,max} = \min(2.0, b_{bf}) \quad (\text{B.109})$$

$$= 2.0 \text{ m} \quad (\text{B.110})$$

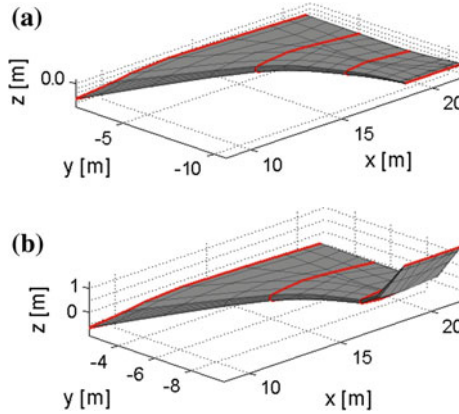


Fig. B.16 Wing shape with locations of splines at $v = 1, 2, 3, 4$ indicated, **a** before bending, **b** after bending

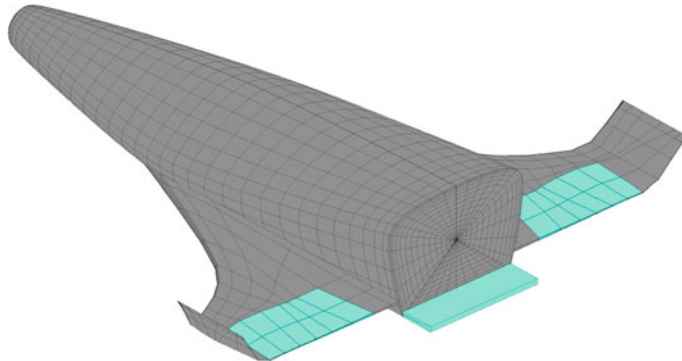


Fig. B.17 Full vehicle configuration with control surfaces indicated in *cyan*

The body flap length is now determined from:

$$L_{bf} = 0.5 + 0.578(2.0 - 0.5) \quad (\text{B.111})$$

$$= 1.37 \text{ m} \quad (\text{B.112})$$

The full vehicle is shown in Fig. B.17 with the control surfaces clearly indicated by color. Different views of the vehicle are shown in Figs. B.18 and B.19. One thing that can be seen in this figure is that the elevon hinge line is not fully straight. This is due to the fact that the control point derivatives w.r.t. v on contour 2 are not 0, as this was found to change the shape of the fins in an unsatisfactory manner. This is an example of how the lack of local control when using Hermite splines, instead of B-splines, can limit the freedom in generating a certain shape.

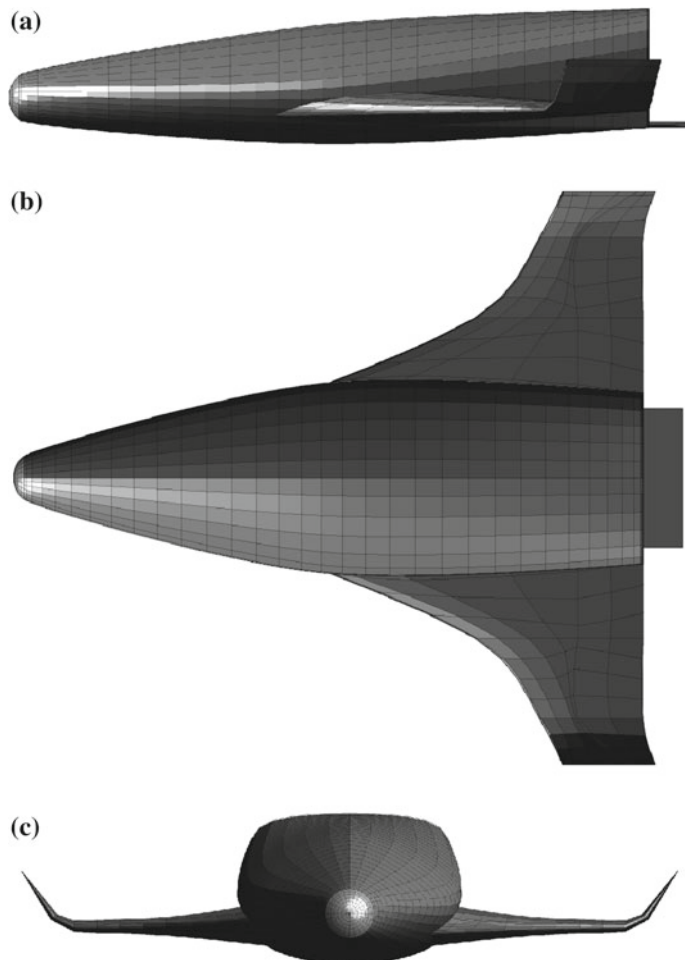
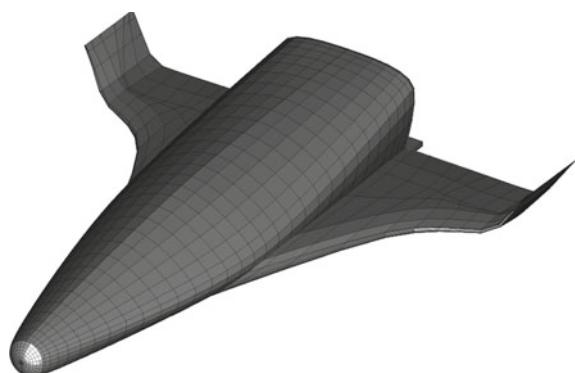


Fig. B.18 Views of vehicle shape generated. **a** Side view. **b** Top view. **c** Front view

Fig. B.19 Isometric view of vehicle shape



Appendix C

Optimal Capsule Shapes

Here, a number of capsule shapes are presented to gain insight into the type of shapes which are generated. First, the evolution of a point on the Pareto front is shown to give insight into the behavior with increasing optimizer iteration. Second, a number of points from the final Pareto front are presented to give insight into the behavior of the optimal solution that is found.

C.1 Evolution of Selected Point on Capsule Pareto Front

This appendix will show the minimum mass shapes for which $s_g > 2.75 \cdot 10^3$ km and $\eta_V > 0.75$ for increasing iteration number in the optimization. It was found that the shape which fulfills this condition changes 11 times during the optimization, so that a total of 12 different shapes will represent the evolution of this shape with increasing iteration number (Table C.1).

Table C.1 Evolution of objective function values for minimum mass solutions with $s_g > 2.75 \cdot 10^3$ km and $\eta_V > 0.75$

Iteration	Stagnation-point heat load (10^6 J/m 2)	Ground track length (km)	Volumetric efficiency (-)
1	63.75	2532	0.7331
2	62.58	2552	0.7287
3	59.26	2514	0.7182
8	57.66	2545	0.7045
28	57.43	2510	0.7037
46	57.35	2510	0.7151
112	56.44	2501	0.7106
139	55.95	2513	0.7055
176	55.71	2511	0.7023
192	55.69	2500	0.7051
237	55.63	2501	0.7052
241	55.62	2503	0.7012

C.2 Optimal Capsule Shapes

Here, the optimal shapes of the capsule shapes, found after 250 iterations with a swarm size of 100, from a selected number of points from the Pareto front is presented (Figs. C.1–C.4).

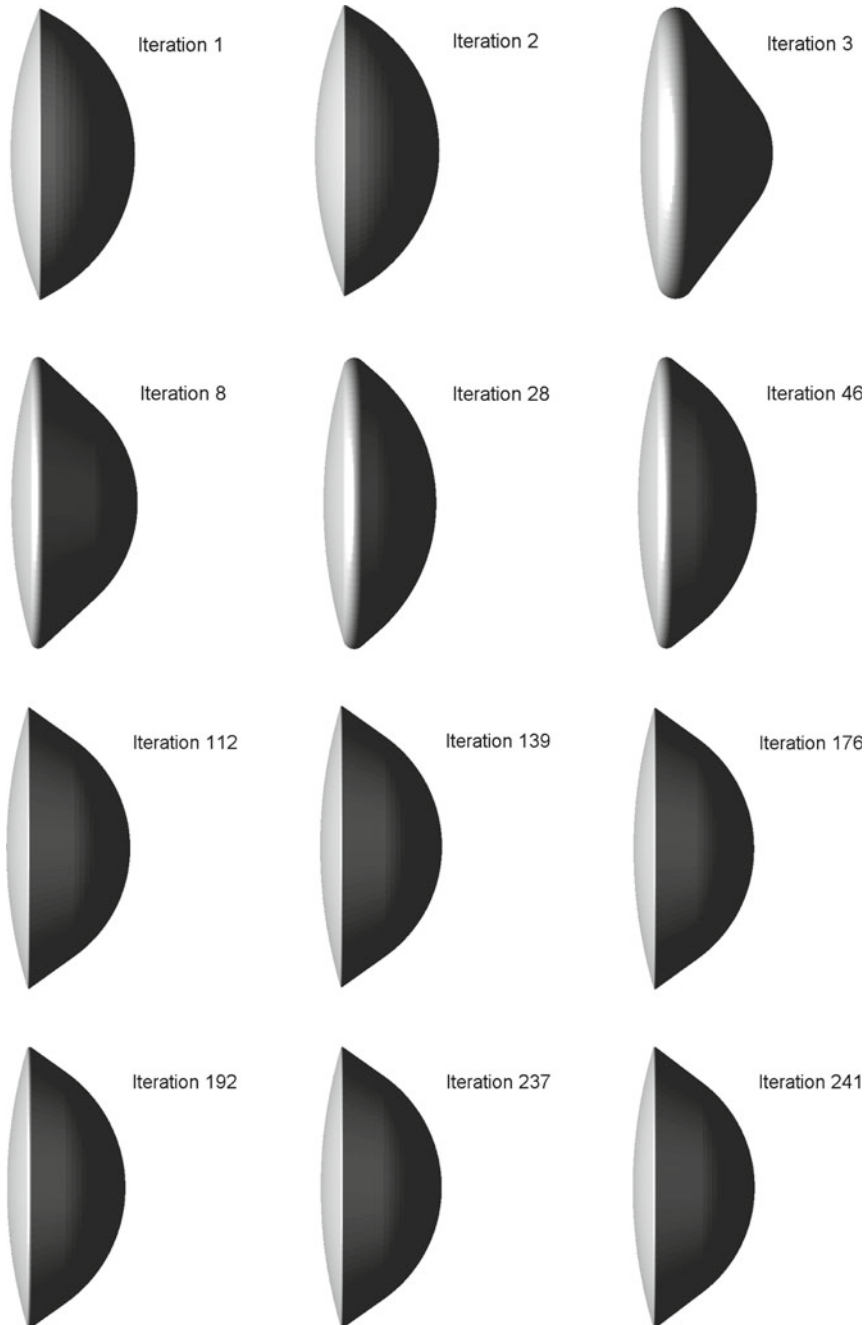


Fig. C.1 Evolution of optimal-mass solution for $s_g > 2.5 \cdot 10^3$ km and $\eta_V > 0.7$

Fig. C.2 Pareto-optimal capsule shapes from benchmark optimization run, $\min Q_s$. **a** No constraints on other objectives, **b** $s_g > 2.75 \cdot 10^3$ km, **c** $\eta_V > 0.75$, **d** $s_g > 2.75 \cdot 10^3$ km and $\eta_V > 0.75$

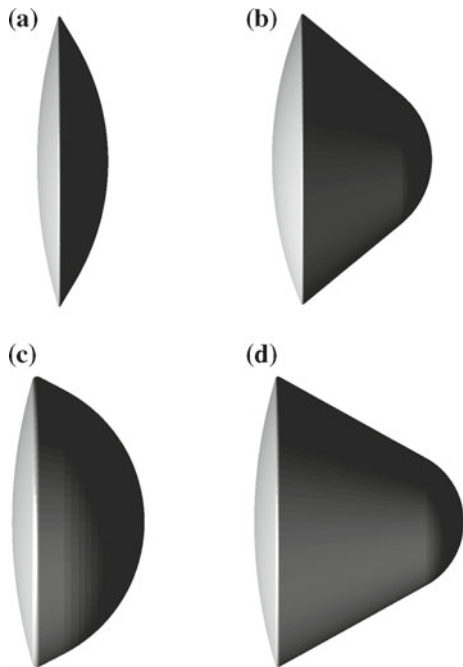


Fig. C.3 Pareto-optimal capsule shapes from benchmark optimization run, $\max s_g$. **a** No constraints on other objectives, **b** $Q_s < 75 \text{ MJ/m}^2$, **c** $\eta_V > 0.75$, **d** $Q_s < 75 \text{ MJ/m}^2$ and $\eta_V > 0.75$

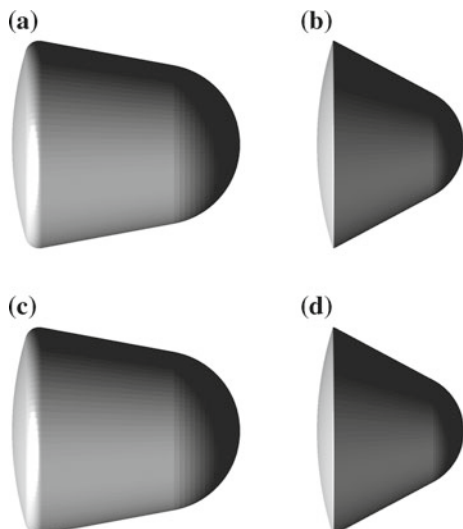
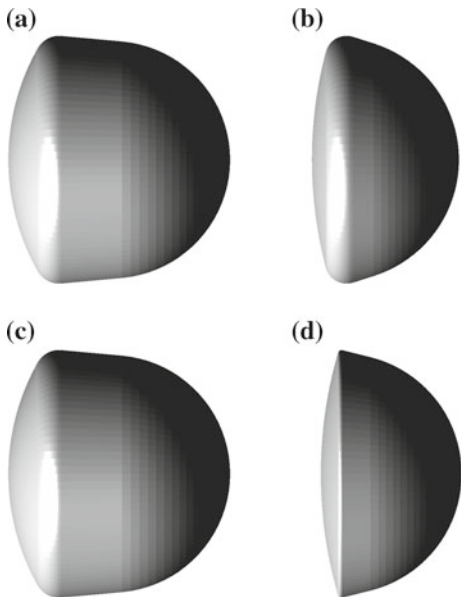


Fig. C.4 Pareto-optimal capsule shapes from benchmark optimization run, $\max \eta_V$. **a** No constraints on other objectives,
b $Q_s < 75 \text{ MJ/m}^2$,
c $s_g > 2.75 \cdot 10^3 \text{ km}$,
d $Q_s < 75 \text{ MJ/m}^2$ and
 $s_g > 2.75 \cdot 10^3 \text{ km}$



Appendix D

Optimal Winged-Vehicle Shapes

Here, a number of capsule shapes are presented to gain insight into the type of shapes which are generated. First, the evolution of a point on the Pareto front is shown to give insight into the behavior with increasing optimizer iteration. Subsequently, a number of points from the final Pareto front are presented to give insight into the behavior of the optimal solution which is found.

D.1 Evolution of Selected Point on Winged-Vehicle Pareto Front

This appendix will show the minimum mass shapes for which $s_g > 5.1 \cdot 10^3$ km and $V > 400 \text{ m}^3$ for increasing iteration number in the optimization (Table D.1).

Table D.1 Evolution of objective function values for minimum mass solutions with $s_g > 5.1 \cdot 10^3$ km and $V > 400 \text{ m}^3$

Iteration	Mass (10^3 kg)	Ground track length (km)	Fuselage volume (m^3)
31	15.84	5138	432.2
36	13.34	5165	422.9
37	13.34	5130	422.5
40	13.15	5198	411.3
41	12.78	5213	400.0
53	12.53	5123	405.1
83	12.11	5121	404.2
86	11.93	5114	410.3
93	11.72	5170	404.4
96	11.70	5165	405.6
101	11.43	5112	402.2
111	11.19	5171	400.7
287	11.18	5115	401.1
301	11.06	5125	403.4

D.2 Optimal Winged-Vehicle Shape Using Benchmark Settings

Here, the optimal shapes of the winged vehicles, found after 400 iterations with a swarm size of 100, from a selected number of points from the Pareto front is presented (Figs. D.1–D.20).

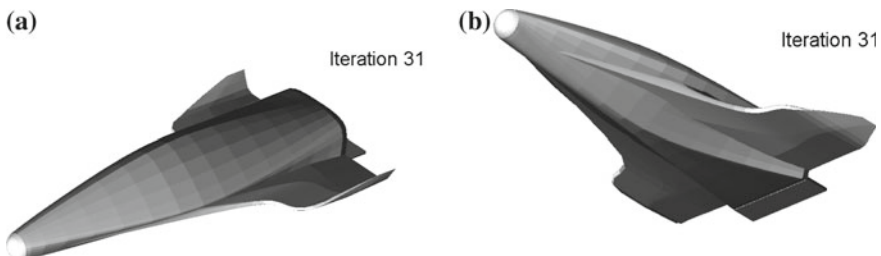


Fig. D.1 First optimal-mass solution for $s_g > 5.1 \cdot 10^3$ km and $V > 400 \text{ m}^3$, which is found. **a** Top view. **b** Bottom view

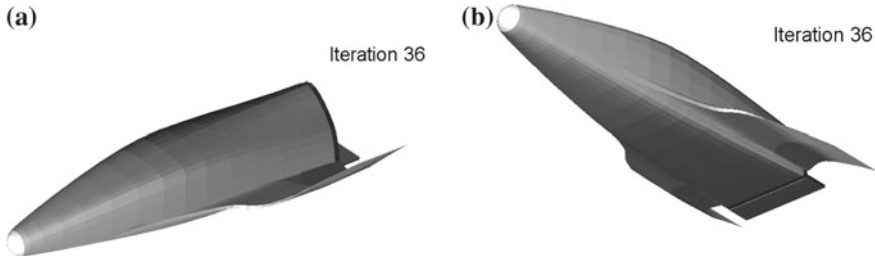


Fig. D.2 Second optimal-mass solution for $s_g > 5.1 \cdot 10^3$ km and $V > 400 \text{ m}^3$, which is found. **a** Top view. **b** Bottom view

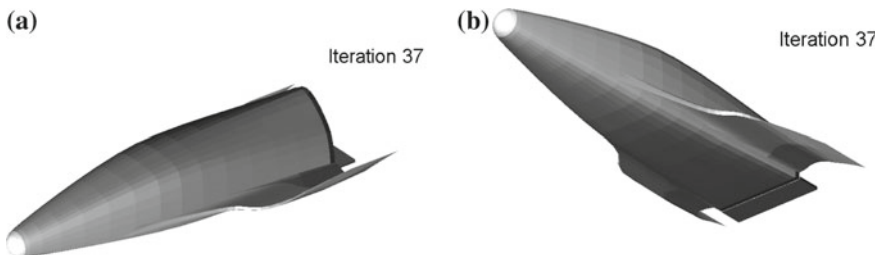


Fig. D.3 Third optimal-mass solution for $s_g > 5.1 \cdot 10^3$ km and $V > 400 \text{ m}^3$, which is found. **a** Top view. **b** Bottom view

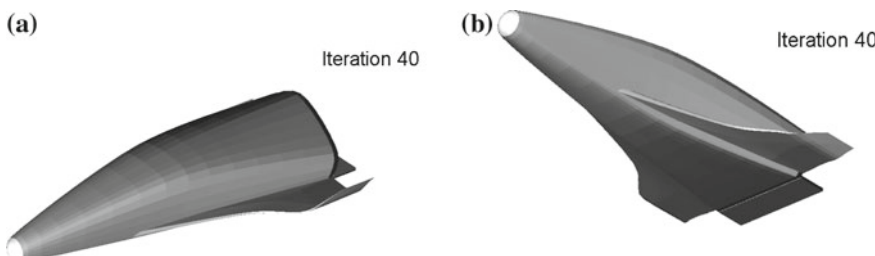


Fig. D.4 Fourth optimal-mass solution for $s_g > 5.1 \cdot 10^3$ km and $V > 400 \text{ m}^3$, which is found. **a** Top view. **b** Bottom view

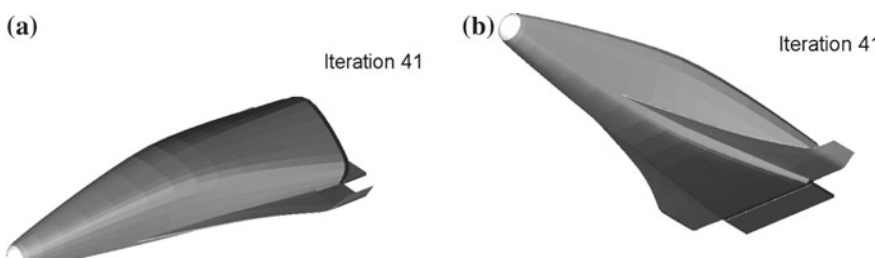


Fig. D.5 Fifth optimal-mass solution for $s_g > 5.1 \cdot 10^3$ km and $V > 400 \text{ m}^3$, which is found. **a** Top view. **b** Bottom view

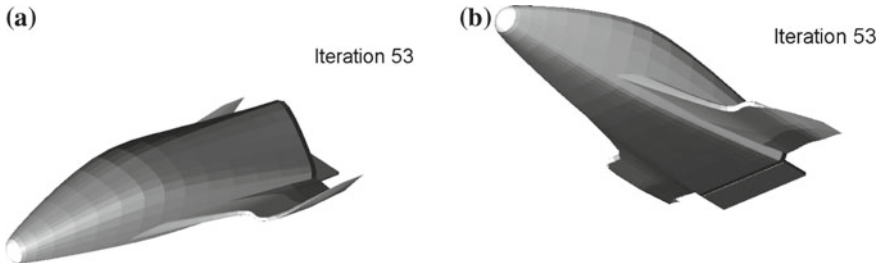


Fig. D.6 Sixth optimal-mass solution for $s_g > 5.1 \cdot 10^3$ km and $V > 400 \text{ m}^3$, which is found.
a Top view. b Bottom view

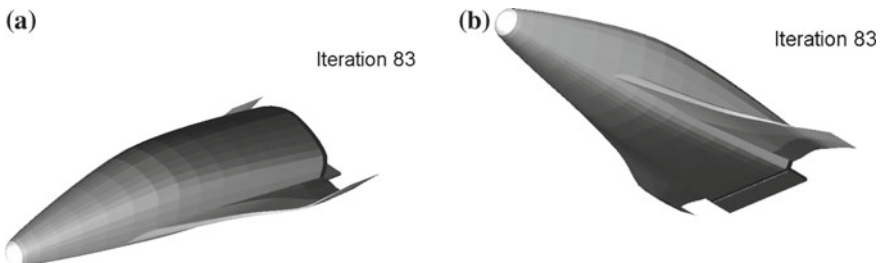


Fig. D.7 Seventh optimal-mass solution for $s_g > 5.1 \cdot 10^3$ km and $V > 400 \text{ m}^3$, which is found.
a Top view. b Bottom view

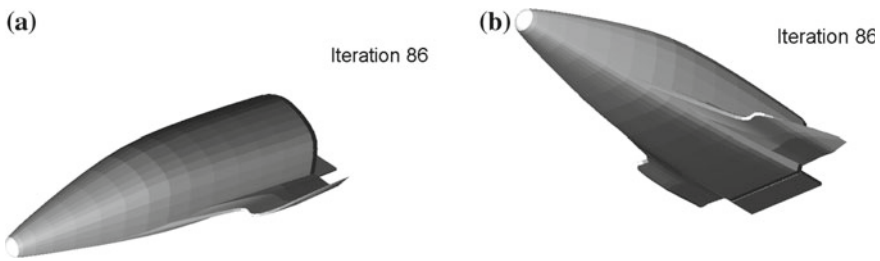


Fig. D.8 Eighth optimal-mass solution for $s_g > 5.1 \cdot 10^3$ km and $V > 400 \text{ m}^3$, which is found.
a Top view. b Bottom view

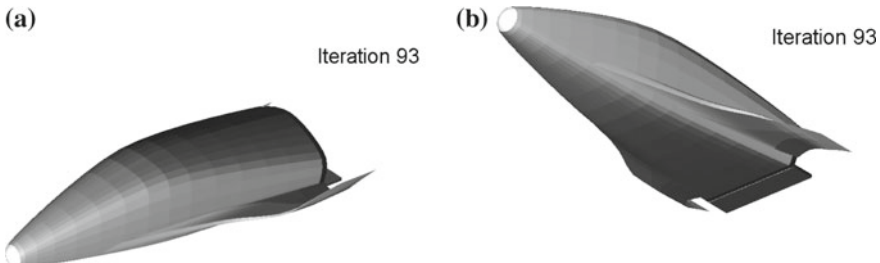


Fig. D.9 Ninth optimal-mass solution for $s_g > 5.1 \cdot 10^3$ km and $V > 400 \text{ m}^3$, which is found.
a Top view. b Bottom view

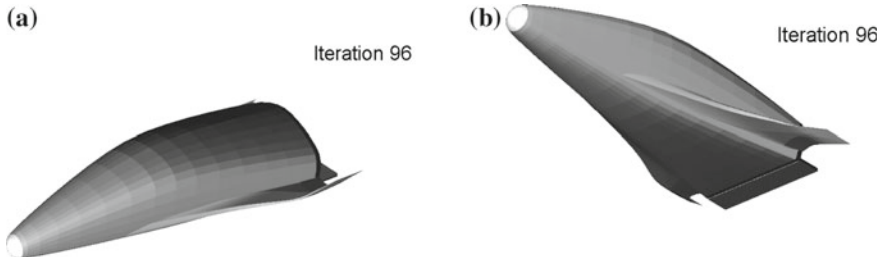


Fig. D.10 Tenth optimal-mass solution for $s_g > 5.1 \cdot 10^3$ km and $V > 400 \text{ m}^3$, which is found.
a Top view. **b** Bottom view

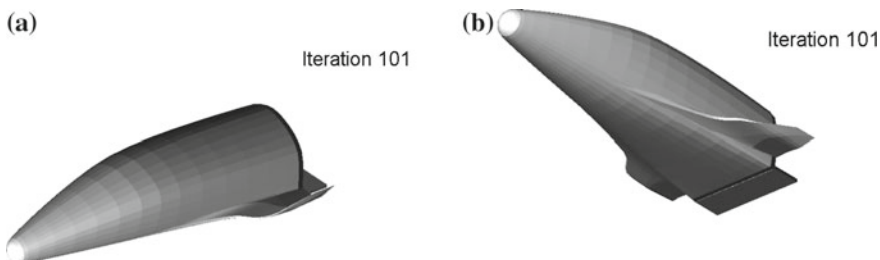


Fig. D.11 Eleventh optimal-mass solution for $s_g > 5.1 \cdot 10^3$ km and $V > 400 \text{ m}^3$, which is found.
a Top view. **b** Bottom view

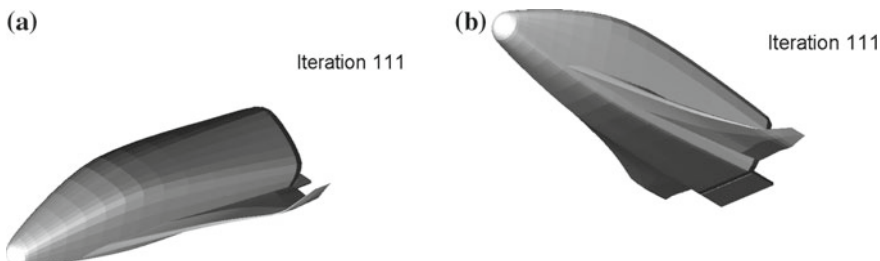


Fig. D.12 Twelfth optimal-mass solution for $s_g > 5.1 \cdot 10^3$ km and $V > 400 \text{ m}^3$, which is found.
a Top view. **b** Bottom view

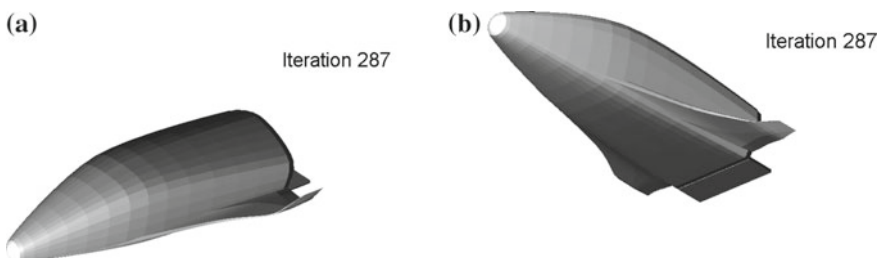


Fig. D.13 Thirteenth optimal-mass solution for $s_g > 5.1 \cdot 10^3$ km and $V > 400 \text{ m}^3$, which is found.
a Top view. **b** Bottom view

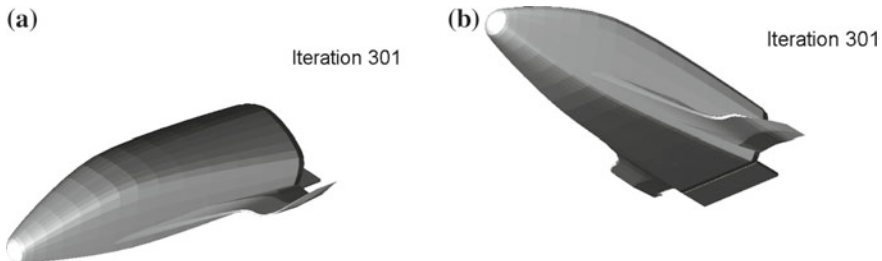


Fig. D.14 Fourteenth optimal-mass solution for $s_g > 5.1 \cdot 10^3$ km and $V > 400 \text{ m}^3$, which is found. **a** Top view. **b** Bottom view

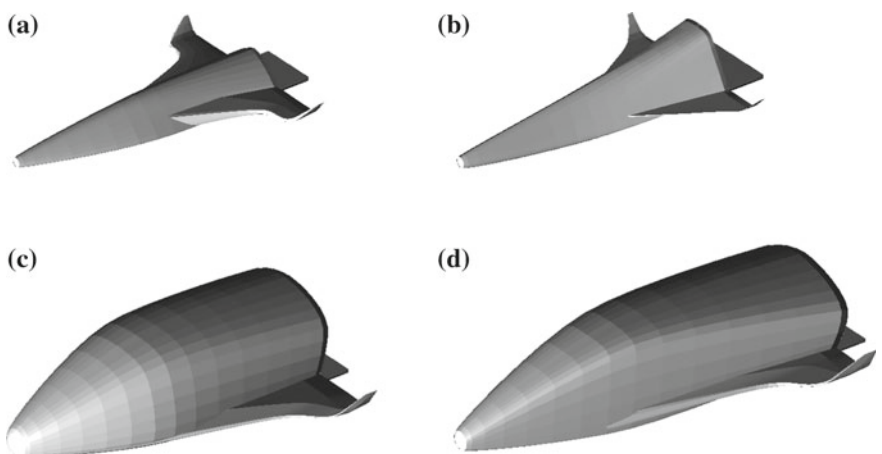


Fig. D.15 Optimal winged-vehicle shapes from benchmark optimization run, $\min m$, *top view*. **a** No constraints on other objectives, **b** $s_g > 5.2 \cdot 10^3$ km, **c** $V > 350 \text{ m}^3$, **d** $s_g > 5.2 \cdot 10^3$ km and $V > 350 \text{ m}^3$

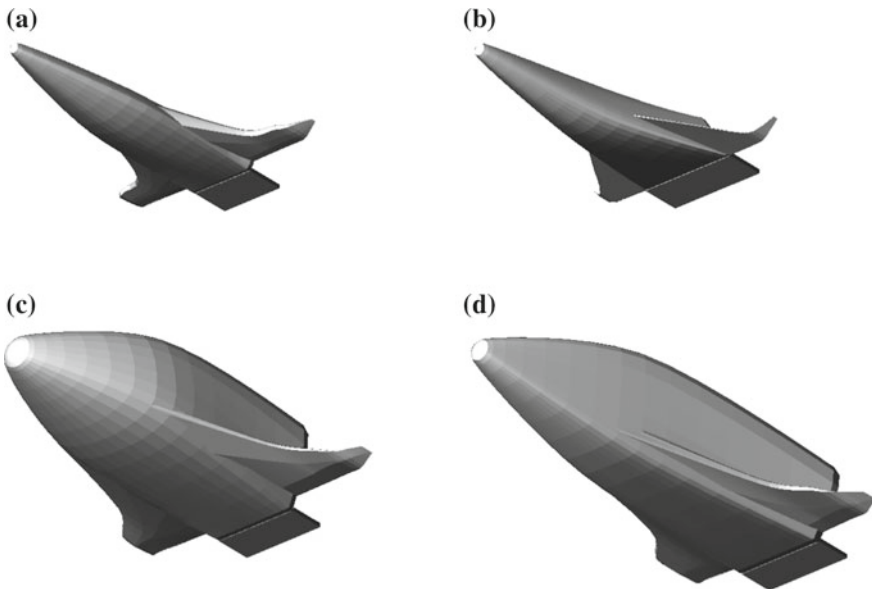


Fig. D.16 Optimal winged-vehicle shapes from benchmark optimization run, $\min m$, *bottom view*.
a No constraints on other objectives, **b** $s_g > 5.2 \cdot 10^3$ km, **c** $V > 350 \text{ m}^3$, **d** $s_g > 5.2 \cdot 10^3$ km and $V > 350 \text{ m}^3$

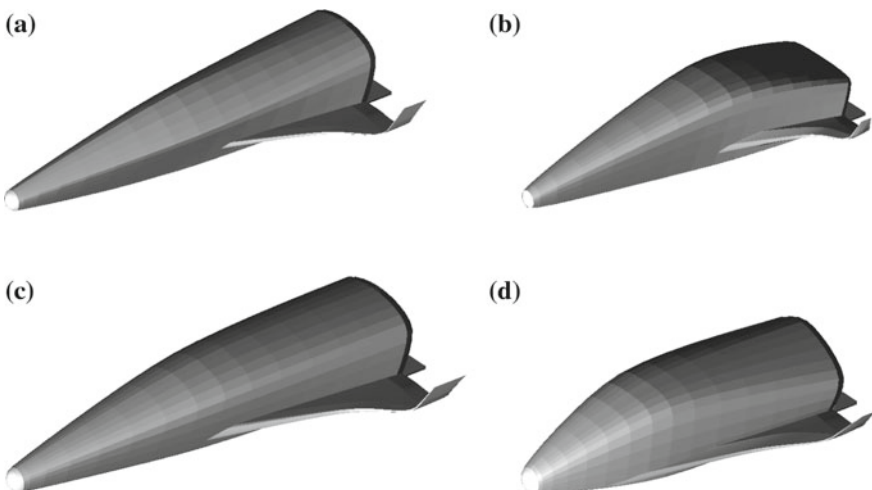


Fig. D.17 Optimal winged-vehicle shapes from benchmark optimization run, $\max s_g$, *top view*.
a No constraints on other objectives, **b** $m < 10,000$ kg, **c** $V > 350 \text{ m}^3$, **d** $m < 10,000$ kg and $V > 350 \text{ m}^3$

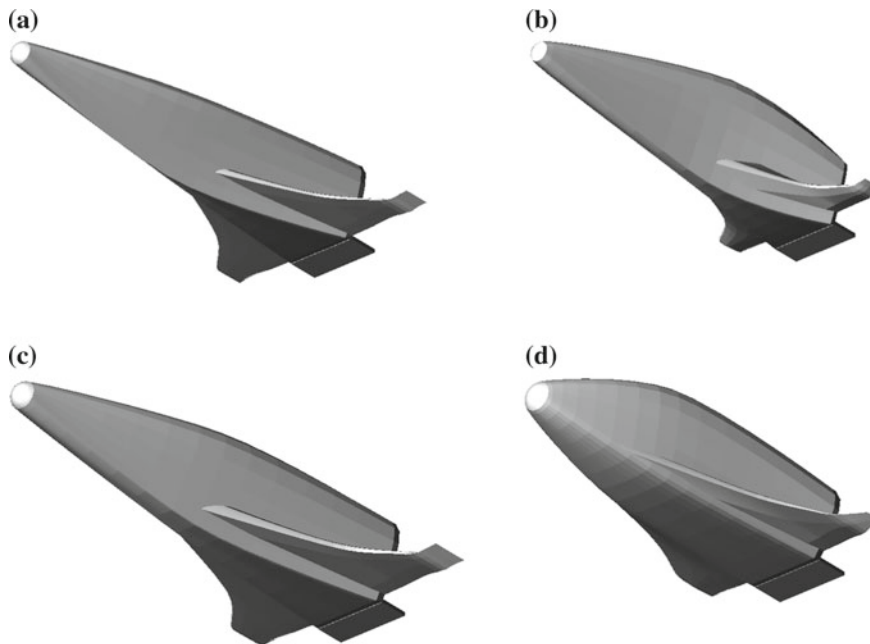


Fig. D.18 Optimal winged-vehicle shapes from benchmark optimization run, $\max s_g$, *bottom view*.
a No constraints on other objectives, **b** $m < 10,000 \text{ kg}$, **c** $V > 350 \text{ m}^3$, **d** $m < 10,000 \text{ kg}$ and $V > 350 \text{ m}^3$

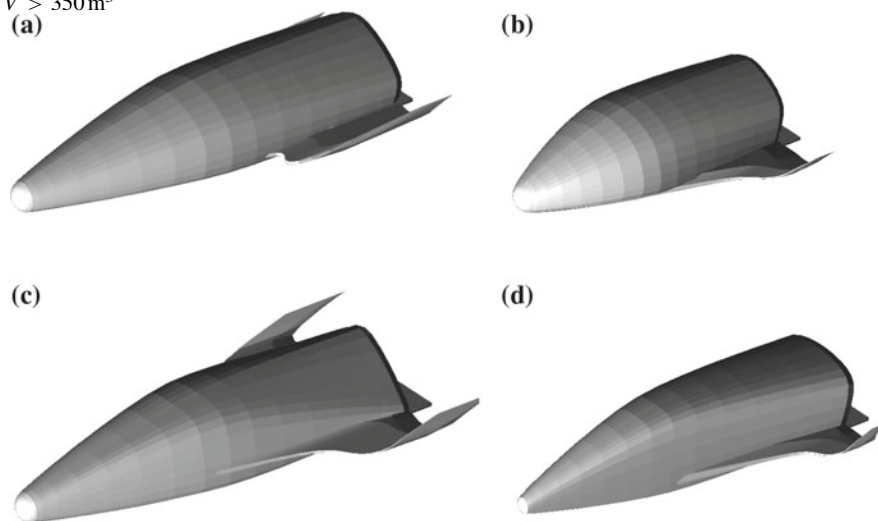


Fig. D.19 Optimal winged-vehicle shapes from benchmark optimization run, $\max V$, *top view*.
a No constraints on other objectives, **b** $m < 10,000 \text{ kg}$, **c** $s_g > 5.2 \cdot 10^3 \text{ km}$, **d** $m < 10,000 \text{ kg}$ and $s_g > 5.2 \cdot 10^3 \text{ km}$

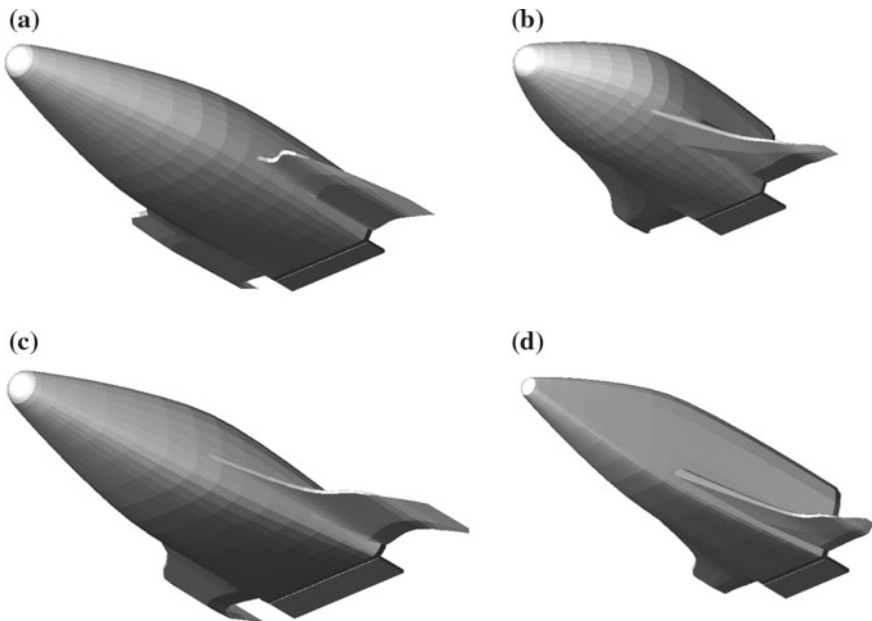


Fig. D.20 Optimal winged-vehicle shapes from benchmark optimization run, max V , bottom view.
a No constraints on other objectives, **b** $m < 10,000 \text{ kg}$, **c** $s_g > 5.2 \cdot 10^3 \text{ km}$, **d** $m < 10,000 \text{ kg}$ and $s_g > 5.2 \cdot 10^3 \text{ km}$

References

- Allen, H., & Eggers, A. Jr. (1958). A Study of the Motion and Aerodynamic Heating of Ballistic Missiles entering the Earth's Atmosphere at High Supersonic Speeds. Technical Report TR-1381, NACA.
- Andersen, B., & Whitmore, S. (2007). Aerodynamic control on a lunar return capsule using trim-flaps. In *45th AIAA Aerospace Sciences Meeting*, number AIAA-2007-0855.
- Anderson, J. (2003). *Modern compressible flow with historical perspective* (3rd ed.). New York: McGraw-Hill.
- Anderson, J. (2006). *Hypersonic and high-temperature gas dynamics*, AIAA Education Series (2nd ed.). Reston: AIAA.
- Armellin, R. (2007). Multidisciplinary Optimization of space vehicles for atmospheric maneuvers. Ph.D. thesis, Politecnico di Milano.
- Bertin, J. (1994). *Hypersonic aerothermodynamics*, AIAA Education Series. Washington: AIAA.
- Bohachevsky, I., & Matos, R. (1965). A direct method for calculation of the flow about an axisymmetric blunt body at angle of attack. Technical Report NASA CR-127572, Cornel Aeronautics Laboratory.
- Bonner, E., Clever, W., & Dunn, K. (1981). *Aerodynamic preliminary analysis system 2. Part 1: Theory*, NASA-CR-165627.
- Bowcutt, K., Krurvila, G., Grandine, T., Hogan, T., & Cramer, E. (2008). Advancements in multidisciplinary design optimization applied to hypersonic vehicles to achieve closure. In *15th AIAA International Space Planes and Hypersonic Systems and Technologies Conference*, number AIAA 2008-2591.
- Brykina, I., & Scott, C. (1998). An approximate axisymmetric viscous shock layer aeroheating method for three-dimensional bodies. Technical Report TM-98-207890, NASA.
- Castellini, F. (2012). Multidisciplinary design optimization for expendable launch vehicles. Ph.D. thesis, Politecnico di Milano.
- Castellini, F., & Lavagna, M. (2012). Comparative analysis of global techniques for performance and design optimization of launchers. *Journal of Spacecraft and Rockets*, 49(2), 274–285.
- Chapman, D. (1958). An approximate analytical method for studying entry into planetary atmospheres. Technical Report TN-4276, NACA.
- Coello Coello, C., Pulido, G., & Lechuga, M. (2004). Handling multiple objectives with particle swarm optimization. *IEEE Transactions on Evolutionary Computation*, 8(3), 256–279.
- Craiden, C. (1985). A description of the langley wireframe geometry standard (LaWGS) format. Technical Report TM 85767, NASA.

- Crowder, R., & Moote, J. (1969). Apollo entry aerodynamics. *Journal of Spacecraft and Rockets*, 6(3), 302–307.
- Cruz, C., & Ware, G. (1989). Predicted aerodynamic characteristics for HL-20 lifting-body using aerodynamic preliminary analysis system (APAS). In *AIAA 17th Aerospace Ground Testing Conference*, number AIAA-1992-3941.
- Cruz, C., & White, A. (1989). Prediction of high-speed aerodynamic characteristics using the aerodynamic preliminary analysis system. In *AIAA 7th Applied Aerodynamics Conference*, number AIAA-1989-2173.
- Deb, K. (2000). An efficient constraint handling method for genetic algorithms. *Computer Methods in Applied Mechanics and Engineering*, 186(2–4), 311–338.
- Deb, K. (2005). *Multi-objective optimization using evolutionary algorithms*. Chichester: Wiley.
- Dekking, F., Kraaijkamp, C., Lopuhaä, H., & Meester, L. (2005). *A modern introduction to probability and statistics: Understanding why and how*. New York: Springer Science & Business Media.
- Derbyshire, T., & Sidwell, K. (1982). PANAIR - summary document (version 1.0). Technical Report CR 3250, NASA.
- Dirkx, D., & Mooij, E. (2011). Continuous aerodynamic modelling of entry shapes. In *AIAA atmospheric flight mechanics conference*, number AIAA-2011-6575.
- Dirkx, D., & Mooij, E. (2014). Optimization of entry-vehicle shapes during conceptual design. *Acta Astronautica*, 94(1), 198–214.
- Doornbos, E. (2011). Thermospheric density and wind determination from satellite dynamics. Ph.D. thesis, TU Delft.
- Dorrance, W. (1962). *Viscous hypersonic flow*. New York: McGraw-Hill.
- East, R., & Hutt, G. (1988). Comparison of predictions and experimental data for hypersonic pitching motion stability. *Journal of Spacecraft and Rockets*, 25(3), 225–233.
- Eckert, E. (1955). Engineering relations for friction and heat transfer to surfaces in high velocity flow. *Journal of the Aeronautical Sciences*, 22(8), 585–587.
- Ericsson, L. (1975). Generalized unsteady embedded Newtonian flow. *Journal of Spacecraft and Rockets*, 12(12), 718–726.
- Farin, R. (2003). *Curves and surfaces for computer aided geometric design, a practical guide* (3rd ed.). New York: Academic Press Inc.
- Fay, J., & Riddell, F. (1958). Theory of stagnation point heat transfer in dissociated air. *Journal of the Aeronautical Sciences*, 25(2), 73–85.
- Fuller, J., & Tolson, R. (2009). Improved methods for estimation of spacecraft free-molecular aerodynamic properties. *Journal of Spacecraft and Rockets*, 46(5), 938–948.
- Gentry, A., Smyth, D., & Oliver, W. (1973). *The Mark IV supersonic-hypersonic arbitrary body program, volume II - program formulation*, Douglas Aircraft Company.
- Golubkin, V., & Negodam, V. (1995). Optimum lifting body shapes in hypersonic flow at high angles of attack. *Theoretical and Computational Fluid Dynamics*, 7, 29–47.
- Gomez, G. (1990). Influence of local inclination methods on the S/HABP aerodynamic analysis tool. Technical Report EWP 1793, ESA.
- Grant, M. & Braun, R. (2010). Analytic hypersonic aerodynamics for conceptual design of entry vehicles. In *48th AIAA Aerospace Sciences Meeting Including the New Horizons Forum and Aerospace Exposition*, number AIAA 2010-1212.
- Grant, M. J., Clark, I. G., & Braun, R. D. (2011). Rapid simultaneous hypersonic aerodynamic and trajectory optimization using variational methods. In *AIAA Atmospheric Flight Mechanics Conference* (Number AIAA-2011-6640).
- Hall, I. (1975). Inversion of the Prandtl-Meyer relation. *Aeronautical Journal*, 79(777), 417–418.
- Hansen, C. (1958). Approximation for the thermodynamic and transport properties of high-temperature air. Technical Report TN-4150, NASA.
- Harloff, G., & Berkowitz, B. (1988). HASA-hypersonic aerospace sizing analysis for the preliminary design of aerospace vehicles. Technical Report CR 182226, NASA.

- Hayes, W., & Probstein, R. (1966). *Hypersonic flow theory I: Inviscid flows*. New York: Academic Press.
- Heppenheimer, T. (2007). *Facing the heat barrier: A history of hyperspronics*. NASA History Series (NASA SP-2007-4232).
- Hillje, E. (1969). Entry aerodynamics at lunar return conditions obtained from the flight of Apollo 4 (AS-501). Technical Report NASA TN D-5399, NASA.
- Hirschel, E. (2005). *Basics of aerothermodynamics*. New York: Springer.
- Hirschel, E., & Weiland, C. (2009). *Selected aerothermodynamic design problems of hypersonic flight vehicles*. New York: Springer/AIAA.
- Hoeijmakers, H., Sudmeijer, K., & Wegereef, J. (1996). Hypersonic aerothermodynamic module for the NLRAERO program. Technical Report, Delft University of Technology.
- Huertas, I., Mollmann, C., Weikert, S., & Martinez Barrio, A. (2010). Re-entry vehicle design by multidisciplinary optimisation in ASTOS. In *4th International Conference on Astrodynamics Tools and Techniques*.
- Jenkins, D. (2001). *Space shuttle: The history of the national space transportation system the first 100 missions* (3rd ed.). Dennis R. Jenkins Publishing.
- Johnson, J., Starkey, R., & Lewis, M. (2007). Aerothermodynamic optimization of reentry heat shield shapes for a crew exploration vehicle. *Journal of Spacecraft and Rockets*, 44(4), 849–859.
- Jones, R. (1963). Heat-transfer and pressure distributions of two flat-faced sharp-cornered bodies of revolution at a mach number of 8 and comparison with data for a round corner. Technical Report TM X-774, NASA.
- Kenedy, J., & Eberhart, R. (1995). Particle swarm optimization. In *IEEE International Conference on Neural Networks* (pp. 1942–1948).
- Kenwright, D., Henze, C., & Levit, C. (1999). Feature extraction of separation and attachment lines. *IEEE Transactions on Visualization and Computer Graphics*, 5(2), 135–144.
- Kinney, D. (2004). Aero-thermodynamics for conceptual design. In *42nd AIAA Aerospace Sciences Meeting and Exhibit*, number AIAA-2004-31.
- Kinney, D. (2006). Aerodynamic shape optimization of hypersonic vehicles. In *44th AIAA Aerospace Sciences Meeting and Exhibit*, number AIAA-2006-239.
- Krieger, R. (1989). Summary of design and performance characteristics of aerodynamic configured missiles. In *AIAA 19th Aerospace Sciences Meeting*, number AIAA-81-0286.
- Kulfan, B. (2008). Universal parametric geometry representation methods. *Journal of Aircraft*, 45(1), 142–158.
- Lambert, J. (1991). *Numerical methods for ordinary differential equations: The initial value problem*. Chichester: Wiley.
- Lee, D. (1972). Apollo experience report - aerothermodynamics evaluation. Technical Report TN D-6843, NASA.
- Lee, D., & Goodrich, W. (1972). The aerothermodynamic environment of the Apollo command module during superorbital entry. Technical Report TN D-6792, NASA.
- Loh, W. (1968). *Re-entry and planetary entry physics and technology*. New York: Springer.
- Marvin, J., & Sinclair, A. (1967). Convective heating in regions of large favorable pressure gradient. *AIAA Journal*, 5(11), 1940–1948.
- Massobrio, F., Viotto, R., Serpico, M., Sansone, A., Caporicci, M., & Muylaert, J.-M. (2007). EXPERT: An atmospheric re-entry testbed. *Acta Astronautica*, 60(12), 974–985.
- Maughmer, M., Ozoroski, L., Straussfogel, D., & Long, L. (1993). Validation of engineering methods for predicting hypersonic vehicle control forces and moments. *Journal of Guidance, Control and Dynamics*, 16(4), 762–782.
- Maus, J., Griffitj, B., & Szerna, K. (1983). Hypersonic mach number and real gas effects on space shuttle orbiter aerodynamics. *Journal of Spacecraft and Rockets*, 21(2), 136–141.
- MBB-Space. (1988). Study on Re-entry Guidance and Control, Final Report Volume 2, Ref. Vehicle Definition and Orbital Constraints. Technical Report TIDC-CR-6692, MBB Space.

- McNamara, J., Crowell, A. R., Friedmann, P., Glaz, B., & Gogulapati, A. (2010). Approximate modeling of unsteady aerodynamics for hypersonic aeroelasticity. *Journal of Aircraft*, 47(6), 1932–1945.
- Miele, A. (1965). *Theory of optimum aerodynamic shapes*. New York: Academic Press Inc.
- Mooij, E. (1995). The HORUS-2B reference vehicle. Technical Report, Delft University of Technology.
- Mooij, E. (1998). *The motion of a vehicle in a planetary atmosphere*. Ph.D. thesis, Delft University of Technology.
- Mooij, E., & Hänninen, P. (2009). Distributed global trajectory optimization of a moderate lift-to-drag re-entry vehicle. In *AIAA Guidance, Navigation and Control Conference*, number AIAA 2009-5770.
- Moore, M. & Williams, J. (1989). Aerodynamic prediction rationale for analyses of hypersonic configurations. In *27th Aerospace Sciences Meeting*, number AIAA-1989-525.
- NOAA, Nasa. (1976). *US standard atmosphere*, (1976). Technical Report. U.S: Government Printing Office.
- North American Aviation. (1965). Aerodynamic Data Manual for Project Apollo. Technical Report NASA-CR-82907.
- Press, W., Teukolsky, S., Vetterling, W., & Flannery, B. (2007). *Numerical recipes: The art of scientific computing*. Cambridge: Cambridge University Press.
- Price, K., Storn, R., & Lampinen, J. (2005). *Differential evolution, a practical approach to global optimization*. New York: Springer.
- Rasmussen, M. (1994). *Hypersonic flow*. New York: Wiley.
- Regan, F., & Anandakrishnan, S. (1993). *Dynamics of atmospheric re-entry*, AIAA Education Series.
- Reyes-Sierra, M., & Coello Coello, C. (2006). Multi-Objective particle swarm optimizers: A survey of the state-of-the-art. *International Journal of Computational Intelligence Research*, 2(3), 287–308.
- Ridder, S. D., & Mooij, E. (2011). Optimal longitudinal trajectories for reusable space vehicles in the terminal area. *Journal of Spacecraft and Rockets*, 48(4), 642–653.
- Ridolfi, G. (2013). Space systems conceptual design - analysis methods for engineering-team support. Ph.D. thesis, TU Delft.
- Ridolfi, G., Mooij, E., Dirkx, D., & Corpino, S. (2012). Robust multi-disciplinary optimization of unmanned entry capsules. In *AIAA Modelling and Simulation Technologies Conference*, number AIAA-2012-5006.
- Robinson, J., & Wurster, K. (2009). Entry trajectory and aeroheating environment definition for capsule-shaped vehicles. *Journal of Spacecraft and Rockets*, 46(1), 74–86.
- Rockwell International. (1980). Aerodynamic Design Data Book, Volume 1, Orbiter Vehicle, STS-1. Technical Report SD72-SH-0060.
- Saaris, G., & Tinoco, E. (1992). A5021 user's manual - PANAIR technology program for solving problems of potential flow about arbitrary configurations. Technical Report, Boeing.
- Sänger, E., & Bredt, I. (1944). A Rocket Drive for Long Range Bombers (Über einen Raketenantrieb für Fernbomber). Technical Report UM 3538, Deutsche Luftfahrtforschung. Translated by Hamermesh, M.
- Schlichting, H., & Gersten, K. (1999). *Boundary layer theory* (8th ed.). New York: Springer.
- Schneider, S. (2006). Laminar-turbulent transition on reentry capsules and planetary probes. *Journal of Spacecraft and Rockets*, 43(6), 1153–1173.
- Shampine, L. (1994). *Numerical solution of ordinary differential equations*. New York: Chapman and Hall.
- Shirley, P., Ashikhmin, M., Gleicher, M., Marschner, S., Reinhard, E., Sung, K., Thompson, W., & Willemsen, P. (2005). *Fundamentals of computer graphics* (2nd edn.). A K Peters, Ltd.
- Smith, A. (1997). Capsule aerothermodynamics. Technical Report R-808, AGARD.
- Sobieczky, H. (1998). Parametric airfoils and wings. *Notes on Numerical Fluid Mechanics*, Vieweg Verlag, 68, 71–88.

- Spies, J. (2003). RLV hopper: Consolidated system concept. *Acta Astronautica*, 53(4–10), 709–717.
- Sziroczak, D. & Smith, H. (2016). A review of design issues specific to hypersonic flight vehicles. *Progress in Aerospace Sciences*, 84, 1–28.
- Tan, K. C., Khor, E. F., Lee, T. H., & Yang, Y. J. (2003). A tabu-based exploratory evolutionary algorithm for multiobjective optimization. *Artificial Intelligence Review*, 19(3), 231–260.
- Tauber, M., Menees, G., & Adelman, H. (1987). Aerothermodynamics of transatmospheric vehicles. *Journal of Aircraft*, 24(9), 594–602.
- Theisinger, J., & Braun, R. (2009). Multi-objective hypersonic entry aeroshell shape optimization. *Journal of Spacecraft and Rockets*, 46(5), 957–966.
- Theisinger, J., Braun, R., & Clark, I. (2010). Aerothermodynamic shape optimization of hypersonic entry aeroshells. In *13th AIAA/ISSMO Multidisciplinary Analysis Optimization Conference*, number AIAA 2010-9200.
- Thomas, A., Smith, R., & Tiwari, S. (2004). Rational B-Spline and PDE surfaces with unstructured grid for aerospace vehicle design. In *32nd Aerospace Sciences Meeting and Exhibit*, number AIAA-1994-419.
- Tsuchiya, T., Takenaka, Y., & Taguchi, H. (2007). Multidisciplinary design optimization for hypersonic experimental vehicle. *AIAA Journal*, 45(7), 1655–1662.
- Udin, S., & Anderson, W. (1991). Wing mass formula for subsonic aircraft. *Journal of Aircraft*, 29(4), 725–727.
- Underwood, J. & Cooke, D. (1982). A preliminary correlation of the orbiter stability and control aerodynamics from the first two space shuttle flights (STS-1 & 2) with preflight predictions. In *12th Aerodynamic Testing Conference*, number AIAA 82-0564.
- Vallado, D. (2007). *Fundamentals of astrodynamics and applications*. New York: Microcosm press/Springer.
- van Driest, E. (1958). On the aerodynamic heating of blunt bodies. *Zeitschrift für Angewandte Mathematik und Physik*, 9, 233–248.
- Varvill, R., & Bond, A. (2004). The SKYLON spaceplane. *Journal of the British Interplanetary Society*, 57, 22–32.
- Vinh, N., Busemann, A., & Culp, R. (1980). *Hypersonic and planetary entry flight mechanics*. Ann Arbor: The University of Michigan Press.
- Wadhams, T., Cassady, A., MacLean, M., & Holden, M. (2009). Experimental studies of the aerothermal characteristics of the project orion CEV heat shield in high speed transitional and turbulent flows. In *47th AIAA Aerospace Sciences Meeting*, number AIAA 2009-677.
- Wahde, M. (2008). *Biologically inspired optimization methods: An introduction*. Boston: WIT Press.
- White, F. (2006). *Viscous fluid flow*. New York: McGraw-Hill.
- Zoby, E., & Sullivan, E. (1965). Effects of corner radius on stagnation-point velocity gradients on blunt axisymmetric bodies. Technical Report TM X-106, NASA.

Index

Note: Page numbers followed by f and t indicate figures and tables respectively

A

- ACM empirical method, 56, 58
- Aerodynamic forces, 19, 29–30, 41, 49–51, 54, 139, 180, 188, 214
- Aerodynamics model, 149
 - Apollo capsule, 137–139, 138f
 - Space Shuttle, 139–144
- Aerothermodynamics, 16
 - concepts, 41
 - heat transfer
 - capsule shaped vehicles, 68–71, 68f, 70t
 - convective, 65–67, 67t
- loads
 - aerodynamics coefficients, 52–53
 - forces and moments, 50–51
 - friction, 50
 - pressure distribution, 50–52
- local-inclination method
 - ACM empirical method, 56, 58
 - effect on pressure prediction, 56, 57f
 - leeward side method, 53–54
 - Mach number effect on pressure prediction, 56, 57f, 58
 - modified Newtonian method, 54–55
 - Newtonian method, 54
 - PANAIR code, 60
 - Prandtl–Meyer expansion method, 55
 - pressure distribution on Space Shuttle, 58–60, 59f
 - selection, 60–64, 61t, 62f, 63t
 - tangent-wedge method, 55–56, 56f
 - windward side method, 53
- properties, 42–45

super/hypersonic flow characteristics
(*see* Supersonic and hypersonic flow)
viscosity, 49–50

Airfoil

- cross-sectional shape, 101–102
- PARSEC wing parameterization, 102–103
- shape parameterization, 101, 102, 102f
- spline, 105

Apollo-shaped capsule vehicle, 17

- aerodynamic coefficients
 - drag and lift coefficient, 137, 138f
 - North American Aviation, 137
 - pitch moment coefficient, 137–138, 138f
- pre-flight vs. actual in-flight coefficients, 138–139

- streamline pattern, difference in, 138
- entry trajectory, 144–145, 145f, 145t

Approach and Landing Test Vehicle (ALTV), 11

- Atmosphere model, 132, 149
- Atmospheric Reentry Demonstrator (ARD), 1, 9, 181
- Atmospheric Reentry Experimental Vehicle (AREV), 9

Atomic bomb, 3

B

- Becker, John, 3
- Bézier spline curves, 78–82, 80–81f
- Bilinear interpolation, 76
- Bredt, Irene, 3

C

Capsule-shaped vehicles, *see also* Apollo-shaped capsule vehicle
 evolution of selected point on Pareto front, 253, 254f
 guidance and control system, 149–150
 heat transfer
 angle-of-attack, 70
 coefficient determination, 71
 corner heating, 69–70, 70f
 effective nose radius, 68, 68f
 heat-rate predictions, 68–69
 stagnation region, 68
 Monte Carlo analysis
 constraint functions values, 153, 154f
 feasible and Pareto optimal solutions, 160–161, 161f
 maximum corner heat flux, 157, 158f
 maximum load factor, 155, 156f
 maximum shoulder heat flux, 153
 Newtonian stagnation-point location, 156, 158f
 in objective space, 157, 159, 159f
 Pareto-optimal results, 161, 162f
 solutions from, 159, 160f
 stagnation-point heat flux, 153–155, 155f
 untrimmable time steps, 155–156, 157f
 vehicle lengths, 157, 159f
 optimal, 254, 255–257f
 optimization, 179–181
 three-dimensional analysis, 176–179, 176–178f
 two-dimensional analysis, 162–175, 163–175f
 CARGUS (unmanned stage), 6
 Cartesian variables, 30
 Central body shape model, 132, 149
 Computational Fluid Dynamics (CFD) models, 7
 Conjugate-gradient method, 14
 Constraint function values
 capsule-shaped vehicles
 feasible and Pareto optimal solutions, 160–161, 161f
 histograms, 153, 154f
 maximum corner heat flux, 157, 158f
 maximum load factor, 155, 156f
 maximum shoulder heat flux, 153
 Newtonian stagnation-point location, 156, 158f
 in objective space, 157, 159, 159f

Pareto-optimal results, 161, 162f
 solutions from, 159, 160f
 stagnation-point heat flux, 153–155, 155f
 untrimmable time steps, 155–156, 157f
 vehicle lengths, 157, 159f
 winged vehicle
 dynamic-pressure values, 191
 histograms, 185, 186f
 maximum load factors, 187–188
 vs. parameters, 185, 187t
 Pareto-optimal solutions, 191
 Pitch stability, 191, 191f
 solutions from, 188–189, 189f–191f
 Control system, 34, 132, 149
 Crew Exploration Vehicle (CEV), 70
 Cubic spline curves, *see* Spline interpolation

D

Differential Evolution (DE) algorithm, 116
 Double Grid-MOPSO (DG-MOPSO) method, 119
 Equations of motion, 24
 aerodynamic forces, 29–30
 entry equations, 30–33
 gravitational forces, 29
 reference frames
 aerodynamic frame, 26, 27f
 body frame, 26–27, 27f
 definition, 24
 inertial frame, 24–25, 25f
 rotating frame, 25, 25f
 rotation order, 27–28
 trajectory frame, 26, 26f, 27f
 unit-axis transformations, 27–28
 vertical frame, 25–26, 25–26f

E

Euler (inviscid) solution, 138
 EXPERT (European eXperimental Re-entry Test-bed) program, 8, 9

F

Feasible over infeasible method, 118
 Fin shape, winged vehicle, 209–211, 210–211f
 Flight mechanics, 16
 environment
 atmosphere, 22–24
 central body shape, 20–21, 20f

- Earth shape, 19–20
 gravitational force, 21–22
 equations of motion, 24
 aerodynamic forces, 29–30
 entry equations, 30–33
 gravitational forces, 29
 reference frames, 24–28, 25f–27f
 guidance and control approach, 33
 attitude stability characteristics, 37–39
 capsule-shaped vehicles, 33–35
 winged vehicle, 35–37
 Force estimation methods, *see* Local-inclination methods
 Friction coefficient, 227–229
 Function evaluation, vehicle shape
 defined, 129
 top-level flow
 aerodynamic coefficient generation, 130–131, 133f
 capsule shape generation, 129–130, 131f
 evaluation of vehicle shape, 129, 130f
 of state derivative calculation, 135, 136f
 of trajectory propagation, 132–135, 134f
 winged vehicle shape generation, 129–130, 132f
 Fuselage shape, winged vehicle
 generation example, 231–243, 232f, 233t, 235f, 236f, 238f, 239f, 240t, 241–243f
 parameterization, 197–203
 constraints, 95–96, 96f
 cross-section splines determination, 93–94, 98–99
 definition, 92, 197, 199–201f
 free-form, 94
 minimum and maximum shape envelope, 96–97
 nose segment, 92–93
 radius, 97–98
 shape generation, 99–100, 99f
 spline-surface control net, 94–95, 95f
 Future European Space Transportation Initiative Programme (FESTIP), 9
 Future Launchers Preparatory Program (FLPP), 9
- G**
 Gagarin, Yuri, 5
- Genetic Algorithms (GAs), 116
 Geostationary Transfer Orbit (GTO), 9
 Glenn, John, 5
 Gravitational acceleration, 22, 36
 Gravitational forces, 19, 21, 29, 30, 33
 Gravity model, 132, 149
 Greenwich Mean Sidereal Time (GMST), 25
 Guidance and control (G&C) system, 19
 Guidance Navigation and Control (GNC) System, 132
 Guidance system, 132, 133, 135, 149
- H**
 Heat transfer
 capsule shaped vehicles
 angle-of-attack, 70
 coefficient determination, 71
 corner heating, 69–70, 70t
 effective nose radius, 68, 68f
 heat-rate predictions, 68–69
 stagnation region, 68
 conceptual design tools, 65
 convective, 65–67, 67t
 Hermite spline curves, 78–82, 80–81f
 HORUS (manned stage), 6–7, 8f, 60, 103, 125, 126, 150, 198, 207
 HORUS 2B vehicle, 92, 93f, 109
 Hypersonic Aerospace Sizing Analysis (HASA), 107–109
 Hypersonic local inclination methods, 149
- I**
 Intercontinental ballistic missiles (ICBMs), 3
 Intermediate eXperimental Vehicle (IXV), 9
 International Space Station (ISS), 7
- L**
 Langley Wireframe Geometry (LaWGS) Format, 109–111, 110f
 Lift-over-drag capsule-shaped vehicle, *see* Apollo-shaped capsule vehicle
 Linear interpolation, 75
 Local-inclination methods, 16, 53–54
 ACM empirical method, 56, 58
 effect on pressure prediction, 56, 57f
 leeward side method, 53–54
 Mach number effect on pressure prediction, 56, 57f, 58
 Newtonian method, 54
 modified, 54–55

PANAIR code, 60
Prandtl–Meyer expansion method, 55
pressure distribution on Space Shuttle,
 58–60, 59f
selection, 60–64, 61t, 62f, 63t
tangent-wedge method, 55–56, 56f
windward side method, 53
Local-pressure methods, 13
Low Earth Orbit (LEO), 2, 13

M

Mach 5, 2, 3, 10
Mach angle, 46
Mach-7 wind tunnel, 3
Mass model, 107–109
Mercury-Atlas-6 flight, 5
Model validation, 17

aerodynamics model
 Apollo capsule, 137–139, 138f
 Space Shuttle, 139–144
trajectories
 Apollo capsule, 144–145, 145f, 145t
 Runge-Kutta 4th order integrator,
 144, 149
 Shuttle-Shape, 146–148, 146f, 147f,
 148t

Modified Newtonian-Prandtl Meyer theory,
 55

Monte Carlo analysis, 151
capsule-shaped vehicles
 feasible and Pareto optimal solutions,
 160–161, 161f
 histograms, 153, 154f
 maximum corner heat flux, 157, 158f
 maximum load factor, 155, 156f
 maximum shoulder heat flux, 153
 Newtonian stagnation-point location,
 156, 158f
 in objective space, 157, 159, 159f
 Pareto-optimal results, 161, 162f
 solutions from, 159, 160f
 stagnation-point heat flux, 153–155,
 155f
 untrimmable time steps, 155–156,
 157f
 vehicle lengths, 157, 159f

winged vehicle
 constraint function values (*see* Con-
 straint function values)
 shape parameters, 183
 simulation, 183

Monte Carlo simulation, 183

MOPSO, *see* Multi-Objective Particle Swarm Optimization (MOPSO) method
Multidisciplinary Design Optimization (MDO), 14, 15, 181, 226
Multi-Objective Particle Swarm Optimiza-
tion (MOPSO) method, 16, 119
advantages, 120
default settings, 120, 121t
DG-MOPSO method, 119
modification, 119
non-dominated initial solutions, 119
objective space, 119
optimization iterations, 119–120
optimizer, 120
Pareto-optimal solutions, 119
roulette-wheel selection, 120

N

Navigation system, 132
Newtonian method, 54
Non-Uniform Rational B-Splines (NURBS)
surfaces, 12
Numerical interpolation
basic concepts, 73
 bilinear interpolation, 76
 continuity and convexity, 74–75, 75f
 linear interpolation, 75
Hermite-spline surfaces, 84–85, 84f
splines
 Bézier and Hermite, 79–82, 80–81f
 computer modeling and visualization
 of curves, 77
 control points, 78
 data points, 78
 definition, 77
 derivative, 78
 intermediate points, 78
 rational B-splines, 77
 self-intersection and concavity elim-
 ination, 82–84
 types and order, 78–79
 use of, 77
typical applications, 73

O

Optimization, *see also* Shape optimization
algorithm (*see* Particle Swarm Optimiza-
tion (PSO) method)
general problem (design)
 multi-objective, 114–116, 116f
 single-objective, 114

- statement, 113–114
shape
 constraints, 123–127
 performance criteria, 121–123
Orbital Test Vehicle (OTV), 11
- P**
Pareto fronts, 115–116, 116f
'Particles-in-a-box' model, 42
Particle Swarm Optimization (PSO) method,
 113
 constraint handling, 118
 exploration vs. exploitation, 117
 multi-objective
 advantages, 120
 default settings, 120, 121t
 DG-MOPSO method, 119
 modification, 119
 non-dominated initial solutions, 119
 objective space, 119
 optimization iterations, 119–120
 optimizer, 120
 Pareto-optimal solutions, 119
 roulette-wheel selection, 120
 number of iterations, 117–118
 particle initialization, 117
 personal and group best particle, 117
Prandtl–Meyer expansion method, 55, 58
Prandtl–Meyer function, 48, 49t
Prandtl number, 66
PSO method, *see* Particle Swarm Optimiza-
tion (PSO) method
- R**
Rankine–Hugoniot relations, 45
Reaction Control System (RCS), 33
Re-entry missions
 in 20th century
 'Aerospace Plane', 4
 atmospheric entry, 5–6, 6f
 Bredt, Irene, 3
 HORUS vehicle, 6–7, 8f
 rocketry and spaceflight research, 2–
 3
 Sänger, Eugen, 3
 Sänger II, 6
 Space Shuttle Atlantis, development
of, 6, 7f
 three entry capsules 1960s, 5, 5f
 V-2 rocket, 3
 X-20/ Dyna-Soar, 4, 4f
 X-15 in flight, 4, 4f
- X-38 vehicle during drop test, 7, 9f
in 21th century
 AREV, 9
 EXPERT program, 8–9
 FESTIP, horizontal launch, 9–10
 FLPP, 8–9
 IXV, 9
 sound technology programs, 8
 space plane concept, 10
 Space Ship Two, 11, 13f
 Test-flight vehicle Phoenix-1, 10, 10f
 X-37B Orbital Test Vehicle, 11, 12f
Reference atmospheres, 22, 23
Reference frames
 aerodynamic frame, 26, 27f
 body frame, 26–27, 27f
 definition, 24
 inertial frame, 24–25, 25f
 rotating frame, 25, 25f
 rotation order, 27–28
 trajectory frame, 26, 26f, 27f
 unit-axis transformations, 27–28
 vertical frame, 25–26, 25–26f
Reynolds-Average Navier Stokes (RANS)
 aerodynamics model, 15
Reynolds number, 49, 227, 229
Runge–Kutta–Fehlberg methods, 31
- S**
Sänger, Eugen, 3
Sänger II, 6
Second-Order Shock-Expansion (SOSE)
 code, 15
Shape optimization, 1
 aerodynamics code, 15
 aeroshell shapes, 12–13
 capsule-shaped vehicles, 179–181
 three-dimensional analysis, 176–
 179, 176–178f
 two-dimensional analysis, 162–175,
 163–175f
 constraints
 capsule-shaped vehicle, 124–125
 entry vehicle, 123
 minimum and maximum values of
 shapes, 127
 winged vehicle, 125–126
 design variables, 13–14
 HL-20, 13–14, 15f
 NURBS surfaces, 12
 parameterizations, 14–15
 performance criteria, 121–123

- problem of, 12, 13
robust shape, 13
selected multi-objective optimal shapes, 12, 14f
vehicle shapes, 15, 16f
of waverider vehicles, 13
winged vehicle, 224–226
 - baseline optimization, 192–211, 192–211f
 - heat-rate tracking optimization, 217–224, 217–223f
 - pitch-stable optimization, 211–216, 212–215f
- Shape parameterization
 - definition, 87
 - fuselage shape vehicle (*see* Fuselage shape, winged vehicle)
 - minimum and maximum values, 87–88
 - physical parameter, 87
 - wing shape vehicle (*see* Winged vehicle parameterization)
- Simulation code
 - architecture, 129
 - implementation of, 129
 - settings
 - aerodynamics model, 149
 - atmosphere model, 149
 - capsule-shaped vehicle, 149–150
 - central body characteristics, 149
 - forces, 149
 - gravity model, 149
 - integrator Runge-Kutta 4th order, 149
 - wind model, 149
 - winged vehicle, 150–151
- top-level flow
 - aerodynamic coefficient generation, 130–131, 133f
 - capsule shape generation, 129–130, 131f
 - evaluation of vehicle shape, 129, 130f
 - of state derivative calculation, 135, 136f
 - of trajectory propagation, 132–135, 134f
 - winged vehicle shape generation, 129–130, 132f
- validation of aerodynamics code (*see* Model validation)
- Space Shuttle, 1, 2, 4, 6, 7f, 17, 126
- Space Shuttle-shaped vehicle
 - aerodynamic coefficients
 - body flap increments, 142–143f, 143
 - elevon increments, 140–143, 141–142f
 - flight vs. wind-tunnel coefficients, 140, 140f
 - lift vs. drag coefficients, 139, 139f
 - longitudinal force coefficients, 143
 - moment coefficients, 139–140, 140f
 - pitch moment coefficients, 143–144
 - shadowing effect, 140
 - stability derivatives, 140, 141f
 - yaw-moment coefficients, 144
 - entry trajectory, 146–148, 146f, 147f, 148t
- Space Shuttle wireframe model, 110, 110f
- Space Transportation System (STS), 6
- Spherical harmonics gravity model, 22
- Spline interpolation
 - Bézier and Hermite, 79–82, 80–81f
 - computer modeling and visualization of curves, 77
 - control points, 78
 - data points, 78
 - definition, 77
 - derivative, 78
 - intermediate points, 78
 - rational B-splines, 77
 - self-intersection and concavity elimination, 82–84
 - types and order, 78–79
 - use of, 77
- Standard atmospheres, 22, 23
- Stanton number, 65, 66
- Supersonic and hypersonic flow
 - coefficients in Prandtl–Meyer function inversion, 48–49, 49f
 - continuum flow, 49
 - expansion waves, 48
 - flow behavior of sharp vs. blunt vehicles, 46–48, 47f
 - oblique shock waves
 - flow over, 45–46, 46f
 - $\theta - \beta - M$ plot for, 46, 47f
 - Rankine–Hugoniot relations, 45
- Supersonic/Hypersonic Arbitrary Body Program (S/HABP), 7
- T**
- Tabu-search method, 119
- Tangent-wedge method, 55–56, 56f
- Thermal protection system (TPS), 3, 4, 6, 13, 132
- Three-dimensional optimization

- capsule-shaped vehicles
 constraint function values, 178, 179f
 full front and projected on three objective planes, 176, 176f
 shape parameters, 177f, 179
 vs. two-dimensional optimization, 179
- winged vehicle, 192, 192f
- Total enthalpy, 44, 45, 65, 66
- TPS, *see* Thermal protection system (TPS)
- Two-dimensional optimization
 capsule-shaped vehicles
 range *vs.* heat load, 162–167, 163–166f
 range *vs.* volumetric efficiency, 171–175, 172–175f
 volumetric efficiency *vs.* heat load, 167–170, 168–171f
 winged vehicle, 192, 193f
- Two-Stage-To-Orbit (TSTO) concept, 6
- V**
- Vehicle external geometry
 capsule shape parameterization
 constituent shape parameters, 88–89, 90f
 exploded view of, 88, 89f
 minimum and maximum values, 91, 91t
 re-entry, 88, 88f
 definition, 88
 meshed surfaces
 fusiform objects, 111
 LaWGS Format, 109–111
 objects, 109–110
 panel, definition of, 110
 planar objects, 111
 settings, 111
 Space Shuttle wireframe model, 110, 110f
 total surface area and internal volume determination, 111
 winged-vehicle shape parameterization
 fuselage (*see* Fuselage shape, winged vehicle)
 fuselage-wing interface, 105–107
 mass model, 107–109
 wing shape, 100–105
- Viscous-force approximation, 227–230
- V-2 rocket, 3
- W**
- Winged vehicle, *see also* Space Shuttle-shaped vehicle, 1–2
 evolution of selected point on Pareto front, 259, 260t
 generation example
 fuselage shape, 231–243, 232f, 233t, 235f, 236f, 238f, 239f, 240t, 241–243f
 wing shape, 243–252, 244–252f
- Monte Carlo analysis
 constraint function values (*see* Constraint function values)
 shape parameters, 183
 simulation, 183
 optimal, 260, 260–267f
 representative views of, 183, 184f
 shape optimization, 224–226
 baseline optimization, 192–211, 192–211f
 heat-rate tracking optimization, 217–224, 217–223f
 pitch-stable optimization, 211–216, 212–215f
 simulation settings, 150–151
- Winged vehicle parameterization
 airfoil shapes (*see* Airfoil)
 fuselage
 constraints, 95–96, 96f
 cross-section splines determination, 93–94, 98–99
 definition, 92
 free-form, 94
 minimum and maximum shape envelope, 96–97
 nose segment, 92–93
 radius, 97–98
 shape generation, 99–100, 99f
 spline-surface control net, 94–95, 95f
 fuselage-wing interface
 determining *z*-translation of wings, 105
 leading-edge matching, 106, 107f
 relative position, 105
 generation algorithm, 104–105
 Hermite-spline surface, 104
 HORUS 2B reference vehicle, 92, 93f
 mass model, 107–109
 platform shape, 101–104, 103f
 with splines locations, 103, 104f
 wing shape
 airfoil shapes (*see* Airfoil)
 generation algorithm, 104–105
 Hermite-spline surface, 104

- platform shape, 101–104, 103f
with splines locations, 103, 104f
- Wing shape, 61, 203–209, 204–206f
generation example, 243–252, 247f,
248f, 250f, 250t, 251–252f
- winged vehicle parameterization
airfoil shapes (*see* Airfoil)
definition, 203, 204–205f
generation algorithm, 104–105
Hermite-spline surface, 104
- platform shape, 101–104, 103f
with splines locations, 103, 104f

X

- X-37B Orbital Test Vehicle, 11, 12f
- X-20/ Dyna-Soar vehicle, 4, 4f
- X-15 vehicle, 4, 4f
- X-38 vehicle, 7, 9f